Bridging between Boron & Nanoworld: Versatile Combinations & Emerging Applications

Jewel Ann Maria Xavier

UAB
Universitat Autònoma de Barcelona

Bridging between Boron & Nanoworld:
Versatile Combinations & Emerging Applications

Jewel Ann Maria Xavier

DOCTORAL THESIS
Doctoral Program in Chemistry

Supervisor
Prof. Francesc Teixidor Bombardó

Institut de Ciència de Materials de Barcelona (ICMAB) – CSIC
Department de Química – Facultat de Ciències
2023

A thesis submitted towards the partial fulfilment of Doctoral degree in Chemistry by Jewel Ann Maria Xavier.

Prof. Francesc Teixidor Bombardó

Research Professor (Ad- Honorem),

Inorganic Materials & Catalysis Laboratory (LMI)

Institut de Ciència de Materials de Barcelona – CSIC

Bellaterra, 13th September 2023

El Prof. Francesc Teixidor Bombardó, Profesor de Investigació actualmente Ad-Honorem del Consejo Superior de Investigaciones Científicas (CSIC) del Institut de Ciència de Materiales de Barcelona (ICMAB)

CERTIFICA:

Que Jewel Ann Maria Xavier, graduada y master en Ciència, ha realizado bajo su dirección el trabajo de tesis que lleva por título "**Bridging between Boron & Nanoworld: Versatile Combinations & Emerging Applications**" que queda recogido en esta memoria para optar al título de Doctora en Química por la Universidad Autónoma de Barcelona.

Para que así conste y tenga los efectos oportunos, firma este certificado en Bellaterra a 13 de Septiembre de 2023.

Prof. Francesc Teixidor Bombardó

ICMAB-CSIC

This work was financially supported by Programme for Centres of Excellence in R&D (CEX2019-000917-S) as well as the Spanish Ministerio de Economia y Competitividad (CTQ2016-75150-R) and Generalitat de Catalunya (2014/SGR/149). The research also received support from the Projecte de la Unió Europea H2020-LEIT-NMBP/0345, KARDIATOOL (Grant Nº -768686). J. A. M. Xavier also acknowledges the DOC-FAM programme with funding from the European Union's Horizon 2020 research and innovation programme under the Marie Sklodowska-Curie grant agreement No 754397.

The thesis Committee evaluating the dissertation consists of:

- President: **Prof. Salvador Ventura**, Insititut de Biotechnologia i Biomedicina, UAB
- Secretary: **Prof. Montserrat Diéguez**, Universitat Rovira i Vigili
- Vocal: **Dr. Santiago Nonell**, Universitat Ramon Llull

- Substitute 1: **Prof. Joan Bausells -** Institut de Microelectrònica de Barcelona (IMB-CNM)
- Substitute 2: **Dr. Oscar Pamies –** Universitat Rovira i Vigili

The thesis is dedicated to my Amma, Appa & Immy.

Acknowledgement

Gratitude is the memory of the heart.
Ph.D. has been a long and challenging journey with its own triumphs and blows; and I would like to express my sincere heartfelt gratitude to all who have been present throughout the journey. Their unwavering support, guidance and encouragement have been indispensable in shaping the work. A ‘thank you’ would not suffice but it is my sincerest attempt to convey the depth of my appreciation to all who have been part of my journey.

I would like to begin by thanking the person without whom none of this would have been possible, my supervisor and mentor, Prof. Francesc Teixidor. For the past four years he has been an unwavering pillar of support, guiding me through all the ups and downs with the utmost patience and kindness. He has been a tremendous mentor who has an invaluable wealth of knowledge and experience both scientifically and in life. I would never forget the scientific discussions, brain-storming sessions and the immense amount of chatter on all things under the sun we have had. I’m truly honoured to have had the privilege of working with you, thank you! You have truly inspired and moulded me into a better researcher and someday I hope to have at least have the amount of love and passion that you have for science.

I would like to further extend my gratitude to Prof. Clara Viñas who has been there throughout with her extensive knowledge and keen observations and remarks. My sincerest gratitude to Dr. Rosario Nuñez and Dr. Jose Giner who have kind-heartedly been there with their unquivering support and guidance throughout. It was a pleasure to have had the opportunity to collaborate with Dr. Isabel Romero on various topics and projects. I would like express my gratitude to Prof. Encarnacion and Dr. Tania who had gladly welcomed me to their group in Madrid as part of my research stay. I’m grateful for all the opportunities I have received from these astounding researchers.

Most of my Ph.D. life have been in and around our LMI group and there aren’t enough words to express my gratitude I have for each and every, past and current, members of the group. I would like to thank Dr.Arpita who welcomed me to the lab and patiently introduced me to its inner workings, helping me acclimatize to the environment. Extending my sincerest gratitude to all the group members, Dr. Isabel Guerrero, Dr. Miquel, Dr. Sohini, Dr. Zhen, Dr. Maria Jose, Xiao and all the former members. I am grateful to Dr. Isabel Guerrero for always being willing to help and for being an amazing collaborator. Special thanks to Miquel and Sohini with whom I have shared lots of memorable and ‘tricky’ moments in the lab. Thank you all for being always there and making the Ph.D. journey a lot easier. Thank you! Special mention to our laboratory assistant Jordi Cortes for ensuring we have everything and the lab runs smoothly, despite the chaos we create.

ICMAB has been the definition of home for me for the past few years and all the members of the institute have been kind and pleasurable to work with. Dr. Adara, Dr. Sumithra, Dr. Artur, Dr. Daniel, Dr. Marta, Aiswarya, Teresa, Amanda, Raquel, Joseline, Jose Catalan, Vladimir and all other ICMABers who have been made the journey even more memorable with the lunchtime chats, ‘chai’ breaks and office chit-chats. It was a pleasure to have had the opportunity to work with you all. I would also like to express my gratitude to all the DOC-FAM fellows and Dr. Laura for the invaluable net-working experience and connections. I would like to all the technicians, particularly Dr. Judith, Dr. Amable, Dr. Anna, Dr. Vega, for all their support and patience. I would also like to thank all the administrative staff as well the communication team of ICMAB for their endeavouring assistance. Extending my gratitude to the former, Prof. Xavier, and current, Dr. David, directors of ICMAB for providing all the necessary requirements needed for the completion of the thesis. Thank you ICMAB for everything! I also wish to thank the Department of Chemistry, UAB, Ph.D. co-ordinator Dr. Gregory and secretary, Elena for all their support throughout the years. My Ph.D. journey would have been incomplete without each and every one of you.

Home away from home – Barcelona has been the place where I learnt to be independent, pushing my comfort zone to its edges. And it would not have been an easy journey in an unknown country with a rich and varied culture, if not for a few people – my ‘Only stickers’ group people. From the first Costa Brava trip till date, you guys have been amazing and I’m grateful to have known each and every one of you. For all the ‘egg puffs’ and all the vegetables you made me eat, I’m extremely grateful for having found you, Adara. You have seen the good, bad and ugly and yet have always stood by me. Thank you for all the care and advice you gave. Tagging along us, Diya, has been my ‘chica’ who with her realistic views on life have always kept me grounded. You are amazing and I’m thankful for a friend like you. Kudos, GOPP!! The first friend in Barcelona, Sohini, has always had my back and she never fails to amaze me with her multi-tasking and extremely meticulous planning skills. Aiswarya, Ashitha and Aparna with their ‘new-gen’ energy has always kept my spirits up and trips with them has always been memories to be cherished. We began our journey almost at the same time and you guys have been very supportive throughout, Sebin and Chithran. Thomas, Stephy, Sarath, Jyothish, Vrinda, Rinu, Vikas, Nitesh, Namitha, Gayathri and all my dear ones in Barcelona, thank you from the bottom of heart for just being you and being there. Life in Barcelona would be incomplete without mentioning Nati with whom I have been living since the time I arrived and has always cared for me like a mother.

My two pillars of strengths, Govind and Swetha, who have been bearing with me for the past 10 years without ever getting tired. I am lucky to have friends who would even forge your sign to make you apply for a position. If it was not for Sarangi, I may not even be writing this thesis. So, thank you both for helping me through all the lows and highs of life without any judgments. Anu and Kezia have always been the cheerful souls who have always wanted the best for me. Thank you all!! I would also like to thank Jithin, Jesil, Gokul, Alma, Ashley, Nived, Sharafu, Devuchi and Rintu chechi for all their support.

These pages would be incomplete without thanking my beloved parents, Appa and Amma. They have always supported and stood by my decisions. Their constant encouragement and advice have propelled me to excel in life with confidence. Thank you so much for all that you have done! My grandmother, Immy, and my sister, Innus, who have always wanted the best for me. Thank you!! And then, my person – Eldhos, there isn’t anything that I can say to thank you for all that you are to me. The only one who has seen the bad, the ugly and the ugliest, who has gone through all the turmoil of a Ph.D. journey without actually doing one. You know what you mean to me and I’m extremely grateful to have you in my life. Thank you!!!!

The whole experience of Ph.D. has turned me to be a better researcher and an even better human, teaching values and lessons beyond science. Thank you to all who ever a part of the journey.

Lots of love,
Jewel

Research articles accepted by the Department of Chemistry, UAB, to be presented in thesis as a ‘compendium’ of articles with the authorization from all the concerning co-authors in the order of their appearance:

- Potential application of metallacarboranes as an internal reference: an electrochemical comparative study to ferrocene.
  Jewel Ann Maria Xavier, Clara Viñas, Encarnación Lorenzo, Tania García-Mendiola* and Francesc Teixidor* *Chem. Commun.*, **2022**, 58, 4196-4199. https://doi.org/10.1039/D2CC00424K.

- Single stop analysis of a protein surface using molecular probe electrochemistry.
  Jewel Ann Maria Xavier, Isabel Fuentes, Miquel Nuez-Martinez, Clara Viñas and Francesc Teixidor*, *J. Mater. Chem. B*, **2023,** Advance Article. https://doi.org/10.1039/D3TB00816A.

- Non-covalently Linked Metallacarboranes on Functionalized Magnetic Nanoparticles as Highly Efficient, Robust and Reusable Photocatalysts in Aqueous Medium.
  Isabel Guerrero, Arpita Saha, Jewel Ann Maria Xavier, Clara Vinas, Isabel Romero Garcia * and Francesc Teixidor* *ACS Appl. Mater. Interfaces*, **2020**, 12(50), 56372-56384. https://doi.org/10.1021/acsami.0c17847.

List of Publications

- **Xavier, J.A.M**.; Fuentes, I.; Nuez-Martínez, M.; Viñas, C.; Teixidor, F. Single Stop Analysis of a Protein Surface Using Molecular Probe Electrochemistry. *J. Mater. Chem. B* **2023**, Advance article.
- **Xavier, J.A.M**.; Viñas, C.; Lorenzo, E.; García-Mendiola, T.; Teixidor, F. Potential Application of Metallacarboranes as an Internal Reference: An Electrochemical Comparative Study to Ferrocene. *Chem. Commun.* **2022**, *58,* 4196–4199.
- **Xavier, J.A.M**; Fuentes, I.; Nuez-Martínez, M.; Kelemen, Z.; Andrio, A.; Viñas, C.; Compañ, V.; Teixidor, F. How to Switch from a Poor PEDOT:X Oxygen Evolution Reaction (OER) to a Good One. A Study on Dual Redox Reversible PEDOT:Metallacarborane. *J. Mater. Chem. A* **2022**, *10,* 16182–16192.
- Bennour, I.; Ramos, M.N.; Nuez-Martínez, M.; **Xavier, J.A.M**.; Buades, A.B.; Sillanpää, R.; Teixidor, F.; Choquesillo-Lazarte, D.; Romero, I.; Martinez-Medina, M.; et al. Water Soluble Organometallic Small Molecules as Promising Antibacterial Agents: Synthesis, Physical–Chemical Properties and Biological Evaluation to Tackle Bacterial Infections. *Dalt. Trans.* **2022**, *51*, 7188–7209.
- Abdelgawwad, A.M.A.; **Xavier, J.A.M.**; Roca-Sanjuán, D.; Viñas, C.; Teixidor, F.; Francés-Monerris, A. Light-Induced On/Off Switching of the Surfactant Character of the o-Cobaltabis(Dicarbollide) Anion with No Covalent Bond Alteration. *Angew. Chemie Int. Ed.* **2021**, *60*, 25753–25757.
- Nuez-Martinez, M.; Pinto, C.I.G.; Guerreiro, J.F.; Mendes, F.; Marques, F.; Muñoz-Juan, A.; **Xavier, J.A.M.**; Laromaine, A.; Bitonto, V.; Protti, N.; et al. Cobaltabis(Dicarbollide) ([o-Cosan]−) as Multifunctional Chemotherapeutics: A Prospective Application in Boron Neutron Capture Therapy (BNCT) for Glioblastoma. *Cancers.* **2021**, *13,* 6367.
- Guerrero, I.; Saha, A.; **Xavier, J.A.M.**; Viñas, C.; Romero, I.; Teixidor, F. Noncovalently Linked Metallacarboranes on Functionalized Magnetic Nanoparticles as Highly Efficient, Robust, and Reusable Photocatalysts in Aqueous Medium. *ACS Appl. Mater. Interfaces* **2020**, *12,* 56372–56384.
- **Xavier, J.A.M.**; Viñas, C.; Teixidor, F. “Synthesis of Colloidal Long-lived Iron-oxide Magnetic Nanoparticles: A Simplistic Laboratory Approach.” (Submitted)

Abstract

The work presented in this thesis entails the research carried out in the Inorganic Materials and Catalysis Laboratory group (LMI) under the supervision of Prof. Francesc Teixidor over the course of the Doctoral program. The dissertation is presented as a compendium of articles published or to be published in the near future. The doctoral thesis delves into the multifaceted world of boron chemistry, particularly focusing on θ-metallacarboranes, and their integration with tailored nanoparticles, uncovering a realm of novel applications and opportunities. The characterizations and applications of θ-metallacarboranes and nanoparticles together present a dynamic frontier in modern materials chemistry with an expansive range of possibilities.

The thesis begins with a brief *Introduction* on the diverse facets of metallacarboranes and nanoparticles serving as a foundation for comprehending the subsequent chapters. The comprehensive investigations commence with a detailed and thorough study on the electrochemical properties of metallacarboranes, particularly cobaltabis(dicarbollide) and ferrabis(dicarbollide), in both aqueous and non-aqueous systems with a comparative study of *Metallacarboranes vs. Ferrocene*. Ferrocene and its derivatives have long been the benchmark internal reference in electrochemistry for various processes. Yet, their applications are constrained by challenges related to solubility and chemical modifications. In this regard, the chapter deals with potential advent of metallacarboranes as 'universal' internal reference systems.

The following chapter on *Metallacarboranes & Proteins* stems from the pre-requisite knowledge of the strong non-covalent interaction between [*o*-COSAN]$^-$ and amine groups through N-H···B-H dihydrogen bond formation. Visualization of proteins in their native form and environment without any interferences has always been a challenging task. Hence, in this study we have tackled the 'surface' of a protein with respect to their interaction with the 'small molecule' redox-active probe, [*o*-COSAN]$^-$, employing facile and robust electrochemical measurements. These studies aid in gaining a deeper insight on protein surfaces which can be valuable for modifying proteins for drug designs and bio-technology.

Tailoring metallacarboranes onto surface engineered magnetic nanoparticles opens a new avenue for exploring and exploiting the virtues of both these materials. Thus, the subsequent chapter explores the synthesis and characterization of magnetic nanoparticles and delves into the applications of the conjecture: *Metallacarboranes & MNPs*. Synthesis of size-controlled, colloidally stable magnetic nanoparticles with appreciable magnetic properties has always been a challenge. Hence, in the chapter we propose a novel method for the synthesis of colloidally stable magnetic nanoparticles without any surfactant or capping agents. The tailoring of the metallacarboranes onto the surface functionalized magnetic nanoparticles is achieved, yet again, by exploiting the strong non-covalent di-hydrogen bonds. The chapter explores the application of these hybrid materials in photocatalysis of alcohols as well as begets the question of modifying a system according to the needs.

The lack of fluorescence as well as the capability of metallacarboranes as efficient and robust catalysts are further explored in the chapter on *Metallacarboranes & Energy* wherein the ability of [*o*-COSAN]$^-$ as a 'small molecule' electrode is investigated. The catalytic prowess of the metallacarboranes is studied in detail. Extending the study further into the lack of fluorescence in metallacarboranes, the ability of [*o*-COSAN]$^-$ as an efficient fluorescence quencher with regard to amine functionalized carbon quantum dots is studied. The fundamentals of the photophysical process underlying between *Metallacarboranes & C-dots* are investigated thoroughly and in-depth. These hybrid materials incorporating the virtue of an 'on/off' fluorescence switching mode opens new avenues to be ventured.

The thesis navigates through various applications of metallacarboranes and nanoparticles aiming to address critical challenges and open new avenues for scientific advancement and technological progress.

Resumen

El trabajo presentado en esta tesis implica la investigación llevada a cabo en el grupo de Laboratorio de Materiales Inorgánicos y Catálisis (LMI) bajo la supervisión del Prof. Francesc Teixidor a lo largo del programa de doctorado. La tesis se presenta como un compendio de artículos publicados o que se publicarán en un futuro próximo. La tesis doctoral profundiza en el mundo multifacético de la química del boro, centrándose particularmente en los θ-metalacarboranos, y su integración con nanopartículas a medida, descubriendo un reino de nuevas aplicaciones y oportunidades. Las caracterizaciones y aplicaciones de θ-metalacarboranos y nanopartículas juntas presentan una frontera dinámica en la química de materiales moderna con una amplia gama de posibilidades.

La tesis comienza con una breve *Introducción* sobre las diversas facetas de los metalacarboranos y nanopartículas que sirve de base para comprender los capítulos siguientes. Las investigaciones exhaustivas comienzan con un estudio detallado y exhaustivo sobre las propiedades electroquímicas de los metalacarboranos, particularmente cobaltabis (dicarbolluro) y ferrabis (dicarbolluro), tanto en sistemas acuosos como no acuosos con un estudio comparativo de *Metalacarboranos vs. Ferroceno*. El ferroceno y sus derivados han sido durante mucho tiempo la referencia interna de referencia en electroquímica para diversos procesos. Sin embargo, sus aplicaciones están limitadas por dificultades relacionadas con la solubilidad y las modificaciones químicas. En este sentido, el capítulo trata del posible advenimiento de los metalacarboranos como sistemas de referencia internos "universales".

El siguiente capítulo sobre *Metalacarboranos & Proteínas* deriva del conocimiento previo de la fuerte interacción no covalente entre los grupos $[o\text{-COSAN}]^-$ y amina a través de la formación de enlaces de dihidrógeno N-H···B-H. La visualización de proteínas en su forma y entorno nativos sin interferencias siempre ha sido una tarea desafiante. Por lo tanto, en este estudio hemos abordado la 'superficie' de una proteína con respecto a su interacción con la sonda redox activa basada en una 'molécula pequeña', [o-COSAN]-, empleando mediciones electroquímicas fáciles y eficientes. Estos estudios ayudan a obtener una visión más profunda de las superficies de las

proteínas que pueden ser valiosas para modificar las proteínas para el diseño de fármacos y la biotecnología.

La adaptación de metalacarboranos a nanopartículas magnéticas de ingeniería superficial abre una nueva vía para explorar y explotar las virtudes de estos dos materiales. Así, el siguiente capítulo explora la síntesis y caracterización de nanopartículas magnéticas y profundiza en las aplicaciones de la conjetura: *Metalacarboranos & MNPs.* La síntesis de nanopartículas magnéticas coloidalmente estables y de tamaño controlado con propiedades magnéticas atractivas siempre ha sido un desafío. Por ello, en este capítulo proponemos un método novedoso para la síntesis de nanopartículas magnéticas coloidalmente estables sin tensioactivos ni agentes de recubrimiento.La adaptación de los metalacarboranos a las nanopartículas magnéticas funcionalizadas en la superficie se logra, una vez más, explotando los fuertes enlaces de dihidrógeno no covalentes. El capítulo explora la aplicación de estos materiales híbridos en la fotocatálisis de alcoholes, así como la cuestión de modificar un sistema de acuerdo con las necesidades.

La falta de fluorescencia, así como la capacidad de los metalacarboranos como catalizadores eficientes y robustos se exploran más a fondo en el capítulo sobre *Metalacarboranos & Energía,* en el que se investiga la capacidad de [*o*-COSAN]$^-$ como un electrodo tipo "molécula pequeña". La capacidad catalítica de los metalacarboranos se estudia en detalle. Ampliando el estudio sobre la falta de fluorescencia en los metalacarboranos, se estudia la capacidad del [o-COSAN]- como eficiente quencher de fluorescencia con respecto a los puntos cuánticos de carbono funcionalizados con aminas. Los fundamentos del proceso fotofísico subyacente entre *Metalacarboranos & C-dots* se investigan a fondo y en profundidad. Estos materiales híbridos que incorporan la característica de un modo de conmutación de fluorescencia 'on/off' abren nuevas vías para explorar.

La tesis navega a través de diversas aplicaciones de metalacarboranos y nanopartículas con el objetivo de abordar desafíos críticos y abrir nuevas vías para el avance científico y el progreso tecnológico.

Resum

El treball presentat en aquesta tesi implica la recerca duta a terme en el grup de Laboratori de Materials Inorgànics i Catàlisi (LMI) sota la supervisió del Prof. Francesc Teixidor al llarg del programa de doctorat. La tesi es presenta com un compendi d' articles publicats o que es publicaran en un futur proper. La tesi doctoral aprofundeix en el món multifacètic de la química del bor, centrant-se particularment en els θ-metal·lacarborans, i la seva integració amb nanopartícules a mida, descobrint un regne de noves aplicacions i oportunitats. Les caracteritzacions i aplicacions de θ-metal·lacarborans i nanopartícules juntes presenten una frontera dinàmica en la química de materials moderna amb una àmplia gamma de possibilitats.

La tesi comença amb una breu *Introducció* sobre les diverses facetes dels metal·lacarborans i nanopartícules que serveix de base per comprendre els capítols següents. Les investigacions exhaustives comencen amb un estudi detallat i exhaustiu sobre les propietats electroquímiques dels metal·lacarborans, particularment cobaltabis(dicarbollur) i ferrabis(dicarbollur), tant en sistemes aquosos com no aquosos amb un estudi comparatiu de *Metal·lacarborans vs. Ferrocè*. El ferrocè i els seus derivats han estat durant molt de temps la referència interna de referència en electroquímica per a diversos processos. No obstant això, les seves aplicacions estan limitades per problemes relacionats amb la solubilitat i les modificacions químiques. En aquest sentit, el capítol tracta del possible adveniment dels metal·lacarborans com a sistemes de referència interns "universals".

El següent capítol sobre *Metal·lacarborans & Proteïnes* es deriva del coneixement previ de la forta interacció no covalent entre els grups [o-COSAN]$^-$ i amina a través de la formació d'enllaços de dihidrogen N-H···B-H. La visualització de proteïnes en la seva forma i entorn nadius sense interferències sempre ha estat una tasca desafiant. Per tant, en aquest estudi ens hem apropat a la 'superfície' d'una proteïna respecte a la seva interacció amb la sonda redox activa de 'molècula petita', [o-COSAN]-, emprant mesuraments electroquímics fàcils i eficaces. Aquests estudis ajuden a obtenir una visió més profunda de les superfícies de les proteïnes que poden ser valuoses per modificar les proteïnes per al disseny de fàrmacs i la biotecnologia.

L'adaptació de metal·lacarborans a nanopartícules magnètiques d'enginyeria superficial obre una nova via per explorar i explotar les capacitats d'aquests dos materials. Així, el següent capítol explora la síntesi i caracterització de nanopartícules magnètiques i aprofundeix en les aplicacions de la conjectura: *Metal·lacarborans & MNPs*. La síntesi de nanopartícules magnètiques col·loïdalment estables i de mida controlada amb propietats magnètiques apreciables sempre ha estat un desafiament. Per tant, en el capítol proposem un mètode nou per a la síntesi de nanopartícules magnètiques col·loïdalment estables sense cap surfactant o agent que cobreixi. L' adaptació dels metal·lacarborans a les nanopartícules magnètiques funcionalitzades a la superfície s' assoleix, una vegada més, explotant els forts enllaços dihidrogen no covalents. El capítol explora l' aplicació d' aquests materials híbrids a la fotocatàlisi d' alcohols, així com la qüestió de modificar un sistema d' acord amb les necessitats.

La manca de fluorescència, així com la capacitat dels metal·lacarborans com a catalitzadors eficients i robustos s'exploren més a fons en el capítol sobre *Metal·lacarborans & Energia,* en el qual s'investiga la capacitat de l' [o-COSAN]$^-$ com un elèctrode de "molècula petita". La destresa catalítica dels metal·lacarborans s' estudia en detall. Estenent l'estudi encara més en la falta de fluorescència en metal·lacarborans, s'estudia la capacitat de l' [o-COSAN]$^-$ com un extintor de fluorescència eficient respecte als punts quàntics de carboni funcionalitzats amb amines. Els fonaments del procés fotofísic subjacent entre *Metal·lacarborans & C-dots s'* investiguen a fons i en profunditat. Aquests materials híbrids que incorporen la capacitat de commutació de fluorescència 'on/off' obren noves vies on aventurar-se.

La tesi navega a través de diverses aplicacions de metal·lacarborans i nanopartícules amb l'objectiu d'abordar desafiaments crítics i obrir noves vies per a l'avenç científic i el progrés tecnològic.

Table of Contents

1. Introduction

2. Metallacarboranes *vs.* Ferrocene: An electrochemical comparative study to unearth the better internal reference

3. Metallacarboranes & Proteins: A ‘small molecule’ probe for understanding the ‘effective’ surface area of a protein

4. Metallacarboranes & Magnetic Nanoparticles: Synthesis, Characterizations & Applications

5. Metallacarboranes & Energy:

A ‘small molecule’ electrode for complete photocatalytic water-splitting

6. Metallacarboranes & Carbon quantum dots:

A photophysical investigation on amine functionalized C-dots with metallacarboranes

Chapter 1

1.1 Element – Boron (B)

The periodic table is an orchestration of straight lines, solid rows and columns with meticulously positioned elements, carefully depicting their properties and reactivities. However, a jagged line strikes across the right-hand side of the table forming two distinct classes: metal elements to the left and non-metals to the right. At its summit, astrayed from the remaining metallic group 13 members, sits boron (B). Boron (Z=5) is a metalloid, behaving like a semi-conductor, with trivalent configuration and an empty *p* orbital. Thus, the quintessential boron compounds are deficient of electrons: a Lewis acid and an electrophile, deprived of electrons required to satisfy the classic octet rule.

Boron compounds, particularly its mineral forms such as borax, initially found applications as glazes and flux in metallurgy in civilizations such as Chinese and Egyptian, dating back to 300 AD.[1,2] Being a naturally scarce element, it wasn't until 1842 that boron was recognized as an element. Even then, boron chemistry failed to thrive due to its scarcity and difficulty in synthesis owing to their high moisture and air sensitivity and flammability. In 1912, A. Stock pioneered boron hydride chemistry by synthesizing a series of boron-hydrogen compounds including the di-borane (B_2H_6) and separated them using the first modified vacuum line.[3] Contrary to being a direct replica of ethane, the nature of bonding in B_2H_6 was illustrated in 1943 by H.C. Longuet-Higgins to being a 3-center 2-electron (3c-2e) boron-hydrogen-boron bond complacent with the Leweis rule of $2e^-$ per bond as well as molecular orbital theory, satisfying the octet rule for each of the boron.[4] Owing to high energy content per unit mass, boranes gained popularity as energy fuels for aviation during World War II but due to several challenges such as complex storage and handling, corrosiveness, their use was discontinued.[5] Boranes regained popularity as reducing agents for organic synthesis in 1979 with H.C Brown being recognized with Nobel Prize for the same.[6] Over the years, several advancements in boron chemistry relating to organic and inorganic applications have spiked the researchers to explore new avenues.

W. N Lipscomb was awarded the Nobel Prize in Chemistry for his studies pertaining to understanding the structure of boranes and boron clusters which could later be expanded to other electron deficient inter-metallic compounds.[7] Lipscomb *et al.* proposed the use of '*styx*' numbers to understand the types of bonds in boron clusters and thus predict their possible topological structures.[8] Briefly, the '*styx*' denotes the various types of bonds that exists in boron hydrides such as:

- The 3-center 2-electron (3c-2e) B-H-B bond denoted by 's';
- Closed/open 3c-2e B-B-B bonds denoted by 't';
- 2c-2e B-B bonds as 'y' &
- 2c-2e terminal B-H bonds as 'x'

These numbers are related to the valence electrons of the cluster, B_pH_{p+q}, as: p = s +t & q = s+x.

Following this, in the 1970s K. Wade, R. E. Williams, R.W. Rudolph and D. M. P. Mingos studied the stoichiometric and structural properties based on available electrons and number of vertices.[9–13] Subsequently, the Polyhedron Skeletal Electron Pair Theory (PSEPT) or the classic Wade's rule was proposed to classify the clusters as: *closo, nido* & *arachno*.[9] The B-H groups in polyhedral boranes is perceived to contribute $2e^-$ to the bonding structure and the remaining valence electron of the B atom constitutes the B-H bond. The rule states that for *n* B-H groups (*n* – number of vertices) with *n*+1 skeletal electron pair prefer a closed polyhedral structure forming *closo*-structures while an increase of $2e^-$, i.e. *n*+2 electron pairs leads to *nido*-structures. Further addition of an electron pair, i.e. *n*+3 electron pairs forms *arachno*-clusters. Sequential removal of vertices from *closo*-clusters leads to *nido*- as well as *arachno*-clusters. Wade's rule relates to the '*styx*' numbers in terms of the q values being equal to 2, 4 and 6 for each of the boron hydrides.[14] The rule was extended later as Jemmis *mno* rule wherein an electron counting rule for polycondensed polyhedral clusters such as $B_{20}H_{16}$ is explained in terms of the number of individual polyhedral involved in the condensation (*m*), the total number of vertices (*n*) and the number of single vertex bridging (*o*).[15] According to the rule, *m*+*n*+*o* skeletal electron pairs are required for the formation of stable polycondensed polyhedral boranes. Consequently, Wade's *n*+1 rule becomes a case of *mno* rule where *m* = 1 and *o* = 0.[16]

1.1.1 Carbon (C) & Boron (B) – Tale of two neighbours

Hydrocarbons have been the basis of life since time immemorial and hence the major thrust of research have been focused on them. Recently, M. Solà, F. Teixidor *et. al.* has established a clear analogy between hydrocarbons and boron hydrides using simple valence electron counting rules and confined spaces supported by DFT calculations demonstrating the existence of a common root in the number of valence electrons between hydrocarbons and boron hydrides in a similar confined space.[17] Despite being close to each other in the periodic table, C and B exhibit entirely different properties, majorly due to the electron deficient character of B. As mentioned earlier, borohydrides, due to the electron deficiency of B, prefers to form multicentred σ and π bonds whereas in hydrocarbons 2-center 2-electron (2c-2e) localized σ and delocalized π bonds are observed. Consequently, even though strong B-B single σ bonds exists, examples of linear catenation of boron are rare.[18] Tizando *et. al.* has also demonstrated that classical B_nH_{n+2} structures of 2c-2e B-B and B-H σ bonds become increasingly less stable with increasing *n*.[19]

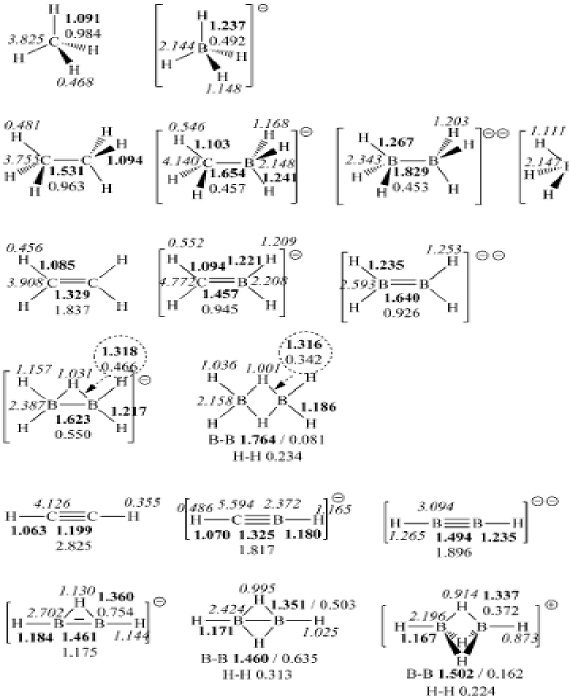

Fig. 1.1 Hydrocarbon analogues of borohydrides with bond lengths.[17]

The iso-lobal principle has been employed to understand the molecular and electronic structures of organometallic compounds to their organic analogues and thus, a similar approach has been adopted to establish a link between hydrocarbons and borohydrides. Hence, it has been shown that BH_4^- is the equivalent of CH_4 while $B_2H_6^{2-}$ is iso-electronically and iso-structurally equal to ethane. A. I Boldyrev *et. al.* had also demonstrated the equivalence of $B_6H_6^{6-}$ kernel to benzene as an all-boron containing planar aromatic structure.[20] However, the high charge per B atom in this hypothetical molecule makes it very unrealistic to prepare and therefore the equivalent form of benzene in boron hydrides is a cluster where 4 of the excess electrons in $B_6H_6^{6-}$ are transmuted into a BH unit (4 e^-) to give rise to $B_7H_7^{2-}$ which is the stable equivalent of benzene in boron hydrides.[17] Hence, it was possible to consider borohydrides with respect to their hydrocarbon analogues (Fig. 1.1).

The process of modifying hydrocarbons to borohydrides by substitution of C by B followed by the addition of additional electrons equivalent to the substituted C atoms in the original hydrocarbons is known as electronic transmutation.[21] Electronic transmutation has been employed to deduct several hydrocarbon analogues of borohydrides which helps in simplifying the boron chemistry as well as in the rational design of novel boron containing compounds. This approach has even be employed to macrostructures such as C_{60}, equivalent to B_{80} (Scheme 1.1).[22]

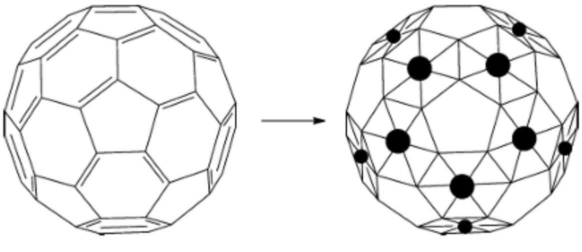

Scheme 1.1 Schematic representation of C_{60} and B_{80} in confined space.[17]

1.1.2 Carboranes

The formal exchange of a boron atom with any of the hetero-atoms such as C, N, O, Si, S among other gives rise to a whole new class of hetero-boranes.[23,24] Of these, carboranes having one or more B atoms substituted by C atoms is the extensively studied group owing to their advantageous properties. Carboranes are represented by the empirical formula $[C_nB_mH_{m+n+p}]^{x-}$, where n is the number of substituted C atoms, m is the number B atoms, p is the number of bridging H atoms and x is the charge of the cluster. Considering electron counting, every B-H group contributes $2e^-$ to the cluster, the bridging H gives $1e^-$ whereas each C-H or C-R contributes with $3e^-$ to the cluster. For the particular case of the icosahedral $[B_{12}H_{12}]^{2-}$ the substitution of two B by two C leads to the prominently studied dicarba-*closo*-dodecaboranes with the formula $C_2B_{10}H_{12}$ owing to their high thermal stability and chemical resistance, consequence of its 3D aromaticity and subsequent electronic delocalization in the cluster.[24–32] Depending on the relative position of the carbon atoms in the cluster, three isomeric forms are obtained: 1,2-dicarba-*closo*-dodecaborane or *ortho*-carborane, 1,7-dicarba-*closo*-dodecaborane or *meta*-carborane and 1,12-dicarba-*closo*-dodecaborane or *para*-carborane. Thermal isomerization of *o*-carborane yields the other two isomers.[33,34]

The stability of these carboranes increases with increase in separation of the carbon atoms and thus, *p*-carborane is more stable than *m*-carborane followed by *o*-carborane. As a consequence of the difference in the carbon and boron electronegativities, the hydrogen atom bonded to the carbon exhibits an acidic character.[26,35–37] Thus, carboranes are reactive and their reactivity varies depending on the vertices as well as the isomer.[38,39] Of the three isomers, significant research has been carried out on *o*-carborane owing to their electron withdrawing nature and ease of functionalization (Fig.1.2).[24,40]

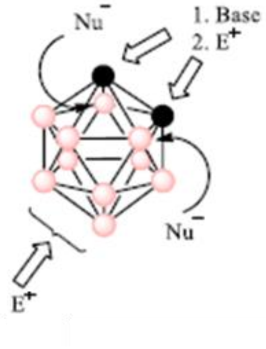

Fig. 1.2 Reactivity of different vertices of *o*-carborane.[41–45]

1.2 Metallacarboranes

Metallacarboranes (Mcb) act as an intersection between coordination and boron cluster chemistry. Mcb are a class of polyhedral carborane clusters formed by a transition metal atom such as Fe, Co, Ni, Au occupying a shared vertex merging the two icosahedra $[1,2\text{-}C_2B_9H_{11}]^{2-}$ units producing θ-shaped anionic molecule with the empirical formula $[3,3`\text{-}M(1,2\text{-}C_2B_9H_{11})_2]^-$.[46–48]

The first metallacarborane was synthesized in 1965 by M.F. Hawthorne and co-workers with Fe(III) as the central metal forming ferrabis(dicarbollide) or *o*-FESAN with the formula $[3,3'\text{-}Fe(1,2\text{-}C_2B_9H_{11})_2]^-$.[49] Following Fe, Co(III) was used as the transition metal centre to synthesize cobaltabis(dicarbollide) or *o*-COSAN with the formula $[3,3'\text{-}Co(1,2\text{-}C_2B_9H_{11})_2]^-$and later other metals such as Ni(III), Cr(III), Cu, Au were also synthesized by the group.[50–54] A typical synthesis of the metallacarboranes involves the partial de-boronation of the *o*-carborane in a selective manner via nucleophilic attack to obtain *nido*-$[7,8\text{-}C_2B_9H_{11}]^-$. Subsequently, the bridging hydrogen is extracted using a strong base such as t-BuOK, NaH or n-BuLi in anhydrous conditions to obtain the dianionic dicarbollide $[7,8\text{-}C_2B_9H_{11}]^{2-}$.[51] Finally, anhydrous $CoCl_2$ or $FeCl_2$ is added for metal complexation followed by the oxidation of the metal to obtain the corresponding metallacarboranes. Recently, C. Viñas *et. al.* has reported a facile and high-throughput method for the green synthesis of *o*-COSAN in solid state, which can further facilitate the research on these compounds.[55]

In both, *o*-COSAN and *o*-FESAN, the central metal atom has a +3 oxidation state and thus, the Mcb are mono-anionic compounds with the negative charge being delocalized throughout the molecule leading to low charge density.[56] Possessing low charge density together with high molecular volume and low nucleophilic character gives the compounds high chemical and thermal stability. During the course of the thesis, we would discuss in detail the various properties and the multi-faceted applications of these metallacarboranes (Fig.1.3).

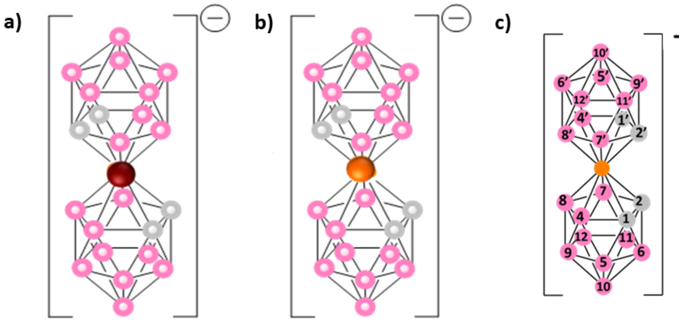

Fig.1.3 Schematic representation of **(a)** *o*-FESAN and **(b)** *o*-COSAN with **(c)** the number of vertices.

1.2.1 Solubility

The most consistent and basic properties of the metallacarboranes is its solubility.[47] Depending on the nature of the counter cation, anionic *o*-COSAN and *o*-FESAN are soluble in different organic solvents as well as in water. For instance, the solubility of *o*-COSAN in water, at room temperature, varies strongly from Na^+, Li^+, H^+, K^+, Cs^+ and $[NMe4]^{+}$ as 1509 mM, 1175 mM, 846 mM, 747 mM, 1.5 mM and 0.019 mM, respectively.[57] This property widens the scope of solvents which can be used for the studies involving Mcb. Hence, depending on the application, it is possible to choose the appropriate counter cation for the Mcb to achieve the desired effect.

1.2.2 Self-assembly/Surfactant behaviour

The *o*-COSAN and *o*-FESAN anions display three different rotational isomers: *transoid (trans)*, *cisoid(cis)* and *gauche* which can be distinguished in terms of their relative position of the carbon atoms in the carborane cluster (Fig.1.4).[58] Even though the *trans* rotamer possess the lowest energy in vacuo,[59,60] it was demonstrated that the *cis* rotational isomer is the most abundant form in solid state as well as in aqueous phase due to the molecule-molecule interactions.[58] In order to move from one rotamer to another, a rotational energy barrier needs to be overcome which vastly depends on the environment of the molecule.[61] Among other factors, it was observed that the ability to form C_c-H···B-H dihydrogen bonds is the highest in the *cis* isomer.

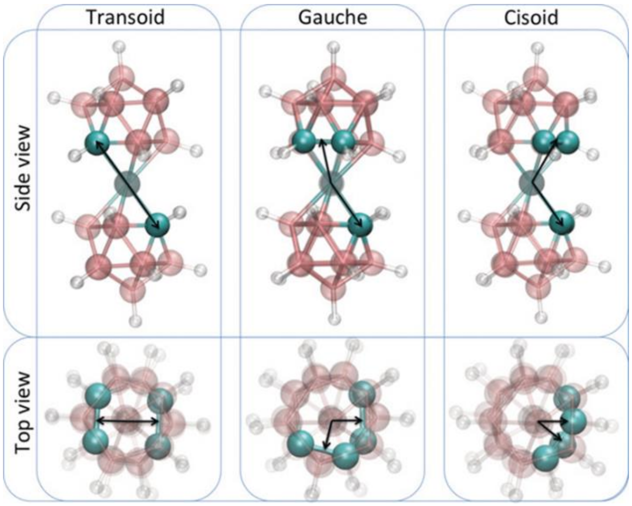

Fig.1.4 The different rotational isomers for *o*-COSAN.[62]

Owing to their ability to form hydrogen, C_c-H···O, and dihydrogen bonds, C_c-H···B-H, metallacarboranes exhibit self-assembling properties in aqueous solution. P. Bauduin as well as F.Teixidor *et. al.* has demonstrated the non-classical surfactant behaviour of *o*-COSAN in water.[48,62] Using DFT and MD calculations, it was demonstrated that the *cisoid* rotamer has a well-defined 'hydrophilic' polar head region as well as a 'hydrophobic' non-polar tail region while the *transoid* rotamer lacks well-defined 'head' and 'tail' region. The hydrophobic region or "pocket" is defined by the 4 neighboring carbon atoms in the *cis* rotamer while the hydrophilic region is dictated by the boron atoms which defines a negatively charged region that strongly interacts with the water molecule.

P. Bauduin *et. al.* has studied the effect of varying concentration of *o*-COSAN to form micelles and vesicles.[48] It was observed that at lower concentration of the Mcb forms monolayer vesicles and with increasing concentration a phase transition occurs to form micelles resulting in the co-existence of both the aggregation state in higher concentration in aqueous solutions (Fig. 1.5).[48,63–65]

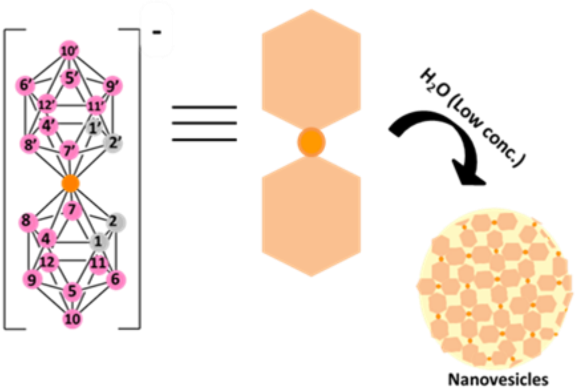

Fig.1.5 Formation of monolayer vesicles at low concentration of *cis*-[*o*-COSAN] in aqueous solution.

1.2.3 3D – Aromaticity

Since its discovery, metallacarboranes have always been considered as sandwich type complexes analogous to metallocenes such as ferrocene.[49] A large number of studies consider complexes such as ferrocene and dibenzenechromium as aromatic molecules owing to the fact that aromaticity is often associated with higher stability and lower chemical reactivity in comparison to the associated non-aromatic and anti-aromatic systems. Hence, ferrocene undergoes electrophilic substitution and not an electrophilic addition. M. Sola, F. Teixidor *et. al.* had previously categorized *closo*-borohydrides by establishing a connection between Huckel's $(4n+2)\pi$ rule for planar organic compound to Wade-Mingo's rule of three-dimensional aromaticity using retro-electronic confined space analogy (ECSA).[66] Subsequently, computational as well as NMR studies were carried out which showed that the aromaticity in *closo*-boranes and -carboranes can be extended to their *nido* counterparts conforming to the statement that, "*the aromaticity of a sandwich complex implies that, in general, its ligands have to be also aromatic.*"[32]

But a significant distinction between the aromaticity of the metallacarborane and the metallocenes is that Mcb display global 3D-aromaticity whereas the metallocenes exhibit a planar 2D local aromaticity in the ligands proven by the fact that the highest current density in a magnetic field is located within the icosahedron in COSAN, close to the Co atom. Thus, the metallacarboranes are not a surrogate of the metallocenes. Further studies have also been reported correlating 3D and 2D fusion aromaticity suggesting the lack of such fusion aromaticity due to the ineffective overlap between the molecular orbitals.[67,68]

1.2.4 Electrochemical properties

The transition metal centre with the delocalized charge due to 3D-aromaticity empowers the Mcb to possess highly remarkable electrochemical properties. *o*-COSAN and *o*-FESAN with their redox active metal centres possess different redox accessible processes such as $Co^{2+/+}$ (-2.64 V *vs.* Fc), $Co^{3+/2+}$ (-1.75 V *vs.* Fc), $Co^{4+/3+}$ (1.22 V *vs.* Fc) and $Fe^{3+/2+}$ (-0.78 V *vs.* Fc).[57] *o*-FESAN also has an irreversible redox process at 0.76 V *vs.* Fc corresponding to $Fe^{4+/3+}$. Interestingly, these redox properties can be tuned by derivatizing the metallacarboranes with different substituents such as halogens.[69,70] The facile modification of the redox properties enables the Mcb to be used in various applications such as water splitting among others.[70]

All the properties described above makes the metallacarboranes an attractive option to explored and exploited.

1.3 Nanoparticles

Beneath the lens of scientific marvels, an enigmatic realm awaits - a realm of nanoparticles, where the essence of matter spins intricate stories of size-defying marvels. Particles when their dimensions are confined to the nano (10^{-9}) meter scale regime exhibit remarkable size-dependent properties and thus, emerged the field of nanoscience. The nanoparticles act as the bridge between the atoms and the bulk material, offering properties and applications quite different from either (Scheme 1.2). Owing to their high surface-to-volume ratio, ease of surface functionalization, size-tuneable optical and electrical properties, they have sparked revolutions across scientific frontiers.[71–74]

These particles can vary depending on their size, shape and composition such metal nanoparticles (Au, Ag), magnetic nanoparticles (Fe_3O_4) and quantum dots (CdSe, InP).[75] At this miniscule scale, the laws of quantum mechanics dominate over the macroscopic physics. As a result, a range of unique optical and electrical properties emerge such as surface plasmon resonance (SPR), enhanced Raman scattering, formation of highly energetic “hot electrons”, size-dependent photoluminescence, quantum tunnelling, quantum point contacts among several others.

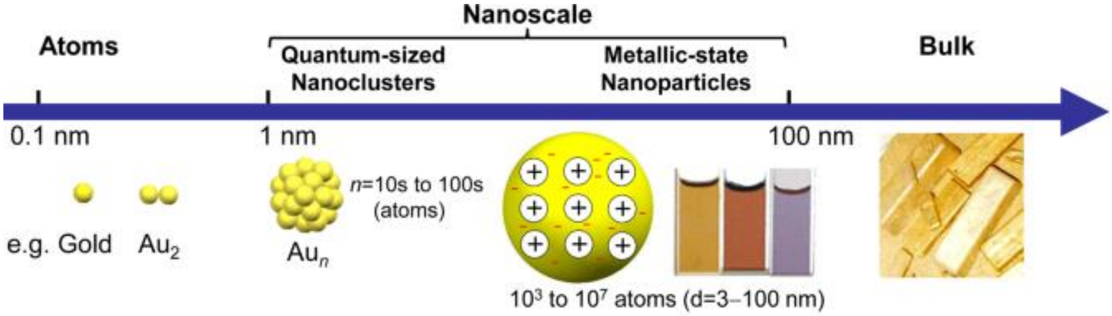

Scheme 1.2 Schematic representation showing the relative position of nanoparticles in the spectrum of various dimensions.[76]

Thus, nanoparticles are used for several applications such as catalysis, imaging purposes, drug delivery, light emitting diodes, sensors etc.[77–81] In this thesis, we would focus on primarily magnetic nanoparticles and quantum dots exploiting their properties such as superparamagnetism and quantum confinement effect.

1.3.1 Magnetism

The movement of electrons within an atom gives rise to the magnetic properties in materials. Each electron possesses a magnetic moment, μ_i, which is the sum of orbital magnetic moment (induced by the current due to the orbital movement of the electrons) and the spin magnetic moment (induced by the rotational motion of the electrons).[82] A bulk material has several atoms with even more electrons and as a result, the magnetic moment of each individual electron gets accumulated to give rise to a magnetic state of the material. Magnetic state or phase of a material depends on various factors such as temperature, pressure and applied magnetic field.[83,84] Depending on the individual atomic magnetic moment, they are classified as:

- Null Magnetic moment (Diamagnetic): When the magnetic moments are arranged anti-parallel and have the same magnitude, the net magnetic moment of the crystal becomes zero. Such materials with no permanent magnetic dipoles are known as diamagnetic materials and they are repelled in presence of an external magnetic field. For instance, when an atom has a closed shell electronic configuration there is no net magnetic moment and hence the atom exhibits diamagnetism.

- Non-zero magnetic moment: When the cancellation of the magnetic moments is partial, there is non-zero net magnetic moment. Such atoms with permanent magnetic moments can exhibit paramagnetism, ferromagnetism, ferrimagnetism and anti-ferromagnetism. For instance, atoms with unpaired electrons give rise to non-zero magnetic moments.
  - Paramagnetic: In the absence of an external magnetic field, the magnetic moments are randomly oriented so as to give a zero net magnetic moment. But upon the application of a magnetic field, the moments align in the direction of the applied field to give rise to a small net magnetic moment.
  - Ferrimagnetic: The crystal has a net magnetic moment arising from two different types of atoms with moments of different strengths arranged in an anti-parallel manner.
  - Anti-ferromagnetic: The individual atomic magnetic moments are arranged anti-parallel resulting in a zero net magnetic moment, quite similar to diamagnetic materials.
  - Ferromagnetic: The magnetic moments are aligned even in the absence of an external magnetic field. Hence, they possess a net permanent magnetization such as iron oxide particles.

There are different types of magnetic nanoparticles but for the purpose of this thesis, we would focus on iron-oxide nanoparticles (IONPs). The strong magnetic moment of the iron atom can be attributed to the presence of four unpaired electrons in its 3d orbitals. Iron being a ferromagnetic material inherently possesses a permanent net magnetic moment. In the case of ferromagnetic materials, the magnitude of magnetization (M) is explained in terms of Weiss domains where the material is sub-divided into domains having individual magnetization vector arising from each of the atomic moments (Refer Chapter 4).[85,86] Upon the application of an external magnetic field, H (Oe), on a ferromagnetic material, the magnetization value, M increases till it reaches a saturation magnetization, M_s (emu/g). Once the saturation is attained, and even if the magnetic field is removed, the material would continue to have a residual magnetization, M_R (emu/g) without relaxing to the initial state and would trace a loop known as the hysteresis. The failure of the domains to relax back to its original orientation leads to the remnant magnetization. To revert it back to zero, a coercive magnetic field, H_c (Oe) needs to be applied in a direction opposite to initial applied field (Fig. 1.6).

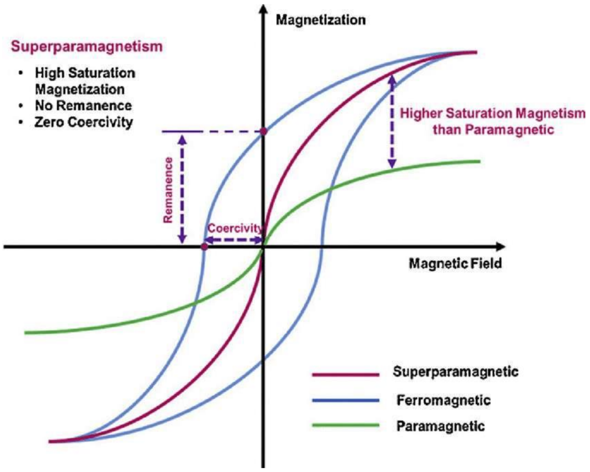

Fig. 1.6 Magnetic hysteresis of different materials portraying their differences.

When the particle size become reduced to the nanoscale regime, ferromagnetic materials such as iron-oxide becomes superparamagnetic in nature. Superparamagnetic materials (Fig.1.6), unlike traditional ferromagnetic materials, lack a net permanent magnetization and exhibit transient magnetic behaviour. The application of the property - superparamagnetism along with surface functionalization for IONPs is explored in the thesis in Chapter 4.

1.3.2 Quantum Confinement

Quantum confinement is a phenomenon which occurs when the particle size is diminished to a regime lower than the Bohr excitonic radius, thus confining the electron-hole pair.[87] An exciton is an electron-hole pair formed by the absorption of photon by a semiconductor bound together by the Coulombic force of attraction and the Bohr excitonic radius (R) is defined as the separation between the electron-hole pair analogue to the hydrogen atom. Quantum confinement occurs when the continuum of energy levels in a bulk material collapse to discrete, atomic-like energy levels accompanied by the widening of the energy band gap (E_g) (Fig.1.7).

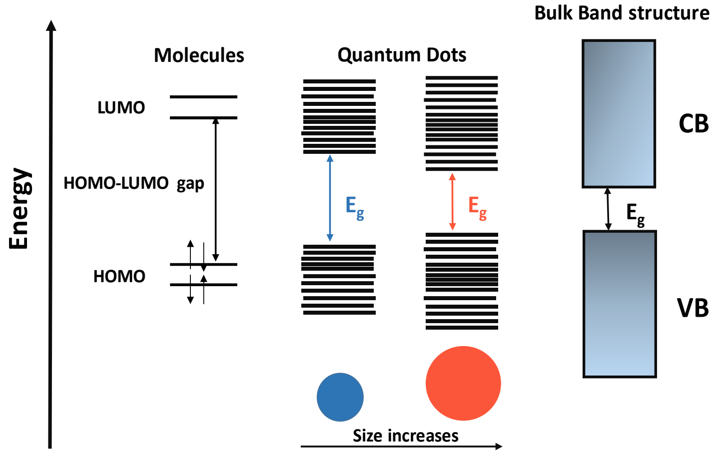

$$E_{g(qd)} = E_{\mathrm{bulk}} + \frac{h^2}{8R^2}\left(\frac{1}{m_e^*}+\frac{1}{m_h^*}\right) - \frac{1.786e^2}{4\pi\varepsilon_o\varepsilon_r R^2}$$

Fig. 1.7 Schematic representation showing the effect of quantum confinement tuning the optical properties in a size-dependent manner, from molecules to bulk where E_g is the band gap of the quantum dot given by the Braus equation and R is the Bohr excitonic radius. [Adapted from ref. 87]

As the size of the particles (given by R) increases, the band gap decreases thus resulting in size-dependent optical properties. Quantum dots are mainly exploited for their photoluminescence properties due to the fact that depending on the size different wavelengths can be obtained from a single material.

In this thesis, we explore the rather non-classical carbon quantum dots (CDs) as they are not the traditional semiconductor ones. In Chapter 6, we would explore in detail the different characterization techniques and properties of CDs, particularly in relation to metallacarboranes.

1.4 Amines & Metallacarboranes

As discussed earlier, metallacarboranes have the ability to form strong dihydrogen bonds and consequently, forms strong N-H···B-H bonds. The ability of the Mcb to form such non-covalent interactions have been explored by Teixidor *et. al.* to form ion-selective membranes for drugs such as isoniazid and pyrazinamide as well as enantioselective membranes.[88,89] The interaction of θ-metallacarboranes with several biologically active components containing protonated amines such as amino acids, antibiotics, neurotransmitters and analgesics are well reported in the literature (Fig. 1.8).[90]

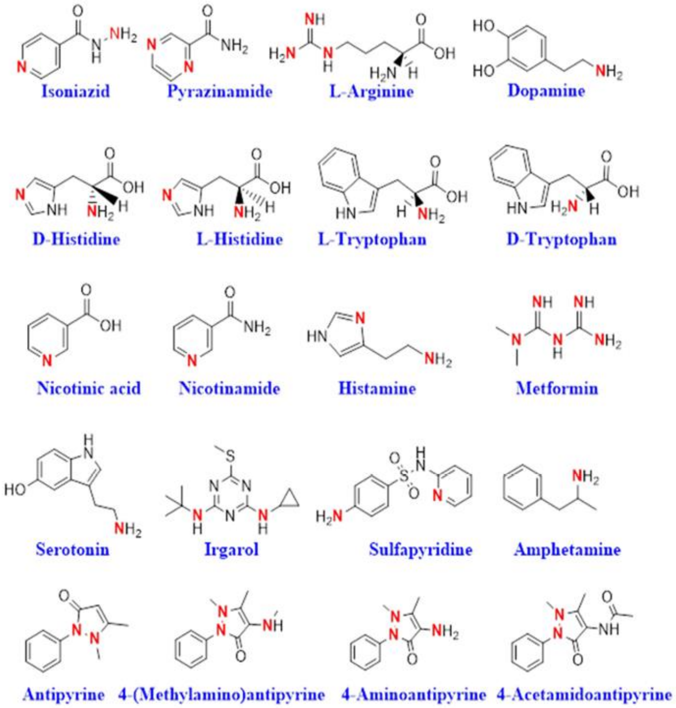

Fig. 1.8 Structures of biologically active components highlighting the amino groups basic enough to form ion-pair complex with metallacarboranes.[90]

Consequently, in this thesis we will exploit the N-H···B-H bond formation of metallacarboranes by surface functionalizing the nanoparticles with amine terminating groups. We also explore the relation of θ-metallacarboranes, particularly [*o*-COSAN]$^-$, with various proteins as can be seen in Chapter 3. In addition to the dihydrogen bond formation, θ-metallacarboranes being monoanionic in nature further facilitates the interaction with protonated amine groups through electrostatic interactions. The ease of surface functionalization of nanoparticles with the non-covalent interactions of θ-metallacarboranes is explored throughout the thesis in different scenarios resulting in various applications.

1.5 References

1 W. G. Woods, An introduction to boron: history, sources, uses, and chemistry., *Environ. Health Perspect.*, 1994, **102**, 5–11.

2 D. E. Garrett, ed. D. E. B. T.-B. Garrett, Academic Press, San Diego, 1998, pp. 1–50.

3 A. Stock and C. Massenez, Borwasserstoffe, *Berichte der Dtsch. Chem. Gesellschaft*, 1912, **45**, 3539–3568.

4 H. C. Longuet-Higgins and R. P. Bell, 64. The structure of the boron hydrides, *J. Chem. Soc.*, 1943, 250–255.

5 S. Hermanek, Boron-11 NMR spectra of boranes, main-group heteroboranes, and substituted derivatives. Factors influencing chemical shifts of skeletal atoms, *Chem. Rev.*, 1992, **92**, 325–362.

6 H. C. Brown, *Hydroboration*, W. A. Benjamin, 1962.

7 W. N. Lipscomb, The Boranes and Their Relatives, *Science (80-.).*, 1977, **196**, 1047–1055.

8 W. H. Eberhardt, B. Crawford Jr. and W. N. Lipscomb, The Valence Structure of the Boron Hydrides, *J. Chem. Phys.*, 2004, **22**, 989–1001.

9 R. W. Rudolph and W. R. Pretzer, Hueckel-type rules and the systematization of borane and heteroborane chemistry, *Inorg. Chem.*, 1972, **11**, 1974–1978.

10 D. M. P. MINGOS, A General Theory for Cluster and Ring Compounds of the Main Group and Transition Elements, *Nat. Phys. Sci.*, 1972, **236**, 99–102.

11 R. E. Williams, Carboranes and boranes; polyhedra and polyhedral fragments, *Inorg. Chem.*, 1971, **10**, 210–214.

12 R. W. Rudolph, Boranes and heteroboranes: a paradigm for the electron requirements of clusters?, *Acc. Chem. Res.*, 1976, **9**, 446–452.

13 H. J. Emeléus and A. G. Sharpe, 1959.

14 W. N. Lipscomb, Relationship of the styx rules to Wade's rules, *Inorg. Chem.*, 1979, **18**, 2328.

15 E. D. Jemmis and P. N. V Pavankumar, Stability of polyhedral borane anions and carboranes, *Proc. Indian Acad. Sci. - Chem. Sci.*, 1984, **93**, 479–489.

16 E. D. Jemmis, M. M. Balakrishnarajan and P. D. Pancharatna, A Unifying Electron-Counting Rule for Macropolyhedral Boranes, Metallaboranes, and Metallocenes, *J. Am. Chem. Soc.*, 2001, **123**, 4313–4323.

17 J. Poater, M. Solà, C. Viñas and F. Teixidor, A Simple Link between Hydrocarbon and Borohydride Chemistries, *Chem. – A Eur. J.*, 2013, **19**, 4169–4175.

18 H. Braunschweig, Q. Ye, A. Vargas, R. D. Dewhurst, K. Radacki and A. Damme, Controlled homocatenation of boron on a transition metal, *Nat. Chem.*, 2012, **4**, 563–567.

19 E. Osorio, J. K. Olson, W. Tiznado and A. I. Boldyrev, Analysis of Why Boron Avoids sp2 Hybridization and Classical Structures in the BnHn+2 Series, *Chem. – A Eur. J.*, 2012, **18**, 9677–9681.

20 A. N. Alexandrova, K. A. Birch and A. I. Boldyrev, Flattening the B6H62- Octahedron. Ab Initio Prediction of a New Family of Planar All-Boron Aromatic Molecules, *J. Am. Chem. Soc.*, 2003, **125**, 10786–10787.

21 J. K. Olson and A. I. Boldyrev, Electronic transmutation: Boron acquiring an extra electron becomes 'carbon', *Chem. Phys. Lett.*, 2012, **523**, 83–86.

22 N. Gonzalez Szwacki, A. Sadrzadeh and B. I. Yakobson, B}}_{80 Fullerene: An Ab Initio Prediction of Geometry, Stability, and Electronic Structure, *Phys. Rev. Lett.*, 2007, **98**, 166804.

23 R. E. Kirk, D. F. Othmer, M. Grayson and D. Eckroth, *Kirk-Othmer Concise encyclopedia of chemical technology*, Wiley New York, New York SE -, 1985.

24 R. N. Grimes, *Carboranes*, Elsevier Inc. New York, New York, 3rd edn., 2016.

25 R. N. Grimes, Carboranes, anti-crowns, and big wheels, *Angew. Chemie Int. Ed. English*, 1993, **32**, 1289–1290.

26 F. Teixidor, G. Barberà, A. Vaca, R. Kivekäs, R. Sillanpää, J. Oliva and C. Viñas, Are Methyl Groups Electron-Donating or Electron-Withdrawing in Boron Clusters? Permethylation of o-Carborane, *J. Am. Chem. Soc.*, 2005, **127**, 10158–10159.

27 H. Kimura, K. Okita, M. Ichitani, T. Sugimoto, S. Kuroki and I. Ando, Structural Study of Silyl–Carborane Hybrid Diethynylbenzene–Silylene Polymers by High-Resolution Solid-State 11B, 13C, and 29Si NMR Spectroscopy, *Chem. Mater.*, 2003, **15**, 355–362.

28 I. N. Klyukin, A. P. Zhdanov, A. Y. Bykov, V. M. Retivov, K. Y. Zhizhin and N. T. Kuznetsov, Synthesis of Boron-Containing Siloxanes by Reaction of Hydroxy-closo-Decaborates with Dihalosilanes, *Russ. J. Inorg. Chem.*, 2018, **63**, 213–218.

29 A. González-Campo, B. Boury, F. Teixidor and R. Núñez, Carboranyl Units Bringing Unusual Thermal and Structural Properties to Hybrid Materials Prepared by Sol–Gel Process, *Chem. Mater.*, 2006, **18**, 4344–4353.

30 E. Hao, B. Fabre, F. R. Fronczek and M. G. H. Vicente, Syntheses and electropolymerization of carboranyl-functionalized pyrroles and thiophenes, *Chem. Mater.*, 2007, **19**, 6195–6205.

31 O. K. Farha, A. M. Spokoyny, K. L. Mulfort, M. F. Hawthorne, C. A. Mirkin and J. T. Hupp, Synthesis and hydrogen sorption properties of carborane based metal-organic framework materials., *J. Am. Chem. Soc.*, 2007, **129**, 12680–12681.

32 J. Poater, C. Viñas, I. Bennour, S. Escayola, M. Solà and F. Teixidor, Too Persistent to Give Up: Aromaticity in Boron Clusters Survives Radical Structural Changes, *J. Am. Chem. Soc.*, 2020, **142**, 9396–9407.

33 S. Papetti and T. L. Heying, p-Carborane [1,12-

Dicarbaclovododecaborane(12)], *J. Am. Chem. Soc.*, 1964, **86**, 2295.

34 D. Grafstein and J. Dvorak, Neocarboranes, a New Family of Stable Organoboranes Isomeric with the Carboranes, *Inorg. Chem.*, 1963, **2**, 1128–1133.

35 A. V. Puga, F. Teixidor, R. Sillanpää, R. Kivekäs, M. Arca, G. Barberà and C. Viñas, From Mono- to Poly-Substituted Frameworks: A Way of Tuning the Acidic Character of Cc☐H in o-Carborane Derivatives, *Chem. – A Eur. J.*, 2009, **15**, 9755–9763.

36 A. M. Spokoyny, C. D. Lewis, G. Teverovskiy and S. L. Buchwald, Extremely Electron-Rich, Boron-Functionalized, Icosahedral Carborane-Based Phosphinoboranes., *Organometallics*, 2012, **31**, 8478–8481.

37 K. Hermansson, M. Wójcik and S. Sjöberg, o-, m-, and p-carboranes and their anions: Ab initio calculations of structures, electron affinities, and acidities, *Inorg. Chem.*, 1999, **38**, 6039–6048.

38 F. Teixidor, R. Núñez, C. Viñas, R. Sillanpää and R. Kivekäs, The Distinct Effect of the o-Carboranyl Fragment: Its Influence on the I– I Distance in R3PI2 Complexes, *Angew. Chemie*, 2000, **112**, 4460–4462.

39 D. Grafstein, J. Bobinski, J. Dvorak, H. Smith, N. Schwartz, M. S. Cohen and M. M. Fein, Carboranes. III. Reactions of the Carboranes, *Inorg. Chem.*, 1963, **2**, 1120–1125.

40 J. Ochi, K. Tanaka and Y. Chujo, Recent progress in the development of solid-state luminescent o-carboranes with stimuli responsivity, *Angew. Chemie Int. Ed.*, 2020, **59**, 9841–9855.

41 G. Barberà, C. Viñas, F. Teixidor, G. M. Rosair and A. J. Welch, Self-assembly of carborane molecules via C–H···I hydrogen bonding: the molecular and crystal structures of 3-I-1,2-closo-C2B10H11, *J. Chem. Soc. Dalt. Trans.*, 2002, 3647–3648.

42 H. Schroeder, T. L. Heying and J. R. Reiner, A new series of organoboranes. II.

The chlorination of 1, 2-dicarbaclovododecaborane (12), *Inorg. Chem.*, 1963, **2**, 1092–1096.

43 J. F. Sieckhaus, N. S. Semenuk, T. A. Knowles and H. Schroeder, Icosahedral carboranes. XIII. Halogenation of p-carborane, *Inorg. Chem.*, 1969, **8**, 2452–2457.

44 C. Viñas, G. Barberà, J. M. Oliva, F. Teixidor, A. J. Welch and G. M. Rosair, Are Halocarboranes Suitable for Substitution Reactions? The Case for 3-I-1,2-closo-C2B10H11: Molecular Orbital Calculations, Aryldehalogenation Reactions, 11B NMR Interpretation of closo-Carboranes, and Molecular Structures of 1-Ph-3-Br-1,2-closo-C2B10H10 and 3-Ph-1,2-closo-C2B10H11, *Inorg. Chem.*, 2001, **40**, 6555–6562.

45 C. Viñas, G. Barberà and F. Teixidor, The B- I activation in o-carborane clusters: their fate towards B-H. Easy synthesis of [7, 10-C2B10H13]−, *J. Organomet. Chem.*, 2002, **642**, 16–19.

46 E. P. Andreichuk, S. A. Anufriev, K. Y. Suponitsky and I. B. Sivaev, The First Nickelacarborane with closo-nido Structure., *Molecules*, , DOI:10.3390/molecules25246009.

47 R. Grimes, Metallacarboranes in the new millennium, *Coord. Chem. Rev.*, 2000, **200**, 773–811.

48 P. Bauduin, S. Prevost, P. Farràs, F. Teixidor, O. Diat and T. Zemb, *Angew. Chemie.*, 2011, 50, 5298–5300.

49 M. F. Hawthorne, D. C. Young and P. A. Wegner, Carbametallic Boron Hydride Derivatives. I. Apparent Analogs of Ferrocene and Ferricinium Ion, *J. Am. Chem. Soc.*, 1965, **87**, 1818–1819.

50 H. W. Ruhle and M. F. Hawthorne, .pi.-Dicarbollyl derivatives of chromium. Metallocene analogs, *Inorg. Chem.*, 1968, 7, 2279–2282.

51 M. F. Hawthorne, D. C. Young, T. D. Andrews, D. V Howe, R. L. Pilling, A. D. Pitts, M. Reintjes, L. F. J. Warren and P. A. Wegner, .pi.-Dicarbollyl

derivatives of the transition metals. Metallocene analogs, *J. Am. Chem. Soc.*, 1968, **90**, 879–896.

52 E. C. Santos, A. B. Pinkerton, S. A. Kinkead, P. K. Hurlburt, S. A. Jasper, C. W. Sellers, J. C. Huffman and L. J. Todd, Syntheses of nido-9,11-X2-7,8-C2B9H10− anions (X=Cl, Br or I) and the synthesis and structural characterization of N(C2H5)4[commo-3,3′-Co(4,7-Br2-3,1,2-CoC2B9H9)2], *Polyhedron*, 2000, **19**, 1777–1781.

53 M. F. Hawthorne and T. D. Andrews, Carborane analogues of cobalticinium ion, *Chem. Commun.*, 1965, 443–444.

54 L. F. Warren and M. F. Hawthorne, (3)-1,2-Dicarbollyl Complexes of Nickel(III) and Nickel(IV), *J. Am. Chem. Soc.*, 1967, **89**, 470–471.

55 I. Bennour, A. M. Cioran, F. Teixidor and C. Viñas, 3,2,1 and stop! An innovative, straightforward and clean route for the flash synthesis of metallacarboranes, *Green Chem.*, 2019, **21**, 1925–1928.

56 C. Masalles, S. Borrós, C. Viñas and F. Teixidor, Are Low-Coordinating Anions of Interest as Doping Agents in Organic Conducting Polymers?, *Adv. Mater.*, 2000, **12**, 1199–1202.

57 M. Tarrés, V. S. Arderiu, A. Zaulet, C. Viñas, F. Fabrizi de Biani and F. Teixidor, How to get the desired reduction voltage in a single framework! Metallacarborane as an optimal probe for sequential voltage tuning, *Dalt. Trans.*, 2015, **44**, 11690–11695.

58 E. J. Juárez-Pérez, R. Núñez, C. Viñas, R. Sillanpää and F. Teixidor, The Role of C–H···H–B Interactions in Establishing Rotamer Configurations in Metallabis(dicarbollide) Systems, *Eur. J. Inorg. Chem.*, 2010, **2010**, 2385–2392.

59 M. Bühl, J. Holub, D. Hnyk and J. Macháček, Computational Studies of Structures and Properties of Metallaboranes. 2. Transition-Metal Dicarbollide Complexes, *Organometallics*, 2006, **25**, 2173–2181.

60 M. Bühl, D. Hnyk and J. Macháček, Computational Study of Structures and Properties of Metallaboranes: Cobalt Bis(dicarbollide), *Chem. – A Eur. J.*, 2005, **11**, 4109–4120.

61 F. Teixidor and C. Viñas, Boron and carbon: Antagonistic or complementary? Proposal for a simple prototype of a molecular clutch or molecular switch, 2012, **84**, 2457–2465.

62 D. C. Malaspina, C. Viñas, F. Teixidor and J. Faraudo, *Angew. Chemie.*, 2020, 59, 3088–3092.

63 D. Brusselle, P. Bauduin, L. Girard, A. Zaulet, C. Viñas, F. Teixidor, I. Ly and O. Diat, *Angew. Chemie.*, 2013, 52, 12114–12118.

64 A. Zaulet, F. Teixidor, P. Bauduin, O. Diat, P. Hirva, A. Ofori and C. Viñas, Deciphering the role of the cation in anionic cobaltabisdicarbollide clusters, *J. Organomet. Chem.*, 2018, **865**, 214–225.

65 C. Viñas, M. Tarrés, P. González-Cardoso, P. Farràs, P. Bauduin and F. Teixidor, Surfactant behaviour of metallacarboranes. A study based on the electrolysis of water, *Dalt. Trans.*, 2014, **43**, 5062–5068.

66 J. Poater, M. Solà, C. Viñas and F. Teixidor, Hückel's Rule of Aromaticity Categorizes Aromatic closo Boron Hydride Clusters, *Chem. – A Eur. J.*, 2016, **22**, 7437–7443.

67 J. Poater, C. Viñas, D. Olid, M. Solà and F. Teixidor, Aromaticity and Extrusion of Benzenoids Linked to [o-COSAN]−: Clar Has the Answer, *Angew. Chemie Int. Ed.*, 2022, **61**, e202200672.

68 J. Poater, C. Viñas, M. Solà and F. Teixidor, 3D and 2D aromatic units behave like oil and water in the case of benzocarborane derivatives, *Nat. Commun.*, 2022, **13**, 3844.

69 T. García-Mendiola, V. Bayon-Pizarro, A. Zaulet, I. Fuentes, F. Pariente, F. Teixidor, C. Viñas and E. Lorenzo, Metallacarboranes as tunable redox potential electrochemical indicators for screening of gene mutation, *Chem.*

Sci., 2016, **7**, 5786–5797.

70 J. A. Maria Xavier, I. Fuentes, M. Nuez-Martínez, Z. Kelemen, A. Andrio, C. Viñas, V. Compañ and F. Teixidor, How to switch from a poor PEDOT:X oxygen evolution reaction (OER) to a good one. A study on dual redox reversible PEDOT:metallacarborane, *J. Mater. Chem. A*, 2022, **10**, 16182–16192.

71 C. N. R. Rao, G. U. Kulkarni, P. J. Thomas and P. P. Edwards, *Chem. a Eur. journal.*, 2002, 8, 28–35.

72 J. Ann Maria Xavier, G. Devatha, S. Roy, A. Rao and P. P. Pillai, Electrostatically regulated photoinduced electron transfer in "cationic" eco-friendly CuInS2/ZnS quantum dots in water, *J. Mater. Chem. A*, 2018, **6**, 22248–22255.

73 F. Ahmad, M. M. Salem-Bekhit, F. Khan, S. Alshehri, A. Khan, M. M. Ghoneim, H.-F. Wu, E. I. Taha and I. Elbagory, Unique Properties of Surface-Functionalized Nanoparticles for Bio-Application: Functionalization Mechanisms and Importance in Application., *Nanomater. (Basel, Switzerland)*, , DOI:10.3390/nano12081333.

74 I. Khan, K. Saeed and I. Khan, Nanoparticles: Properties, applications and toxicities, *Arab. J. Chem.*, 2019, **12**, 908–931.

75 Y. Khan, H. Sadia, S. Z. Ali Shah, M. N. Khan, A. A. Shah, N. Ullah, M. F. Ullah, H. Bibi, O. T. Bafakeeh, N. B. Khedher, S. M. Eldin, B. M. Fadhl and M. I. Khan, *Catalysts*, 2022, 12.

76 R. Jin and T. Higaki, Open questions on the transition between nanoscale and bulk properties of metals, *Commun. Chem.*, 2021, **4**, 28.

77 C.-H. M. Chuang, P. R. Brown, V. Bulović and M. G. Bawendi, Improved performance and stability in quantum dot solar cells through band alignment engineering, *Nat. Mater.*, 2014, **13**, 796–801.

78 M. Bruchez Jr., Semiconductor Nanocrystals as Fluorescent Biological Labels,

Science (80-.)., 1998, **281**, 2013–2016.

79 M. Lunz, V. A. Gerard, Y. K. Gun'Ko, V. Lesnyak, N. Gaponik, A. S. Susha, A. L. Rogach and A. L. Bradley, Surface plasmon enhanced energy transfer between donor and acceptor CdTe nanocrystal quantum dot monolayers, *Nano Lett.*, 2011, **11**, 3341–3345.

80 H. Zhong, Z. Bai, B. Zou and I. Colloidal, Tuning the Luminescence Properties of III–Nanocrystals for Optoelectronics and Biotechnology Applications., *Chem Lett*, 2012, **3 SRC-G**, 3167–3175.

81 A. R. Clapp, I. L. Medintz, J. M. Mauro, B. R. Fisher, M. G. Bawendi and H. Mattoussi, Fluorescence Resonance Energy Transfer between Quantum Dot Donors and Dye-Labeled Protein Acceptors, *J. Am. Chem. Soc.*, 2004, **126**, 301–310.

82 K.-H. Speidel, O. Kenn and F. Nowacki, Magnetic moments and nuclear structure, *Prog. Part. Nucl. Phys.*, 2002, **49**, 91–154.

83 S. Zhang, Y. Zhang, L. Zhang, Z. Li, Y. Ren, Q. Jin and Z. Zhang, Temperature Dependence of Magnetic Properties in CoFe/Tb Multilayers with Perpendicular Magnetic Anisotropy, *ACS Appl. Electron. Mater.*, 2022, **4**, 5361–5367.

84 R. Olmos, P.-H. Chang, P. Mishra, R. R. Zope, T. Baruah, Y. Liu, C. Petrovic and S. R. Singamaneni, Pressure-Dependent Magnetic Properties of Quasi-2D Cr2Si2Te6 and Mn3Si2Te6, *J. Phys. Chem. C*, 2023, **127**, 10324–10331.

85 C. KITTEL, Physical theory of Ferromagnetic Domains.

86 C. Wang, C. Wang, X. Gao, M. Tian and Y. Zhang, Research on Microstructure Characteristics of Welded Joint by Magneto-Optical Imaging Method, *Metals (Basel).*, , DOI:10.3390/met12020258.

87 M. G. Bawendi, M. L. Steigerwald and L. E. Brus, The Quantum Mechanics of Larger Semiconductor Clusters ('Quantum Dots'), *Annu. Rev. Phys. Chem.*, 1990, **41**, 477–496.

88 A.-I. Stoica, C. Kleber, C. Viñas and F. Teixidor, Ion selective electrodes for protonable nitrogen containing analytes: Metallacarboranes as active membrane components, *Electrochim. Acta*, 2013, **113**, 94–98.

89 A.-I. Stoica, C. Viñas and F. Teixidor, Cobaltabisdicarbollide anion receptor for enantiomer-selective membrane electrodes, *Chem. Commun.*, 2009, 4988–4990.

90 A.-I. Stoica, C. Viñas and F. Teixidor, *Molecules*, 2022, 27.

Chapter 2

2.1 Introduction

Electrochemical processes are at the heart of inorganic chemistry and hence molecular electrochemistry has, over the years, become a powerful tool of research. Electrochemistry is a field of chemistry which deals with the study of interdependent electrical and chemical effects caused in response to an applied potential resulting in a chemical change or vice-versa. It relates the movement of electrons to chemical changes resulting in a redox process.[1] The electrochemical processes are carried out in an electrochemical cell consisting of at-least two electrodes separated by an electrolyte. Electrodes are electronic conductors where the transfer of charges occur due to the movement of electrons while electrolytes are ionic conductors where the transfer of charges occur due to the movement of ions. The primary difference between an electrochemical and a chemical reaction is the driving force as a chemical reaction mainly depends on the favourable alignment of the energy levels of the reactants whereas an electrochemical reaction involves a ‘heterogenous’ transfer of electron from an electrode modulated by the application of an external potential.[2]

A typical three-electrode electrochemical cell would consist of a reference electrode (RE), a working electrode (WE) and an auxiliary or counter electrode (CE) separated by an electrolyte maintained in an inert atmosphere connected to an external potentiostat (Scheme 2.1).

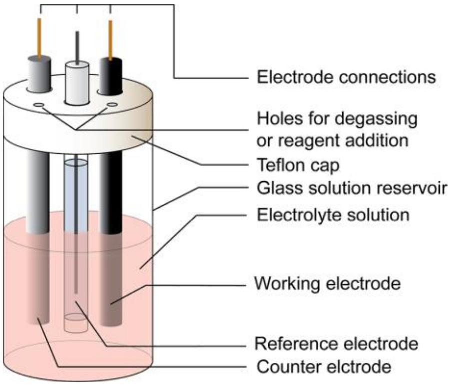

Scheme 2.1 A schematic representation of a 3-electrode electrochemical cell. [From reference 1]

Of the electrodes, choosing the right RE is of utmost importance as it is the potential against which all the other potentials are measured. Generally, the potentials in an electrochemical cell are mentioned as '*vs.*' the potential of the RE. Hence, a RE should have a stable and well-defined standard electrode potential. The commonly employed RE are the normal hydrogen electrode (NHE), standard hydrogen electrode (SHE), the saturated calomel electrode (SCE) or the different forms of Ag/AgCl electrodes. These are predominantly aqueous reference electrodes and are more accurate to measure electrochemical processes in aqueous solutions. The question then arises as to how to measure electrochemical processes in organic solvents? Even though aqueous RE can be used to measure the electrochemical processes in organic solvents, it is not advisable due to the development of unmeasurable potential junctions which alters the reference potentials.[3] Thus, internal references (IR) in conjunction with pseudo or quasi reference electrode (QRE) were introduced to circumvent the problem.[4] The predominantly used IRs are the reversible redox pairs of ferrocene (Fc^+/Fc),[5,6] cobaltocene (Cc^+/Cc)[7] and decamethylferrocene ($DmFc^+/DmFc$).[8,9] Even though these IRs prove to solve the problem of measuring in organic solvents, a major challenge arises when one has to compare electrochemical processes in aqueous and non-aqueous systems as they are predominantly insoluble in water.[10] A workaround the problem is to derivatize these redox pairs to soluble ones having similar one-electron transfer process. An example of this would be the derivatization of ferrocene-to-ferrocene carboxylic acid (FCA),[11] ferrocenemethanol (FcMe),[12] and ferrocene acetic acid (FAA)[6] which are soluble in water and go through the same ferricenium oxidative state. The problem seems to be resolved, but is not quite so as the measurements are not highly precise because functional modifications of the parent species does indeed alter the redox parameters of the electrochemical couple.[13–15] Notably, all the IRs are complexes in which one of the redox pair fulfils the $18e^-$ rule and are octahedrally coordinated to avoid, as much as possible, solvent interaction with the metal centre. Indeed, all these proceed through an outer-sphere electron transfer mechanism. The IRs are generally either anions/alcohols in aqueous solvents or neutral species in organic solvents. Table 2.1 describes the commonly employed IRs and their redox parameters.

Table 2.1 Commonly employed internal references (IRs) and their redox parameters. $TBAPF_6$- Tetrabutylammonium hexafluorophosphate; TBAP- Tetrabutylammonium perchlorate in acetonitrile (ACN).

Redox couple	Electrolyte	E_{pa} (V)	E_{pc} (V)	$E^{0'}$ (V)
Ferrocene (Fc^+/Fc)[15]	0.1M $TBAPF_6$ in ACN	+0.436	+0.370	+0.403 vs SCE
Decamethylferrocene ($DmFc^+/DmFc$)[15]	0.1M $TBAPF_6$ in ACN	-0.093	-0.099	-0.096 vs. NHE
Bis(biphenyl)chromium (BCr^+/BCr)[16]	0.1M TBAP in ACN	-0.674	-0.740	-0.707 vs. NHE
Cobaltacene (Cc^+/Cc)	0.1M $TBAPF_6$ in ACN[13] 0.1M $TBAPF_6$ in ACN[17]	- -0.187	- -0.265	-1.337 vs. Fc^+/Fc -0.226 vs. Ag/AgCl(0.1M TBAC)
Ferrocenemethanol (FcMe)[12]	0.1M KCl	0.213	0.15	0.185 vs. SCE
Ferrocenecarboxylic acid (FCA)[18]	0.1M $TBAPF_6$ in ACN	0.218	0.138	0.178 vs. Fc^+/Fc
Ferroceneacetic acid (FAA)[18]	0.1M $TBAPF_6$ in ACN	-0.047	-0.129	-0.088 vs. Fc^+/Fc

2.2 Motivation & Objective

As mentioned earlier there are several IRs; yet, currently there exists none which is suitable, without any modification, for both aqueous and non-aqueous systems. An effective internal reference redox system must possess certain characteristics such as having a reversible redox couple, preferably a one-electron outer-sphere electron transfer, chemical inertness, electrochemical stability and must be easily synthesizable or available with a relatively long shelf-life.[19]

θ-Metallacarboranes (Mcb) with the empirical formula $[M(C_2B_9H_{11})_2]^-$, (M=Co, Fe), amongst having the advantages described in Chapter 1 (section 1.2) and being redox active has a structural construction akin to ferrocene producing a θ-shaped 3-dimensional molecular anion.[20,21] But unlike ferrocene, these compounds are soluble in both aqueous and non-aqueous solvents without any structural modifications and due to the 3-dimensional nature of the cluster, the metal centre is better shielded from the external solvent environment rendering a ‘canopy effect’ in comparison to ferrocene which offers a 2-dimensional rigidity to the metal centre (Scheme 2.2).

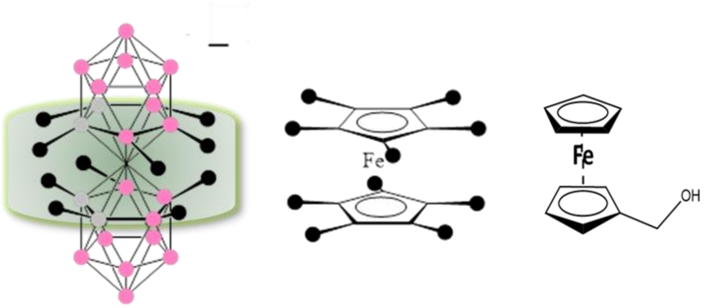

Scheme 2.2 Schematic representation of the ‘canopy effect’ for the 3D [3,3’-M(1,2-$C_2B_9H_{11})_2]^-$ (M= Co, Fe) in comparison to the planar ferrocene (Fc) and ferrocene methanol (FcMe).

Prominent redox active transition metal centre for such θ-shaped π sandwich dicarbollide clusters are Ni, Co and Fe. Remarkably, M’[3,3’-M($C_2B_9H_{11})_2$] (M=Co, Fe), when M’=Na, K is soluble in water and when M’=Cs is soluble in all the common electrochemically active organic solvents.[22] Therefore, metallacarboranes provide with the perfect electrochemical redox couple to be employed as internal references in both aqueous and non-aqueous systems. In this study, we have focused on the alkaline salts of [3,3’-Co($C_2B_9H_{11})_2]^-$, [*o*-COSAN]$^-$, and [3,3’-Fe($C_2B_9H_{11})_2]^-$, [*o*-FESAN]$^-$, to study their electrochemical properties by exploiting the reversible redox active pairs, $Co^{3+/2+}$ and $Fe^{3+/2+}$. The objective of the study would be to ascertain the applicability of these metallacarboranes as internal reference redox systems by comparing its electrochemical behaviour in aqueous (water) and non-aqueous (dry acetonitrile) systems with ferrocene (Fc) and ferrocene methanol (FcMe) in the same solvents.

The investigation was undertaken using the simple and robust technique of cyclic voltammetry (CV) with a three-electrode system: glassy carbon (GC) as the WE, coiled Pt wire as the CE and Ag/AgCl(1M KCl) (for aqueous solvents) or SCE (for organic solvents) as the RE. The key parameters measured to obtain a conclusive understanding of the redox behaviour of the compound were the redox peak potentials, namely cathodic (E_{pc}) at which reduction occurs and anodic (E_{pa}) at which oxidation occurs with the corresponding peak currents i_{pc} and i_{pa}, respectively, the formal peak potential ($E^{o\prime}$) is calculated as:

$$E^{o\prime}=(E_{pc}+E_{pa})/2$$

and the peak-to-peak separation (ΔE) calculated as E_{pa}-E_{pc} (Scheme 2.3). Thermodynamically, for a chemically and electrochemically reversible one-electron transfer process the ΔE is 57mV (calculated as $2.22RT/nF$ where n is the number of electrons transferred following the Nernst equation).[23]

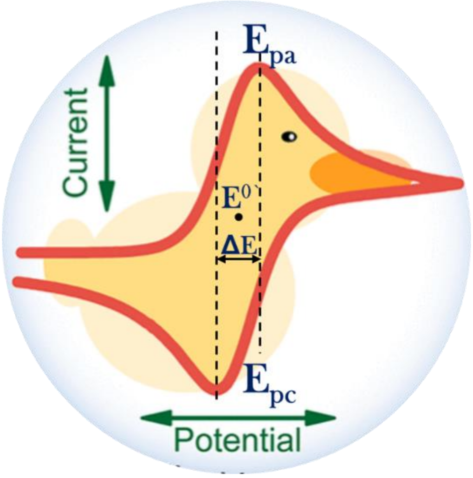

Scheme 2.3 An adapted schematic representation of a typical cyclic voltammogram depicting the different electrochemical parameters which can be obtained from the measurement.[1]

2.3 Results & Discussions

The CV experiments were performed in an Autolab PGSTAT302N potentiostat/galvanostat from Metrohm using its in-built software as well as in an Autolab PGSTAT30 from Eco-Chemie using the software GPES 4.9. The measurements involved 3 scans with a scan rate of 100mV/s in an inert atmosphere, unless stated otherwise, with appropriate potential window for each of the compounds: Na[*o*-COSAN], Na[*o*-FESAN] & FcMe with Ag/AgCl(1M KCl) as the RE in aqueous solvent and Cs[*o*-COSAN], Cs[*o*-FESAN] & Fc with SCE as the RE in non-aqueous solvent.

The solutions were prepared with concentrations suitable enough to produce a rational CV response. The concentration of the compounds were 30 mM (in aqueous) and 5 mM (in non-aqueous) for the Na and Cs salt of [*o*-COSAN]$^-$, respectively, while for the Na and Cs salt of [*o*-FESAN]$^-$ it was 1 mM each as well as for Fc. In the case of FcMe, as it was only partially soluble in water, a stock solution of 10 mM in methanol was prepared to finally produce a 1 mM solution of FcMe in the aqueous electrolyte for measuring. 0.3 M KNO_3 in 3 mL water was used as the aqueous electrolyte while 0.3 M tetrabutylammonium perchlorate (TBAP) in 3 mL dry acetonitrile (AcN) was used as the organic electrolyte. Each of the sub-sequent sections would entail in detail the different conditions and experiments performed by varying different parameters of the general CV measurement to validate the potential use of Mcb as internal redox reference systems.

2.3.1 Effect of electrolyte & electrolyte concentration

The charge transfer kinetics in an electrochemical process is greatly influenced by the electrolyte. As the electron transfer occurs, the electrical neutrality is maintained by the transport of ions through the solution.[24] Hence, it is important to understand the behaviour of these compounds in different electrolytes as the migration of charges is a crucial factor in any redox process. Consequently, a series of CV experiments were performed in different electrolytes, with water as the solvent, such as KNO_3 and KCl, to understand the effect of different anions, while to study the effect of different cations $NaNO_3$ was used. Experiments were also performed in phosphate buffer (PB) and phosphate saline buffer (PBS) due to their biological relevance as well as in acetic acid. Most of the commonly used electrolytes have been investigated to ascertain the constant redox behaviour of the Mcb.

Fig. 2.1 shows the CV response of Na[*o*-COSAN] and Na[*o*-FESAN] in comparison to FcMe obtained in different electrolytes. From the cyclic voltammograms, it can be observed that the Mcb showed negligible variations in the formal potential ($E^{o'}$) and the peak separation (ΔE) in each of the different electrolytes were in agreement to a reversible redox process (Table 2.2).

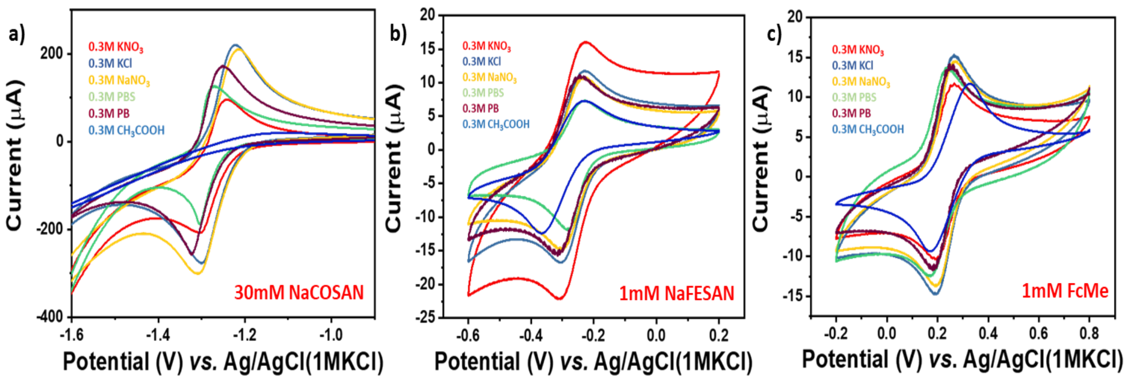

Fig. 2.1 Cyclic voltammetric response in different electrolytes of **(a)** 30 mM Na[*o*-COSAN]; **(b)** 1 mM Na[*o*-FESAN]; **(c)** 1 mM FcMe with GC as the WE and Ag/AgCl(1MKCl) as the RE in water.

From the CV studies, it is evident that the Mcb have consistent redox properties regardless of the electrolyte employed, making it appropriate to be utilized as an internal reference for any electrochemical process. Since the parameters were constant, KNO$_3$ was chosen as the electrolyte for all the aqueous system experiments.

Table 2.2 The cathodic (E_{pc}) and anodic (E_{pa}) peak potentials and the peak-to-peak separation (ΔE) potential for **(a)** 30 mM Na[*o*-COSAN]; **(b)** 1 mM Na[*o*-FESAN]; **(c)** 1 mM FcMe with Ag/AgCl(1MKCl) as the RE.

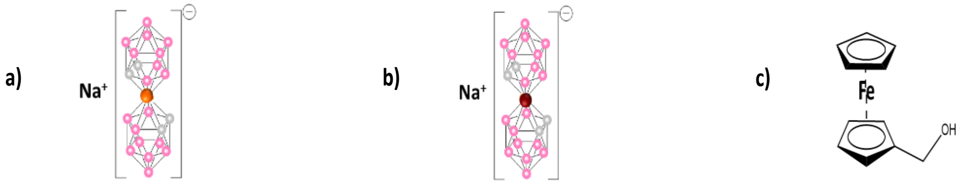

Electrolyte (0.3M)	Epa (V)	Epc (V)	ΔE (V)
KNO$_3$	-1.242	-1.304	0.062
KCl	-1.223	-1.299	0.076
NaNO$_3$	-1.213	-1.307	0.094
PBS	-1.271	-1.305	0.034
PB	-1.251	-1.322	0.071
Acetic Acid	-	-	-

Electrolyte (0.3M)	Epa (V)	Epc (V)	ΔE (V)
KNO$_3$	-0.227	-0.3	0.073
KCl	-0.229	-0.3	0.071
NaNO$_3$	-0.23	-0.3	0.07
PBS	-0.23	-0.28	0.05
PB	-0.238	-0.3	0.069
Acetic Acid	-0.228	-0.368	0.14

Electrolyte (0.3M)	Epa (V)	Epc (V)	ΔE (V)
KNO$_3$	0.262	0.193	0.069
KCl	0.265	0.19	0.075
NaNO$_3$	0.268	0.192	0.076
PBS	0.238	0.169	0.069
PB	0.261	0.19	0.071
Acetic Acid	0.331	0.166	0.165

As crucial as it is the choice of the electrolyte, the concentration of the electrolyte also plays a significant role in an electrochemical process. As a general rule of thumb, the concentration of the electrolyte in any typical electrochemical experiment is usually 100 times more than that of the analyte. A high concentration of the electrolyte is essential to ensure an efficient charge transfer due to increased ionic conductivity as well as to mitigate the migration of the analyte to the electrode surface.[25,26] Therefore, experiments were performed by varying the concentration of the electrolyte, KNO_3 (Fig.2.2) and TBAP (Fig.2.3) in aqueous and non-aqueous solvents, respectively, from 5 – 500 mM by dissolving, sequentially, the required amount of the electrolyte to attain the desired concentration.

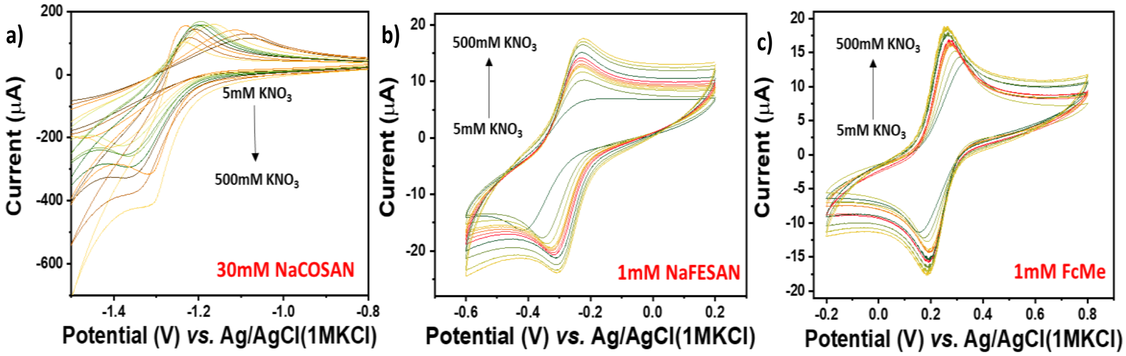

Fig. 2.2 Varying concentration of the electrolyte, KNO_3, from 5-500 mM for **(a)** 30 mM Na[*o*-COSAN]; **(b)** 1 mM Na[*o*-FESAN]; **(c)** 1 mM FcMe with Ag/AgCl(1MKCl) as the RE and 100 mV/s scan rate.

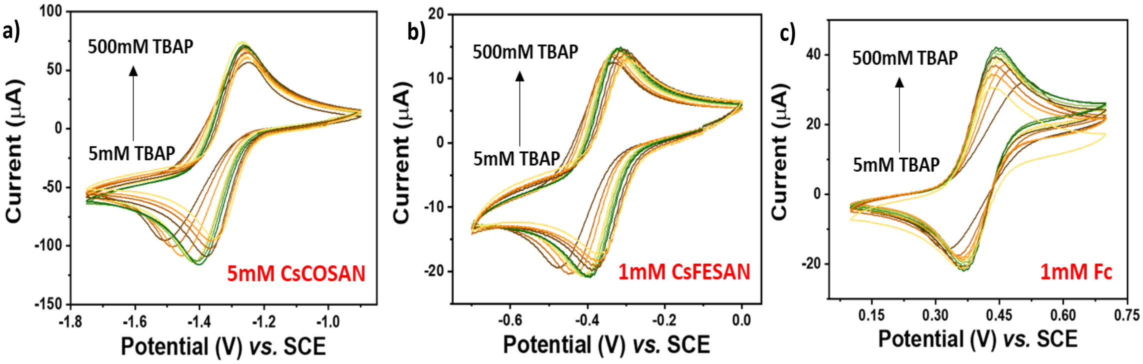

Fig. 2.3 Varying concentration of the electrolyte, TBAP in dry AcN, from 5-500 mM for **(a)** 5 mM Cs[*o*-COSAN]; **(b)** 1 mM Cs[*o*-FESAN]; **(c)** 1 mM Fc with SCE as the RE and 100 mV/s scan rate.

Expectedly, at low electrolytic concentrations, the charge transfer was limited due which the peak separation (ΔE) was large in all the compounds investigated including the standard references, FcMe and Fc. In order to acccomodate all the different concentrations of the compunds studied, 0.3 M was chosen as the preferred electrolyte concentration for the remaining experiments.

These experiments demonstrate that the θ-metallacarboranes are capable of being employed as internal references.

2.3.2 Effect of varying the scan rate

Scan rate (ν) dictates the rate of change of potential in an electrochemical experiment. A higher scan rate would imply a faster decline in the diffusing layer, thereby producing higher peak currents.[27] Hence, to understand the charge transfer kinetics of these redox pairs, a series of electrochemical experiments were carried out by varying the scan rates from 10 – 1000 mV/s in both aqueous and non-aqueous systems (Fig 2.4).

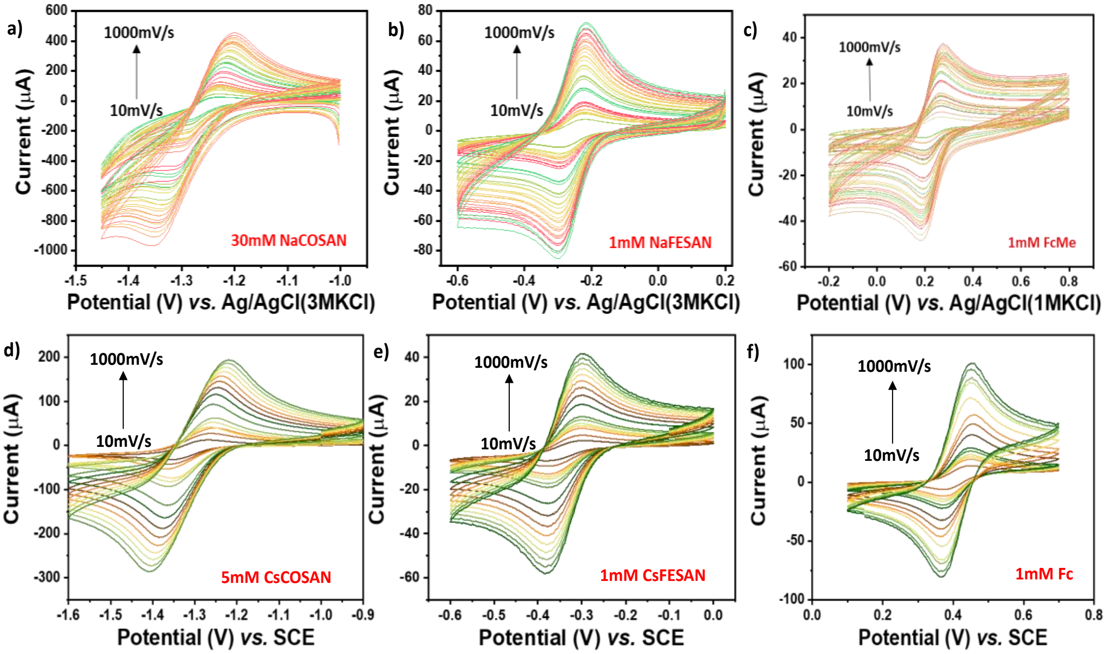

Fig.2.4 Cyclic voltammograms obtained for the different compounds by varying the scan rate from 10 – 1000 mV/s in both, aqueous (0.3M KNO_3) and non-aqueous (0.3M TBAP in dry AcN) as: **(a)** 30 mM Na[*o*-COSAN]; **(b)** 1 mM Na[*o*-FESAN]; **(c)** 1 mM FcMe with Ag/AgCl(1MKCl) as the RE; **(d)** 5 mM Cs[*o*-COSAN]; **(e)** 1 mM Cs[*o*-FESAN]; **(f)** 1 mM Fc with SCE as the RE.

The CV responses show that the formal potential (E^{o}’) as well as the peak separation (ΔE) remains fairly constant at all the different scan rates indicating a stable elctrochemical behaviour of the metallacarboranes. Since an electrochemical experiment can be carried out at any scan rate, it is important to establish that the material employed as internal reference has constant redox parameters irrespective of the scan rate.

For electrochemically reversible processes involving redox species which are freely diffusing, the peak current (i_p) is directly propotional to the square root of the scan rate ($\nu^{1/2}$) following the Randles-Sevick equation as:

$$i_p = 0.446nFAC^o(nF\,\nu D_o/RT)^{1/2}$$

where n is the number of electrons transferred, F is the Faraday's constant, A is the electrode surface area, C^o is the bulk concentration and D_o is the diffusion coefficient of the analyte. Hence, a plot of i_p *vs.* $\nu^{1/2}$ would vary linearly for a diffusion-controlled electron transfer process. Any deviations from the linearity can be attributed to either an electrochemical quasi-reversibility or an electron transfer process occuring due to surface adsorbed species.

Fig. 2.5 describes the Randles-Sevick plot ontained for the different compounds investigated in comparison to the standards, Fc and FcMe, for both aqueous and non-aqueous systems. From the plots, it can be inferred that the electron transfer process for both the metallacarboranes, [*o*-COSAN]$^-$ and [*o*-FESAN]$^-$, is a diffusion-controlled revesible electrochemical process.

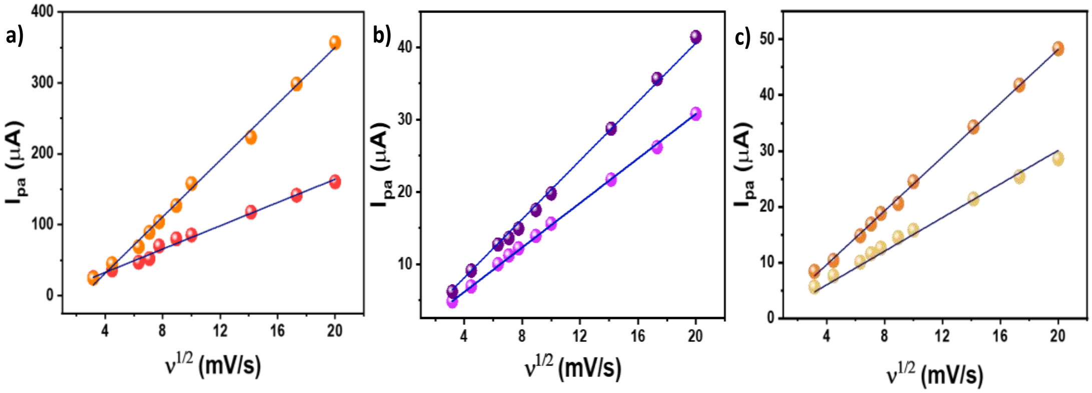

Fig. 2.5 Anodic peak current (i_{pa}) *vs.* $\nu^{1/2}$ obtained for **(a)** Na[*o*-COSAN] and Cs[*o*-COSAN]; **(b)** Na[*o*-FESAN] and Cs[*o*-FESAN]; **(c)** Fc and FcMe.

The feasability of [3,3'-M($C_2B_9H_{11}$)$_2$]$^-$ (M= Co, Fe) as internal redox reference systems are asserted by these positive results.

2.3.3 Effect of self-assembly of $[3,3'\text{-}M(C_2B_9H_{11})_2]^-$ (M= Co, Fe) in aqueous solution

Previously, we had studied the behaviour of metallacarboranes in aqueous and non-aqueous (acetone) solvents and have shown that the metallacarboranes have a remarkable ability to form micelles and vesicles in aqueous solvents upon varying the concentration due to their capacity to form strong hydrogen and di-hydrogen bonds.[28–30] Dynamic light scattering (DLS) experiments were performed by sequentially increasing the concentration of Na[*o*-COSAN] and Na[*o*-FESAN] in water to monitor the aggregate formation (Fig. 2.6). From the experiments, it can be observed that with increasing concentration of the Mcb, the hydrodynamic size decreases which can be attributed to a coloumb explosion of the closely packed monolayer aggregates into small vesicles.[31] The change in the hydrodynamic diameter for Na[*o*-COSAN] was observed at 29 mM while for Na[*o*-FESAN] it was observed at 50 mM.

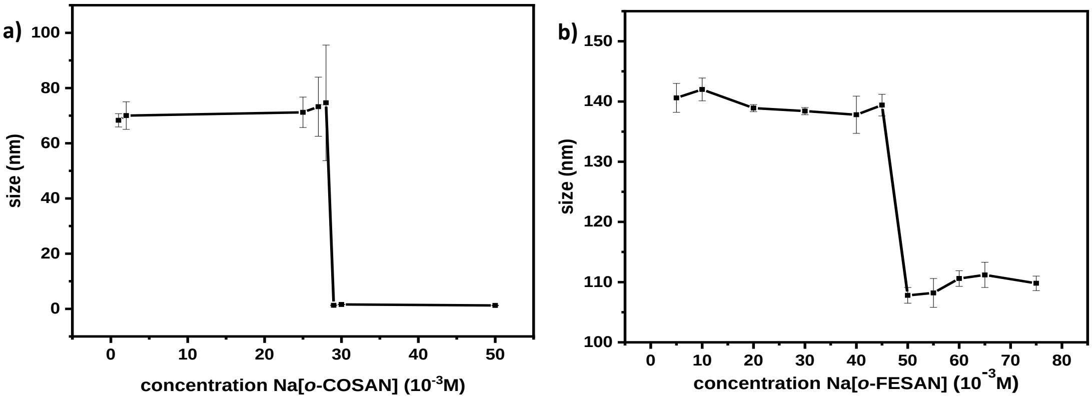

Fig. 2.6 Self-assembly of **(a)** Na[*o*-COSAN] in concentration range 1 – 50 mM and **(b)** Na[*o*-FESAN] in concentration range 5 – 75 mM in aqueous solvent.

Hence, in order to demonstrate that the self-assembling ability of the Mcb in water have minimal influence on the redox parameters, CV experiments were carried out by varying the concentration of Na[*o*-COSAN] from 5- 50 mM and Na[*o*-FESAN] from 1 – 65 mM in 0.3M KNO_3. From fig. 2.7, it can be observed that the self-assembly of Mcb have negligible effect on the redox parameters and the table 2.3 enlists the different E^{o}' and ΔE for the same. Notably, the peak separation remained resonably consistent to the one-electron reversible electron transfer process for Na[*o*-COSAN] at all the different concentrations measured, however for Na[*o*-FESAN] the peak separation was larger at higher concentrations (from 50 mM).

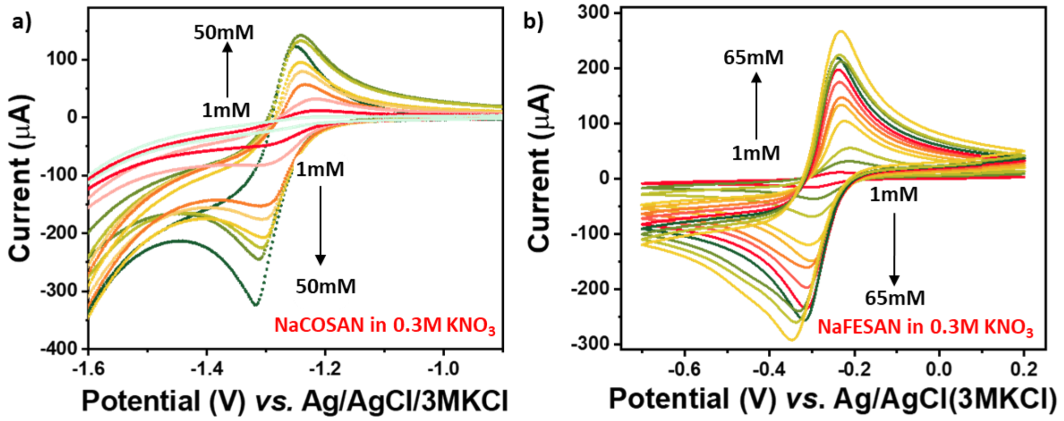

Fig. 2.7 Cyclic voltammograms displaying the effect of self-assembly of **(a)** Na[*o*-COSAN] and **(b)** Na[*o*-FESAN] with 0.3M KNO_3 in water.

The discrepancy in the ΔE for Na[*o*-FESAN] can be ascribed to the high barrier rendered to the charge transfer kinetics due to vesicle formation whereas the self-assembly of Na[*o*-COSAN] did not show any profound effect on the electrochemical response. Nevertheless, both the Mcb displayed remarkably reversible electrochemical response for a wide range of concentration, thereby furthering their potential application as an internal reference.

Table 2.3 The cathodic (E_{pc}) and anodic (E_{pa}) peak potentials as well as the peak separation (ΔE) for **(a)** Na[*o*-COSAN] and **(b)** Na[*o*-FESAN] in 0.3M KNO_3 with Ag/AgCl(1M KCl) as the RE.

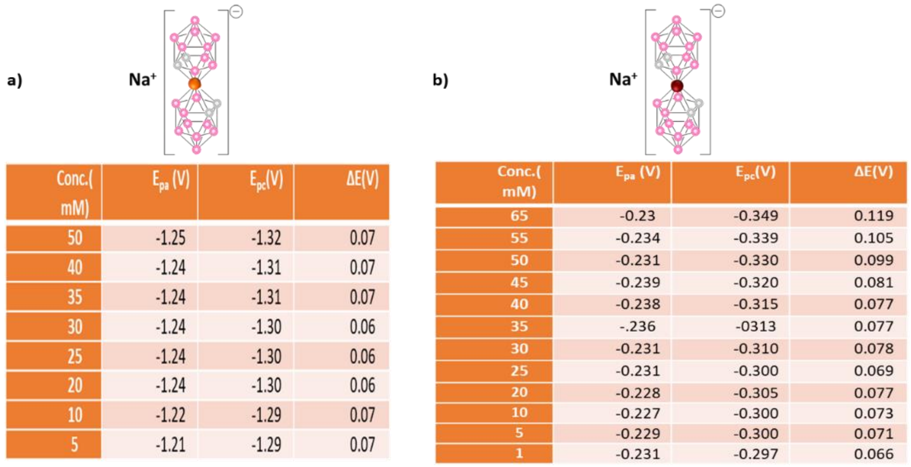

a)

Conc.(mM)	E_{pa} (V)	E_{pc}(V)	ΔE(V)
50	-1.25	-1.32	0.07
40	-1.24	-1.31	0.07
35	-1.24	-1.31	0.07
30	-1.24	-1.30	0.06
25	-1.24	-1.30	0.06
20	-1.24	-1.30	0.06
10	-1.22	-1.29	0.07
5	-1.21	-1.29	0.07

b)

Conc.(mM)	E_{pa} (V)	E_{pc}(V)	ΔE(V)
65	-0.23	-0.349	0.119
55	-0.234	-0.339	0.105
50	-0.231	-0.330	0.099
45	-0.239	-0.320	0.081
40	-0.238	-0.315	0.077
35	-.236	-0313	0.077
30	-0.231	-0.310	0.078
25	-0.231	-0.300	0.069
20	-0.228	-0.305	0.077
10	-0.227	-0.300	0.073
5	-0.229	-0.300	0.071
1	-0.231	-0.297	0.066

2.3.4 Effect of varying temperature and pH on the electrochemical response

The equilibrium of an electrochemical process is dictated by the Nernst equation which equates the potential of an electrochemical cell (E) to the formal potential of the redox species ($E^{o\prime}$) as well as the relative activities or concentration of the oxidized (Ox) and reduced (Red) species as:

$$E = E^{o\prime} + RT/nF * \ln [Ox]/[Red]$$

The Nernstian equilibrium is greatly influenced by the experimental conditions employed such as the temperature and pH.[1] Hence, in order for a material to be considered as an internal reference, it is important to investigate its behaviour in different experimental conditions.

Generally, most of the electrochemical experiments are performed in ambient temperature. But while considering the applicability of a compound as a reference material, it is relevant to subject it to harsh conditions and study the electrochemical response. Consequently, CV measurements were performed by varying the temperature from 25° – 50°C in intervals of 2°C using a temperature controller (Fig. 2.8). The experiments were performed in 0.3 M KNO_3 using glassy carbon as the WE.

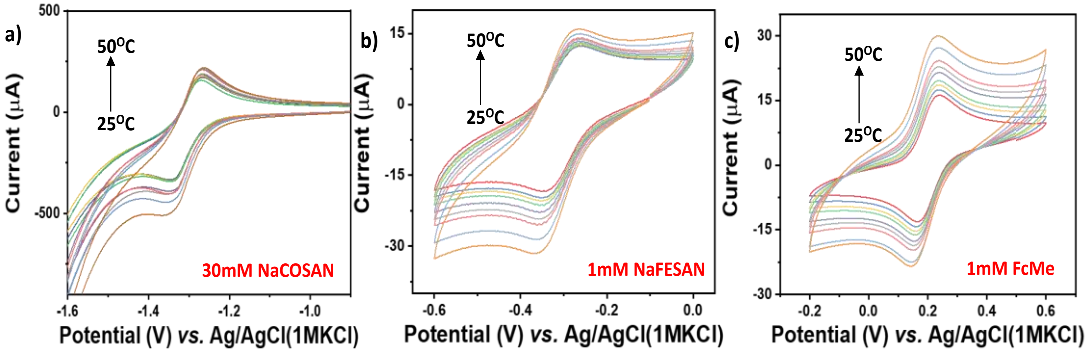

Fig. 2.8 Cyclic voltammograms for **(a)** 30 mM Na[*o*-COSAN]; **(b)** 1 mM Na[*o*-FESAN]; **(c)** 1 mM FcMe with Ag/AgCl(1MKCl) as the RE and 100 mV/s scan rate at different temperatures.

Fig. 2.9 encompasses the formal potential ($E^{o\prime}$) and the peak separation (ΔE) for the Mcb at the different temperatures measured.

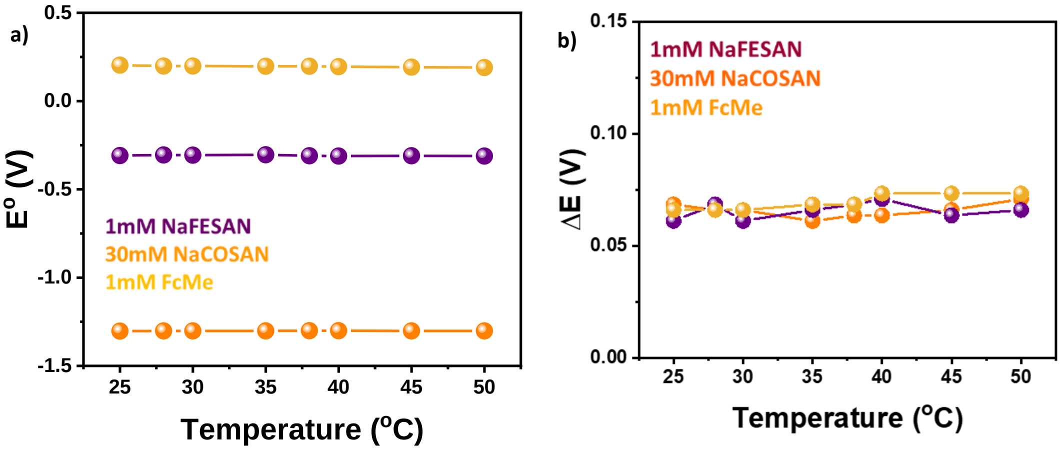

Fig. 2.9 Comparing the effect of changing the temperature on **(a)** the formal potential (E°') and **(b)** the peak separation (ΔE) for the metallacarboranes and FcMe.

From the experiments, it can be observed that the influence of the temperature on the redox parameters for Na[*o*-COSAN] and Na[*o*-FESAN] is insignificant and the compounds indeed show a high thermal stability throughout the measurement.

Similarly, the pH of the electrolytic solution has a significant impact on the Nernstian equilibrium. Depending on the pH, the redox activity of the electroactive species can alter and can even lead to corrosion in case of metals at acidic pH. Therefore, it becomes crucial to understand the electrochemical response of the internal references under varying pH conditions. Subsequently, experiments were carried out using 0.1 M Britton-Robinson (BR) buffer as the electrolyte prepared by dissolving 0.04 M phosphoric acid, 0.04 M acetic acid and 0.04 M boric acid in water. The initial pH of the electrolyte was 2, which was gradually increased to 3, 4, 5 till 12 by the drop-wise addition of 5 M NaOH. The pH of the electrolytic solutions were measured using a calibrated pH meter (Fig. 2.10).

As mentioned previously, the important parameters to be considered are the variations in the formal potential (E°') and the peak separation (ΔE) for the Mcb at different pH (Fig. 2.11). Upon comparing the values for each of the compounds, it was observed that the E°' and ΔE were reasonably constant for Na[*o*-FESAN] and even better than FcMe while for Na[*o*-COSAN] it was challenging to observe the CV response at acidic pH due to the closeness of the potential window to water reduction potential.

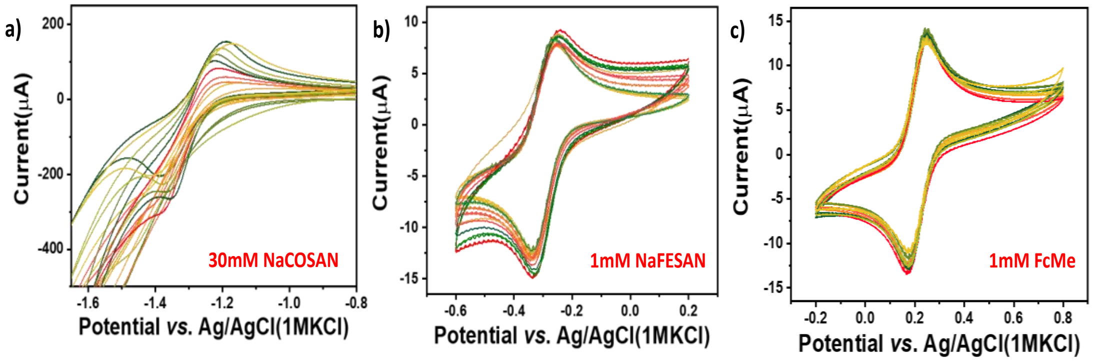

Fig. 2.10 Cyclic voltammograms for **(a)** 30 mM Na[*o*-COSAN]; **(b)** 1 mM Na[*o*-FESAN]; **(c)** 1 mM FcMe in 0.1 M BR electrolyte with Ag/AgCl(1MKCl) as the RE and 100 mV/s scan rate for the different pH from 2 – 12 measured.

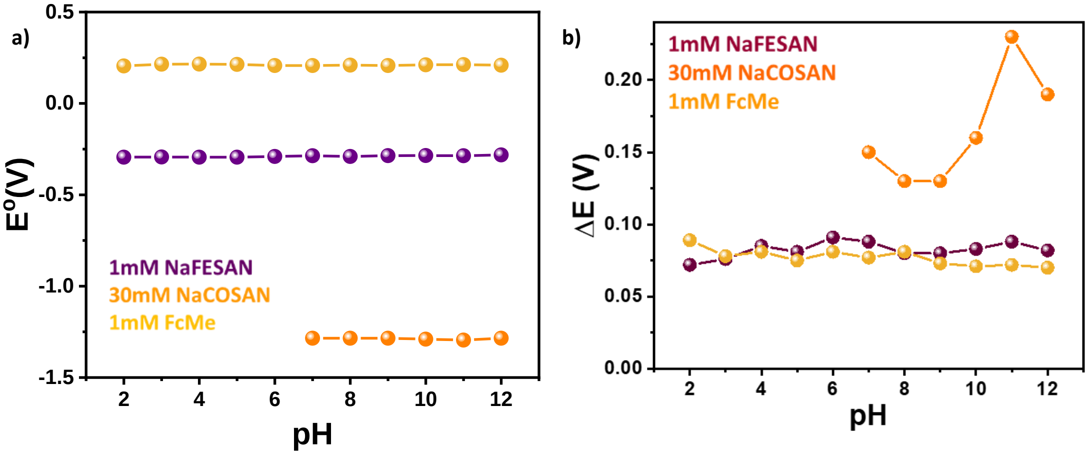

Fig. 2.11 Comparing the effect of varying the pH from 2-12 on **(a)** the formal potential (E°') and **(b)** the peak separation (ΔE) for the metallacarboranes with the standard internal references.

As can be seen from the results, the ΔE displays a similar consistentcy for Na[*o*-FESAN] as the reference, FcMe, indicating that the electron transfer process is reversible at all the different pH measured as opposed to Na[*o*-COSAN] due to water splitting. These results suggest the capability of Mcb to perform as a better internal reference in comparison to the standard ones.

2.3.5 Effect of different working electrode materials

The electrochemical process of interest occurs at the surface of the working electrode whose potential is regulated using a potentiostat with regard to the reference electrode. Generally, WE, composed of redox-inert materials, are chosen specifically according to the potential window of interest. Due to the different electron transfer kinetics, adsorption of redox species as well as the occurrence of electrode specific chemical reactions, different electrode materials can influence the electrochemical response.[1]

Consequently, CV experiments were performed with different WE such as glassy carbon (GC), platinum (Pt) and gold (Au) in both aqueous and non-aqueous electrolytes with the same redox conditions. As the WE is crucial for the electrochemical response, it is imperative that the surface of the electrodes are extremely clean and well-defined. Hence, the GC was polished using a water-alumina slurry while Pt and Au were subjected to diamond polishing as these were more sensitive to adsorption. A pre-treatment of the electrodes were carried out and the characteristic CV responses in 0.1 M and 0.5 M H_2SO_4 for Au and Pt, respectively, at 100 mV/s for 10 scans were recorded.[32]

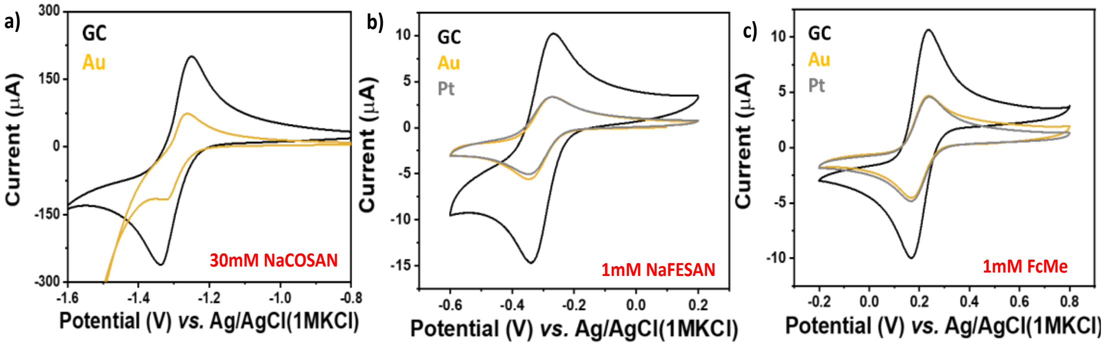

Fig. 2.12 CV responses of **(a)** 30 mM Na[*o*-COSAN]; **(b)** 1 mM Na[*o*-FESAN]; **(c)** 1 mM FcMe in 0.3M KNO_3 with Ag/AgCl(1MKCl) as the RE.

Fig. 2.12 describes the different CV responses obtained for each of the compounds in aqueous electrolyte. As can be observed, the redox parameters remains constant irrespective of the WE material indicating that the Mcb are chemically inert and interact insignificantly with the electrode materials. Notably, the GC offers a much higher current intensity in comparison to both Au and Pt. Table 2.4 enlists the different parameters such as the formal potential ($E^{o\prime}$) and the peak separation (ΔE) for the Mcb obtained using the different WE materials. As can be observed, the Mcb are stable and respond without any alterations in each of the different experiments involving different WE as the parameters are constant and agreeable to the standard.

In case of Na[*o*-COSAN], the Pt electrode could not be employed due to the small potential window of Pt in aqueous electrolyte.

Table 2.4 Description of the various electrochemical parameters such as the anodic peak potential (E_{pa}), cathodic peak potential (E_{pc}), the formal potential (E°') and the peak separation (ΔE) obtained using different working electrode materials in 0.3M KNO_3 with Ag/AgCl (1M KCl) as reference at 100 mV/s.

	Electrode	E_{pa} (V)	E_{pc} (V)	ΔE_p (mV)	$E^{0'}$ (V)
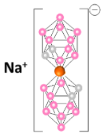	GC	-1.250	-1.338	88.7	-1.294
	Au	-1.260	-1.318	57.7	-1.289
	Pt	-	-	-	-
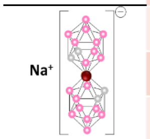	GC	-0.267	-0.339	71.6	-0.303
	Au	-0.270	-0.346	75.5	-0.308
	Pt	-0.270	-0.346	75.6	-0.308
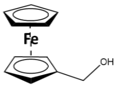	GC	0.238	0.163	74.6	0.200
	Au	0.236	0.165	70.5	0.200
	Pt	0.236	0.166	70.4	0.200

Similar experiments were also repeated in non-aqueous solvent (0.3 M TBAP in dry AcN) and the results were comparable (Fig. 2.13). Even in non-aqueous system, the WE material had negligible influence on the electrochemical characteristics of the Mcb. Since Pt had a wider potential window in non-aqueous electrolyte, it could be employed to study all the compounds investigated and Na[*o*-COSAN] indeed showed minimal impact even with Pt as WE.

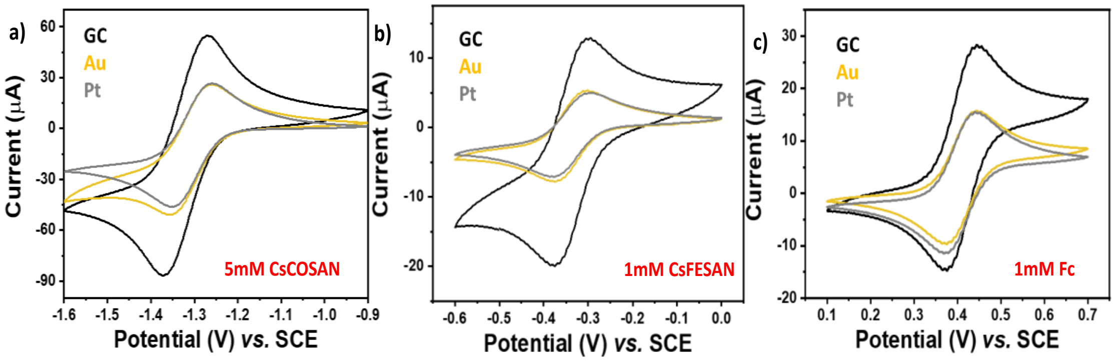

Fig. 2.13 CV response of **(a)** 5 mM Cs[*o*-COSAN]; **(b)** 1 mM Cs[*o*-FESAN]; **(c)** 1 mM Fc with SCE as the RE and 100 mV/s scan rate.

These experiments prove that Mcb are minimally adsorped on the different commonly employed WE and have no electrode-specific chemical reactions or interactions which can alter the electrochemical responses. Hence, metallacarboranes can indeed be a strong candidate for internal references.

2.3.6 Comparison of Na and Cs salts of [o-FESAN] in aqueous electrolyte

Intriguingly, the Cs salts of the metallacarboranes are partially soluble in water upto 4 mg/mL, particularly for [*o*-FESAN]. Hence, it is rational to compare the electrochemical responses of both the Na and Cs salts of [*o*-FESAN] in aqueous electrolyte. Electrochemical experiments were carried out using 1 mM Cs[*o*-FESAN] in 0.3 M KNO_3 using Ag/AgCl as the reference with the same parameters as 1 mM Na[*o*-FESAN] (Fig. 2.14). Suprisingly, the CV curve as well as peak potentials in both the cases were similar except for a slight reduction in the peak current in case of Cs[*o*-FESAN] which can be attributed to its poor solubility in water. Nevertheless, this serves as a proof that even the same salt of Mcb can be used to compare different electrochemical experiments in aqueous and non-aqueous systems. The formal peak potentials are -0.285 V and -0.282 V for Na and Cs salts, respectively, with the peak separation as 70 mV.

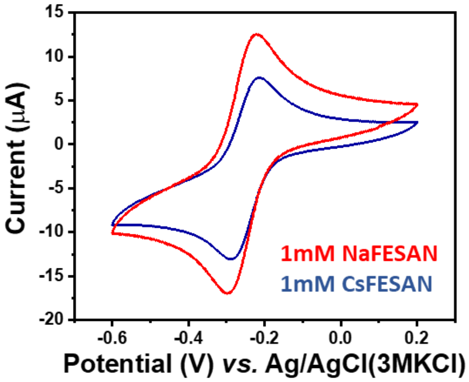

Fig. 2.14 CV of 1 mM Na and Cs [*o*-FESAN] in 0.3M KNO_3 with GC as the working electrode at 100 mV/s.

To further illustrate the applicability of metallacarboranes, experiments using the metallacarboranes as internal reference were performed in THF:water mixture which demonstarted a superior performance in comparison to the conventional Ag/AgCl whose potentials experienced a drift in a binary solvent system due to potential gaps.

2.4 Conclusion

As mentioned in the beginning of the chapter, the main characteristics required for any material to be employed as a reference is to have an enduring redox behaviour with constant peak potentials as well as high chemical and thermal stability in different experimental conditions. Following the comprehensive studies detailed in the chapter, it can be ascertained beyond any doubt that the metallacarboranes does indeed possess the virtues to be considered as a 'universal' internal reference capable of being used in both aqueous and non-aqueous systems without any drastic chemical modifications. Fig. 2.15 shows the different electrochemical responses obtained for the different compounds investigated with the formal potential (E°') as -1.28 V and -1.27 V for Na and Cs [*o*-COSAN] & -0.28 V and -0.29 V for Na and Cs [*o*-FESAN] with respect to Ag/AgCl. The peak separation (ΔE) for the different compounds are 60 mV and 80 mV for Na and Cs [*o*-COSAN] & 70 mV for both the salts of [*o*-FESAN] which are agreeable to the thermodynamic value for one-electron reversible redox process.

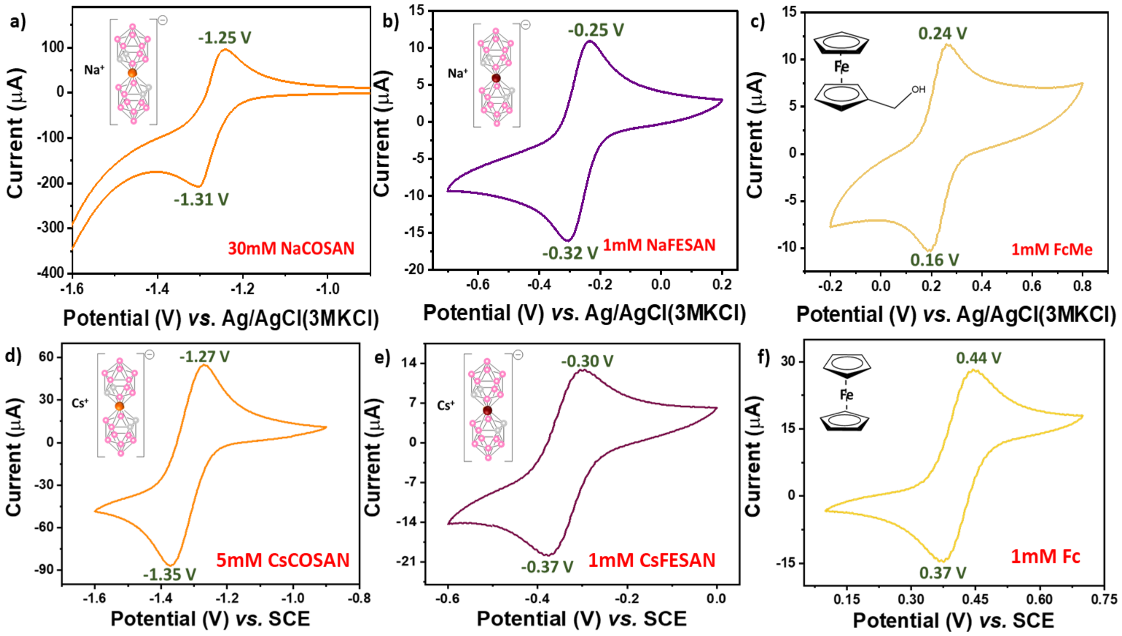

Fig. 2.15 Cyclic voltammograms for the different redox-reversible systems investigated with GC as the working electrode and Pt as counter electrode for: **(a)** 30 mM Na[*o*-COSAN]; **(b)** 1 mM Na[*o*-FESAN]; **(c)** 1 mM FcMe with Ag/AgCl(1MKCl) as the reference; **(d)** 5 mM Cs[*o*-COSAN]; **(e)** 1 mM Cs[*o*-FESAN]; **(f)** 1 mM Fc with SCE as the reference.

The different CV experiments have shown that the metallacarboranes have a steady redox response with remarkable thermal and chemical stability, particularly [*o*-FESAN]$^-$ whose formal potential is closer to NHE than the benchmark ferrocene. These results prove the potential of metallacarboranes to be employed as internal references in any solvent system without further functional or structural modifications. Hence, precisely the same internal reference for both aqueous and organic electrolytes.[33]

This work was carried out as part of a research stay with Dr. Tania and Prof. Encarnacion in the Autonomous University of Madrid (UAM), Spain.

The following chapter will further exploit these redox properties of metallcarboranes, specifically [*o*-COSAN]$^-$, as 'small molecule' probe for identifying the effective surface of various proteins.

2.5 References

1 N. Elgrishi, K. J. Rountree, B. D. McCarthy, E. S. Rountree, T. T. Eisenhart and J. L. Dempsey, A Practical Beginner's Guide to Cyclic Voltammetry, *J. Chem. Educ.*, 2018, **95**, 197–206.

2 R. A. Marcus, Chemical and Electrochemical Electron-Transfer Theory, *Annu. Rev. Phys. Chem.*, 1964, **15**, 155–196.

3 M. P. S. Mousavi, S. A. Saba, E. L. Anderson, M. A. Hillmyer and P. Bühlmann, Avoiding Errors in Electrochemical Measurements: Effect of Frit Material on the Performance of Reference Electrodes with Porous Frit Junctions, *Anal. Chem.*, 2016, **88**, 8706–8713.

4 K. Z. Brainina, A. V Tarasov and M. B. Vidrevich, Silver Chloride/Ferricyanide-Based Quasi-Reference Electrode for Potentiometric Sensing Applications, *Chemosensors*, 2020, **8**, 15.

5 G. Gritzner and J. Kuta, Recommendations on reporting electrode potentials in nonaqueous solvents (Recommendations 1983), *Pure Appl. Chem.*, 1984, **56**, 461–466.

6 R. R. Gagne, C. A. Koval and G. C. Lisensky, Ferrocene as an internal standard for electrochemical measurements, *Inorg. Chem.*, 1980, **19**, 2854–2855.

7 M. J. A. Shiddiky, A. A. J. Torriero, C. Zhao, I. Burgar, G. Kennedy and A. M. Bond, Nonadditivity of Faradaic Currents and Modification of Capacitance Currents in the Voltammetry of Mixtures of Ferrocene and the Cobaltocenium Cation in Protic and Aprotic Ionic Liquids, *J. Am. Chem. Soc.*, 2009, **131**, 7976–7989.

8 M. Matsumoto and T. W. Swaddle, The Decamethylferrocene(+/0) Electrode Reaction in Organic Solvents at Variable Pressure and Temperature, *Inorg. Chem.*, 2004, **43**, 2724–2735.

9 I. Noviandri, K. N. Brown, D. S. Fleming, P. Gulyás, P. A. Lay, A. Masters and L. Phillips, The Decamethylferrocenium/Decamethylferrocene Redox Couple: A Superior Redox Standard to the Ferrocenium/Ferrocene Redox Couple for Studying Solvent Effects on the Thermodynamics of Electron Transfer, *J. Phys. Chem. B*, 1999, **103**, 6713–6722.

10 A. A. J. Torriero, S. W. Feldberg, J. Zhang, A. N. Simonov and A. M. Bond, On choosing a reference redox system for electrochemical measurements: a cautionary tale, *J. Solid State Electrochem.*, 2013, **17**, 3021–3026.

11 S. McCormack, N. R. Russell and J. F. Cassidy, Cyclic voltammetry of ferrocene carboxylic acid cyclodextrin inclusion complexes, *Electrochim. Acta*, 1992, **37**, 1939–1944.

12 H. M. A. Amin, Y. Uchida, E. Kätelhön and R. G. Compton, Determination of standard electrochemical rate constants from semi-circular sweep voltammetry: A combined theoretical and experimental study, *J. Electroanal. Chem.*, 2021, **880**, 114891.

13 A. AJ Torriero, On Choosing Ferrocene as an Internal Reference Redox Scale for Voltammetric Measurements: A Cautionary Tale, *Med. Anal. Chem. Int. J.*, 2019, **3**, 11–13.

14 A. A. J. Torriero, Characterization of decamethylferrocene and ferrocene in ionic liquids: argon and vacuum effect on their electrochemical properties, *Electrochim. Acta*, 2014, **137**, 235–244.

15 A. Paul, R. Borrelli, H. Bouyanfif, S. Gottis and F. Sauvage, Tunable Redox Potential, Optical Properties, and Enhanced Stability of Modified Ferrocene-Based Complexes, *ACS Omega*, 2019, **4**, 14780–14789.

16 G. Gritzner and J. Kůta, Recommendations on reporting electrode potentials in nonaqueous solvents: IUPC commission on electrochemistry, *Electrochim. Acta*, 1984, **29**, 869–873.

17 N. G. Tsierkezos, Electron transfer kinetics for the cobaltocene (+1/0) couple at platinum disk electrode in acetonitrile/dichloromethane binary solvent system, *J. Mol. Liq.*, 2008, **138**, 1–8.

18 P. J. Swarts and J. Conradie, Redox data of ferrocenylcarboxylic acids in dichloromethane and acetonitrile, *Data Br.*, 2020, **30**, 105650.

19 D. J. G. Ives and G. J. Janz, *Reference electrodes*, Academic Press, New York, 1961, vol. 1.

20 R. A. Wiesboeck and M. F. Hawthorne, Dicarbaundecaborane(13) and Derivatives, *J. Am. Chem. Soc.*, 1964, **86**, 1642–1643.

21 R. N. Grimes, *Carboranes*, Elsevier Inc. New York, New York, 3rd edn., 2016.

22 F. T. and P. M. M. Tarrés, C. Viñas, P. González-Cardoso, M. M. Hänninen, R. Sillanpää, V. Dordovic, M. Uchman, Aqueous Self-Assembly and Cation Selectivity of Cobaltabisdicarbollide Dianionic Dumbbells, *Chem. Eur. J.,* 2014, **20**, 6786–6794.

23 P. Zanello, *Inorganic Electrochemistry*, The Royal Society of Chemistry, 2003.

24 H. P. Bennetto, Chapter 8. Electrolyte solutions, *Annu. Rep. Prog. Chem. Sect. A. Inorg. Phys. Chem*, 1973, **70**, 223–248.

25 N. Matubayasi, *Surface tension and related thermodynamic quantities of*

aqueous electrolyte solutions / Norihiro Matubayasi., Boca Raton : Taylor & Francis, 2014.

26 S. Srinivasan, *Fuel cells: From fundamentals to applications,* ed. Springer US, Boston, MA, 2006, pp. 27–92.

27 A. J. Bard, *Electrochemical methods : fundamentals and applications / Allen J. Bard, Larry R. Faulkner*, Wiley, New York, 1980.

28 P. Bauduin, S. Prevost, P. Farràs, F. Teixidor, O. Diat and T. Zemb, A Theta-Shaped Amphiphilic Cobaltabisdicarbollide Anion: Transition From Monolayer Vesicles to Micelles, *Angew. Chemie.*, 2011, **50**, 5298–5300.

29 M. Uchman, V. Ďorďovič, Z. Tošner and P. Matějíček, Classical Amphiphilic Behavior of Nonclassical Amphiphiles: A Comparison of Metallacarborane Self-Assembly with SDS Micellization, *Angew. Chemie.*, 2015, **54**, 14113–14117.

30 D. C. Malaspina, C. Viñas, F. Teixidor and J. Faraudo, Atomistic Simulations of COSAN: Amphiphiles without a Head-and-Tail Design Display “Head and Tail” Surfactant Behavior, *Angew. Chemie.*, 2020, **59**, 3088–3092.

31 I. Bennour, M. N. Ramos, M. Nuez-Martínez, J. A. M. Xavier, A. B. Buades, R. Sillanpää, F. Teixidor, D. Choquesillo-Lazarte, I. Romero, M. Martinez-Medina and C. Viñas, Water soluble organometallic small molecules as promising antibacterial agents: synthesis{,} physical–chemical properties and biological evaluation to tackle bacterial infections, *Dalt. Trans.*, 2022, **51**, 7188–7209.

32 P. Daubinger, J. Kieninger, T. Unmüssig and G. A. Urban, Electrochemical characteristics of nanostructured platinum electrodes – a cyclic voltammetry study, *Phys. Chem. Chem. Phys.*, 2014, **16**, 8392–8399.

33 J. A. M. Xavier, C. Viñas, E. Lorenzo, T. García-Mendiola and F. Teixidor, Potential application of metallacarboranes as an internal reference: an electrochemical comparative study to ferrocene, *Chem. Commun.*, 2022, **58**, 4196–4199.

Chapter 3

3.1 Introduction

Proteins belong to a class of fundamental macromolecular biomolecules whose structure and functions have been and continues to be extensively studied. Yet, visualizing a protein in its native form and environment without any interference has always been a challenge. The shape of a protein is a result of its amino acids, its sequence and their hydrogen bond interactions leading to tertiary and even further to quaternary structures, under the influence of its surrounding environment. These characteristic features describe a protein's function as its ability to interact with other molecules depends on the structure and a fundamental aspect of this interaction is the proteins' surface.[1,2]

'Surface' of a protein has always been an elusive term described mostly by considering a smooth and regular sphere. Contrary to the assumption, protein surfaces are in-fact highly irregular with undulations which are greatly affected by the environment. The effect of different ions and solvent molecules in determining the proteins' structure is profound. Typically, the surface area of a protein is estimated by assuming the hydrodynamic or Stokes radius. In this approach, a uniform smooth-surfaced sphere having the same hydrodynamic characteristics as the biomolecule is defined.[3,4] A significant flaw to this approach is that it does not take into consideration the environment nor the shape of the protein, which can be either globular or non-globular and is extremely irregular.[5–8] The interaction of the amino acid residues with various ions as well as the surrounding water molecules can result in altering the proteins' surface.[9–11]

The current cutting-edge techniques for studying a proteins' structures are computational studies, nuclear magnetic resonance (NMR) spectroscopy of proteins in solution, neutron and X-ray diffraction studies of crystallized proteins and cryo-electron microscopy (cryo-EM).[12–20] Direct electrochemical measurements to study the protein surfaces are also popular, but often the proteins are subjected to unwanted duress such as the application of high voltage causing denaturalization of the proteins.[21–23] Moreover, majority of the redox active amino residues, such as tryptophan and tyrosine, are non-polar and hence prefer to be in the interior of the protein rather than the surface. As a result, there are relatively fewer redox active amino acid residues on the surface.[24] Despite being such resourceful techniques, these methods fall short in their attempts to study the proteins in its native form and environment.

We, among others, have recently shown that $[3,3'\text{-Co}(1,2\text{-C}_2\text{B}_9\text{H}_{11})_2]^-$, [*o*-COSAN]$^-$, interacts strongly with Bovine Serum Albumin (BSA) in a molar ratio of 100:1.[25–27] The interaction as well as the molar ratio were determined as a result of change in physical properties such as fluorescence and size which was measured using techniques such as fluorescence spectroscopy, dynamic light scattering (DLS), zeta potential measurements or by studying the precipitated complex by elemental analysis or energy-dispersive X-ray (EDX) spectroscopy. Of these, zeta potential and DLS studies were vital as the former confirmed the presence of the anion on the surface of BSA due to its negative charge while the latter provided information pertaining to the hydrodynamic diameter of the complex, thus probing us to envision a model of BSA encapsulated by [*o*-COSAN]$^-$ in an end-on position. Remarkably, the strong interaction between the BSA and [*o*-COSAN]$^-$ raises high expectations to enhance the therapeutic activity of peptides.[28]

3.2 Motivation & Objective

The current state-of-the-art techniques fail to understand and visualize a protein in its native form and structure, especially the surface characteristics, due to several limitations. The least non-disruptive and non-invasive technique, preserving the protein's structure would be an electrochemical approach. But here again, directly measuring a protein has its own challenges as mentioned earlier. Hence, a way around this problem would be to take advantage of an external electroactive compound which interacts strongly with the surface amino acid residues of the protein without altering its electrochemical properties. As simple as it may seem, this approach is indeed quite challenging as we would require a water-soluble, redox-reversible substance which is structurally rigid having well-defined and stable electrochemical properties capable of interacting rapidly and strongly with the residues on the protein surface as well as possess self-assembling properties in order to fill the available surface area to the maximum possible extent. Hence, in this chapter we would focus on the application of simple and facile electrochemical techniques for understanding the structure, function and properties of a protein using a highly apt redox-reversible probe.[29]

The electrochemical stability, tendency for basic amine residues through the formation of strong N-H···B-H di hydrogen bonds and self-assembling properties of [*o*-COSAN]$^-$ are well documented.[30–34] As mentioned in the introductory chapter (Section 1.2.2), *cis*-[*o*-COSAN]$^-$ rotamer self-assembles to form nanovesicles (Scheme 3.1).[35] The previous chapter had discussed in detail the electrochemical stability of the metallacarboranes in varying conditions and parameters, probing them to be utilized as 'universal' internal references.[36] Consequently, in this study we aim at gaining a molecular level insight of the 'effective protein surface' (EPS) using the geometrically well-defined and structurally inert anionic molecule, [*o*-COSAN]$^-$, by employing facile and robust electrochemical techniques such as cyclic voltammetry (CV) or differential pulse voltammetry (DPV). We attempt to illustrate the potential application of [3,3'-Co(1,2-$C_2B_9H_{11}$)$_2$]$^-$ as a 'small molecule probe' analogous to a cantilever in scanning electron transmission microscopy (STEM) for determining the nature of the protein surface and to establish the mechanisms of ion-protein interactions.[37,38]

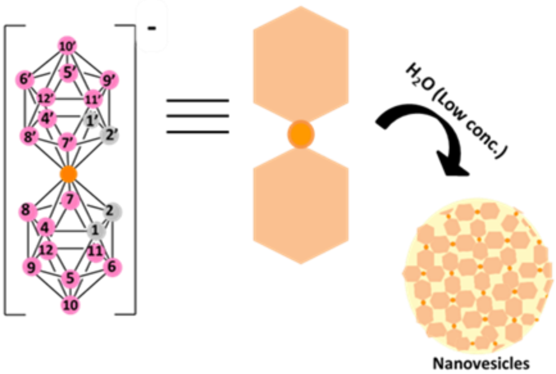

Scheme 3.1 Schematic representation of formation of nanovesicles of *cis*-[*o*-COSAN]$^-$ at low concentrations in aqueous solvent.

In our study involving BSA and [*o*-COSAN]$^-$, we had demonstrated that [*o*-COSAN]$^-$ interacts strongly with BSA, by forming B-H···N-H di-hydrogen bonds, in the molar ratio 100:1. Interestingly, the total number of basic amino acid (histidine, lysine and arginine) residues in a BSA molecule is also 100.[25,39,40] This led us to believe that there was one [*o*-COSAN]$^-$ for every basic residue. Consequently, we postulated the potential use of [*o*-COSAN]$^-$ as a robust 'universal' shield on proteins, protecting them from denaturalization at high temperatures and thereby retaining its activity, irrespective of the nature of the protein.[25] But it was not to be, as the preliminary experiments with enzymes suggested that [*o*-COSAN]$^-$ was not capable of shielding them all in the same manner and indeed 'viewed' them differently. This beseeched us to investigate the different factors that influence the ratio of [*o*-COSAN]$^-$ molecules *vs*. basic amino acid residues.

Our primary investigations with BSA and [*o*-COSAN]$^-$ were carried out in pure water, without any buffer or additives, mostly due to the absence of any electrochemical experiments.[25,41] But within the body, the proteins are in a pH-neutral environment with high electrolyte content. Hence, it is rationale to investigate the interaction of [*o*-COSAN]$^-$ and proteins under physiological conditions in order to obtain a better understanding of the protein surface. In this study, we perform the electrochemical experiments in an electrolyte, 0.1 M NaCl where both Na^+ and Cl^- are part of the Hofmeister series and are chaotropic in nature.[42,43] Subsequently, the hydrodynamic radius as well as the surface area of a protein varies in the presence and absence of NaCl. Considering all these factors, in this study we provide a method for interpreting the surface or rather the 'effective' surface of a protein. With these investigations, we aim at comprehending the influences of the environment on a protein in a concise and precise manner without altering the protein's secondary structure. Notably, owing to the advantageous properties of [*o*-COSAN]$^-$ such as electrochemical reversibility, fixed volume regardless of its rotamer or conformation, strong basic amino acid interactions and self-assembling capacity, we would be able to extract a great deal of information regarding the EPS of a protein.

3.3 Results & Discussions

In a typical electrochemical experiment, a 1mM solution of Na[*o*-COSAN] in 0.1 M NaCl is prepared in an electrochemical cell to which the protein is added in mg, depending on the molecular weight of the different proteins, to attain the required protein concentration, sequentially. To ensure homogenous distribution of the particles, the resulting solution is mixed vigorously. The nine proteins that were investigated in this study were: Bovine serum albumin (BSA), γ- Globulin, Catalase, Hemoglobin, Histone, Lysozyme, Horse radish peroxidase (HRP), Carbonic anhydrase (CA) and Myoglobin. The measurements are performed using a three-electrode system with glassy carbon (GC) as the working, Ag/AgCl (3M KCl) as the reference and Pt wire as the counter electrodes in an inert N2 atmosphere with 3 scans for each measurement at a scan rate of 50mV/s.

3.3.1 Evidence for the interaction of **[o-COSAN]$^-$** *with basic amino acid residues*

Previously, we had explored the interaction of amino acids with [*o*-COSAN]$^-$ in terms of potentiometric membranes for the detection of amino acids as well as for stabilizing amine functionalized magnetic nanoparticles.[40,44,45] However, these studies offered a general and rather vague idea of all the possible interactions. Hence, a study was devised to visualize the [*o*-COSAN]$^-$/amino acid interaction by ^{1}H- and ^{11}B-NMR spectroscopies for a more profound understanding of the interactions, particularly at the molecular level.

The NMR measurements were carried out at a fixed concentration of Na[*o*-COSAN] (2 mM) in D_2O with increasing concentration of the amino acid of interest. The influence of the amino acid was studied by observing the variations in the resonances assumed to be involved in the interactions. Hence, the altercations occurring to the resonance of B-H of [*o*-COSAN]$^-$, appearing at 2.60 ppm, was taken as the reference. The interactions of [*o*-COSAN]$^-$ with L- glutamine, L-arginine, L-lysine and L-histidine were investigated, of which the latter three residues contained basic side chains while L-glutamine was chosen as the blank representing amino acids such as alanine, serine among others.

From the experiments, it was observed that the intensity of the $^1H\{^{11}B\}$-NMR [3,3'-Co(1,2-$C_2B_9H_{11})_2]^-$ B-***H*** (4,4',7,7') signal decreases with increasing concentration of the amino acid (Fig. 3.1). However, this decrement was not in proportion to the amino acid concentration nor was it equal for all, indicating that the [*o*-COSAN]$^-$ distinguishes between each of the amino acids. From Fig. 3.1, it can be observed that the B-H signal completely disappears in case of interaction with L-lysine whereas limited decrease in intensities is observed for L-histidine and L-arginine and negligible variations in the case of L-glutamine. These results indicate that [*o*-COSAN]$^-$ interacts strongly with L-lysine in comparison to L-histidine and L-arginine and none with L-glutamine.

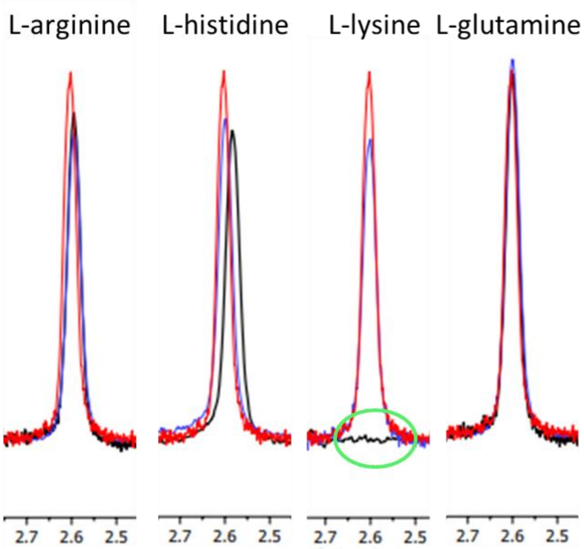

Fig. 3.1 $^1H\{^{11}B\}$-NMR from 2.8 to 2.4 ppm B-H (4,4',7,7') measured for the different mixtures of [*o*-COSAN]$^-$ and the amino acids (L-arginine, L-histidine, L-lysine and L-glutamine). Na[*o*-COSAN] 2mM, Na[*o*-COSAN] 2mM + 2mM of the corresponding amino acid and Na[*o*-COSAN] 2mM + 60mM of the corresponding amino acid; the green circle highlights the flatline due to interaction with L-lysine at 60mM. The solvent used was D_2O.

We hypothesize that the disappearance of the B-H resonance is due to the formation of nano-aggregates generated by the basic amino acids and [*o*-COSAN]$^-$, which are larger than the individual components and hence would adopt a landscape layout. Consequently, this would prevent the free rotation of the aggregate resulting in broad resonances, invisible in the spectrum. Additionally, neither colloids nor precipitates were observed during these measurements.

Consistent with these results are the $^{11}B\{^1H\}$-NMR $[3,3'\text{-}Co(1,2\text{-}C_2B_9H_{11})_2]^-$/amino acid spectra. The $^{11}B\{^1H\}$-NMR spectrum of $Na[3,3'\text{-}Co(1,2\text{-}C_2B_9H_{11})_2]$ displays different characteristics when measured in water or acetone. In water, the different signals are wider compared to in acetone because in the latter, the spectrum corresponds to free rotating molecules while in water the spectrum corresponds to aggregates, due to self-assembly, which are larger and more difficult to rotate. Therefore, the $^{11}B\{^{1}H\}$-NMR spectrum will be even broader when there is interaction between the $[3,3'\text{-Co}(1,2\text{-}C_2B_9H_{11})_2]^-$ and the amino acid. As observed before, there is a decrease or broadening in the intensity of the signal but not as prominent as the proton NMR. But the results are coherent with the fact that the strongest interactions of [*o*-COSAN]$^-$ are with L-lysine followed by L-histidine and L-arginine and absent for L-glutamine (Fig.3.2).

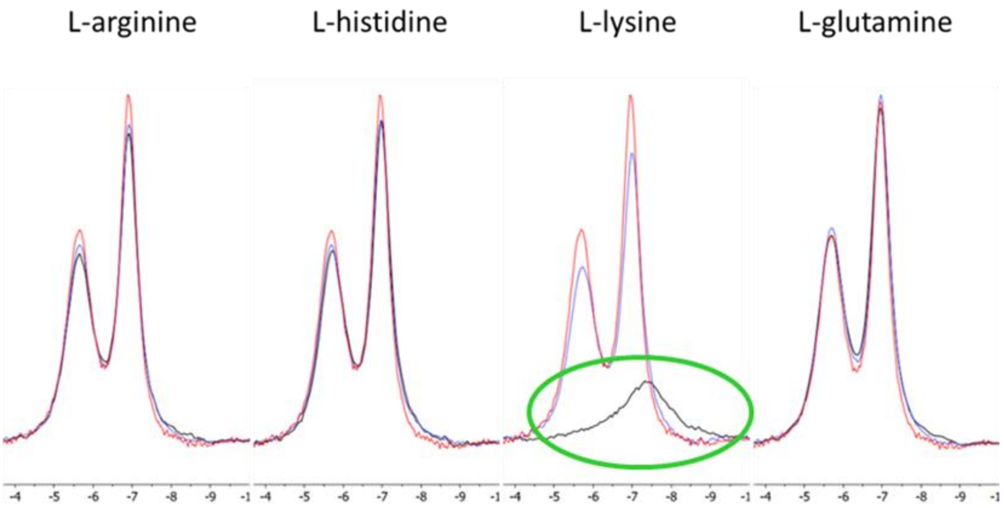

Fig. 3.2 $^{11}B\{^{1}H\}$-NMR from -4. to -10 ppm (B (4,4',7,7',9,9',12,12') signal region) measured for the different mixtures of [*o*-COSAN]$^-$ and the amino acids. Na[*o*-COSAN] 2mM as a reference, Na[*o*-COSAN] 2mM + 2mM of the corresponding amino acid and Na[*o*-COSAN] 2mM + 60mM of the corresponding amino acid; the green circle highlights the signal broadening due to interaction with L-lysine at 60mM. The solvent used was D_2O.

3.3.2 Differential Pulse Voltammetry: Intensity of current vs. ratio of [protein]/[o-COSAN]$^-$

As mentioned earlier, the study involves the sequential addition of proteins to a fixed concentration of Na[*o*-COSAN] and measuring the current in response to varying potential. Since an amperometry measurement is carried out, an electrolyte is required which in this case is 0.1 M NaCl. The presence of an electrolyte also allows us to create an environment similar to the physiological one rendering the measurements to be more realistic. Caution was taken to ensure that the experimental conditions such as the applied potential nor the current does not affect the stability of the protein. Upon performing the DPV experiment, a graph is obtained wherein a decrease in the current intensity of Na[*o*-COSAN] can be observed with increasing concentration of the proteins (Fig. 3.3). Table 3.1 tabulates the current intensity values obtained from the experiments. A similar experiment has also been undertaken using [*o*-FESAN]$^-$ and DNA for developing a DNA bio-sensor.[46]

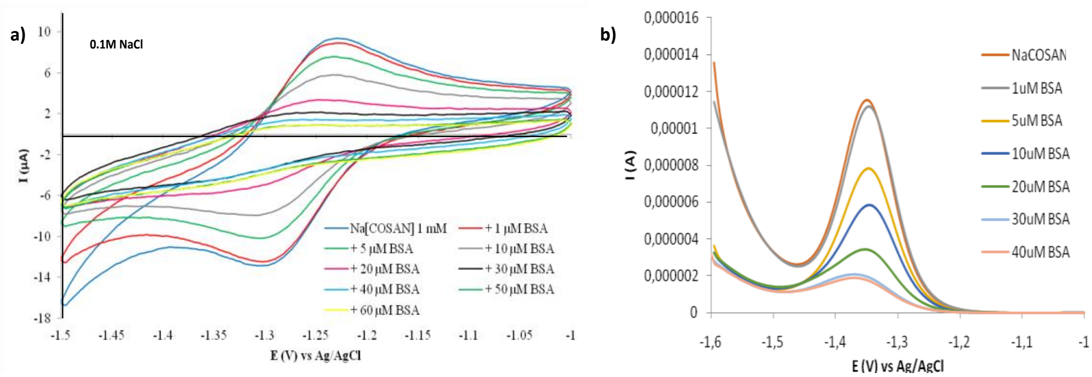

Fig. 3.3 Representative electrochemical measurements: ***(a)*** CV and **(b)** DPV curves for 1 mM of Na[*o*-COSAN] in 0.1 M NaCl with increasing concentration (in mg) of the protein BSA measured at 50 mV/s.

Table 3.1 The current intensity (I) values measured at the potential -1.33 V (*vs.* Ag/AgCl) obtained from the DPV experiment for [o-COSAN]$^-$ with increasing concentration of different proteins; [X] defines the concentration of the protein.

[X]/[*o*-COSAN]	**Current, I (μA)**								
	BSA	**γ-Globulin**	**Catalas**	**Hemo-globin**	**Histone**	**Lysozym**	**HRP**	**CA**	**Myo-globin**
0	11.52	11.30	11.52	11.25	11.20	11.56	10.56	11.3	10.84
0.001	11.2	11.33	10.18	10.34	10.95	11.25	10.08	11.26	10.50
0.005	7.81	9.65	6.54	8.07	10.37	10.71	9.08	10.55	9.47
0.01	5.84	7.24	3.81	5.69	9.12	9.82	8.03	9.93	8.64
0.02	3.46	4.66	1.82	2.24	6.91	8.27	6.87	8.86	7.33
0.03	2.08	3.16	1.17	1.27	5.06	6.43	5.97	7.92	6.21
0.04	1.90	1.96	0.89	1.14	3.41	5.01	5.33	6.95	5.10

0.05	1.57	1.84	0.78	1.22	2.17	4.09	4.69	6.001	4.13
0.06	1.53	1.80	0.56	1.14	1.27	3.37	4.07	5.21	3.31

The major contribution to the current intensity is from the 'free' [*o*-COSAN]$^-$ that remain in the solution. Even though, the [*o*-COSAN]$^-$ bound to the protein can also transfer electrons with the electrode, the contribution would be much lower in comparison to free [*o*-COSAN]$^-$ and hence, can be considered negligible as a first approach. Therefore, the current intensity is highest in the absence of any interacting proteins and decreases with increasing protein concentration without ever intersecting the y-axis at 0 due to bound [*o*-COSAN]$^-$. As mentioned, we are not factoring the residual current due to the bound [*o*-COSAN]$^-$ but with further advancements in the technique this residual current could yield a deeper insight.

The nature of the curve obtained from the electrochemical experiments are different for different proteins indicative of an underlying variation in the nature of interaction of various proteins with [*o*-COSAN]$^-$. The aim of the study is to elucidate and understand the various factors responsible for these differences. The following plot (Fig. 3.4) illustrates the current intensity of [*o*-COSAN]$^-$ *vs.* the [protein]/ [*o*-COSAN]$^-$ at 10^{-3} M [*o*-COSAN]$^-$ concentration in 0.1 M NaCl.

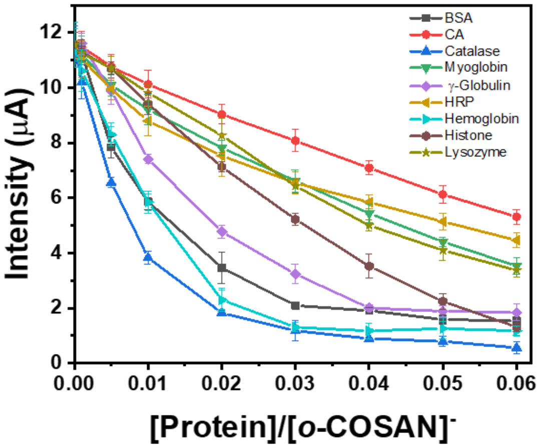

Fig. 3.4 The current (I) *vs.* [protein]/[*o*-COSAN]$^-$ ratio obtained for different proteins from the DPV experiment measured in 0.1 M NaCl with glassy carbon (GC) as the working and Ag/AgCl (3M KCl) as the reference electrode.

3.3.3 Bound [*o*-COSAN]$^-$ *vs. ratio of [protein]/* [*o*-COSAN]$^-$

As the study pertains to understanding the nature of interaction between the proteins and [*o*-COSAN]$^-$, a more appropriate parameter to evaluate the situation would be the amount of [*o*-COSAN]$^-$ bound on the surface of the protein. Tentatively, the amount of [*o*-COSAN]$^-$ bound on the surface of the protein can be calculated as the difference between the initial current intensity of [*o*-COSAN]$^-$, i.e., in the absence of any protein, and the intensity of [*o*-COSAN]$^-$ in presence of the protein. Although, the [*o*-COSAN]$^-$ bound to the surface of the protein are still electrochemically active, the contribution to the current intensities would be negligible and this serves as a fairly good approximation for the purpose of this study. Thus, if we consider bound [*o*-COSAN]$^-$ as:

Bound [*o*-COSAN]$^-$ = Initial current intensity of [*o*-COSAN]$^-$ - current intensity of [*o*-COSAN]$^-$ in presence of the protein, the following plot is obtained for bound [*o*-COSAN]$^-$ current intensity *vs*. the [protein]/[*o*-COSAN]$^-$ (Fig. 3.5).

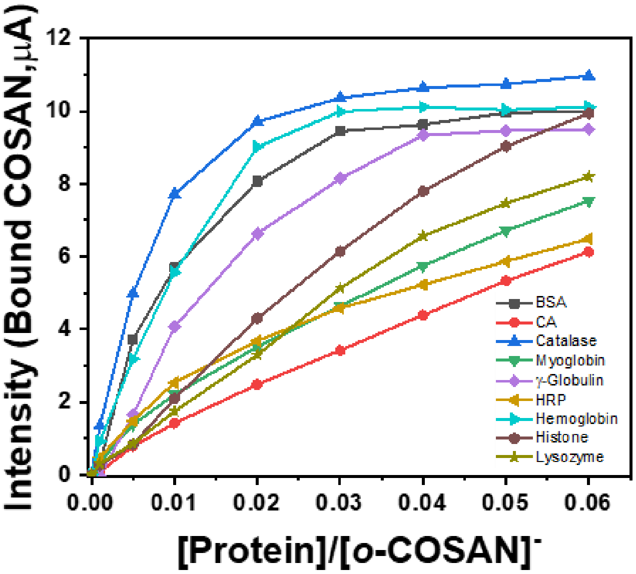

Fig. 3.5 The calculated intensity for the bound [*o*-COSAN]$^-$ *vs*. the protein to [*o*-COSAN]$^-$ fraction for different proteins.

From Fig 3.5, it can be observed that there is a possibility of two different types of interactions which can be attributed to two different classes of proteins. The former consisting of catalase, hemoglobin, BSA and γ-globulin and the latter of histone, HRP, myoglobin, lysozyme and CA.

3.3.4 Normalization of the intensity of current with regard to proteins' hydrodynamic radius (r_H)

As mentioned in the introduction, the 'surface' of a protein is an ambiguous term but is of utmost importance while studying the nature of interactions between protein and a molecule. The results discussed thus far, only considers the protein concentrations and not the surface of the protein where the interactions actually occur. Hence, it is rationale to consider the surface of a protein in terms of its surface area. For harmonization, the factor r_H^2 has been taken into account with r_H being the hydrodynamic radius of a protein. Thus, the normalized *current density* can be calculated as:

$$\text{Normalized current density} = \text{Bound } [o\text{-COSAN}]^- / (r_H)^2$$

$$\text{where } r_H - \text{hydrodynamic radius of the protein}$$

The hydrodynamic or Stokes radius of a protein can be described as the radius of a sphere having the same hydrodynamic properties as the biomolecule.[47,48] The radiuses mentioned in this study have been obtained from literature wherein the measurements have been carried out in buffers such as Tris-HCl. Additionally, we have also corroborated these values by performing dynamic light scattering (DLS) experiments in 0.1 M NaCl.

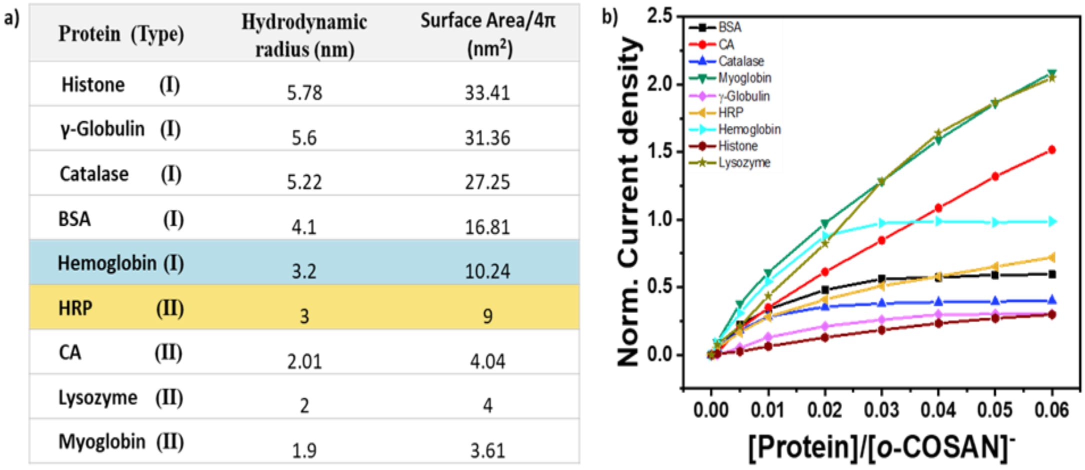

a)

Protein (Type)	Hydrodynamic radius (nm)	Surface Area/4π (nm²)
Histone (I)	5.78	33.41
γ-Globulin (I)	5.6	31.36
Catalase (I)	5.22	27.25
BSA (I)	4.1	16.81
Hemoglobin (I)	3.2	10.24
HRP (II)	3	9
CA (II)	2.01	4.04
Lysozyme (II)	2	4
Myoglobin (II)	1.9	3.61

Fig. 3.6 (a) Displays **Table 3.2** with the hydrodynamic radius as well the calculated surface area/4π, with the two different classifications of the curves as type I and type II; the two borderline proteins are

highlighted **(b)** Displays the normalized current density (μA/nm^2) calculated by considering the surface area of each of the protein *vs.* the protein to [*o*-COSAN]$^-$ fraction for different proteins.

Fig. 3.6(b) displays the normalized *current density,* by considering the surface area of a protein as r_H^2, because the area of a sphere is $4\pi r^2$, *vs.* the fraction of [protein]/[*o*-COSAN]$^-$. Table 3.2 gives the overall view of all the proteins studied with their different classifications.

After incorporating the 'surface' of the protein, in terms of r_H^2, the classes of proteins mentioned earlier seems to be maintained where histone could be added to the former one, having BSA, γ-globulin, catalase and hemoglobin, with some reservations. All of these proteins display a characteristic plateau. Majority of them have a low maximum current density value, except hemoglobin, in comparison to other proteins. Indeed, these proteins attain a current density limit while those without the plateau continue to increase, reaching values two or three times higher. Consequently, the current density for BSA, γ-globulin, catalase and histone does not exceed 0.6 at 0.06 [protein]/[*o*-COSAN]$^-$ fraction while other proteins such as CA, myoglobin and lysozyme display a value of 1.6, 2.0 and 2.0, respectively. The two exceptions, one for each group, are hemoglobin with a value of 1.0, in the plateau group, and HRP with 0.7, in the non-plateau group. Hence, it can be deducted that there are primarily two tendencies: one which generates a plateau (Type I) and the one having a continuous slope (Type II) as shown in Fig. 3.7.

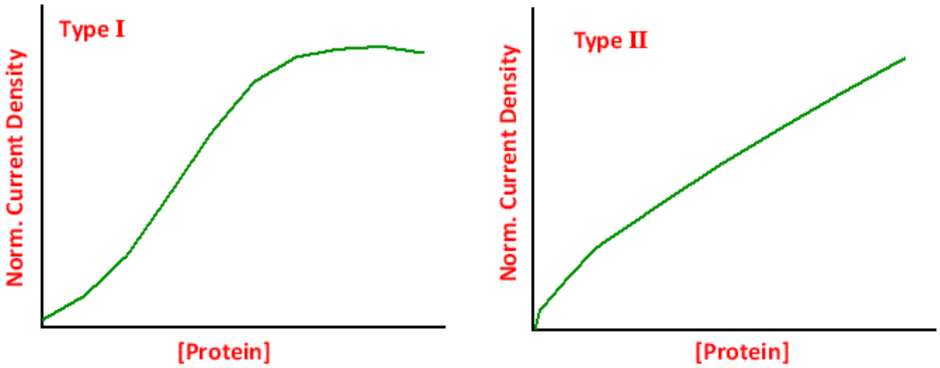

Fig. 3.7 Two types of behaviours observed after the incorporation of 'surface' to the current intensity obtained using [*o*-COSAN]$^-$ as a 'small molecule' probe.

Hence, two different protein-[*o*-COSAN]$^-$ interaction models can be proposed. Type I initially has a characteristic increase and eventually saturates whereas Type II has a 'kink' followed by a linear path. Thus, the proteins can be classified as:

- Type I: Histone, γ-Globulin, Catalase, BSA & Hemoglobin
- Type II: HRP, CA, Lysozyme & Myoglobin

The above models have been proposed solely on the experimental evidences and the following section entails the possible elucidations for the same.

3.3.5 Interpreting the experimental evidences

The distinguishing feature for each of the models proposed is their curvature observed at different [protein] to [*o*-COSAN]$^-$ fraction which can be interpreted in terms of the basic amino acid densities. In contemplation of such an interpretation, based on the content and density of basic amino acid residues on the protein surface, we hypothesize that owing to their hydrophilic nature, basic amino acid residues prefer to be predominantly present on the surface of the protein and hence, can interact strongly with [*o*-COSAN]$^-$. Table 3.3 indicates the number of amino acids with emphasis on the number of basic amino acid residues (L-lysine, L-histidine and L-arginine) for each of the proteins studied. A column has also been included to compare the total number of amino acids of each protein to the protein with the highest number, assigned as 100.

Table 3.3 The different basic amino acid residues and the total number of amino acids present in the different proteins studied.

Protein	Lys	His	Arg	Amino acid (AA)	Norm. AA
Histone	13	5	13	133	23
Catalase	23	17	26	488	84
γ-Globulin	15	19	11	390	67
BSA	59	18	23	583	100
Hemoglobin	11	11	3	141	24
HRP	6	4	21	306	52
Myoglobin	19	13	4	151	26

Lysozyme	13	2	13	164	28
CA	24	12	7	257	44

The following table (Table 3.4) displays the possible interpretations based on our understanding of the plausible interactions between protein and $[o\text{-COSAN}]^-$ wherein each of the column represents the following:

- Column 2: The number of basic amino acid residues.
- Column 3: The ratio of basic amino acid to the total number of amino acids.
- Column 4: The density of basic amino acid residues on the surface calculated by considering the r_H^2.
- Column 5: The number of basic amino acid residues on the surface of the protein with regard to the total number of amino acids.

Table 3.4 Table displaying plausible relations to the tendencies observed for the different proteins.

Protein (Type)	Basic Amino acid (AA)	Basic AA/ Total AA	Basic AA/ Area	(Basic AA/Total AA)*Area
Histone (I)	31	0.23	0.92	7.79
Catalase (I)	66	0.14	2.4	3.69
γ-Globulin (I)	45	0.12	1.4	3.62
BSA (I)	100	0.17	5.9	2.88
Hemoglobin (I)	25	0.18	2.4	1.82
HRP (II)	31	0.10	3.4	0.91
Myoglobin (II)	36	0.24	9.97	0.86
Lysozyme (II)	28	0.17	7	0.68
CA (II)	43	0.17	10.6	0.67

A saturated curve, or a plateau as observed in type I mentioned earlier, is indicative of a strong interaction between the basic amino acid residues and $[o\text{-COSAN}]^-$. This is usually accompanied by the initial steep rise of the slope which suggests a strong interaction as initially, when the [*o*-COSAN]$^-$ concentration is high in comparison to the protein, all the available binding sites will be occupied by [*o*-COSAN]$^-$ if there is a strong interaction. The intensity then observed can be attributed to the residual intensity from the bound [*o*-COSAN]$^-$, which would roughly be the same at all the further higher protein concentrations subjected to diffusion characteristics.

Thus, considering columns 2 and 3 alone, does not generate a well-defined correlation with the tendencies observed. But the correlation improves, when we factor in the surface area as observed in column 4. In column 4, three of the four proteins belonging to type II have the highest density of basic amino acid residues. HRP is the discordant figure among the type II while BSA in the other. But the correlation improves drastically when we consider the number of basic amino acid residues on the surface to the total amino acids in a protein. The two groups which have been generated agrees well with the experimental groups, the one which forms a plateau and the other which do not. Though conceptually related, the most significant distinction between the density of amino acids and the total number of amino acids in a protein with specific dimensions, is the ratio of basic to non-basic amino acids with respect to the surface, which indirectly takes into account the non-basic properties of the other amino acids in the protein.

The reason for observing two different models of interactions between proteins and [*o*-COSAN]$^-$, can be explained as in the former case where a plateau is observed there is a higher proportion of basic amino acid residues on the surface with regard to the total number of amino acids and hence, a greater number of [*o*-COSAN]$^-$ can interact with the basic residues producing a sturdy coating with well-ordered [*o*-COSAN]$^-$, preventing further growth by self-assembly (Scheme 3.2). At the other extreme, having a smaller ratio of basic amino acid residues on the surface results in two sets of interactions with [*o*-COSAN]$^-$, those that are anchored due to the interaction and those which are not. The latter are less ordered or loosely packed which allows them to settle easily in between the anchored [*o*-COSAN]$^-$ and facilitate self-assembly allowing unlimited growth in the number of [*o*-COSAN]$^-$ (Scheme 3.2).

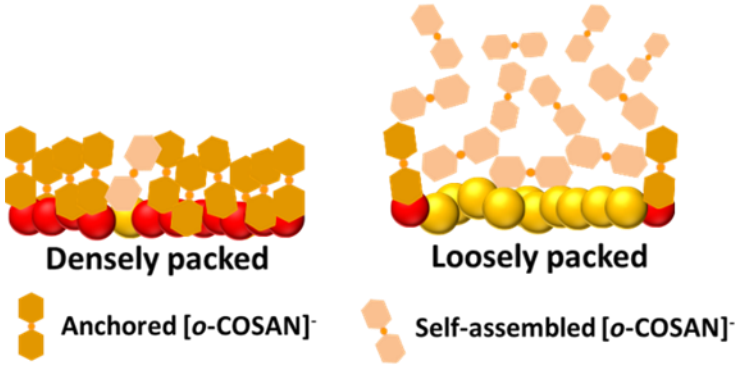

Scheme 3.2 A visual representation of the two types of possible protein-[*o*-COSAN]$^-$ interactions explaining the two groups of classifications obtained.

Therefore, the proteins can be classified as High Surface Base Density (HSBD) (Type I) and Low Surface Base Density (LSBD) (Type II), distinguishable by [*o*-COSAN]$^-$, the electrochemical 'small molecule' probe.

A deeper insight on the significance of the surface of a protein given by the r_H^2 can be obtained if we focus on the hydrodynamic radius (r_H) and plot the normalized current intensity against r_H at different [protein]/[*o*-COSAN]$^-$ fractions such as: 0.03, 0.04, 0.05 & 0.06. From Fig. 3.8, it can be observed that at lower [protein]/[*o*-COSAN]$^-$ fractions a linear relation is obtained whereas at higher fractions, the trend deviates from linearity. All, however, results in complementary information to the former interpretation that *size and surface are related*.

From the plots (Fig. 3.8), it can be observed that as the hydrodynamic radius decreases, the bound [*o*-COSAN]$^-$ on the protein surface decreases. A smaller protein size implies a larger surface-to-volume ratio. Consequently, it is reasonable to assume that the density of the amino acids on the protein surface, particularly the polar ones, is higher for smaller proteins in comparison to the larger ones. This proximity of the amino acids that serve as an anchoring point for the [*o*-COSAN]$^-$ would facilitate a more tightly packed structure.

As seen in the plots, the type II proteins CA and HRP deviate from the trendline while being in agreement with each other. The deviation from the trendline can be attributed to the fact that the surface area calculated by considering the r_H may vary from the 'effective' protein surface due to the presence of voids and/or moors rather than the assumed smooth, spherical structure. Consequently, the more the difference from the realistic surface, more would be the deviation. Hence, it is rationale to assume that for proteins such as HRP and CA, the deviation from hypothetical smooth surface is much more prominent than the others.

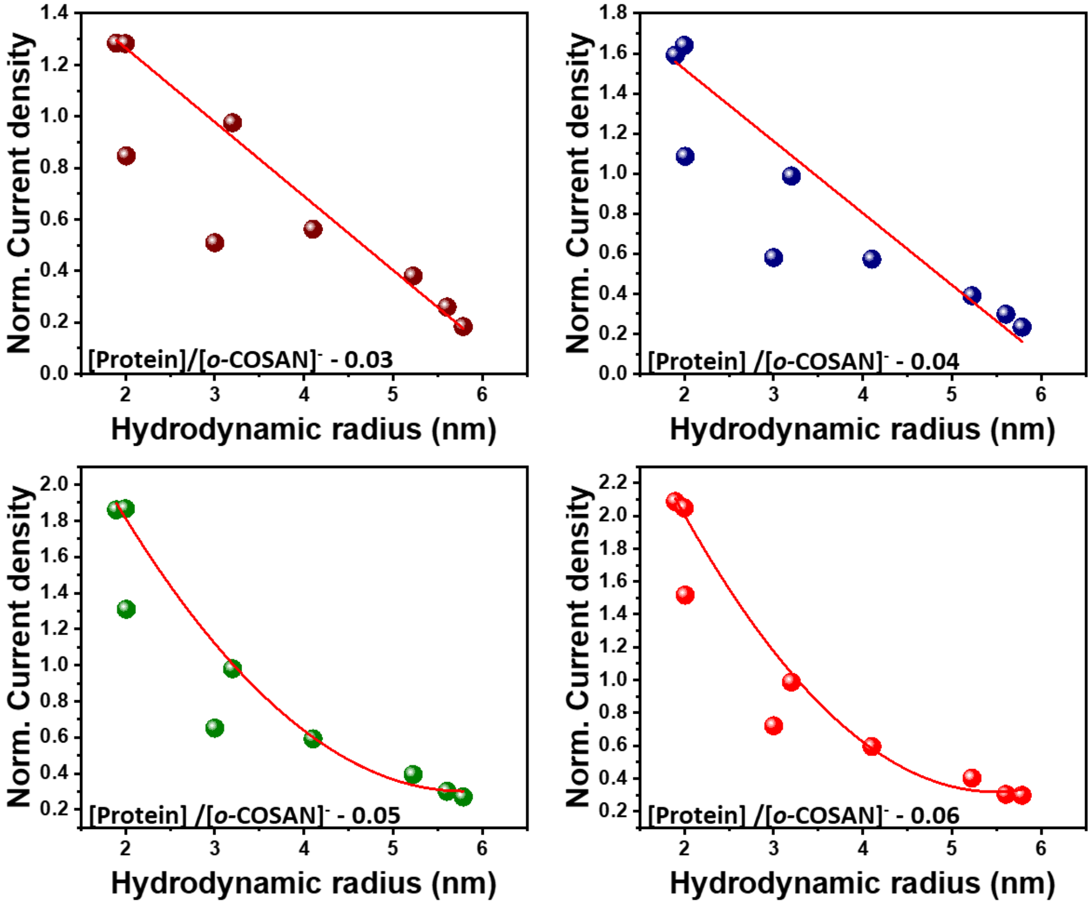

Fig. 3.8 The normalized current density *vs.* the hydrodynamic radius at different [protein]/[*o*-COSAN]$^-$ fractions from 0.03 to 0.06. [From smallest to largest hydrodynamic radius: Myoglobin, Lysozyme, CA, HRP, Hemoglobin, BSA, Catalase, γ-Globulin & Histone].

3.3.6 Influence of the electrolyte

In this study, the electrochemical measurements were carried out in presence of an electrolyte, 0.1 M NaCl, in order facilitate the diffusion of the electroactive substance to the electrode surface. In such a scenario where two anions, namely Cl$^-$ and [*o*-

COSAN]$^-$, are present in a ratio of 100:1 there is a possibility of competition between the two to occupy the protein surface. The Cl$^-$ ions primarily interact through electrostatic forces whereas in case of [*o*-COSAN]$^-$ both electrostatics as well as the N-H···B-H di-hydrogen bonds come into play.[39] Consequently, [*o*-COSAN]$^-$ displays a stronger interaction with the protein capable of displacing the Cl$^-$ ions despite being in higher concentration.

Interestingly, the radii of the proteins mentioned in the study are measured under specific conditions, particularly in presence of buffer solutions. These hydrodynamic radiuses describe the ideal, flawless surface of the protein rather than the reactive, functional core. In order to confer with the reported hydrodynamic radiuses, DLS measurements were performed with NaCl as the solvent. The values obtained did indeed concur with the literature values (Fig. 3.9).

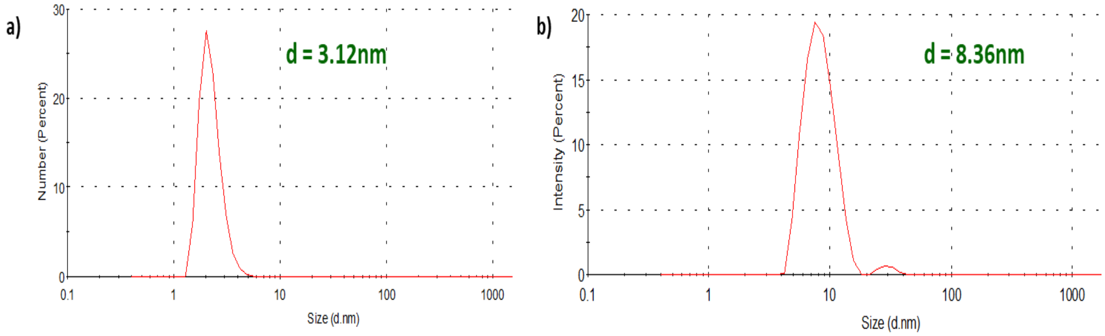

Fig. 3.9 Representative of the DLS measurements carried out for the various proteins showing the hydrodynamic diameter of BSA in **(a)** Water & **(b)** 0.1 M NaCl (electrolyte).

In a previous work, we had studied the interaction of BSA with [*o*-COSAN]$^-$ in the absence of any electrolyte and had found that the hydrodynamic radius of BSA in water was 1.6 nm smaller than the 4.1 nm reported in the study. Thus, further DLS measurements were carried out to measure the protein radius in water alone (Table 3.4). Table 3.4 proves the significance and influence of anions and their co-ions in determining the protein diameter.

Table 3.4 Hydrodynamic diameters obtained for the different proteins from DLS measurements in different conditions.

Protein	**Hydrodynamic Diameter, d_H (nm)**	
	Water	**0.1M NaCl**
BSA	3.12	8.26
γ-Globulin	7.9	10.90
Hemoglobin	6.90	6.40
Histone	1.55	11.60
Lysozyme	1.42	4.01
HRP	5.27	6.08
CA	8.66	4.02
Myoglobin	4.09	3.80

3.3.7 Determining the number of bound [*o*-COSAN]⁻

Considering HSBD (type I) proteins such as BSA, catalase, γ-globulin, hemoglobin and histone which has a saturating nature, two intersecting trendlines can be determined. The intersecting point corresponding to a particular [protein]/[*o*-COSAN]⁻ value signifies the maximum number of [*o*-COSAN]⁻ capable of binding to a single protein surface under the given conditions. Table 3.5 display the results obtained for the different type I proteins and interestingly, it can be observed that as the protein size increases, the amount of bound [*o*-COSAN]⁻ on the surface decreases in agreement with the earlier proposed hypothesis.

Table 3.5 Amount of bound [*o*-COSAN]⁻ estimated for the different HSBD proteins.

Protein	**Hydrodynamic radius (nm)**	**Intersection (point of maximum coverage)**	**Number of [*o*-COSAN]⁻ (experimental)**
Histone	5.78	0.041	25
γ-Globulin	5.6	0.027	37
Catalase	5.2	0.013	77
BSA	4.1	0.012	83
Hemoglobin	3.2	0.020	50

It can be seen that hemoglobin is an exception to the general rule but can be justified as hemoglobin is a borderline protein between HSBD (Type I) and LSBD (Type II) proteins. Notably, the number of [*o*-COSAN]$^-$ bound on the BSA surface, calculated to be 100, is also lower than the one obtained in the previous study in the absence of any ions. Thus, it can be deduced that the environment surrounding the protein greatly defines the available surface area. Intuitively, we could postulate that the water molecules are easier to replace in comparison to Cl^- anions. Moreover, the retained anions as they are difficult to displace would form a persistent layer upon which the [*o*-COSAN]$^-$ molecules are deposited. Thus, further hindering the interaction of the [*o*-COSAN]$^-$ with the protein surface. Despite these simplifications, the results obtained from the study is relatively realistic to be applicable.

3.4 Conclusion

Our investigations focus on the intricacies of defining the surface of a protein. We explore the 'effective' protein surface (EPS) with respect to the anionic, redox-active [*o*-COSAN]$^-$ with self-assembling abilities and formation of hydrogen and di-hydrogen bonds. We have successfully demonstrated the application of a 'small molecule' probe with unique characteristics for visualizing the protein surface using facile and rational calculations and approximations. We also illustrate the influence of the surrounding environment on the structure as well as the interactions of the protein, modulating the self-assembling properties of [*o*-COSAN]$^-$. We indeed demonstrate the ability of [*o*-COSAN]$^-$ to distinguish between the proteins, suggesting its potential application as a convenient and powerful probing and imagine tool.

The work introduces an effective and innovative method to analyse the surface of a protein in its native form without any harsh conditions or interferences. These studies would further stimulate research aimed at utilizing small molecular probes such as [*o*-COSAN]$^-$ for better understanding the surface and hence the functions of a protein. We aim to pave a way for extended research in deciphering the protein surface realistically.

The following chapter takes advantage of the ability of [*o*-COSAN]$^-$ to form strong di-hydrogen bonds to integrate metallacarboranes and magnetic nanoparticles wherein the nanoparticles functionalized with amines pose as protein mimics.

3.5 References

1 C. I. Branden and J. Tooze, *Introduction to Protein Structure*, Garland Science, 2nd edn., 2012.

2 C. A. Orengo, A. E. Todd and J. M. Thornton, From protein structure to function, *Curr. Opin. Struct. Biol.*, 1999, **9**, 374–382.

3 G. N. Ramachandran, C. Ramakrishnan and V. Sasisekharan, Stereochemistry of polypeptide chain configurations, *J. Mol. Biol.*, 1963, **7**, 95–99.

4 R. M. Jackson and M. J. E. Sternberg, Protein surface area defined, *Nature*, 1993, **366**, 638.

5 V. N. Uversky, Intrinsically disordered proteins from A to Z, *Int. J. Biochem. Cell Biol.*, 2011, **43**, 1090–1103.

6 C. J. Oldfield, Y. Cheng, M. S. Cortese, C. J. Brown, V. N. Uversky and A. K. Dunker, Comparing and Combining Predictors of Mostly Disordered Proteins, *Biochemistry*, 2005, **44**, 1989–2000.

7 K. Mazmanian, K. Sargsyan and C. Lim, How the Local Environment of Functional Sites Regulates Protein Function, *J. Am. Chem. Soc.*, 2020, **142**, 9861–9871.

8 S. L. Speer, W. Zheng, X. Jiang, I.-T. Chu, A. J. Guseman, M. Liu, G. J. Pielak and C. Li, The intracellular environment affects protein–protein interactions, *Proc. Natl. Acad. Sci.*, 2021, **118**, e2019918118.

9 B. Yu, C. C. Pletka and J. Iwahara, Quantifying and visualizing weak interactions between anions and proteins, *Proc. Natl. Acad. Sci.*, 2021, **118**, e2015879118.

10 Y. Okuno, J. Yoo, C. D. Schwieters, R. B. Best, H. S. Chung and G. M. Clore, Atomic view of cosolute-induced protein denaturation probed by NMR solvent paramagnetic relaxation enhancement, *Proc. Natl. Acad. Sci.*, 2021, **118**, e2112021118.

11 Z. Jing, R. Qi, C. Liu and P. Ren, Study of interactions between metal ions and

protein model compounds by energy decomposition analyses and the AMOEBA force field., *J. Chem. Phys.*, 2017, **147**, 161733.

12 M. Ozboyaci, D. B. Kokh, S. Corni and R. C. Wade, Modeling and simulation of protein-surface interactions: achievements and challenges., *Q. Rev. Biophys.*, 2016, **49**, e4.

13 T. C. Terwilliger, D. Stuart and S. Yokoyama, Lessons from Structural Genomics, *Annu. Rev. Biophys.*, 2009, **38**, 371–383.

14 C. J. Lanci, C. M. MacDermaid, S. Kang, R. Acharya, B. North, X. Yang, X. J. Qiu, W. F. DeGrado and J. G. Saven, Computational design of a protein crystal, *Proc. Natl. Acad. Sci.*, 2012, **109**, 7304–7309.

15 E. Laine and A. Carbone, Local Geometry and Evolutionary Conservation of Protein Surfaces Reveal the Multiple Recognition Patches in Protein-Protein Interactions, *PLOS Comput. Biol.*, 2015, **11**, 1–32.

16 L. Ronda, S. Bruno, S. Bettati, P. Storici and A. Mozzarelli, From protein structure to function via single crystal optical spectroscopy, *Front. Mol. Biosci.*, 2015, **2**, 12.

17 U. Heinemann, K. Büssow, U. Mueller and P. Umbach, Facilities and Methods for the High-Throughput Crystal Structural Analysis of Human Proteins, *Acc. Chem. Res.*, 2003, **36**, 157–163.

18 K. Palczewski, T. Kumasaka, T. Hori, C. A. Behnke, H. Motoshima, B. A. Fox, I. Le Trong, D. C. Teller, T. Okada, R. E. Stenkamp, M. Yamamoto and M. Miyano, Crystal Structure of Rhodopsin: A G Protein-Coupled Receptor, *Science*, 2000, **289**, 739–745.

19 Y. Hu, K. Cheng, L. He, X. Zhang, B. Jiang, L. Jiang, C. Li, G. Wang, Y. Yang and M. Liu, NMR-Based Methods for Protein Analysis, *Anal. Chem.*, 2021, **93**, 1866–1879.

20 K. Murata and M. Wolf, Cryo-electron microscopy for structural analysis of dynamic biological macromolecules, *Biochim. Biophys. Acta - Gen. Subj.*, 2018,

1862, 324–334.

21 F. Zhao, S. M. Matt, J. Bu, O. G. Rehrauer, D. Ben-Amotz and S. A. McLuckey, Joule Heating and Thermal Denaturation of Proteins in Nano-ESI Theta Tips, *J. Am. Soc. Mass Spectrom.*, 2017, **28**, 2001–2010.

22 K. J. Freedman, S. R. Haq, J. B. Edel, P. Jemth and M. J. Kim, Single molecule unfolding and stretching of protein domains inside a solid-state nanopore by electric field, *Sci. Rep.*, 2013, **3**, 1638.

23 W. Chen, Electroconformational denaturation of membrane proteins., *Ann. N. Y. Acad. Sci.*, 2005, **1066**, 92–105.

24 E. V Suprun, Direct electrochemistry of proteins and nucleic acids: The focus on 3D structure, *Electrochem. commun.*, 2021, **125**, 106983.

25 I. Fuentes, J. Pujols, C. Viñas, S. Ventura and F. Teixidor, Dual Binding Mode of Metallacarborane Produces a Robust Shield on Proteins., *Chemistry*, 2019, **25**, 12820–12829.

26 M. Y. Losytskyy, V. B. Kovalska, O. A. Varzatskii, M. V Kuperman, S. Potocki, E. Gumienna-Kontecka, A. P. Zhdanov, S. M. Yarmoluk, Y. Z. Voloshin, K. Y. Zhizhin, N. T. Kuznetsov and A. V Elskaya, An interaction of the functionalized closo-borates with albumins: The protein fluorescence quenching and calorimetry study, *J. Lumin.*, 2016, **169**, 51–60.

27 T. M. Goszczyński, K. Fink, K. Kowalski, Z. J. Leśnikowski and J. Boratyński, Interactions of Boron Clusters and their Derivatives with Serum Albumin., *Sci. Rep.*, 2017, **7**, 9800.

28 K. Fink, J. Boratyński, M. Paprocka and T. M. Goszczyński, Metallacarboranes as a tool for enhancing the activity of therapeutic peptides, *Ann. New York Acad. Sci.*, 2019, **1457**, 128–141.

29 R. Núñez, M. Tarrés, A. Ferrer-Ugalde, F. F. De Biani and F. Teixidor, Electrochemistry and Photoluminescence of Icosahedral Carboranes, Boranes, Metallacarboranes, and Their Derivatives, *Chem. Rev.*, 2016, **116**, 14307–

14378.

30 M. Uchman, V. Ďorďovič, Z. Tošner and P. Matějíček, Classical Amphiphilic Behavior of Nonclassical Amphiphiles: A Comparison of Metallacarborane Self-Assembly with SDS Micellization, *Angew. Chemie.*, 2015, **54**, 14113–14117.

31 D. C. Malaspina, C. Viñas, F. Teixidor and J. Faraudo, Atomistic Simulations of COSAN: Amphiphiles without a Head-and-Tail Design Display “Head and Tail” Surfactant Behavior, *Angew. Chemie.*, 2020, **59**, 3088–3092.

32 P. Bauduin, S. Prevost, P. Farràs, F. Teixidor, O. Diat and T. Zemb, A Theta-Shaped Amphiphilic Cobaltabisdicarbollide Anion: Transition From Monolayer Vesicles to Micelles, *Angew. Chemie.*, 2011, **50**, 5298–5300.

33 P. Farràs, E. J. Juárez-Pérez, M. Lepšík, R. Luque, R. Núñez and F. Teixidor, Metallacarboranes and their interactions: theoretical insights and their applicability, *Chem. Soc. Rev.*, 2012, **41**, 3445–3463.

34 R. N. Grimes, *Carboranes*, Elsevier Inc. New York, New York, 3rd edn., 2016.

35 C. Viñas, M. Tarrés, P. González-Cardoso, P. Farràs, P. Bauduin and F. Teixidor, Surfactant behaviour of metallacarboranes. A study based on the electrolysis of water, *Dalt. Trans.*, 2014, **43**, 5062–5068.

36 J. A. M. Xavier, C. Viñas, E. Lorenzo, T. García-Mendiola and F. Teixidor, Potential application of metallacarboranes as an internal reference: an electrochemical comparative study to ferrocene, *Chem. Commun.*, 2022, **58**, 4196–4199.

37 J.-N. Longchamp, S. Rauschenbach, S. Abb, C. Escher, T. Latychevskaia, K. Kern and H.-W. Fink, Imaging proteins at the single-molecule level, *Proc. Natl. Acad. Sci.*, 2017, **114**, 1474–1479.

38 T. O. Pleshakova, N. S. Bukharina, A. I. Archakov and Y. D. Ivanov, Atomic Force Microscopy for Protein Detection and Their Physicochemical Characterization., *Int. J. Mol. Sci.*, 2018, **19**, 1142.

39 A.-I. Stoica, C. Kleber, C. Viñas and F. Teixidor, Ion selective electrodes for

protonable nitrogen containing analytes: Metallacarboranes as active membrane components, *Electrochim. Acta*, 2013, **113**, 94–98.

40 A.-I. Stoica, C. Viñas and F. Teixidor, Cobaltabisdicarbollide anion receptor for enantiomer-selective membrane electrodes, *Chem. Commun.*, 2009, **33**, 4988–4990.

41 M.-C. Bellissent-Funel, A. Hassanali, M. Havenith, R. Henchman, P. Pohl, F. Sterpone, D. van der Spoel, Y. Xu and A. E. Garcia, Water Determines the Structure and Dynamics of Proteins, *Chem. Rev.*, 2016, **116**, 7673–7697.

42 H. I. Okur, J. Hladílková, K. B. Rembert, Y. Cho, J. Heyda, J. Dzubiella, P. S. Cremer and P. Jungwirth, Beyond the Hofmeister Series: Ion-Specific Effects on Proteins and Their Biological Functions, *J. Phys. Chem. B*, 2017, **121**, 1997–2014.

43 M. G. Cacace, E. M. Landau and J. J. Ramsden, The Hofmeister series: salt and solvent effects on interfacial phenomena, *Q. Rev. Biophys.*, 1997, **30**, 241–277.

44 A.-I. Stoica, C. Viñas and F. Teixidor, History of Cobaltabis(dicarbollide) in Potentiometry, No Need for Ionophores to Get an Excellent Selectivity, *Molecules*, 2022, **27**, 8312.

45 I. Guerrero, A. Saha, J. A. M. Xavier, C. Viñas, I. Romero and F. Teixidor, Noncovalently Linked Metallacarboranes on Functionalized Magnetic Nanoparticles as Highly Efficient, Robust, and Reusable Photocatalysts in Aqueous Medium, *ACS Appl. Mater. Interfaces*, 2020, **12**, 56372–56384.

46 T. García-Mendiola, V. Bayon-Pizarro, A. Zaulet, I. Fuentes, F. Pariente, F. Teixidor, C. Viñas and E. Lorenzo, Metallacarboranes as tunable redox potential electrochemical indicators for screening of gene mutation, *Chem. Sci.*, 2016, **7**, 5786–5797.

47 H. P. Erickson, Size and shape of protein molecules at the nanometer level determined by sedimentation, gel filtration, and electron microscopy., *Biol. Proced. Online*, 2009, **11**, 32–51.

48 V. La Verde, P. Dominici and A. Astegno, Determination of Hydrodynamic Radius of Proteins by Size Exclusion Chromatography., *Bio-protocol*, 2017, 7, e2230.

Chapter 4

4.1 Introduction

Throughout the years, nanoparticles have been gaining popularity owing to their diverse properties and functionalities. A major thrust of research has been focused on understanding the behaviour and properties of these particles emerging as a consequence of constraining them in the nanoscale regime (1-100nm).[1,2] These unknown, and often counter-intuitive, properties are explained using quantum mechanics.[3–5] Nanoparticles exhibit a diverse range of functionalities owing to their high surface-to-volume ratio, size dependent physical and chemical properties, diverse and ease of surface functionalization among the other hundreds of virtues.[6–9] Of these, magnetic nanoparticles (MNPs) pertain to a class of their own owing to their unique magnetic and electrical properties.

There are several different types of MNPs, each with its own unique characteristics and properties. The predominantly studied and explored ones are: iron oxide nanoparticles (Fe_3O_4) owing to their remarkable magnetic properties and biocompatibility, cobalt-based magnetic nanoparticles ($CoFe_2O_4$) owing to their high magnetic moments and chemical stability, nickel-based magnetic nanoparticles ($NiFe_2O_4$) owing to their high saturation magnetization values and rare-Earth metal such as neodymium (Nd), samarium (Sm), or gadolinium (Gd) based nanoparticles owing to their high coercivity as well as magnetization values.[10–18] A common feature in most of these MNPs is the metal - iron (Fe). Iron (Fe) is a metal in the first transition series of the periodic table with variable oxidation states, from +2 to +6 although predominantly it exists in +2 and +3 states. It finds itself in a wide variety of applications and is essential for sustaining life on Earth.[19,20] A characteristic which makes Fe^{2+} so enticing is its strong magnetic moment which can be attributed to the presence of four unpaired electrons in its 3d orbitals. Iron being a ferromagnetic material inherently possesses a permanent net magnetic moment. In the case of bulk ferromagnetic materials, the magnitude of magnetization (M) is generally less than its value when all the atomic moments are perfectly aligned and this is explained in terms of magnetic domains or Weiss domains (Fig. 4.1).[21,22]

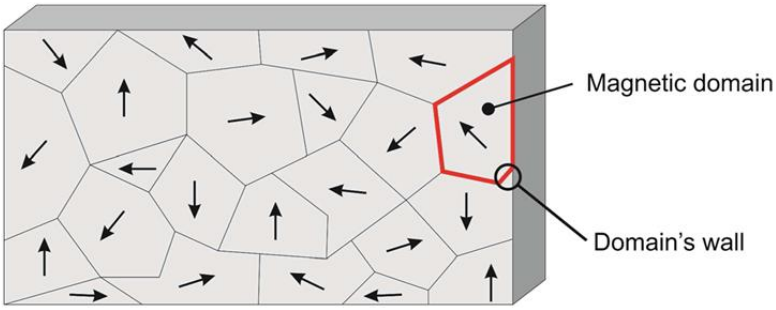

Fig. 4.1 Schematic representation of the magnetic domains present in a bulk ferromagnetic material. [From reference 22]

According to this theory, the ferromagnets are sub-divided into domains with each of them having its own magnetization vector arising from the alignment of the individual atomic moments within the domain. The physical regions separating the domains are called domain walls where the magnetization vector rotates coherently from the direction in one domain to that in the next domain. Thus, in the absence of an external magnetic field, the magnetization vectors of all the domains may not be aligned in the same direction and hence possess an overall low magnetization. This is also the reason why an iron material, despite having a non-zero magnetic moment, doesn't behave as a magnet in room temperature.

What happens when the particle size is reduced from the bulk to nanoscale regime? When the size of the material becomes small, the number of domains is reduced until only a single domain remains when the characteristic size of the material is below a critical size (D_c) in the nanoscale.[23] Single domain describes a region within the magnetic material which has uniform magnetization and has no hysteresis loop after the removal of the external field (Fig. 4.2).[24] In this case, the individual magnetic particles have a large constant magnetic moment and behave like a giant paramagnetic atom with a fast response to the applied magnetic field without remnant magnetization and the material is said to be superparamagnetic (red trace). For a single domain ferromagnetic material such as the MNPs, their magnetic energies become comparable to their thermal energy. Thus, when the size of the particles is reduced below the size of the single domain, their thermal energies overcome their magnetic energy and hence in the absence of any external magnetic field, the magnetization vector of single domain particles is reversed spontaneously. Thus, the particles become superparamagnetic in nature. The size dependant magnetic properties like superparamagnetism, remanence enhancement, exchange averaging of anisotropy and giant magnetoresistance all come to fore when the size of the particle drops to the nanoscale.[25]

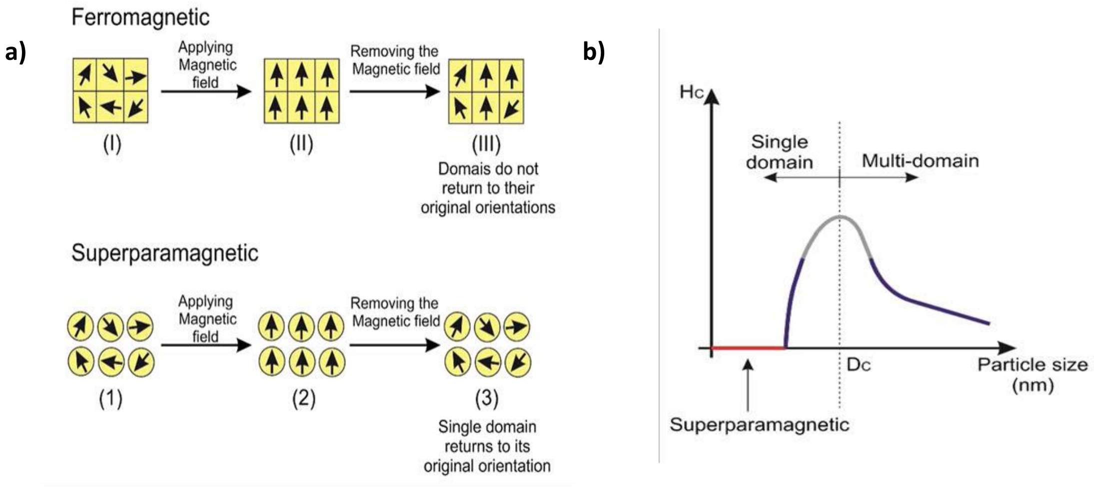

Fig. 4.2 (a) Schematic representation of the behaviour of magnetic particles in the presence and absence of an external field. **(b)** Magnetic characteristics of ferromagnetic materials as a function of particle size.[26,27]

Understanding the correlation between the magnetic properties and the size and shape of iron-oxide nanoparticles (IONPs) is a pre-requisite for the widespread application of magnetism in data storage and bio-sensing fields.

4.2 Motivation & Objective

Recent years have seen the rise of numerous synthetic techniques for the preparation of highly stable, shape-controlled MNPs with narrow size distribution. These approaches can vary from physical to chemical to biological techniques.[15] Popular physical methods include the mechanical size reduction of bulk iron oxide in presence of large amounts of surfactants such as oleic acid using crushing ball mill, grounded for weeks. Although the method is cost-effective, it is tedious and time-consuming yielding nanoparticles with a broad distribution and hence rarely preferred.[28,29] Thus, chemical methods such as co-precipitation or thermal decomposition are generally opted. Among the chemical methods, owing to being simple, cost-effective, excellent size controlling ability and easy tunability with high yields of nanoparticles, co-precipitation technique is the most desirable option among researchers.[30,31] Generally, co-precipitation involves mixing of ferric and ferrous ions in a 2:1 molar ratio in a basic solution or at elevated temperatures, under inert atmosphere to prevent the particles from oxidation. The size, crystal structure, chemical and magnetic properties of MNPs prepared by the co-precipitation method depends upon the type of the iron salts used (eg. chlorides, sulphates, nitrites), pH and the ionic strength of the precipitating solution.[32] Although, co-precipitation is a classic technique for synthesizing IONPs with high magnetic values, it still has its shortcomings such as the broad particle size distribution and the utilization of strong base in the reaction process. Another technique which is commonly employed to produce high quality monodisperse and monocrystalline IONPs is thermal decomposition of iron precursors in organic solvents containing stabilizing surfactants such as oleyl amine, oleic acid and stearic acid.[33–35] With a view of shifting to a sustainable and environment friendly approach, high pressure hydrothermal synthesis have also been developed which relies on hydrolysis and dehydration of iron salts by water under elevated temperatures (> 200°C) and pressure (> 2000 psi) (super-critical conditions of water).[36] The obtained metal oxides and hydroxides have very low solubility in water leading to high supersaturated solutions which finally yields super-fine crystals. Thermal decomposition of iron precursors from gaseous phase has also been reported using hi-tech spray and laser pyrolysis techniques. For a versatile green synthesis at room temperature sol-gel methods are preferred. The method involves two consecutive reactions, hydroxylation and condensation of molecular precursors, in solution leading to a ‘sol’ of nanoparticles. Further condensation and inorganic polymerization lead to a three-dimensional metal oxide network denominated as wet gel. These reactions are performed at room temperature followed by further heat treatments to acquire the final crystalline structure.[37] The final structure depends greatly on the properties and structure of the gel formed which is dictated by the nature of salt precursors, temperature, pressure, pH and agitation.

Among all the synthetic approaches mentioned, despite polydispersity and minimal shape control, co-precipitation is probably the simplest synthetic route while thermal decomposition, even though is experimentally demanding, affords the best results in terms of size and shape control. To date, these two routes are the most explored for synthesizing highly magnetic IONPs, particularly for large scale production.

MNPs are a popular subject of research owing to their multi-functional applications. Catalysis is considered as an essential part of the chemical industry. Among the nanoparticles used for catalysis, MNPs stands out due to their ease of separation and reusability making them an attractive alternate to the normal catalytic systems, particularly organometallic systems.[38–40] MNPs are known for their robust magnetic properties even in smaller dimensions. Catalytic systems involving MNPs can be many but generally, they have been employed as a support for the active catalyst creating hybrid structures. Another important application of MNPs is in data storage. For data storage, one of the major requirements is a magnetic material with a stable and switchable magnetic state which is not affected by temperature fluctuations, having high remanence and coercivity, uniformly sized and highly resistant to corrosion and friction. Ferrofluids consisting of magnetite nanoparticles are often used for these purposes. The ferrofluids employ magnetite NPs of 10 to 12 nm in dimension covered with surfactants and suspended in a liquid medium.[41–43] These become magnetic under the application of an external magnetic field and can move as a fluid based on the application of the field. They have interesting optical anisotropy and can be used in switches too. Sensors are the most commonly used electronic devices in all walks of life. The sensing technology has its uses spawned from biological applications to food industry, cars, motors and more. In this regard, the MNPs have found wide spread attention. Along being prominently used as biosensors in biomedical field, they have also been widely used in magnetic field-based micro/nano electromechanical systems (MEMS/NEMS).[44–46] Magnetic nanoparticles as mentioned above have a myriad of applications other than their most dominant applicative uses in the biomedical field. One of the major emerging fields for the application of MNPs in the present scenario is their use in sustainable environment applications. Water pollution, considered as one of the major millennial problems, is on the rise and maintaining the purity of water is of utmost essence for survival on this planet. Water pollutants mostly consist of toxic metals and various microbes. With the recent advances in the core-shell MNPs, it is possible to use them effectively in the process of waste water treatment and removing pollutants from water bodies.[47] The reason behind the MNPs being so advantageous is that these surface modified MNPs have reduced toxicity and hence pose no threat to produce secondary pollutant in the process of pollutant removal. Moreover, the surface of the MNPs once modified by shell coating could be functionalized in multiple ways and it also provides more surface-active sites for trapping the pollutants. Along with its ability to easily trap the pollutants in solution due to the modified surface, their most attractive property lies in the ease with which they can be recovered from the medium, simply by the application of an external magnetic field. This easy recovery helps in an effective way of removing the pollutants from the water medium without further contaminating or using extra steps for removal and cleaning residual materials from the system. Thus, magnetic nanoparticles are intriguing materials with a wide range of prospective uses in industries including medical, electronics, and environmental research due to their unique characteristics, biocompatibility, adaptability and capacity to be targeted and controlled.

As mentioned above, there is a generic challenge in obtaining highly stable, size-controlled MNPs with narrow size distribution. Hence, techniques for producing stable and robust IONPs, particularly in large quantities and in a sustainable manner, are gaining new interests. In this chapter, we would discuss two different types of iron-oxide magnetic nanoparticles: core-shell IONPs and 'naked' IONPs, produced by following a previously reported and a novel co-precipitation method, respectively. The chapter would discuss in detail the synthetic techniques adopted as well as the different characteristic properties of the as-formed systems. We would further discuss the possibilities and advantages of integrating the metallacarboranes, mainly cobaltabis(dicarbollide) ($[3,3'\text{-Co}(C_2B_9H_{11})_2]^-$, [*o*-COSAN]$^-$), with IONPs from two different perspective applications: photo-redox catalysis and bio-sensing devices (Fig. 4.3). The MNPs are further surface functionalized with amine ligands and the strong di-hydrogen interaction of [*o*-COSAN]$^-$ with amine groups, N-H···H-B dihydrogen bonds, have been exploited.[48,49] Amine functionalized core-shell MNPs decorated with [*o*-COSAN]⁻ have been employed as a heterogenous catalyst for photo-oxidation of alcohols while 'naked' amine functionalized MNPs have been proposed a protein 'mimic'.[50] The chapter would explore the need to adapt and modify a system under study to suit the applications.

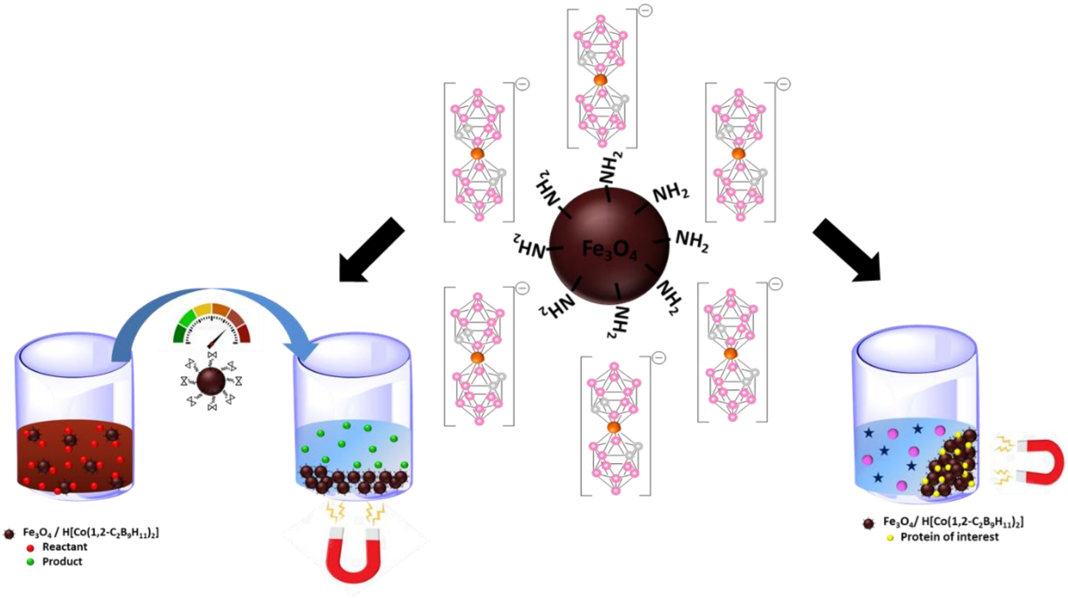

Fig. 4.3 Schematic representation of amine functionalized MNPs decorated with [*o*-COSAN]⁻ employed in two different applications: photoredox catalysis & bio-sensing.

4.3 Results & Discussions

As stated previously, two different synthetic approaches have been adopted to synthesize iron oxide magnetic nanoparticles using the same iron precursors in basic solutions. Subsequently, we will observe how we could modify the system for the betterment of the purpose.

The transmission electron microscopy (TEM) analysis was performed on JEOL JEM 1210 at 120 kV. Infrared (IR) measurements were carried out on a JASCO FTIR-4600 spectrometer. The magnetic measurements were carried out in Quantum Design MPMS-XL based on a SQUID detector with the maximum magnetic field of up to 70 kOe. The samples were dried and weighed before being given for the measurement in a capillary. Zeta potential measurements were performed on a Zetasizer Nano ZS (Malvern Instrument Ltd.) using the electrophoretic scattering principle. All the measurements were performed with water as the solvent at 25°C at neutral pH. Powder diffraction (P-XRD) measurements were performed on Bruker D8-Discover with Cu k_α radiation (1.54 A°).

4.3.1 Synthesis of amine functionalized $Fe_3O_4@SiO_2$ core-shell MNPs

Fe_3O_4 MNPs were synthesized following a reported co-precipitation method and further encapsulated by silica shell using Stöber process.[51,52] Briefly, chloride salts of ferrous (2 g) and ferric ions (5.2 g) were mixed in 1:2 molar ratio in 25 mL water followed by the slow addition of 15 M NaOH (25 mL). With vigorous stirring, 12 M HCl (0.85 mL) was added dropwise to the mixture to form black solid MNPs precipitates. The resulting mixture was degassed and maintained in an inert atmosphere at 80°C for 4h. The product was obtained by magnetic decantation, washed with water and ethanol and dried at 80°C for 10h. For encapsulating the particles in silica shell, the as-formed MNPs were dispersed in a mixture of ethanol and water (4:1 v/v). To the colloidal dispersion 30% NH_3 (2.5 mL) was added followed by the drop-wise addition of the silica precursor, 1.5 mL tetraethoxysilane (TEOS). The solution was mechanically stirred for 6h at room temperature before being magnetically decanted and washed. The particles were dried at 80°C for 10h and stored for further studies.

These nanoparticles were functionalized with amine groups using 3-(2-aminoethylamino)propylmethyldimethoxy silane (APMS) ligand. The core-shell MNPs (200 mg) were dissolved in 45 mL ethanol, to which the APMS ligand (5 mL in 20 mL ethanol) was added (Fig. 4.4). The reaction mixture was stirred at 50°C for 5h for the hydrolysis of the methyl groups and aged overnight to obtain stable MNPs. The particles were precipitated using NaCl and washed and finally dried at 80°C.

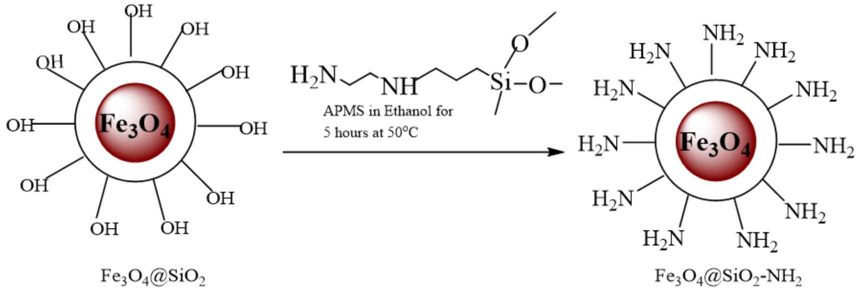

Fig. 4.4 Synthesis of amine functionalized $Fe_3O_4@SiO_2$ MNPs using the APMS ligand.

4.3.2 Anchoring of [*o*-COSAN]$^-$ onto *amine functionalized* $Fe_3O_4@SiO_2$ *core-shell MNP*

The amine functionalized silica-shell iron oxide, $Fe_3O_4@SiO_2$-NH_2 (50 mg), magnetic nanoparticles were suspended in 10 mL of water containing 5 mM H[*o*-COSAN] and was sonicated in an ultrasound bath for 30 min. Subsequently, the particles were magnetically separated and washed 10 times, before drying at 80°C in vacuum (Fig. 4.5).

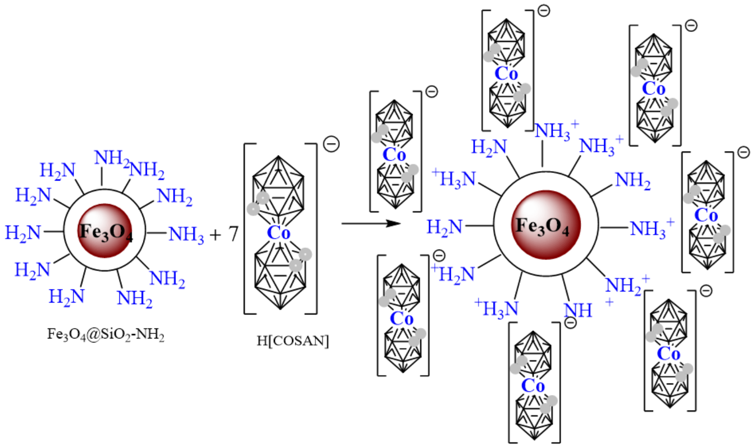

Fig. 4.4 Synthesis of [*o*-COSAN]$^-$ decorated $Fe_3O_4@SiO_2$-NH_2 magnetic nanoparticles.

4.3.3 Characterization of the as-formed MNPs systems

The mean size of the silica coated Fe_3O_4 MNPs were estimated to be around 9.34 ± 1.6 nm from TEM analysis. The spherical shape of these particles can also be observed from the TEM images. The amine functionalized MNPs displayed an agglomerated mean diameter of 11.22 ± 2.13 nm while [*o*-COSAN]$^-$ decorated MNPs showed an increased mean size of 14.17 ± 1.03 nm thereby confirming the successful anchoring of [*o*-COSAN]$^-$ onto the amine functionalized MNPs (Fig. 4.5).

The XRD analysis of Fe_3O_4 MNPs and $Fe_3O_4@SiO_2$ MNPs showed similar pattern and confirmed the magnetite structure of the nanoparticles (Fig. 4.6).[53,54] However, it is probable that the particles are a mix of both the magnetite and maghemite (γ- Fe_3O_4) due to the high similarity of both the XRD patterns. Nevertheless, the magnetic properties required for the scope of our study remains unaltered.

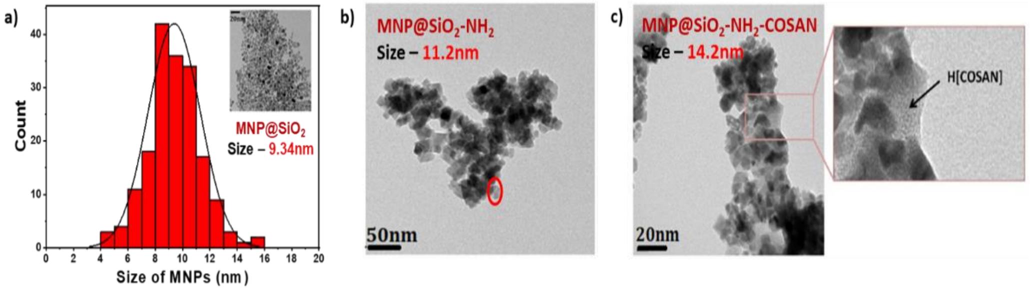

Fig. 4.5 (a) Gaussian size distribution of $Fe_3O_4@SiO_2$ (Inset: TEM image of $Fe_3O_4@SiO_2$). **(b)** TEM image of aggregated $Fe_3O_4@SiO_2$-NH_2. **(c)** TEM image of [*o*-COSAN]$^-$ decorated $Fe_3O_4@SiO_2$-NH_2 with an enlarged view showing H[*o*-COSAN] located between MNPs.

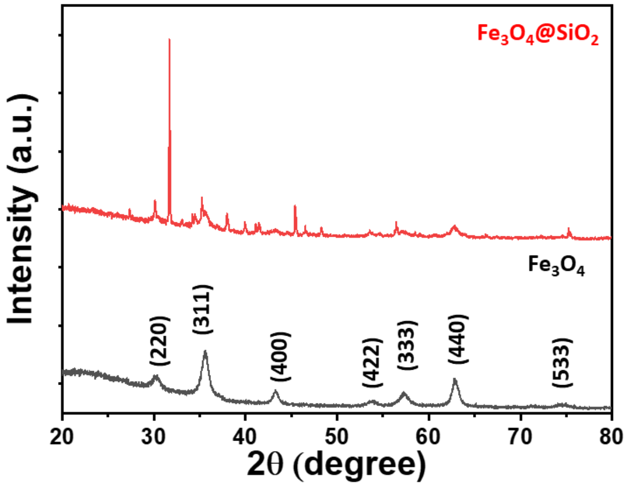

Fig. 4.6 XRD pattern confirming the magnetite structure of the MNPs with the crystallographic faces of magnetite marked.

IR spectra of $Fe_3O_4@SiO_2$-NH_2 and $Fe_3O_4@SiO_2$-NH_2/[*o*-COSAN]$^-$ displayed $\nu_{Fe\text{-}O}$ stretching modes at 546 and 542 cm^{-1}, respectively, while $\nu_{Si\text{-}O}$ stretching modes can be observed at 1074 and 1071 cm^{-1}. The N-H bending band can be observed at 1638 cm^{-1} for $Fe_3O_4@SiO_2$-NH_2 and at 1632 cm^{-1} for $Fe_3O_4@SiO_2$-NH_2/[*o*-COSAN]$^-$. A further affirmation for the successful anchoring of [*o*-COSAN]$^-$ onto the MNPs can be observed in the IR from the $\nu_{B\text{-}H}$ stretching mode at 2560 cm^{-1}, typical for a borane compound (Fig. 4.7).

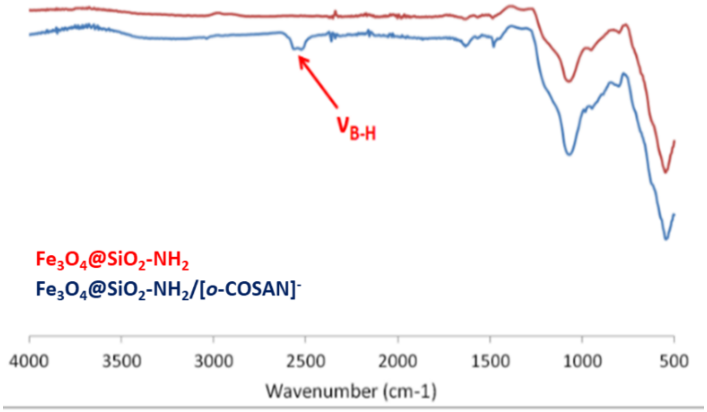

Fig. 4.7 IR spectra of $Fe_3O_4@SiO_2-NH_2$ and $Fe_3O_4@SiO_2-NH_2/[o\text{-COSAN}]^-$ with the stretching mode of B-H vibration marked.

Fig. 4.8 shows the hysteresis curve before and after the anchoring of $[o\text{-COSAN}]^-$ with the saturation magnetization (M_s) value of 29.1 emu/g. The M_s value remains unaltered even after the anchoring of the photocatalyst onto the MNPs, thereby retaining the magnetic characteristics of the $Fe_3O_4@SiO_2-NH_2$ nanoparticles. The absence of any hysteresis indicates the super-paramagnetic behavior of the particles.

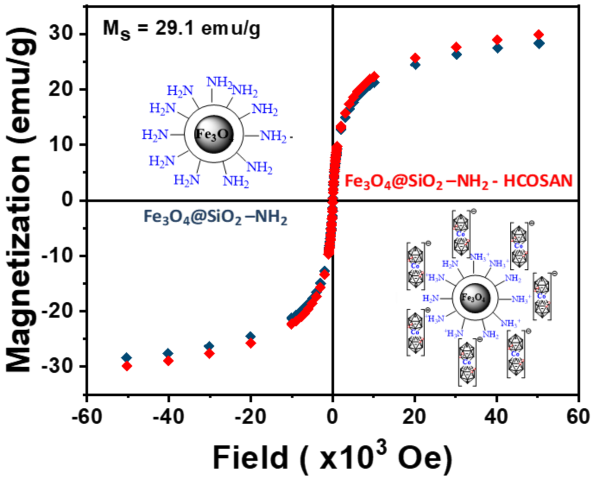

Fig. 4.8 Hysteresis curve of the MNPs before and after anchoring of $[o\text{-COSAN}]^-$.

Zeta potential (ζ) measurements were carried out to ascertain the surface charge of these MNPs. $Fe_3O_4@SiO_2-NH_2$ nanoparticles displayed a + value of 13.7 mV affirming the presence of ammonium cations on the surface of these MNPs. Upon the anchoring of the [*o*-COSAN]$^-$ anion, the ζ-potential shifted from + to – value of 15.2 mV, confirming the successful anchoring (Fig. 4.9). It is noteworthy that these values are lower than the absolute value of 30 mV, generally considered as the threshold value to interpret stability of the colloidal solutions. ζ-potential values above the threshold value tend to yield colloidal solutions having high stability and hence prolonged dispersed state while those with values lower than the threshold possess particles that tend to aggregate. Hence, these colloidal solutions are unstable.

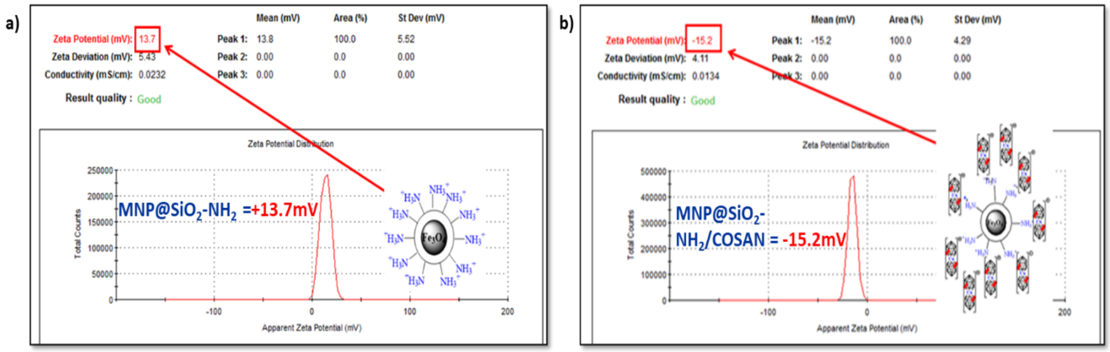
a)

Zeta Potential (mV): 13.7
Zeta Deviation (mV): 5.43
Conductivity (mS/cm): 0.0232
Result quality : Good

	Mean (mV)	Area (%)	St Dev (mV)
Peak 1:	13.8	100.0	5.52
Peak 2:	0.00	0.0	0.00
Peak 3:	0.00	0.0	0.00

b)

Zeta Potential (mV): -15.2
Zeta Deviation (mV): 4.11
Conductivity (mS/cm): 0.0134
Result quality : Good

	Mean (mV)	Area (%)	St Dev (mV)
Peak 1:	-15.2	100.0	4.29
Peak 2:	0.00	0.0	0.00
Peak 3:	0.00	0.0	0.00

Fig. 4.9 Zeta potential measurements of **(a)** $Fe_3O_4@SiO_2\text{-}NH_2$ & **(b)** $Fe_3O_4@SiO_2\text{-}NH_2$/[*o*-COSAN]$^-$.

UV-visible studies were performed to estimate the approximate amount of H[*o*-COSAN] anchored on the MNPs. As H[*o*-COSAN] in aqueous solution has a characteristic absorbance peak at 446 nm, the gradual decrease in the intensity upon the addition of the amine functionalized MNPs can be corroborated with the interaction of H[*o*-COSAN] with $Fe_3O_4@SiO_2\text{-}NH_2$. The difference between the subsequent absorption intensities yields the amount of H[*o*-COSAN] non-covalently bonded on the surface of the MNPs. The MNPs along-with the anchored H[*o*-COSAN] are removed from the solution by magnetic separation and the clear supernatant is measured to quantify the remaining H[*o*-COSAN]. Fig. 4.10 shows the study performed and the total amount of H[*o*-COSAN] anchored on the surface of $Fe_3O_4@SiO_2\text{-}NH_2$ was estimated to be around 0.0028 mmol/100 mg of nanoparticles. For every 5 mg of MNPs, 0.14 ± 0.03 mM H[*o*-COSAN] is anchored and the saturation, ie. amount of MNPs at which no further decrease in the absorption intensity of [*o*-COSAN]$^-$, takes place at 30 mg of the MNPs. The UV-visible study also confirms the successful anchoring of H[*o*-COSAN] onto the $Fe_3O_4@SiO_2\text{-}NH_2$ magnetic nanoparticles.

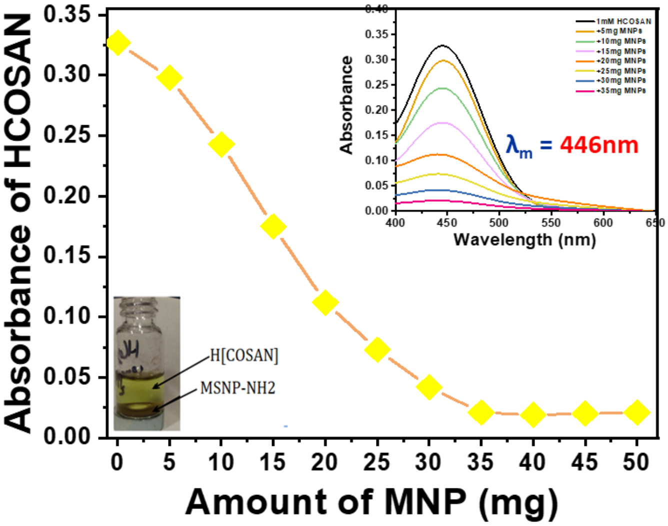

Fig. 4.10 Evolution of absorbance of 1 mM H[*o*-COSAN] in water with the addition of $Fe_3O_4@SiO_2\text{-}NH_2$ nanoparticles. (Inset: UV-Vis spectra of H[*o*-COSAN] with increasing amount of MNPs).

These studies confirm the successful anchoring of the photo-redox catalyst onto the amine functionalized iron oxide magnetic nanoparticles.

4.3.4 Photoredox catalysis of alcohols using $Fe_3O_4@SiO_2\text{-}NH_2$/[o-COSAN]$^-$

The ability of the carboranes to perform as catalysts for different processes have been explored over the years.[55–58] Recently, we have also demonstrated the potential application of [*o*-COSAN]$^-$ as an efficient and robust homogenous photo-redox catalyst for alcohol oxidation in water through single-electron transfer process.[59] Lack of photoluminescence (further explained in the subsequent chapters), high oxidizing capacity of the $Co^{4+/3+}$ couple and their solubility in water, make [*o*-COSAN]$^-$ an attractive candidate for photo-catalysis.[60] With the incorporation of MNPs, the advantages increase even further due to the ease of catalyst recovery as well as reusability. $Fe_3O_4@SiO_2\text{-}NH_2$/[o-COSAN]$^-$ have been employed as a heterogenous catalyst for the photo-oxidation of aliphatic and aromatic alcohols in water using small amounts of catalyst (0.01 mol%) with short catalytic duration.

The heterogenous photo-catalytic activity of the anchored $[o\text{-COSAN}]^-$ was studied for the oxidation of various alcohols in water (pH = 7, K_2CO_3) using $Na_2S_2O_8$ as the sacrificial or oxidizing agent. The experiments were performed by exposing the reaction quartz tubes to UV irradiation (~300 nm) placed in a photo-reactor at room temperature and atmospheric pressure (Scheme 4.1). The catalysts were separated using magnets at the end of the experiments and the reaction products were quantified using ^1H NMR and confirmed by gas chromatography-mass spectrum (GC-MS) analysis.

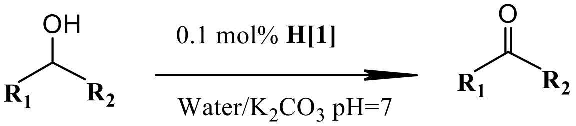

Scheme 4.1 Photocatalytic oxidation of alcohols using $[o\text{-COSAN}]^-$ denoted as [**1**] anchored on amine functionalized MNPs or Na[**1**] (0.1μmol), substrate (0.1 mmol), $Na_2S_2O_8$ (0.2 mmol), 5 mL potassium carbonate solution at pH=7 ;light irradiation 8h using a lamp with λ =300 nm; sonication after 4 hours.

Table 4.1 displays the various reactants as well as the conditions and the product yields. It can be clearly observed from the reaction yield as well as the turnover number (TON) with high selectivity, that the photo-redox catalyst is highly efficient and robust.

Table 4.1 Various reaction and substrates analyzed for the photocatalysis following the general procedure. [a] Absence of light; [b] Without sonication.

Entry	Catalyst	Substrate	Yield (%) (TON)
1	MNP-NH_2	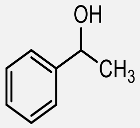	6
2	Na[**1**]	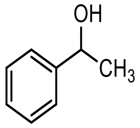	>99 (100)
3	MNP-NH_2/H[**1**]	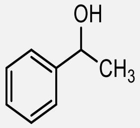	4[a]

4	MNP-NH_2/H[**1**]	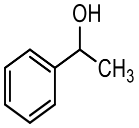	76 (760)[b]
5	MNP-NH_2/H[**1**]	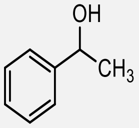	>99 (1000)
6	MNP-NH_2/H[**1**]	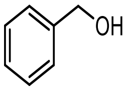	90 (900)
7	MNP-NH_2/H[**1**]	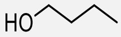	97 (970)

Blank experiments were carried out with the MNPs alone (1) as well as in the absence of light (3) which resulted in very low yield of the product, acetophenone, suggesting that the [*o*-COSAN]$^-$ is indeed the catalyst and is necessary for the photo-oxidation to occur. Homogeneous (2) and heterogeneous (5) catalysis both displayed remarkably high yields (>99%) indicating that the magnetic nanoparticle support does not hinder the reaction nor alter the catalytic properties of [*o*-COSAN]$^-$. The reaction proceeded with similar turnover number for both aliphatic and aromatic alcohols, thereby widening the substrate scope of the catalyst.

Notably, in all the reactions the pH of the initial solution changed from 7 to slightly acid pH (5-6) over time which was readjusted to 7 after 4h of reaction. To eliminate the possibility of leaching of the catalyst from the magnetic nanoparticle support, UV-visible experiments were performed on the reaction mixture after the oxidation and removal of the MNPs. The absence of the characteristic absorbance peak of H[*o*-COSAN] ascertained the lack of leaching of the active catalytic species.

The recyclability of the catalyst, Fe_3O_4@SiO_2-NH_2/[o-COSAN]$^-$, were investigated on two different aromatic alcohols (0.1 mmol), 1-phenylethanol and diphenylmethanol, with 4h of irradiation and 0.001 mmol catalyst (Fig. 4.11). After 4h of catalysis, the photocatalysts were recovered, washed and dried before being exposed to fresh substrate. The results indicate that the catalyst remains highly effective even after 12 successive runs suggesting that the heterogeneous catalyst is indeed robust and highly efficient.

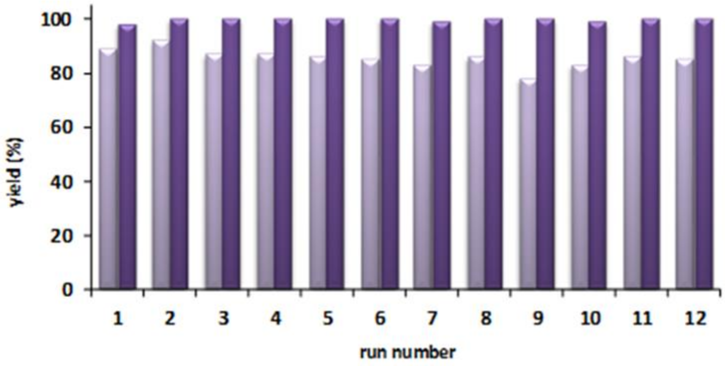

Fig.4.11 Photo-oxidation of diphenylmethanol and 1-phenylethanol using the heterogenous catalyst for successive cycles.

All these results suggest the potential application of $Fe_3O_4@SiO_2$-NH_2/[o-COSAN]$^-$ as a non-covalently bonded heterogeneous catalyst with remarkably high TON and wide substrate scope with the ability of being easily recovered and reutilized in environment friendly, aqueous media, without any harsh reaction conditions. This system paves path for a green and sustainable catalysis. The catalytic studies were carried out in collaboration with Dr. Isabel Guerrero and Dr. M. Isabel Romero.

4.3.5 Synthesis of 'naked' iron oxide nanoparticles by novel co-precipitation method

As we have seen, $Fe_3O_4@SiO_2$-NH_2 nanoparticles possess highly impressive characteristics which is advantageous for several applications. Despite, the virtues, these MNPs are not without their shortcomings such as their tendency to agglomerate, low colloidal stability and low saturation magnetization values. This probed us to explore different synthetic techniques for synthesizing stable, monodispersed MNPs with high M_s values in a green and sustainable manner. Hence, we developed a novel co-precipitation method for the synthesis of uniformly sized, highly stable super-paramagnetic iron oxide nanoparticles (SPIONs) in aqueous medium using repetitive ultrasonication with comparatively affordable precursors without any capping agent or non-magnetic layer.

The iron oxide (Fe_3O_4) magnetic nanoparticles were synthesized by a sonochemical co-precipitation method wherein the precursor chloride salts of ferric and ferrous ions were mixed in a 2:1 molar ratio followed by dropwise addition of 3M KOH basic solution with continuous sonication under inert atmosphere. To briefly explain the synthesis, solutions of $FeCl_3.6H_2O$ (0.833g, 3.1mmol) and $FeCl_2.4H_2O$ (0.278g, 1.4mmol), 17mL water each, and 8.33mL of 3M KOH were degassed, three times, to remove the dissolved oxygen. The iron salt's solutions were mixed and placed in an ultrasonic bath (HF45kHz, 80W) in a closed 50mL round bottom flask. To this, the KOH solution was added drop-wise, with the help of a syringe, with continuous sonication under N_2 atmosphere to obtain black solid precipitates. Following the addition, the temperature of the bath was raised to 60°C and after attaining the temperature (approximately 5-7 min), the colloidal dispersion was sonicated for 5, 10, 15, 30, 45 and 60 min in open air atmosphere. After the corresponding time of sonication, the precipitates were centrifuged at 6000rpm for 15min. The black precipitates were isolated by decantation and redispersed in 34mL water and 8.33mL of 3M KOH, to recreate the initial reaction conditions except for the iron salts. This process of sonication with corresponding durations, without the temperature, and centrifugation (15 min) was repeated sequentially for three more times before incubating the particles in a furnace at 60°C, overnight, for ageing. Following the process of ageing, the particles were centrifuged and redispersed as two equal portions of 10mL each, one in water and the other in ethanol, and stored for further studies.

By varying the sonication time as 5, 10,15, 30, 45 and 60 min, we were able to obtain stable iron oxide nanoparticles of different sizes with similar or comparable magnetic properties without any surfactant or capping agents.

4.3.6 Characterization of 'naked' iron oxide nanoparticles

The as-synthesized MNPs were characterized using various microscopic and spectroscopic techniques such as IR, TEM, XRD. The IR spectra for the various nanoparticles displayed the characteristic stretching mode, ν_{Fe-O}, at 544 cm^{-1} and the hydroxyl stretching mode, $\nu_{O\text{-}H}$, at 3349 cm^{-1} confirming the presence of hydroxyl groups on the SPIONs surface. Fig. 4.12 shows the different particle sizes obtained for the MNPs at different sonication time from the TEM analysis.

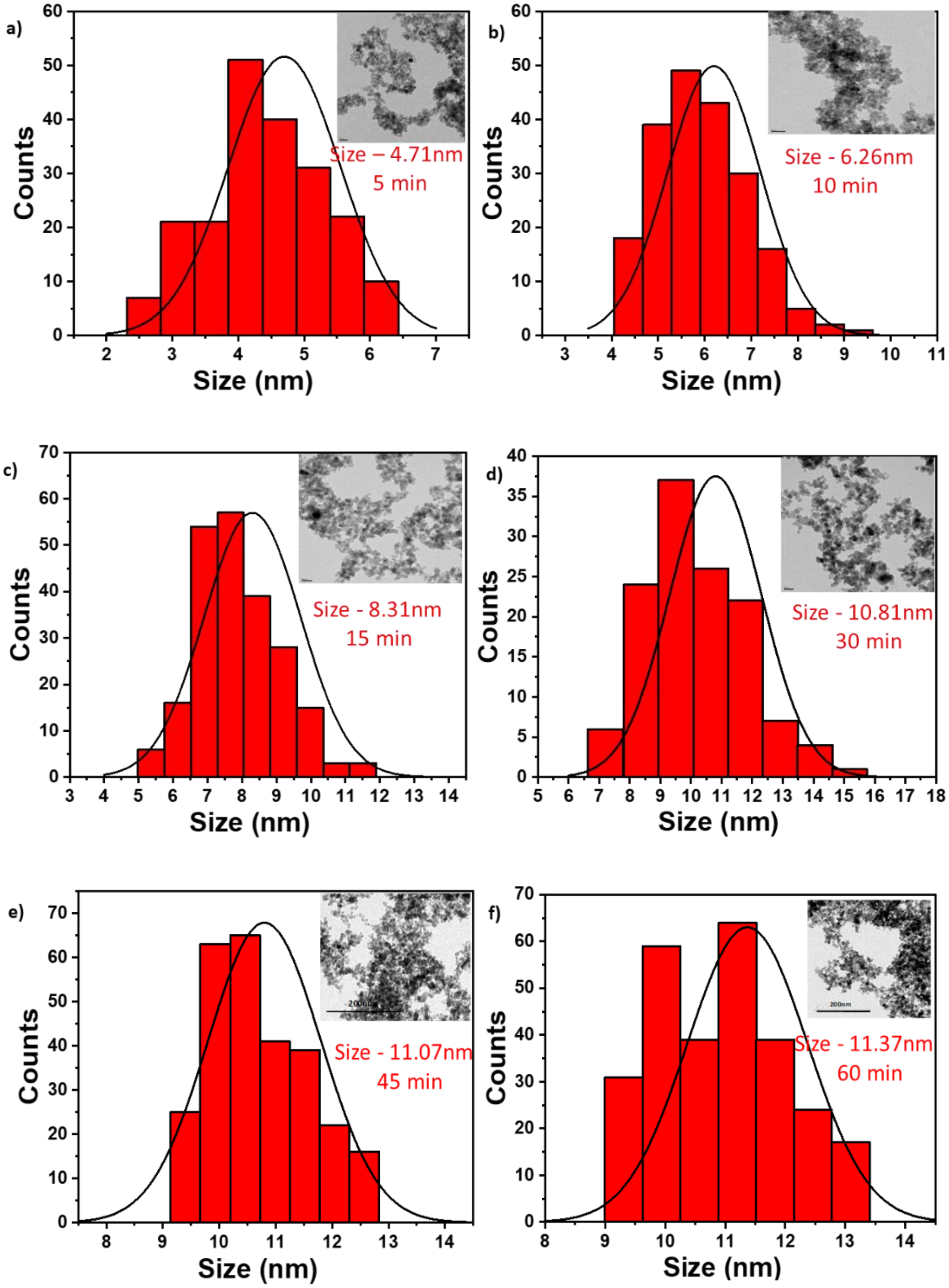

Fig. 4.12 Gaussian depicting the particle size obtained from the TEM images for the different duration of sonication time: **(a)** 5 min; **(b)** 10 min; **(c)** 15 min; **(d)** 30 min; **(e)** 45 min & **(f)** 60 min. (Inset: TEM images for the corresponding sonication time with the scale bar).

From the TEM analysis, it can be observed that the particle size gradually increases with increase in time from 4.71 ± 1.2 nm for 5 min to 11.37 ± 1.3 nm for 60 min of sonication. The gradual increase in size can be attributed to coalescence or Ostwald ripening of smaller particles to attain a more thermodynamically stable state.[61,62] Distinguishably, the increment in the particle size reaches a saturation at 30 min with a mean diameter of 10.81 ± 1.7 nm and henceforth the increment becomes negligible as can be seen in Fig. 4.13(a). The electron diffraction pattern confirms the cubic spinel structure of these MNPs.

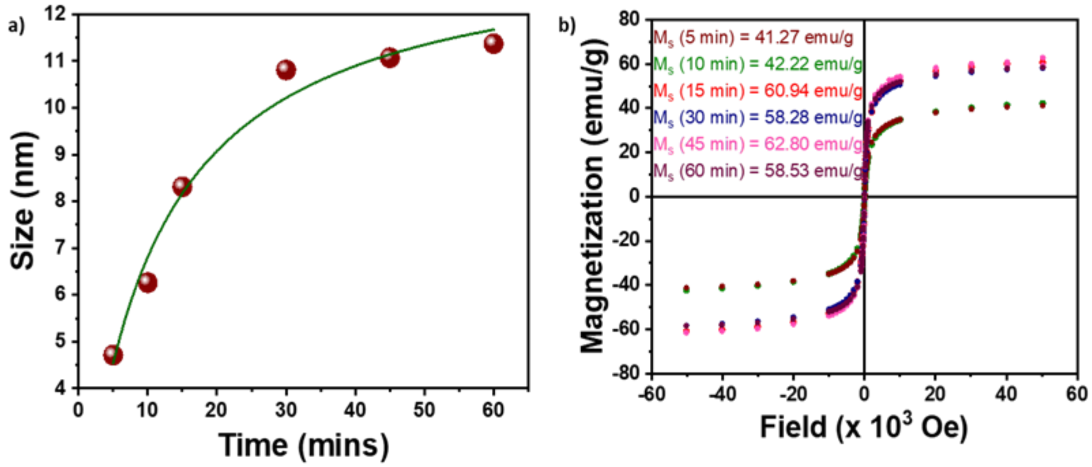

Fig. 4.13 (a) Evolution of the particle size with increase in duration of sonication time. **(b)** Hysteresis curve for the different MNPs at different duration of sonication time measured at 300K.

When the particle size is smaller than the single domain size, the particles exhibit super-paramagnetism. The absence of any hysteresis as well as coercivity observed from the hysteresis curve (Fig. 4.13(b)) confirms that all these particles are superparamagnetic in nature and are indeed SPIONs. A similar trend, as observed for the particle size, can also be observed in the saturation magnetization (M_s) values obtained from the hysteresis curve. The M_s values reaches a steady magnitude of 60 emu/g for particles formed from 15 min of sonication. M_s values of 60 emu/g is considered relatively high for iron oxide magnetic nanoparticles.[63] From these results, a plausible conclusion that we can ascertain is that the minimum size required to attain the maximum M_s value of these particles seems to be obtained with 15 min of sonication. These particles were also readily attracted to an external magnetic field and their re-dispersal into a colloid state, once the external magnetic field was removed. It is also quite remarkable how a clearly visible correlation exists between the size and M_s values of these particles.

Zeta potential (ζ) measurements were carried out in water at pH=7 to study the colloidal stability as well as the surface charge of these particles. As mentioned previously, an absolute zeta potential value greater than 30 mV is indicative of a stable colloid. Fig. 4.14(a) shows the zeta potential values obtained for the different particles. It can be observed that the values are well above 30 mV with minute increase in the values with increasing duration of sonication suggesting that all the particles formed at various duration of sonication are colloidally stable. Particles formed with 60 min of sonication have the highest ζ value of -45.7 mV. The negative surface charge confirms the presence of the hydroxyl groups on the surface of these MNPs which renders the stability to the particles due to repulsive forces and prevents the particles from agglomerating.

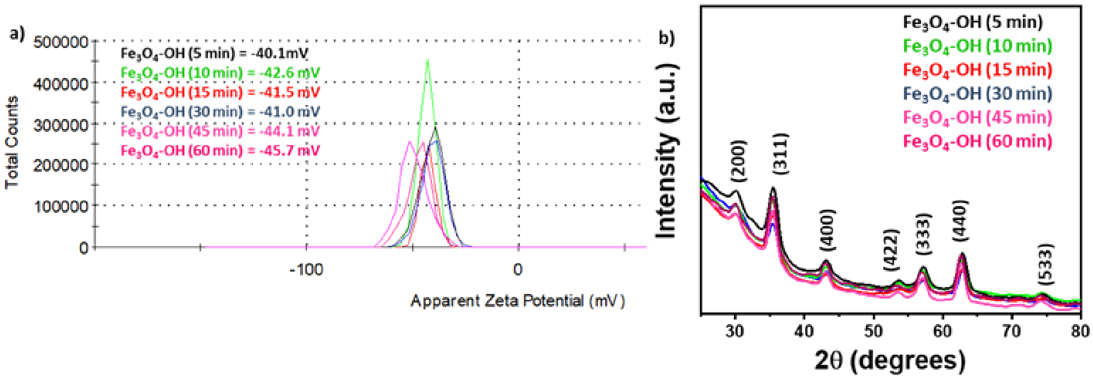

Fig. 4.14 (a) Zeta potential measurements performed in water at pH =7 for the MNPs obtained by different duration of sonication. **(b)** XRD pattern confirming the magnetite structure of the MNPs.

Fig. 4.14(b) shows the XRD pattern for the various particles obtained and it can be observed that the pattern remains nearly same with changes in the intensity suggestive of the differences in particle grain size.[53,54] The XRD pattern confirms the magnetite (Fe_3O_4) structure of the particles.

The particles that were formed by the method of repetitive sonication and centrifugation without any surfactant were highly stable even after ~60 days as can be observed from the zeta potential measurements (Fig. 4.15). Negligible sedimentation of the SPIONs were observed. Achieving colloidal stability has been a challenge faced by many of the synthetic techniques for MNPs and hence, with this procedure we have demonstrated a viable option for the synthesis of stable MNPs.

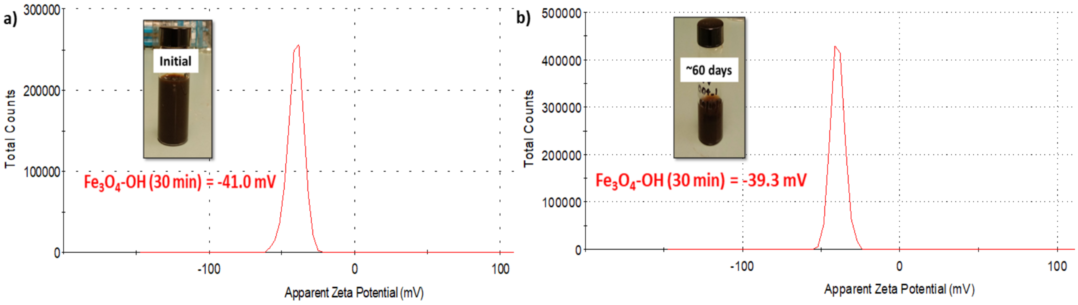

Fig. 4.15 Zeta potential studies performed on MNPs formed by 30 min of sonication measured at **(a)** 0 days & **(b)** ~ 60 days showing negligible change in the zeta potential value.

Table 4.2 summarizes the characteristic properties for the various SPIONs obtained by varying the duration of sonication.

Table 4.2 Summary of the particle characteristics for the various measurements.

Duration of sonication (min)	Size (TEM) (nm)	Magnetization (M_s) (emu/g)	Zeta Potential (ζ) (mV)
5	4.71 ± 1.2	41.27	-40.1
10	6.26 ± 1.6	42.22	-42.6
15	8.31 ± 1.8	60.94	-41.5
30	10.81 ± 1.7	58.28	-41.0
45	11.07 ± 1.1	62.80	-44.1
60	11.37 ± 1.3	58.53	-45.7

From these results, it can be concluded that the method of repetitive sonication and centrifugation can be used for the synthesis of highly stable MNPs with tunable size and saturation magnetization values without any additional non-magnetic layer.

4.3.7 Surface functionalization of 'naked' iron oxide nanoparticles

As stated earlier, these MNPs can be utilized as 'protein mimic' as well as for bio-sensing application if their surface can be modified with amine terminating ligands. Hence, we surface functionalized these MNPs with amine groups using APMS by exploiting the hydroxyl groups present on the surface of these particles. Briefly, 5mL ethanolic solutions of MNPs (Fe_3O_4, 2mL of the stock in ethanol) were sonicated for 10 min in a 25mL round bottom flask. 25%(v/v) of the silane ligand (APMS, 0.5mL) in 2mL ethanol was prepared with the pH adjusted to 11 using few drops of TMAH. The as-prepared ligand solutions were added to the MNP solution drop-wise under continuous stirring. The reaction temperature was raised to 50^{o}C and the mixture was stirred for 5h. Afterwards, the mixture was left for overnight ageing at room temperature. Magnetic decantation was performed with a mix of water and ethanol and the particles were finally suspended in water, with a few drops of 0.1M HCl to impart a positive charge on the surface of the particles, and stored for further experiments.

The process of functionalization of MNPs with the amine ligands is similar for both, the core-shell as well as 'naked' MNPs due to the presence of the hydroxyl groups, with very minute changes. Successful functionalization of the MNPs were confirmed by various techniques. Fig. 4.16 displays the zeta potential measurements carried out for the various particles after amine functionalization. The change in the zeta potential value from + to – indicates the successful surface functionalization of the MNPs with the amine groups. A similar trend as observed for the parent MNPs can be seen with the highest ζ value for particles formed from 30 min of sonication as +47.4 mV. Appreciably, all the particles showed high colloidal stability in par with the parent MNPs.

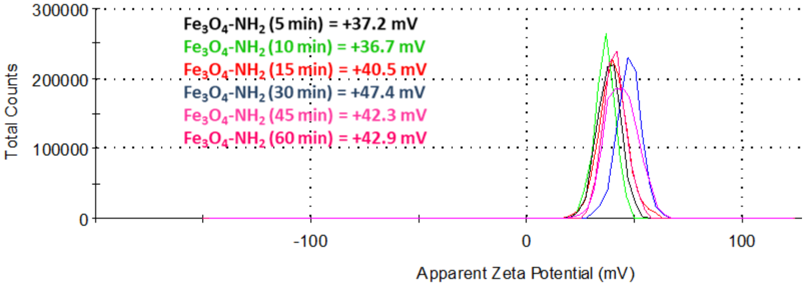

Fig. 4.16 Zeta potential values for the different amine functionalized MNPs.

Fig. 4.17(a) displays the evolution of size as a function of time for the amine functionalized particles. A trend consistent to the 'naked' MNPs is observed even after functionalization indicating that the latter has not altered the physical structure of the MNPs. Comparing the particles, before and after functionalization, a constant increase in size can be observed with approximately 2 nm difference between the corresponding parent particle and the amine functionalized MNPs which can be attributed to the presence of the silane ligand on the surface. The difference in the sizes before and after the functionalization further reinforces the successful functionalization of the surface of the MNP with the non-magnetic layer of amine terminating silane ligands.

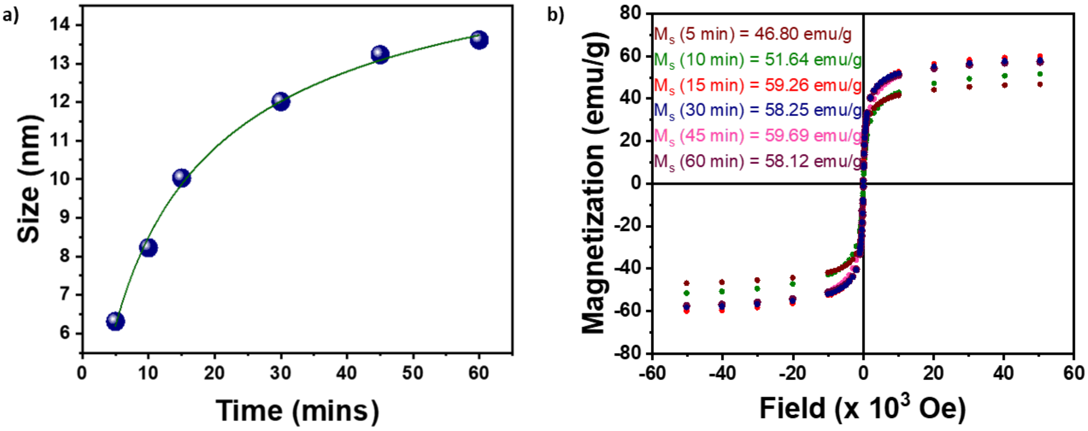

Fig. 4.17 (a) Change in size obtained from TEM analysis for the different amine functionalized MNPs. **(b)** Hysteresis curve for the various amine functionalized MNP s measured at 300K.

The M_S values remains almost unaltered after the functionalization as can be observed from Fig. 4.17(b). The particles are superparamagnetic as can be confirmed due to the lack of hysteresis. The different characteristic properties of the amine functionalized MNPs are summarized in Table 4.3.

Table 4.3 Summary of the characteristic properties of the different amine functionalized MNPs.

Duration of sonication (min)	Size (TEM) (nm)	Magnetization (M_s) (emu/g)	Zeta Potential (ζ) (mV)
5	6.31 ± 1.1	46.80	+37.2
10	8.22 ± 1.2	51.64	+36.7
15	10.03 ± 1.0	59.26	+40.5
30	12.01 ± 1.1	58.25	+47.4
45	13.23 ± 2.0	59.69	+42.3
60	13.61 ± 1.8	58.12	+42.9

All these measurements confirm the successful functionalization of the MNPs with the retention of the magnetic properties as well as the stability. These amine functionalized MNPs can be used for further applications such as mimicking proteins, for sensing applications and many more.

These experiments involving the ‘naked’ MNPs were carried out as part of a EuroMission project – Kardiatool where functionalized MNPs were proposed to be utilized as pre-concentrators for fabricating a lap-on-a-chip point-of-care device.

4.4 Conclusion

In this chapter, we have discussed in detail the characteristic properties and plausible applications of two different types of iron-oxide magnetic nanoparticles: core-shell and ‘naked’ SPIONs, particularly within the scope of integration of metallacarboranes. We have successfully synthesized and characterized these MNPs as well as demonstrated their possible applications. On comparing the key characteristics such as size, stability and magnetic properties, the ‘naked’ iron oxide nanoparticles may seem to be the preferred choice as they have tunable size from 4 – 11 nm, high M_s value of 60 emu/g and high colloidal stability. But it begs to ponder, whether is that all there is. While considering a magnetic nanoparticle for applications such as catalysis more than the magnetic properties and colloidal stability, chemical stability and ease of separation gains more significance. Hence, silica-coated iron-oxide nanoparticles are better suited as a support for a photo-redox catalyst as the silica layer protects the core structure from the harsh reaction conditions and prevents the oxidation of these particles, thereby enhancing the efficiency as well as the reusability of the catalyst. Furthermore, having a low colloidal stability may indeed be a boon in disguise as these MNPs inherently possess a tendency to sediment, they can be easily recovered in shorter time. On the other hand, for applications such as sensing, high M_s and colloidal stability with easily functionalized surface are necessary for the prolonged use of the nanoparticles making the ‘naked’ iron oxide nanoparticles the better choice. Consequently, we can conclude that it is crucial to modify and adapt a system to suit the need.

4.5 References

1 M. Auffan, J. Rose, J.-Y. Bottero, G. V. Lowry, J.-P. Jolivet and M. R. Wiesner, Towards a definition of inorganic nanoparticles from an environmental, health and safety perspective, *Nat. Nanotechnol.*, 2009, **4**, 634–641.

2 D. Guo, G. Xie and J. Luo, Mechanical properties of nanoparticles: basics and applications, *J. Phys. D. Appl. Phys.*, 2013, **47**, 13001.

3 M. G. Bawendi, M. L. Steigerwald and L. E. Brus, The Quantum Mechanics of Larger Semiconductor Clusters (‘Quantum Dots’), *Annu. Rev. Phys. Chem.*, 1990, **41**, 477–496.

4 A. Fernando, K. L. D. M. Weerawardene, N. V Karimova and C. M. Aikens, Quantum Mechanical Studies of Large Metal, Metal Oxide, and Metal Chalcogenide Nanoparticles and Clusters, *Chem. Rev.*, 2015, **115**, 6112–6216.

5 J. A. Scholl, A. L. Koh and J. A. Dionne, Quantum plasmon resonances of individual metallic nanoparticles, *Nature*, 2012, **483**, 421–427.

6 C. N. R. Rao, G. U. Kulkarni, P. J. Thomas and P. P. Edwards, Size-dependent chemistry: properties of nanocrystals. *Chem. Eur. J.*, 2002, **8**, 28–35.

7 J. Ann Maria Xavier, G. Devatha, S. Roy, A. Rao and P. P. Pillai, Electrostatically regulated photoinduced electron transfer in “cationic” eco-friendly CuInS2/ZnS quantum dots in water, *J. Mater. Chem. A*, 2018, **6**,

22248–22255.

8 I. Khan, K. Saeed and I. Khan, Nanoparticles: Properties, applications and toxicities, *Arab. J. Chem.*, 2019, **12**, 908–931.

9 Y. Khan, H. Sadia, S. Z. Ali Shah, M. N. Khan, A. A. Shah, N. Ullah, M. F. Ullah, H. Bibi, O. T. Bafakeeh, N. B. Khedher, S. M. Eldin, B. M. Fadhl and M. I. Khan, Classification, Synthetic, and Characterization Approaches to Nanoparticles, and Their Applications in Various Fields of Nanotechnology: A Review. *Catalysts*, 2022, **12**, 1386.

10 N. V. Long, Y. Yang, T. Teranishi, C. M. Thi, Y. Cao and M. Nogami, Biomedical Applications of Advanced Multifunctional Magnetic Nanoparticles, *J. Nanosci. Nanotechnol.*, 2015, **15**, 10091–10107.

11 K. Trepka and Y. Tao, Magnetic characterization of rare-earth oxide nanoparticles, Magnetic characterization of rare-earth oxide nanoparticles. *Appl. Phys. Lett.*, 2020; **117**, 122410.

12 C. Bouzigues, T. Gacoin and A. Alexandrou, Biological Applications of Rare-Earth Based Nanoparticles, *ACS Nano*, 2011, **5**, 8488–8505.

13 E. Manova, B. Kunev, D. Paneva, I. Mitov, L. Petrov, C. Estournès, C. D'Orléan, J.-L. Rehspringer and M. Kurmoo, Mechano-Synthesis, Characterization, and Magnetic Properties of Nanoparticles of Cobalt Ferrite, CoFe2O4, *Chem. Mater.*, 2004, **16**, 5689–5696.

14 K. Woo, J. Hong, S. Choi, H.-W. Lee, J.-P. Ahn, C. S. Kim and S. W. Lee, Easy Synthesis and Magnetic Properties of Iron Oxide Nanoparticles, *Chem. Mater.*, 2004, **16**, 2814–2818.

15 S. Laurent, D. Forge, M. Port, A. Roch, C. Robic, L. Vander Elst and R. N. Muller, Magnetic Iron Oxide Nanoparticles: Synthesis, Stabilization, Vectorization, Physicochemical Characterizations, and Biological Applications, *Chem. Rev.*, 2008, **108**, 2064–2110.

16 T. Ishizaki, K. Yatsugi and K. Akedo, Effect of Particle Size on the Magnetic

Properties of Ni Nanoparticles Synthesized with Trioctylphosphine as the Capping Agent, *Nanomaterials,* 2016, **6**, 172.

17 M. R. Ahghari, V. Soltaninejad and A. Maleki, Synthesis of nickel nanoparticles by a green and convenient method as a magnetic mirror with antibacterial activities, *Sci. Rep.*, 2020, **10**, 12627.

18 K. K. Senapati, C. Borgohain and P. Phukan, Synthesis of highly stable CoFe2O4 nanoparticles and their use as magnetically separable catalyst for Knoevenagel reaction in aqueous medium, *J. Mol. Catal. A Chem.*, 2011, **339**, 24–31.

19 C. Bolm, A new iron age, *Nat. Chem.*, 2009, **1**, 420.

20 S. Lasocki, T. Gaillard and E. Rineau, Iron is essential for living!, *Crit. Care*, 2014, **18**, 678.

21 C. Kittel, Physical theory of Ferromagnetic Domains, *Reviews of Modern Phys.,* 1949, **21**, 541.

22 C. Wang, C. Wang, X. Gao, M. Tian and Y. Zhang, Research on Microstructure Characteristics of Welded Joint by Magneto-Optical Imaging Method, *Metals*, 2022, **12**, 258.

23 J. Frenkel and J. Doefman, Spontaneous and Induced Magnetisation in Ferromagnetic Bodies, *Nature*, 1930, **126**, 274–275.

24 E. P. Wohlfarth, Magnetic properties of single domain ferromagnetic particles, *J. Magn. Magn. Mater.*, 1983, **39**, 39–44.

25 Q. Li, C. W. Kartikowati, S. Horie, T. Ogi, T. Iwaki and K. Okuyama, Correlation between particle size/domain structure and magnetic properties of highly crystalline Fe3O4 nanoparticles, *Sci. Rep.*, 2017, **7**, 1–4.

26 D. Alcantara and L. Josephson,Chapter 11 in *Nanobiotechnology*, Elsevier, 2012, vol. 4, pp. 269–289.

27 M. Mehrmohammadi, K. Y. Yoon, M. Qu, K. P. Johnston and S. Y. Emelianov,

Enhanced pulsed magneto-motive ultrasound imaging using superparamagnetic nanoclusters, *Nanotechnology*, 2011, **22**, 45502.

28 C. L. DeCastro and B. S. Mitchell, Nanoparticles from mechanical attrition, *Synth. Funct. Surf. Treat. nanoparticles*, 2002, **5**.

29 S. S. Papell, Low viscosity magnetic fluid obtained by the colloidal suspension of magnetic particles Patent.

30 A. L. Willis, N. J. Turro and S. O'Brien, Spectroscopic Characterization of the Surface of Iron Oxide Nanocrystals, *Chem. Mater.*, 2005, **17**, 5970–5975.

31 B. L. Cushing, V. L. Kolesnichenko and C. J. O'Connor, Recent Advances in the Liquid-Phase Syntheses of Inorganic Nanoparticles, *Chem. Rev.*, 2004, **104**, 3893–3946.

32 H.-C. Roth, S. P. Schwaminger, M. Schindler, F. E. Wagner and S. Berensmeier, Influencing factors in the CO-precipitation process of superparamagnetic iron oxide nano particles: A model based study, *J. Magn. Magn. Mater.*, 2015, **377**, 81–89.

33 S. Sun, H. Zeng, D. B. Robinson, S. Raoux, P. M. Rice, S. X. Wang and G. Li, Monodisperse MFe2O4 (M = Fe, Co, Mn) Nanoparticles, *J. Am. Chem. Soc.*, 2004, **126**, 273–279.

34 F. X. Redl, C. T. Black, G. C. Papaefthymiou, R. L. Sandstrom, M. Yin, H. Zeng, C. B. Murray and S. P. O'Brien, Magnetic, Electronic, and Structural Characterization of Nonstoichiometric Iron Oxides at the Nanoscale, *J. Am. Chem. Soc.*, 2004, **126**, 14583–14599.

35 V. Patsula, L. Kosinová, M. Lovrić, L. Ferhatovic Hamzić, M. Rabyk, R. Konefal, A. Paruzel, M. Šlouf, V. Herynek, S. Gajović and D. Horák, Superparamagnetic Fe3O4 Nanoparticles: Synthesis by Thermal Decomposition of Iron(III) Glucuronate and Application in Magnetic Resonance Imaging., *ACS Appl. Mater. Interfaces*, 2016, **8**, 7238–7247.

36 H. Deng, X. Li, Q. Peng, X. Wang, J. Chen and Y. Li, Monodisperse Magnetic

Single-Crystal Ferrite Microspheres, *Angew. Chemie.*, 2005, **44**, 2782–2785.

37 J. Xu, H. Yang, W. Fu, K. Du, Y. Sui, J. Chen, Y. Zeng, M. Li and G. Zou, Preparation and magnetic properties of magnetite nanoparticles by sol–gel method, *J. Magn. Magn. Mater.*, 2007, **309**, 307–311.

38 R. K. Sharma, S. Dutta, S. Sharma, R. Zboril, R. S. Varma and M. B. Gawande, Fe3O4 (iron oxide)-supported nanocatalysts: synthesis, characterization and applications in coupling reactions, *Green Chem.*, 2016, **18**, 3184–3209.

39 D. Wang and D. Astruc, Fast-Growing Field of Magnetically Recyclable Nanocatalysts. *Chem. Rev.*, 2014, **114**, 6949–6985.

40 M. B. Gawande, P. S. Branco and R. S. Varma, Nano-magnetite (Fe3O4) as a support for recyclable catalysts in the development of sustainable methodologies, *Chem. Soc. Rev.*, 2013, **42**, 3371–3393.

41 C. Döpke, T. Grothe, P. Steblinski, M. Klöcker, L. Sabantina, D. Kosmalska, T. Blachowicz and A. Ehrmann, Magnetic Nanofiber Mats for Data Storage and Transfer., *Nanomater.*, 2019, **9**, 92.

42 Y. Gu, G. Valentino and E. Mongeau, Ferrofluid-based reconfigurable optofluidic switches for integrated sensing and digital data storage., *Appl. Opt.*, 2014, **53**, 537–543.

43 G. Reiss and A. Hütten, Applications beyond data storage, *Nat. Mater.*, 2005, **4**, 725–726.

44 J.-S. Im and I.-K. Park, Mechanically Robust Magnetic Fe3O4 Nanoparticle/Polyvinylidene Fluoride Composite Nanofiber and Its Application in a Triboelectric Nanogenerator, *ACS Appl. Mater. Interfaces*, 2018, **10**, 25660–25665.

45 M. Zahn, Magnetic Fluid and Nanoparticle Applications to Nanotechnology, *J. Nanoparticle Res.*, 2001, **3**, 73–78.

46 M. Zeng, D. Huang, P. Wang, D. King, B. Peng, J. Luo, Q. Lei, L. Zhang, L. Wang, A. Shinde, M. Shuai, N. A. Clark and Z. Cheng, Autonomous Catalytic

Nanomotors Based on 2D Magnetic Nanoplates, *ACS Appl. Nano Mater.*, 2019, **2**, 1267–1273.

47 A. M. Gutierrez, T. D. Dziubla and J. Z. Hilt, Recent advances on iron oxide magnetic nanoparticles as sorbents of organic pollutants in water and wastewater treatment., *Rev. Environ. Health*, 2017, **32**, 111–117.

48 A.-I. Stoica, C. Viñas and F. Teixidor, Cobaltabisdicarbollide anion receptor for enantiomer-selective membrane electrodes, *Chem. Commun.*, 2009, 4988–4990.

49 I. Fuentes, J. Pujols, C. Viñas, S. Ventura and F. Teixidor, Dual Binding Mode of Metallacarborane Produces a Robust Shield on Proteins., *Chemistry*, 2019, **25**, 12820–12829.

50 I. Guerrero, A. Saha, J. A. M. Xavier, C. Viñas, I. Romero and F. Teixidor, Noncovalently Linked Metallacarboranes on Functionalized Magnetic Nanoparticles as Highly Efficient, Robust, and Reusable Photocatalysts in Aqueous Medium, *ACS Appl. Mater. Interfaces*, 2020, **12**, 56372–56384.

51 H. Hassani, B. Zakerinasab, M. A. Nasseri and M. Shavakandi, The preparation, characterization and application of COOH grafting on ferrite-silica nanoparticles, *RSC Adv.*, 2016, **6**, 17560–17566.

52 X.-D. Wang, Z.-X. Shen, T. Sang, X.-B. Cheng, M.-F. Li, L.-Y. Chen and Z.-S. Wang, Preparation of spherical silica particles by Stöber process with high concentration of tetra-ethyl-orthosilicate., *J. Colloid Interface Sci.*, 2010, **341**, 23–29.

53 M. M. Can, M. Coşkun and T. Firat, A comparative study of nanosized iron oxide particles; Magnetite (Fe 3O 4), maghemite (γ-Fe 2O 3) and hematite (α-Fe 2O 3), using ferromagnetic resonance, *J. Alloys Compd.*, 2012, **542**, 241–247.

54 M. B. Gawande, A. K. Rathi, J. Tucek, K. Safarova, N. Bundaleski, O. M. N. D. Teodoro, L. Kvitek, R. S. Varma and R. Zboril, Magnetic gold nanocatalyst

(nanocat-Fe-Au): Catalytic applications for the oxidative esterification and hydrogen transfer reactions, *Green Chem.*, 2014, **16**, 4137–4143.

55 A. R. Popescu, F. Teixidor and C. Viñas, Metal promoted charge and hapticities of phosphines: The uniqueness of carboranylphosphines, *Coord. Chem. Rev.*, 2014, **269**, 54–84.

56 P. E. Behnken, D. C. Busby, M. S. Delaney, R. E. I. I. I. King, C. W. Kreimendahl, T. B. Marder, J. J. Wilczynski and M. F. Hawthorne, Metallacarboranes in catalysis. Kinetics and mechanism of acrylate ester hydrogenation catalyzed by closo-rhodacarboranes, *J. Am. Chem. Soc.*, 1984, **106**, 7444–7450.

57 S. P. Fisher, A. W. Tomich, S. O. Lovera, J. F. Kleinsasser, J. Guo, M. J. Asay, H. M. Nelson and V. Lavallo, Nonclassical Applications of closo-Carborane Anions: From Main Group Chemistry and Catalysis to Energy Storage, *Chem. Rev.*, 2019, **119**, 8262–8290.

58 F. Teixidor, M. A. Flores, C. Viñas, R. Sillanpää and R. Kivekäs, exo-nido-Cyclooctadienerhodacarboranes: Synthesis, Reactivity, and Catalytic Properties in Alkene Hydrogenation, *J. Am. Chem. Soc.*, 2000, **122**, 1963–1973.

59 I. Guerrero, Z. Kelemen, C. Viñas, I. Romero and F. Teixidor, Metallacarboranes as Photoredox Catalysts in Water., *Chemistry*, 2020, **26**, 5027–5036.

60 R. Núñez, M. Tarrés, A. Ferrer-Ugalde, F. F. De Biani and F. Teixidor, Electrochemistry and Photoluminescence of Icosahedral Carboranes, Boranes, Metallacarboranes, and Their Derivatives, *Chem. Rev.*, 2016, **116**, 14307–14378.

61 S. T. Gentry, S. F. Kendra and M. W. Bezpalko, Ostwald Ripening in Metallic Nanoparticles: Stochastic Kinetics, *J. Phys. Chem. C*, 2011, **115**, 12736–12741.

62 J. G. Ovejero, M. del P. Morales and S. Veintemillas-Verdaguer, Inductive

Heating Enhances Ripening in the Aqueous Synthesis of Magnetic Nanoparticles, *Cryst. Growth Des.*, 2023, **23**, 59–67.

63 S. M. Dadfar, D. Camozzi, M. Darguzyte, K. Roemhild, P. Varvarà, J. Metselaar, S. Banala, M. Straub, N. Güvener, U. Engelmann, I. Slabu, M. Buhl, J. van Leusen, P. Kögerler, B. Hermanns-Sachweh, V. Schulz, F. Kiessling and T. Lammers, Size-isolation of superparamagnetic iron oxide nanoparticles improves MRI, MPI and hyperthermia performance., *J. Nanobiotechnology*, 2020, **18**, 22.

Chapter 5

5.1 Introduction

One of the greatest challenges of the 21st century is the development of sustainable energy sources without endangering our environment.[1] Intensified demand of energy due exponential growth of population, rapid depletion of fossil fuels and the detrimental effects of over- exploiting non-renewable sources of energy on our environment with growing concerns on the detrimental effect of the greenhouse gases, force our attention towards greener and more sustainable sources of energy.[2] Renewable sources of energy are many: solar, hydro, wind among others; but most of them are non-reliable due to the seasonal and regional variabilities.[3–6] Hence, there is a need for a more permanent and viable alternative.

'Water splitting' is a pivotal chemical process which holds the key to sustainable energy production and environmental preservation. A seemingly simple process of splitting water molecule into its constituent elements, oxygen (O_2) and hydrogen (H_2), has immense potential as it paves way to harvest clean and abundant hydrogen fuel.[7] Hydrogen is considered as the 'fuel of the future' because of its high energy conversion efficiency, environment compatibility and zero CO_2 emission with only water as the by-product in its combustion.[8–13]

Catalytic splitting of water (Eq. 1), even though seemingly easy, is an energetically 'uphill' process with a large positive Gibbs free energy, making the overall reaction non-spontaneous in nature.[14]

$$2H_2O_{(l)} \xrightarrow{\text{cat.}} 2H_{2(g)} + O_{2(g)} \qquad \text{Eq.1}$$

The Gibbs free energy per mol for the process is calculated as:

$$\Delta G^0 = \Delta H - T\Delta S = 285.83\ \text{kJ} - 48.7\ \text{kJ} = +237.1\ \text{kJ}$$

where ΔH is the enthalpy of dissociation and ΔS is the entropy associated with the dissociation of water, considered at 289K and 1 atm.[15,16]

The process occurs via two half reactions: Hydrogen evolution reaction (HER, Eq.2) and Oxygen evolution rection (OER, Eq.3).

$$2H^{+}_{(aq)} + 2e^{-} \longrightarrow H_{2(g)} \qquad \textbf{Eq.2}$$

$$2H_2O_{(l)} \longrightarrow O_{2(g)} + 4H^{+} + 4e^{-} \qquad \textbf{Eq.3}$$

Comparing the half reactions, it can be observed that the OER is four-electrons transfer process with a high energy barrier as it involves the loss of 4 electrons, 4 protons as well as O-O bond formation. Hence, OER is considered as the bottleneck or the rate determining step for the over water splitting process (OWS). Thermodynamically, OER occurs at an energy of 1.23 eV (at pH=0) but to the high demanding electron transfer processes, additional energy is required to drive the OWS (Fig. 5.1). The additional energy required to drive the catalytic process forward can be in the form of either an external excess electrical potential (over-potential) or light known as electrolysis and photolysis, respectively. Since, solar energy is in abundance and is easily accessible while being more sustainable, photocatalytic water splitting has gained considerable attention over the years.[14]

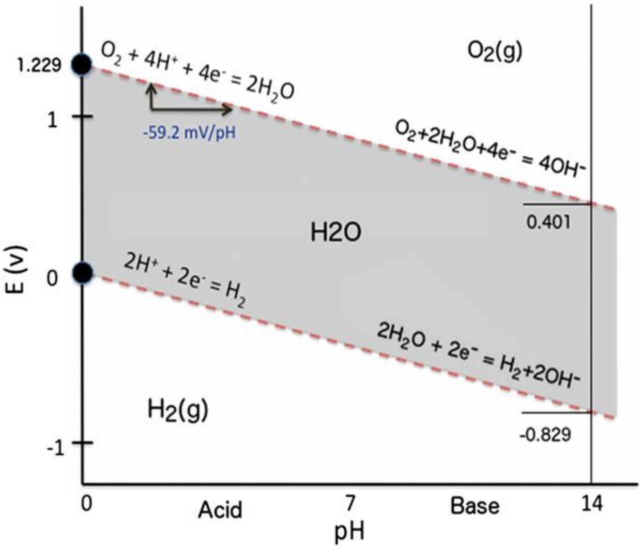

Fig. 5.1 Pourbaix diagram for water plotted with the thermodynamic water-splitting potentials (*vs.* SHE) of HER and OER as a function of pH, including the equilibrium regions for water, hydrogen and oxygen.[17]

5.2 Motivation & Objective

Light induced water splitting is often considered as ‘artificial photosynthesis’ due to its resemblance to natural photosynthesis in terms of production of oxygen and hydrogen using solar energy. In nature, OWS occurs at the photosystem II (PS-II) by the absorption of 4 photons of visible light.[18] The bottleneck process of water oxidation occurs at the oxygen evolving centre (OEC) having four Mn ions and Ca^{2+} (Mn_4CaO_5 cluster) which produces oxygen at rates estimated around 100-400 s^{-1}.[19] Despite several advancements in the field, elucidating the chemistry and replicating the process of water splitting occurring at PS-II has been a challenge. One of the main challenges has been the generation of the singlet oxygen.[20] Singlet oxygen ($^1O_2$) is a highly reactive and powerful oxidizing agent. $^1O2$ is a high-energy form of molecular oxygen (O_2) that results from the excited state of O_2. It is exceptionally reactive and capable of damaging nearby molecules, including organic ligands used in the artificial photosynthesis process. To overcome this challenge, researchers are actively exploring various strategies to mitigate the harmful effects of singlet oxygen.

Besides the production of singlet oxygen, the slow kinetics of the OER demands the need of a catalyst for the process to be feasible. Developing photocatalysts for water splitting was initiated in 1972 with the demonstration of photoelectrochemical (PEC) water splitting using TiO_2 as photoanode and Pt as photocathode with an external bias, known as Honda-Fujishima effect.[21] When a n-type semiconductor such as TiO_2 is illuminated with light having energy greater than its bang gap (E_g), electrons in the valence band (VB) are excited to the conduction band (CB), leaving behind positively charged holes in the VB. On the application of an anodic potential via an external circuit, these electrons migrate through the bulk to the Pt counter electrode where hydrogen reduction occurs while the holes on the surface of TiO_2 oxidize water to form O_2 (Scheme 5.1).[22]

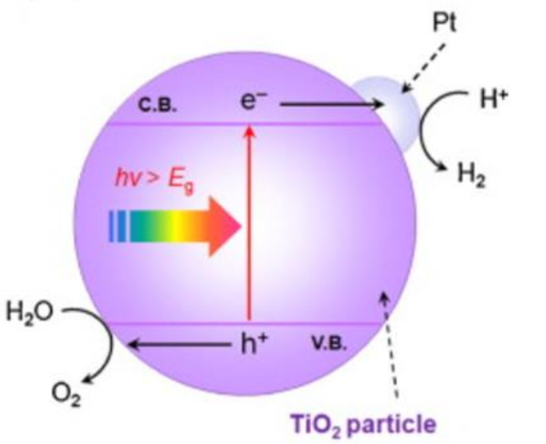

Scheme 5.1 Schematic representation of photocatalytic water splitting occurring on the surface of TiO_2-Pt PEC.[22]

The OWS occurs on the surface of a semi-conductor via three steps: i) absorption of light for the photogeneration of electrons and holes; ii) separation and migration of the photoexcited carriers without recombination; iii) oxidation and reduction of the adsorbed species to produce H_2 and O_2. Several semi-conductor based photocatalysts ranging from macro to nano-sized crystals such as ZnO, CdS, NiO_x among others have been studied and explored.[23]

On the other hand, gaining inspiration from the PS-II, the potential of metal complexes as possible photocatalysts, particularly as water oxidation catalysts (WOC), have also been explored. The goal was to obtain relatively simple metal-containing complexes which combines adequate catalytic activity with appreciable chemical stability.[24] Notably, developments have been made with regard to di- and mono-nuclear ruthenium[25,26], manganese[25,27], cobalt[28,29] and iridium[30,31] complexes as well as a better understanding of their mechanisms for O-O bond formations such as water nucleophilic attack of metal-oxo and direct coupling of two metal-oxos since the development of the first well-defined WOC molecule, 'blue-dimer' with $Ru^{V}ORu^{V}$ as the active catalyst by Meyer and co-workers.[32] These have been reported to have high efficiencies owing the synthetic versatility of transition metal complexes where the coordination sphere of the metal centre can be tuned to exert supramolecular interactions, local acid-base enhancements and hydrogen-bonding effects.[33,34]

As mentioned above, semi-conductors and coordination compounds have been explored over the years as active photocatalysts for water splitting. Nevertheless, they are not with their short-comings. In the case of semi-conductors, a major challenge encountered while considering the efficiency as a photocatalyst is the effectiveness of charge separation and frequency of charge recombination. As the photoexcited species formed are of same masses and opposite charges, following Coulomb's force of attraction, they have a high tendency to recombine. Hence, charge separation becomes a crucial aspect for their successful operation. Now, if we were to consider metal complexes, due to the presence of organic ligands, they have poor chemical stability. In both the cases, sacrificial agents are required to complete the process. Moreover, a single entity never performs the complete OWS, they always work in tandem with a co-catalyst such as Pt, Au etc. As a result, the process becomes high maintenance with high cost.

Hence, it would be ideal if a single molecule is able to perform the complete OWS without the need of any co-catalyst or sacrificial agent, only using light. Virtues of cobalta-bis(dicarbollide), [*o*-COSAN]$^-$, have been discussed throughout the thesis as possessing well-defined redox properties[35], as a bio-sensor[36,37], as surfactants[38] as well as a photocatalyst[39]. Of these, the ability of [*o*-COSAN]$^-$ to perform as a homogenous as well as heterogenous (Chapter 4) photocatalyst for the oxidation of alcohols probed us to ponder on its potential as a photocatalyst for water splitting reaction. The ability of [*o*-COSAN]$^-$ as a redox-active electrolyte for the electrolysis of water have previously been investigated in the group. We have also demonstrated the potential application of [*o*-COSAN]$^-$ and its chlorine derivatives in conjugation with the conducting polymer poly(3,4-ethylenedioxythiophene), PEDOT, as electrocatalysts for water oxidation reaction.[40] Therefore, this chapter would explore the possibility of [*o*-COSAN]$^-$ as a 'single' molecule photocatalyst for complete water splitting without any sacrificial agent or co-catalyst, using only light.

5.3 Results & Discussion

[*o*-COSAN]$^-$ exists as three different rotamers: *cisoid*, *gauche* and *transoid* isomers with their relative population in water at 298K as 85.8%, 12.8% and 1.4%.[41] Thus, the thermodynamically stable rotamer is the *cisoid* in water. The different rotamers are distinguished in terms of the relative position of their carbon atoms in the carborane cluster (Fig. 5.2).

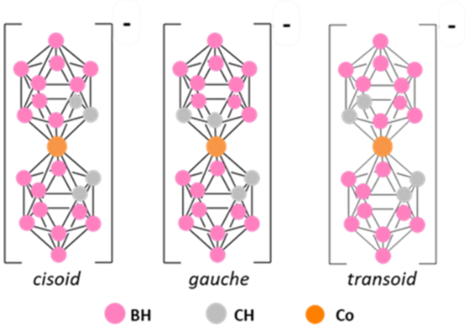

Fig. 5.2 The different rotamers of [*o*-COSAN]$^-$: *cisoid, gauche* and *transoid.*

The UV-vis spectra for 0.1 mM Na[*o*-COSAN]$^-$ was recorded in water as well as acetone (Fig. 5.3). The spectrum displays an intense band at 293 nm which has been attributed to the *transoid* rotamer and two weaker ones at 345 nm and 446 nm where the latter has been ascribed solely to the triplet absorptions of the *cisoid* isomers.[42] These conclusions were attained from theoretical and DFT studies. The obtained values are in agreement with the literature and is interpreted using ligand-field theory wherein d^6 metallocenes exhibit three spin allowed *d-d* transitions.[43] Upon investigating, it was found that the three rotamers exhibit identical electronic properties.

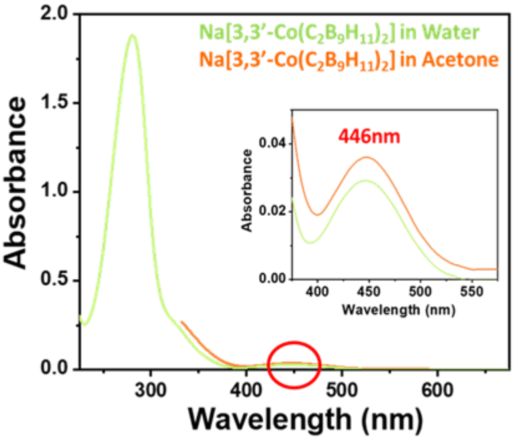

Fig. 5.3 UV-Visible spectrum of 0.01 mM Na[*o*-COSAN] measured in water as well as acetone. [Inset: Enlarged absorption peaks at 446 nm].

Previously, through DFT studies we had demonstrated that upon irradiation of [*o*-COSAN]$^-$, the electrons are excited mainly from orbitals exhibiting more ligand-like character to rather metal-centre based LUMO and LUMO+1 as the ligand is based on the metalloid element, B.[39] Hence, upon irradiation of [*o*-COSAN]$^-$, ligand-to-metal charge transfer (LMCT) takes place which can be attributed as a consequence of the electronegative difference of the bonding elements ($\chi_{Co} - \chi_{B} = -0.16$), the negative charge of the carboranyl ligands and the overall negative charge of the complex. For an efficient photocatalyst for water splitting, it has also been stated that the band gap should not be lower than 1.6 eV and in case of [*o*-COSAN]$^-$, the HUMO-LUMO band gap is estimated to be around 3.5 eV.[39]

We have also studied the non-radiative decay mechanism of [*o*-COSAN]$^-$ by performing 3D-fluorescence experiments (Fig. 5.4). The experiments were performed in a Cary Eclipse fluorescence spectrophotometer. The samples were excited from 300 – 500 nm with an increment of 10 nm per measurement using a slit width of 5. The spectra were recorded from 320 – 580 nm for both the samples as well as the solvent, water. The experiments were referenced to the benchmark fluorophore, quinine sulphate.

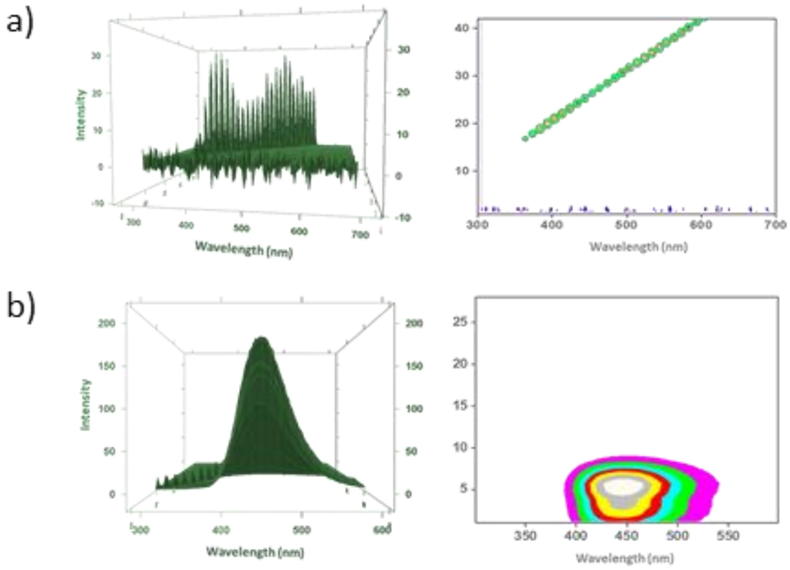

Fig. 5.4 3D fluorescence spectrums of **(a)** Na[*o*-COSAN] & **(b)** Quinine sulphate in water where the fluorescence maximum for quinine sulphate can be observed at 461 nm.

Ligand to metal charge transfer along with lack of fluorescence hints the successful application of [*o*-COSAN]$^-$ as a 'single' molecule photocatalyst for water splitting.

5.3.1 Photocatalytic water splitting using [*o*-COSAN]$^-$

10 mM Na[*o*-COSAN] in 3 mL aqueous solution was prepared in a quartz tube. The tube was degassed and sealed using paraffin. Subsequently, the tubes were placed in a photoreactor having lamps of λ = 350 nm and irradiated for 4 h. After 4 h of irradiation, bubbles were observed in the tubes which hinted the possibility of water splitting (Fig. 5.5).

Fig. 5.5 displays the optical images of the tubes where the formation of bubbles can be observed. Formation of bubbles indicates the presence of gaseous molecules. Bubbles are formed when the solubility of the dissolved gases exceeds its limit in water and therefore, the gaseous molecules aggregate to form bubbles.[44]

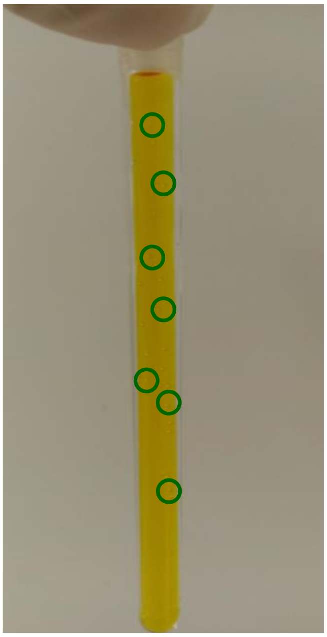

Fig. 5.5 Optical photograph of a sealed quartz tube containing 10 mM Na[*o*-COSAN] in aqueous solution after 4 h of irradiation using 350 nm lamps displaying bubble formation (~ 50 bubbles) encircled in green.

MALDI-TOF was performed on the sample after irradiation and it was seen that the m/z value (324.23) of Na[*o*-COSAN] was retained indicating that the photocatalyst remained unaltered after the catalysis. Similar experiment was also performed using ferra-bis(dicarbollide), [*o*-FESAN]$^-$ but no bubbles were observed suggesting the presence of a fundamental difference between the electronic properties of [*o*-FESAN]$^-$ and [*o*-COSAN]$^-$ (Fig. 5.6a).

As molecular oxygen is known as an efficient fluorescence quencher, an experiment was devised wherein a fluorophore was added to the catalytic mixture and then irradiated. Fluorescein with a bright green fluorescence with negligible absorbance in the UV region was chosen as the organic dye for the experiment as previously we had used a similar experimental set-up to study the electrocatalytic activity of [*o*-COSAN]$^-$ for water oxidation.[40] A mother solution of 1 mg of fluorescein in 5 mL water was prepared. From the stock solution, 300 μL was added to the tube with similar experimental conditions as mentioned earlier. The tube was then placed in the photoreactor for 4 h with 350 nm irradiation. The bubbles formation was monitored hourly and it was observed that the formation of bubbles began after 2 h of irradiation in the tube containing Na[*o*-COSAN] alone and later (~4 h) for Na[*o*-COSAN] with fluorescein. After 4 h, it was observed that the tube with the fluorescein had fewer bubbles (~1/5th) in comparison to the one without the dye (Fig. 5.6b). The absence of bubbles is consistent with involvement of the produced O_2 in fluorescence quenching. Blank experiments with water alone were also performed to eliminate the possibility of bubble formation due to the heat from the lamps.

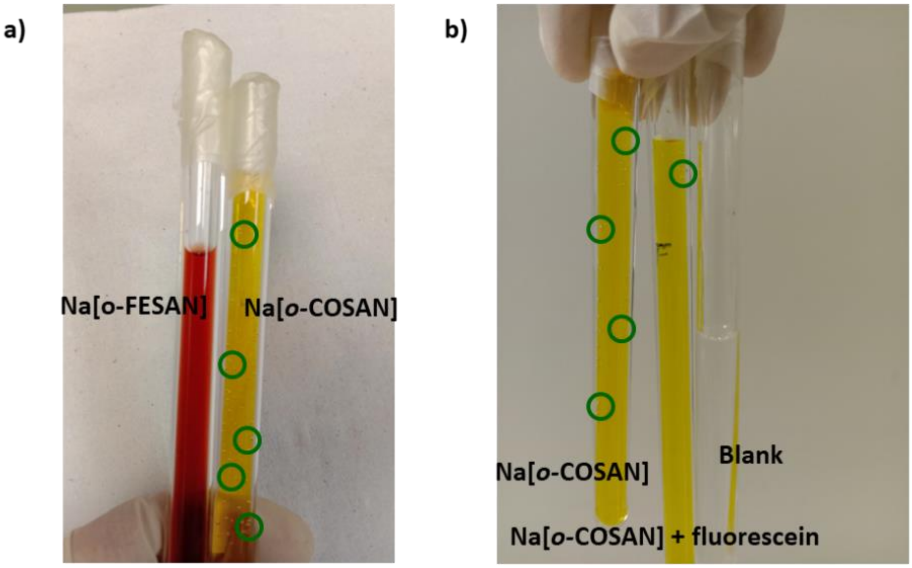

Fig. 5.6 (a) Photocatalytic water splitting using Na[*o*-COSAN] and Na[*o*-FESAN]. **(b)** Photocatalytic water splitting using Na[*o*-COSAN] and Na[*o*-COSAN] with fluorescein along with blank tube containing only water where no bubbles can be seen. The bubbles formed are encircled in green.

5.3.2 Evidence for photocatalytic water splitting using [*o*-COSAN]$^-$

As mentioned earlier as well as in the previous chapter, we had studied the photocatalytic property of [*o*-COSAN]$^-$ for the oxidation of alcohols. The reaction yielded products with high efficiency and high turn-over number (TON), greater 99% and the catalyst could be recycled. Notably, it was also observed that the reaction proceeded only in aqueous solution and not in organic solvents such as acetonitrile indicating the significance of water in the photocatalysis. A reaction mechanism was postulated for the same where it was observed that the oxidation of alcohols occurred via the exchange of two electrons and two protons.[39] Nevertheless, these experiments were performed in presence of a sacrificial agent, $Na_2S_2O_8$, and a base.

With these experiments showcasing the photocatalytic activity of Na[*o*-COSAN], we proposed to utilize the same experimental conditions without the sacrificial agent and base to ascertain the splitting of water by [*o*-COSAN]$^-$. The absence of a sacrificial agent ensured that the only source of oxygen is the oxygen evolved as a result of photolysis. A general photocatalytic experiment involved a sealed quartz tube containing 10 mM of Na[*o*-COSAN] in 5 mL water with 20 mM of 1-phenylethanol exposed to UV irradiation of 352 nm for 4 h, unless stated otherwise (Scheme 5.2). The substrate is added to the reaction mixture at different times depending on the experiment. The reaction product, acetophenone, was characterized and quantified using ^{1}H-NMR spectroscopy.

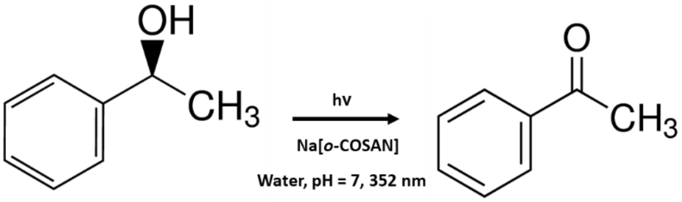

Scheme 5.2 Representation of the photocatalytic oxidation of 1-phenyethanol to acetophenone using Na[*o*-COSAN] without any sacrificial agent.

As expected, the reaction yields were lower in comparison to the previous involving sacrificial agent. Nevertheless, the following experiments were carried out:

1. With and without light

   The photocatalytic oxidation of 1-phenylethanol was carried out in the absence and presence of irradiation. In the experiment with light, the substrate was added after 4 h of irradiation to the reaction tube. Subsequently, the reaction mixture was illuminated further for another 4 h (total reaction time – 8h) and the reaction products were characterized. It was observed that the yield in the presence of light was 2.62 ± 0.1 % while in the absence was 1 ± 0.08 %. This experiment confirmed that the reaction indeed proceeded in the presence of light with Na[*o*-COSAN] alone as well as necessity of light for the reaction.

2. Variation of ratio of substrate:catalyst and the time of introduction of substrate

   Experiments involving different ratio of substrate:catalyst were performed, 2:1 and 300:1, in order to understand the difference in the amount of oxygen produced from the photocatalysis. From the reaction yields, it can be observed that at both the catalyst concentrations similar yield % were obtained (Fig. 5.7). Hence, the photocatalytic reaction occurs even at lower photocatalyst concentration.

   Varying the time of introduction of substrate was performed to understand the difference in dissolved oxygen at the beginning and after 4 h of irradiation. Catalysis can only be performed by dissolved oxygen and from these experiments it was observed that when the substrate was added initially, without the preconcentration of oxygen by irradiating the reaction mixture for 4 h, the yield % was slightly lower (2.04 ± 0.25%) in comparison to the addition of substrate after the generation of photocatalytic oxygen (Fig. 5.7). The experiment confirms a higher amount of oxygen after irradiation for 4 h in the tubes indicating successful photocatalysis of water.

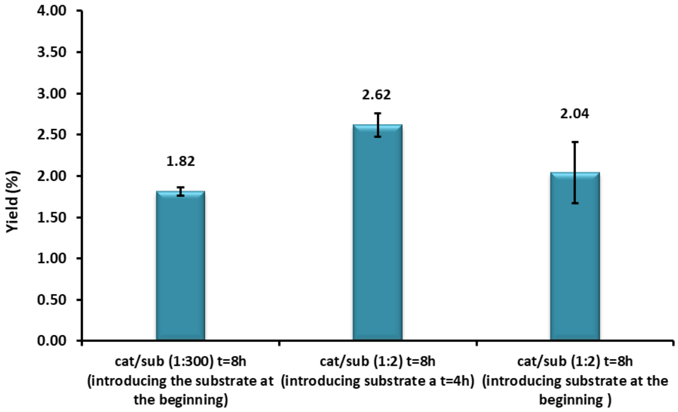

Fig. 5.7 Effect of varying the catalyst concentration and time of introduction of substrate on the photooxidation of 1-phenylethanol using Na[*o*-COSAN].

3. Varying the reaction time

In order to estimate an optimal time of irradiation to produce maximum oxygen, the reaction time were varied by varying the time of irradiation. In these experiments, illumination time were varied as 1, 2, 4, 8 and 16 h before the addition of the substrate. Once the substrate was added all the reactions were irradiated further for 4 h more.

From Fig. 5.8, it can be observed that the highest yield of 2.62 ± 0.1 % was obtained for 4 h of irradiation followed by 12 h with 1.86 ± 0.22 %. The distribution of the yield% for various duration of irradiation forms a Gaussian with the peak at 4 h.

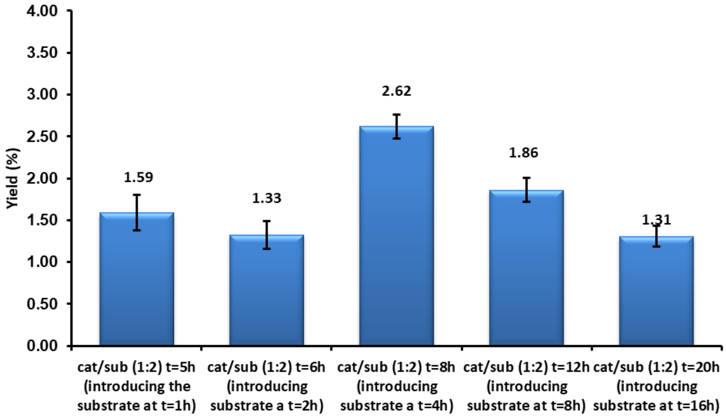

Fig. 5.8 Effect of varying the duration of irradiation before the addition of the substrate.

4. Varying the pH of the solution

pH of the media is important for the OWS as mentioned in the introduction. In order to elucidate the effect of acidic and alkaline conditions, photocatalytic experiments were performed in presence of an acid and/or a base (Fig. 5.9). Interestingly, it was observed that in acidic media the product yield was significantly higher than in neutral pH. To further reinforce the result, the experiments were repeated with two different acids (1 M HCl and 0.5 M H_2SO_4) and a mean yield of ~10% was obtained in both the cases. However, in case of alkaline pH (1 M NaOH) a significant reduction in the product yield was observed. Speculatively, the pH seems to influence the reaction pathway but the explicit reason for the observation is yet to be ascertained.

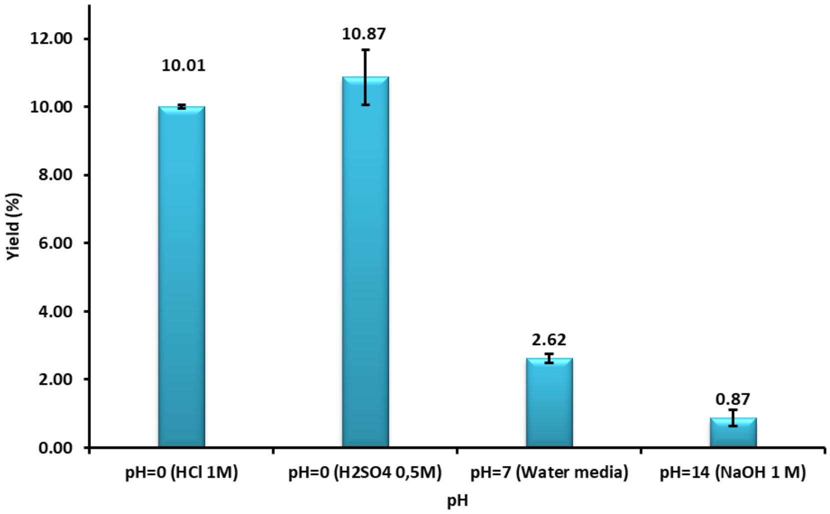

Fig. 5.9 Effect of varying pH on the photocatalytic oxidation of 1-phenylethanol to acetophenone using Na[*o*-COSAN].

5. Closed *vs*. Open system

In order to understand the effect of an open system, the general photocatalytic experiment was performed without the paraffin seal. The experiments were performed in both neutral and acidic pH for 17 h. Upon performing the experiment, it was observed that the product yield decreased drastically for the reaction in acid pH while a significant depletion was also observed in neutral pH. Even after 17 h of reaction time, the mean product yield was ~1. 3%, lower than the closed system reaction yields and comparable to the blank experiments. Hence, it is equivalent to zero production of oxygen. Consequently, it can be rationalized that the oxygen generated by the photocatalysis of water escapes from the reaction tube, thereby lowering the amount of available oxygen for the photooxidation reaction.

Table 5.1 summarizes the results obtained for the various experiments, each of the experiments is repeated twice and the blank experiment is performed for all. From these experiments, we can affirmatively confirm the production of oxygen by the photocatalysis of water using [*o*-COSAN]$^-$.

Table 5.1 Summary of the product yields for the various reaction conditions studied.

Experiments	Yields (%)					
pH 7						
cat/sub (1:300) t=8h (introducing the substrate at the beginning)	1.85	1.78	cat/sub(1:300) (Blank)	0.94	0.89	
cat/sub (1:2) t=8h (introducing substrate at t=4h)	2.52	2.72	cat/sub(1:2) (Blank)	0.91	1.06	1.06
cat/sub (1:2) t=8h (introducing substrate at the beginning)	1.78	2.3			1.09	0.8
pH 7 (oxigen saturation exp.)						
cat/sub (1:2) t=5h (introducing substrate at t=1h)	1.74	1.44	cat/sub(1:2) (Blank)		0.76	
cat/sub (1:2) t=6h (introducing substrate at t=2h)	1.44	1.21			0.62	
cat/sub (1:2) t=12h (introducing substrate at t=8h)	1.96	1.76			0.67	
cat/sub (1:2) t=20h (introducing substrate at t=16h)	1.40	1.22			0.62	
pH 0 (HCl 1M)						
cat/sub (1:2) t=8h (introducing substrate at t=4h)	10.04	9.97	cat/sub(1:2) (Blank)		0.65	
	16.13	14.89				
cat/sub (1:300) t=8h (introducing substrate at t=4h)	3.60	4.67			0.64	
pH 0 (H_2SO_4 0.5 M)						
cat/sub (1:2) t=8h (introducing substrate at t=4h)	10.30	11.44	cat/sub(1:2) (Blank)		0.64	
pH 14 (NaOH 1M)						
cat/sub (1:2) t=8h (introducing substrate at t=4h)	1.03	0.70	cat/sub(1:2) (Blank)		0.74	
OPEN TUBES (air atmosphere contact)						
pH 0 (HCl 1M)						
cat/sub (1:2) t=17h (introducing substrate at t=4h)	1.46					
pH 7						
cat/sub (1:2) t=17h (introducing substrate at t=4h)	1.31					

5.4 Conclusions

In this chapter, we have extensively discussed the potential application of [*o*-COSAN]$^-$ as a single molecule photocatalyst for water splitting, without any sacrificial agent and only using light. Considering that the water oxidation half reaction, provides the electrons and protons required for the second half reaction, i.e. water reduction, it is evident that [*o*-COSAN]$^-$ is able to catalyse both the reactions. On the contrary, the current existing photocatalysts require a co-catalyst for hydrogen evolution. We have demonstrated using the photo-oxidation reaction of alcohol to ketone, the successful OER by [*o*-COSAN]$^-$ in varying reaction conditions. The ability of [*o*-COSAN]$^-$ to perform complete OWS by over-coming the high barrier possessed by the sluggish OER can be viewed as a virtue of its ability to self-assemble. Previously in chapter 2, we have discussed the self-assembling ability of [*o*-COSAN]$^-$ in water to form aggregates depending on the concentrations in nanoscale dimensions. Hence, these nano-aggregates of [*o*-COSAN]$^-$ in water can be visualized as 'nanoscale photoreactors' wherein multiple oxidation/reduction reaction centres are available. As a result, along with its electronic properties, [*o*-COSAN]$^-$ is able to perform as both a water oxidation and reduction centre. Understandably, the study requires further investigations to postulate a reaction mechanism as well as to develop a method to quantify and separate the gases formed to be able to be practically available. Nevertheless, it can be stated that [*o*-COSAN]$^-$ is able to perform complete water splitting as a single entity only using light, undoubtedly. We have demonstrated the use of oxidation of alcohols as an indirect method for the detection of available oxygen in a system.

5.5 References

1 Z. W. Seh, J. Kibsgaard, C. F. Dickens, I. Chorkendorff, J. K. Nørskov and T. F. Jaramillo, Combining theory and experiment in electrocatalysis: Insights into materials design, *Science (80-.).*, 2017, **355**, 4998.

2 M. A. Rosen, Energy Sustainability with a Focus on Environmental Perspectives., *Earth Syst. Environ.*, 2021, **5**, 217–230.

3 S. Baskutis, J. Baskutiene, V. Navickas, Y. Bilan and W. Cieśliński, *Energies*,

2021, **14**.

4 F. A. Farret and M. G. Simões, *Integration of alternative sources of energy*, Wiley Online Library, 2006, 504.

5 D. Gielen, F. Boshell, D. Saygin, M. D. Bazilian, N. Wagner and R. Gorini, The role of renewable energy in the global energy transformation, *Energy Strateg. Rev.*, 2019, **24**, 38–50.

6 P. A. Owusu and S. Asumadu-Sarkodie, A review of renewable energy sources, sustainability issues and climate change mitigation, *Cogent Eng.*, 2016, **3**, 1167990.

7 H. Schwarz, On the usefulness of useless knowledge, *Nat. Rev. Chem.*, 2017, **1**, 1.

8 Q. Hu, G. Li, G. Li, X. Liu, B. Zhu, X. Chai, Q. Zhang, J. Liu and C. He, Trifunctional Electrocatalysis on Dual-Doped Graphene Nanorings–Integrated Boxes for Efficient Water Splitting and Zn–Air Batteries, *Adv. Energy Mater.*, 2019, **9**, 1803867.

9 N. Armaroli and V. Balzani, The Hydrogen Issue, *ChemSusChem*, 2011, **4**, 21–36.

10 J. M. Ogden, Hydrogen: The Fuel of the Future?, *Phys. Today*, 2002, **55**, 69–75.

11 Y. Gong, Y. Zhi, Y. Lin, T. Zhou, J. Li, F. Jiao and W. Wang, Controlled synthesis of bifunctional particle-like Mo/Mn-NixSy/NF electrocatalyst for highly efficient overall water splitting, *Dalt. Trans.*, 2019, **48**, 6718–6729.

12 W. Wang, M. Xu, X. Xu, W. Zhou and Z. Shao, Perovskite Oxide Based Electrodes for High-Performance Photoelectrochemical Water Splitting, *Angew. Chemie Int. Ed.*, 2020, **59**, 136–152.

13 Y. Yan, T. He, B. Zhao, K. Qi, H. Liu and B. Y. Xia, Metal/covalent–organic frameworks-based electrocatalysts for water splitting, *J. Mater. Chem. A*, 2018, **6**, 15905–15926.

14 S. Lin, H. Huang, T. Ma and Y. Zhang, Photocatalytic Oxygen Evolution from Water Splitting, *Adv. Sci.*, 2021, **8**, 2002458.

15 A. Raveendran, M. Chandran and R. Dhanusuraman, A comprehensive review on the electrochemical parameters and recent material development of electrochemical water splitting electrocatalysts, *RSC Adv.*, 2023, **13**, 3843–3876.

16 V. D. Schroeder, *An introduction to thermal physics*, London Addison Wesley Longman, Addison Wesley Longman SE -, 2000.

17 G. W. VanLoon and S. J. T. A.-T. T.- Duffy, *Environmental Chemistry: A global prespective,* 2005, Oxford press, 3ed.

18 Y. Umena, K. Kawakami, J.-R. Shen and N. Kamiya, Crystal structure of oxygen-evolving photosystem II at a resolution of 1.9 Å, *Nature*, 2011, **473**, 55–60.

19 G. C. Dismukes, R. Brimblecombe, G. A. N. Felton, R. S. Pryadun, J. E. Sheats, L. Spiccia and G. F. Swiegers, Development of Bioinspired Mn4O4–Cubane Water Oxidation Catalysts: Lessons from Photosynthesis, *Acc. Chem. Res.*, 2009, **42**, 1935–1943.

20 A. Krieger-Liszkay, Singlet oxygen production in photosynthesis., *J. Exp. Bot.*, 2005, **56**, 337–346.

21 A. Fjuishima and K. Honda, Electrochemical Photolysis of Water at a Semiconductor Electrode, *Nature*, 1972, **238**, 37–38.

22 K. Maeda, Photocatalytic water splitting using semiconductor particles: History and recent developments, *J. Photochem. Photobiol. C Photochem. Rev.*, 2011, **12**, 237–268.

23 N. Serpone and A. V Emeline, Semiconductor Photocatalysis — Past, Present, and Future Outlook, *J. Phys. Chem. Lett.*, 2012, **3**, 673–677.

24 L. Duan, F. Bozoglian, S. Mandal, B. Stewart, T. Privalov, A. Llobet and L. Sun, A molecular ruthenium catalyst with water-oxidation activity comparable to

that of photosystem II, *Nat. Chem.*, 2012, **4**, 418–423.

25 H. Dau, C. Limberg, T. Reier, M. Risch, S. Roggan and P. Strasser, The mechanism of water oxidation: from electrolysis via homogeneous to biological catalysis, *ChemCatChem*, 2010, **2**, 724–761.

26 S. Romain, L. Vigara and A. Llobet, Oxygen–Oxygen Bond Formation Pathways Promoted by Ruthenium Complexes, *Acc. Chem. Res.*, 2009, **42**, 1944–1953.

27 C. S. Mullins and V. L. Pecoraro, Reflections on small molecule manganese models that seek to mimic photosynthetic water oxidation chemistry, *Coord. Chem. Rev.*, 2008, **252**, 416–443.

28 D. J. Wasylenko, C. Ganesamoorthy, J. Borau-Garcia and C. P. Berlinguette, Electrochemical evidence for catalyticwater oxidation mediated by a high-valent cobalt complex, *Chem. Commun.*, 2011, **47**, 4249–4251.

29 Q. Yin, J. M. Tan, C. Besson, Y. V Geletii, D. G. Musaev, A. E. Kuznetsov, Z. Luo, K. I. Hardcastle and C. L. Hill, A fast soluble carbon-free molecular water oxidation catalyst based on abundant metals, *Science.*, 2010, **328**, 342–345.

30 N. D. McDaniel, F. J. Coughlin, L. L. Tinker and S. Bernhard, Cyclometalated iridium (III) aquo complexes: efficient and tunable catalysts for the homogeneous oxidation of water, *J. Am. Chem. Soc.*, 2008, **130**, 210–217.

31 J. F. Hull, D. Balcells, J. D. Blakemore, C. D. Incarvito, O. Eisenstein, G. W. Brudvig and R. H. Crabtree, Highly active and robust Cp* iridium complexes for catalytic water oxidation, *J. Am. Chem. Soc.*, 2009, **131**, 8730–8731.

32 S. W. Gersten, G. J. Samuels and T. J. Meyer, Catalytic oxidation of water by an oxo-bridged ruthenium dimer, *J. Am. Chem. Soc.*, 1982, **104**, 4029–4030.

33 C. W. Chronister, R. A. Binstead, J. Ni and T. J. Meyer, Mechanism of Water Oxidation Catalyzed by the µ-Oxo Dimer [(bpy)2(OH2)RuIIIORuIII(OH2)(bpy)2]4+, *Inorg. Chem.*, 1997, **36**, 3814–3815.

34 F. Liu, J. J. Concepcion, J. W. Jurss, T. Cardolaccia, J. L. Templeton and T. J. Meyer, Mechanisms of Water Oxidation from the Blue Dimer to Photosystem II, *Inorg. Chem.*, 2008, **47**, 1727–1752.

35 J. A. M. Xavier, C. Viñas, E. Lorenzo, T. García-Mendiola and F. Teixidor, Potential application of metallacarboranes as an internal reference: an electrochemical comparative study to ferrocene, *Chem. Commun.*, 2022, **58**, 4196–4199.

36 A.-I. Stoica, C. Kleber, C. Viñas and F. Teixidor, Ion selective electrodes for protonable nitrogen containing analytes: Metallacarboranes as active membrane components, *Electrochim. Acta*, 2013, **113**, 94–98.

37 A.-I. Stoica, C. Viñas and F. Teixidor, Cobaltabisdicarbollide anion receptor for enantiomer-selective membrane electrodes, *Chem. Commun.*, 2009, 4988–4990.

38 C. Viñas, M. Tarrés, P. González-Cardoso, P. Farràs, P. Bauduin and F. Teixidor, Surfactant behaviour of metallacarboranes. A study based on the electrolysis of water, *Dalt. Trans.*, 2014, **43**, 5062–5068.

39 I. Guerrero, Z. Kelemen, C. Viñas, I. Romero and F. Teixidor, Metallacarboranes as Photoredox Catalysts in Water., *Chemistry*, 2020, **26**, 5027–5036.

40 J. A. Maria Xavier, I. Fuentes, M. Nuez-Martínez, Z. Kelemen, A. Andrio, C. Viñas, V. Compañ and F. Teixidor, How to switch from a poor PEDOT:X oxygen evolution reaction (OER) to a good one. A study on dual redox reversible PEDOT:metallacarborane, *J. Mater. Chem. A*, 2022, **10**, 16182–16192.

41 D. C. Malaspina, C. Viñas, F. Teixidor and J. Faraudo, Atomistic Simulations of COSAN: Amphiphiles without a Head-and-Tail Design Display “Head and Tail” Surfactant Behavior, *Angew. Chemie.*, 2020, 59, 3088–3092.

42 A. M. A. Abdelgawwad, J. A. M. Xavier, D. Roca-Sanjuán, C. Viñas, F. Teixidor

and A. Francés-Monerris, Light-Induced On/Off Switching of the Surfactant Character of the o-Cobaltabis(dicarbollide) Anion with No Covalent Bond Alteration, *Angew. Chemie Int. Ed.*, 2021, **60**, 25753–25757.

43 H. B. Gray, Y. S. Sohn and N. Hendrickson, Electronic structure of metallocenes, *J. Am. Chem. Soc.*, 1971, **93**, 3603–3612.

44 B. M. Smirnov and R. S. Berry, Growth of bubbles in liquid., *Chem. Cent. J.*, 2015, **9**, 48.

Chapter 6

6.1 Introduction

Over the years, immense amount of research has been carried out centred around photon-induced processes. Photon or light induced processes encompasses a wide range of phenomena and changes that occur as a response to absorption of light. Of these, the phenomena of photoluminescence pertain to a class of their own owing to their multi-dimensional applicability.[1–3] Photoluminescence refers to any process involving light energy which stimulates the emission of a photon. Fluorescence is a type of photoluminescence which is vastly experienced in nature and hence, deeply explored due to its wide range of applications in various fields.[4–6]

As interesting as the process of fluorescence, is the process of fluorescence quenching. Any process which results in the reduction of fluorescence intensity is known as fluorescence quenching. The quenching of fluorescence can be a result of various molecular interactions such as excited-state interactions, ground state complex formations, energy and electron transfer processes, environmental influences among several others. Hence, fluorescence quenching is widely studied as a fundamental phenomenon as well as a source of information regarding bio-chemical systems.[6–8] The interactions between a fluorophore and a quencher can be predominantly classified as static and dynamic quenching.[9,10] In cases where the quencher forms a stable, non-fluorescent ground-state complex with the fluorophore, the fluorophore is said to be 'statically quenched' (Scheme 6.1).

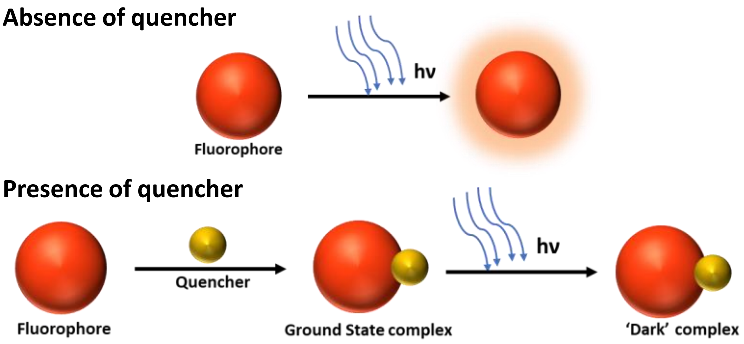

Scheme 6.1 Schematic representation of 'static' quenching of a fluorophore by quencher through the formation of a 'dark' complex.

When the thus formed ground-state complex is excited with light, it is immediately reinstated to the initial ground-state without emitting any photon. Consequently, due to the formation of the 'dark' complex, the number of fluorophores capable of emitting photons decreases resulting in fluorescence quenching. Dynamic quenching, on the other hand, results from the collisional encounters between the fluorophore and quencher molecules which can lead to various non-radiative decays such as energy or electron transfer. Depending on the non-radiative pathway, there are several collisional quenching processes such as Föster resonance energy transfer (FRET), Dexter electron transfer, Photoinduced electron transfer (PET) and others.[11–14] FRET is the non-radiative transfer of energy from a photo-excited donor to an acceptor in the ground state through dipole-dipole interaction and PET is a redox process involving the transfer of an electron from a photo-excited donor to an acceptor thereby forming transient redox species (Scheme 6.2).[15,16]

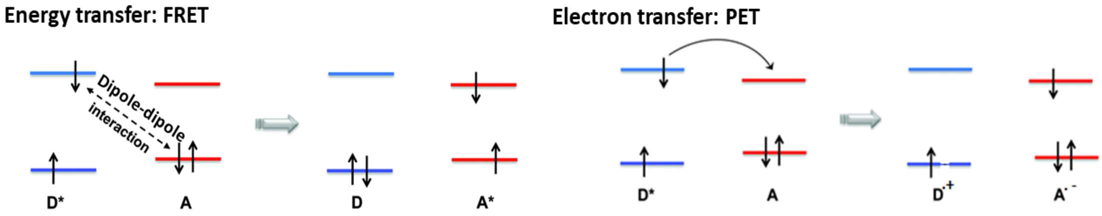

Scheme 6.2 Schematic representation of different dynamic quenching processes.[17] [Adapted version]

For either static or dynamic quenching to occur, the fluorophore and the quencher should be in contact. As a result, numerous applications have emerged such as fluorescence ruler to measure the distance between various biomolecules or protein residues or determining the specific locations of various bio-markers.[13,18]

Static and dynamic quenching mechanisms can be distinguished from life-time as well as temperature dependent steady state measurements. These processes can be distinguished from the spectral characteristics as well as by Stern-Volmer analysis, as we shall see in the subsequent sections. More often than not, it can also be observed that these processes occur in tandem with each other.[19–22]

6.2 Motivation & Objective

Understanding the fundamental photophysical processes is of utmost importance as it helps in devising applications with better purpose and enhanced control. Several materials ranging from organic, inorganic, polymers and nanoparticles have been successfully demonstrated as efficient light harvesters.[23–26] Owing to their size-dependent opto-electronic properties, quantum dots (QDs) form a unique class of light harvesters. The size tuneable photophysical properties of QDs have been exploited for various applications ranging from bio-imaging to light harvesting.[27,28] However, the classic semiconductor based QDs are generally composed of highly toxic metals such as Cd, Pd and Zn.[29,30] This has peeked interest among researches for exploring new environment friendly, less toxic alternatives.

Carbon quantum dots (CDs), since their serendipitous discovery in 2004 from single-walled carbon nanotubes (SWCTs) by preparative electrophoresis, has steadily risen to prominence in the nanocarbon family.[31] CDs have been a ‘hot’ topic of research owing to their unique and distinct photophysical properties resultant of surface defects and quantum-confinement effects (Introduction 1.3.2). They are composed of several distinct, quasispheroidal nanoparticles of size less than 10 nm consisting of distinct sp^3 and sp^2 carbon domains with heterogenous functional groups.[32,33] The distinctive features of the CDs have sparked substantial research, particularly for applications where the cost, biocompatibility and size are crucial considerations.[34,35] In comparison to conventional semiconductor based QDs and organic dyes, CDs, apart from having high fluorescent quantum yields, are highly advantageous due to low toxicity, tuneable photoemission, remarkable biocompatibility, appreciable chemical and photo-bleaching inertness, ease of surface functionalization, high aqueous solubility and availability of abundant and cheap precursor materials.[34,36,37] Consequently, CDs have been recently employed in sensors, drug-delivery systems, bio-imaging, bio-sensing and photocatalysis.[36,38–41] Thus, CDs can be a promising alternate to the traditional QDs.

As we have seen in the previous chapter, cobalta-bis(dicarbollide), [*o*-COSAN]$^-$, is a non-fluorescent anion capable of photo-induced single electron transfer. We have discussed in detail, the excellent photocatalytic ability of [*o*-COSAN]$^-$ for the photo-oxidation of alcohols as well as for water splitting.[42,43] Hence, in this chapter we explore the possible interactions of the highly advantageous fluorescent CDs and non-fluorescent [*o*-COSAN]$^-$ to develop a hybrid material embracing the virtues of both the materials. As has been seen throughout the thesis, [*o*-COSAN]$^-$ is able to form strong N-H···H-B dihydrogen bonds with amine groups. Consequently, owing to the facile surface functionalization of CDs, they have been functionalized with amine terminating silane groups and their interactions with [*o*-COSAN]$^-$ have been explored. It was observed that [*o*-COSAN]$^-$ acted as a quencher in presence of CDs. Hence, this chapter would discuss in detail the nature of interaction between CDs and [*o*-COSAN]$^-$ and would attempt to ascertain the underlying fundamental photophysical process (Scheme 6.3).

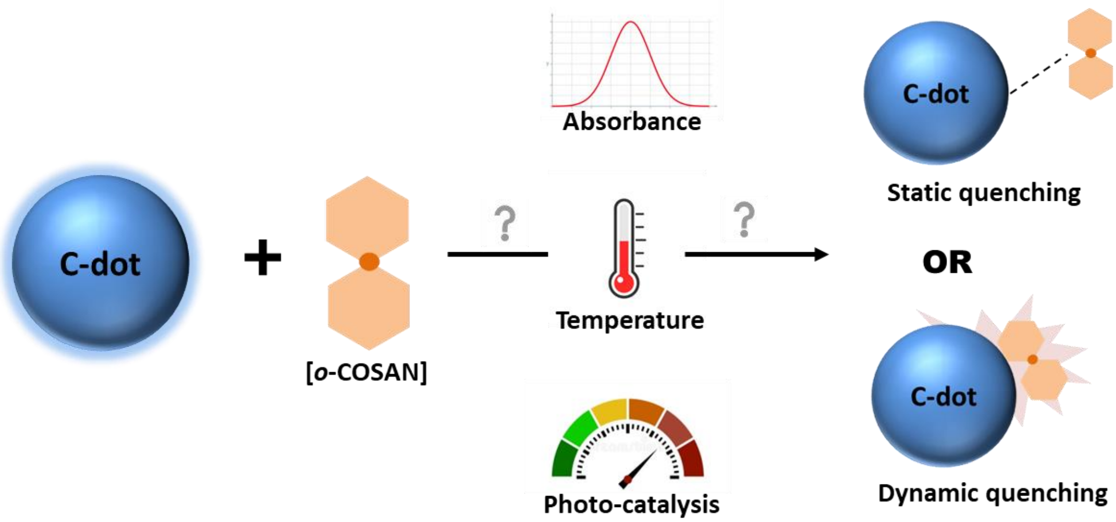

Scheme 6.3 Exploring the photophysical interaction between carbon quantum dots and [*o*-COSAN]$^-$.

6.3 Results & Discussions

The investigation was undertaken using steady-state measurements such as UV-visible and photoluminescence (PL.) measurements. The quantum yield (φ) of the CDs were estimated using quinine sulphate (0.5 M H_2SO_4, $\varphi = 0.546$)[44] as the reference with the formula (Eq.1):

$$\varphi_{Sample} = \varphi_{Ref.} \times \frac{(I_{sample}/A_{sample})}{(I_{ref.}/A_{ref.})} \times (\eta_{sample}/\eta_{ref.})^2 \qquad \textbf{Eq.1}$$

where I is the integrated intensity from the photoluminescence measurements and A is the absorbance at the excitation wavelength.

The quenching efficiency of the CDs photoluminescence by [*o*-COSAN]$^-$ was calculated using the equation (Eq.2)[45,46]:

$$E = 1 - \frac{I}{I_0} \qquad \textbf{Eq.2}$$

where I and I_0 are the PL. intensities of the CDs in the presence and absence of [*o*-COSAN]$^-$, respectively.

The understand the nature of photoluminescence quenching Stern-Volmer analysis was carried out using the equation (Eq.3)[6]:

$$\frac{I_0}{I} = 1 + K_{SV}\,[Q] \qquad \textbf{Eq.3}$$

where I_0 and I are the PL. intensities of the fluorophore in the absence and presence of a quencher, respectively. Ksv (M^{-1}) is the Stern-Volmer constant and [Q] (M) is the quencher concentration. K_{SV} can be determined from the slope of the graph I_0/I *vs.* [Q], with the intercept set as 1.

6.3.1 Synthesis of CDs from citric acid precursor

Carbon dots were synthesized following a reported procedure by the thermal decomposition of the citric acid precursor.[47] Briefly, 4.2 g citric acid monohydrate (20 mmol, 210.14 g/mol) was weighed in a 50 mL round-bottom (RB) flask. Thereafter, the RB was closed with a stopper and immersed in an oil bath and heated to 180°C, while being stirred magnetically at 100 rpm, for 2 h.

Upon reaching the temperature (180°C), the solid citric acid monohydrate melted within 2-3 mins. Following which, aliquots were taken, using a syringe, at regular intervals of 30 mins to assess the progression of the reaction (Fig. 6.1). As the carbonization progressed, the solution turned from colourless to pale yellow to a final solution of yellow colour. The product was dense and oily which was quenched using 7 mL distilled water and stored for further studies. The reaction was also studied using citric acid anhydrous as the precursor. But due to anhydrous nature of the precursor, manual addition of 1 mL of water was required to melt the solid powder. Even though the photophysical properties were comparable, citric acid monohydrate was chosen as the preferred precursor for further studies.

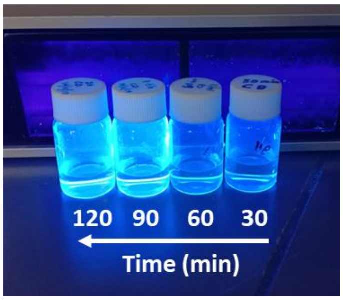

Fig.6.1 Optical photograph monitoring the progression of the thermal decomposition of citric acid monohydrate showing increasing PL. intensity with time.

Upon quenching the reaction, the pH of the solution was measured which was acidic in nature suggesting the presence of carboxylic and/or hydroxyl groups on the surface of the CDs. The thermal decomposition of citric acid involves a complex process of dehydration and reduction. The decomposition process of citric acid monohydrate to yield CDs have been studied extensively by P. Innocenzi and co-workers.[47] From their studies, it was found that the final product entailed a cocktail mix of CDs formed by citric acid and its intermediates, in particular the itaconic acid (*trans*-aconitic acid).

6.3.2 Surface functionalization of CDs with amine ligands

The presence of the carboxylic and/or hydroxyl groups on the surface were exploited to surface functionalize the CDs with the amine terminating silane ligand, 3-(2-aminoethylamino)propylmethyldimethoxy silane (APMS) (Scheme 6.4). Briefly, 0.5 mL CDs from the stock solution was diluted to 5 mL using water. Under continuous stirring at 500 rpm, 0.33 mL of APMS was added to reaction mixture, drop-wise. The mixture was stirred for 24 h at room temperature in a closed vessel. Subsequently, the mixture was precipitated in acetone to obtain a dense, oily liquid which was dispersed in 3 mL water and stored for further studies.

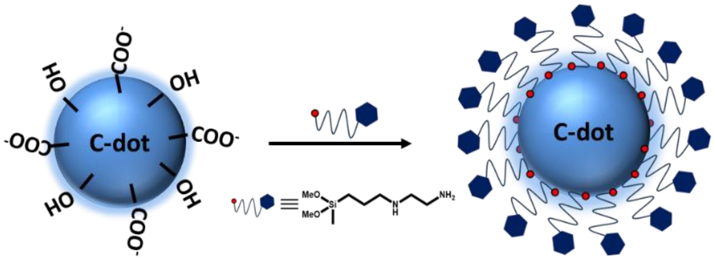

Scheme 6.4 Amine functionalization of carbon dots using APMS ligand.

Upon analysing the pH of the solution, a change from acidic to slightly basic pH was observed, a positive affirmation for the successful amine functionalization.

6.3.3 Characterization of the as-formed CDs

The CDs were characterized using various microscopic and spectroscopic techniques, before and after functionalization (Fig.6.2). The UV-visible spectra showed negligible change before and after functionalization with the first excitonic peak (λ_m) at 332 nm attributed to n→π* of the C=O bonds and an intense absorption band at ~200 nm attributed to π→π* transition from the sp^2 domains confirming the presence of conjugated aromatic structures.[48] The photoluminescence spectra were obtained by excitation (λ_{ex}) at 333 nm where emission peaks (λ_{em}) were observed at 453 nm and 423 nm for CD and CD-APMS, respectively. An increase in the PL. intensity as well as hypochromic shift of 20 nm was observed. While the increase in PL. intensity can be attributed to surface passivation of the CDs by the silane ligand, the latter relates to structural changes possibly to due to the breaking of the π-conjugation in the structures. Consequently, the quantum yield calculations also showed an increase from 23% to 50% upon surface functionalization with the amine ligand suggesting a reduction in surface related defects. The size of the CD was analysed using TEM which showed a mean diameter of 2.98 ± 1.2 nm. Obtaining TEM images were difficult due to the carbonaceous nature of the quantum dots as upon irradiation, the samples were easily burned. Nevertheless, from TEM image it can be inferred that quasispheroidal CDs are formed. The XRD pattern supported the amorphous nature of the CDs and a broad diffraction peak ~20° relating to [002] plane, typical for CDs, was also observed.[47] The CDs were also characterized using IR spectroscopic wherein initial CDs displayed intense $\nu_{c=o}$ stretching band frequencies at 1709 cm^{-1} confirming the presence of carbonyl groups on the surface. After functionalization with amine ligands, the carbonyl peak disappeared and an intense peak at 1557 cm^{-1} due to the scissoring mode of the NH_2 group in the primary amine, APMS, was observed. Thus, confirming successful surface functionalization.

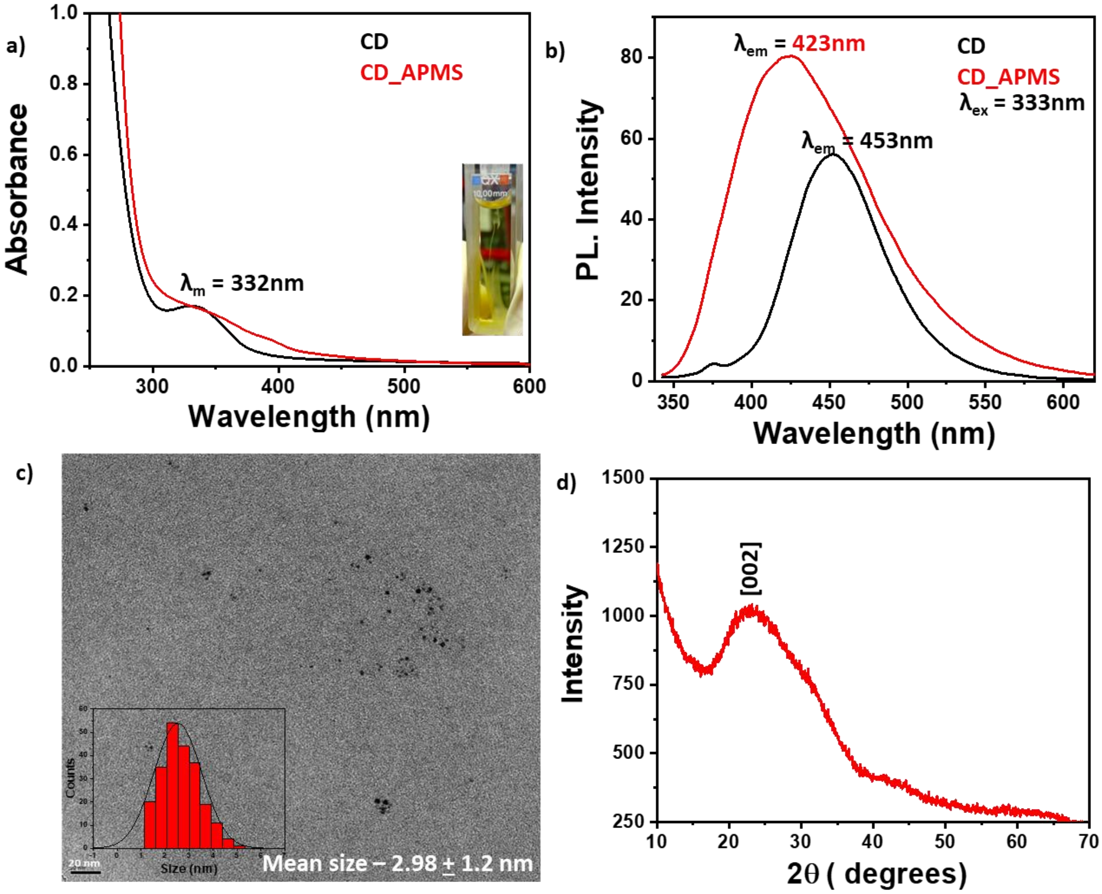

Fig. 6.2 (a) Absorption spectra of CDs before and after functionalization with APMS. [Inset: Optical image of CDs in the quartz cuvette]. **(b)** Photoluminescence spectra of CD and CD-APMS with excitation wavelength 333 nm. **(c)** TEM image of CD at 20 nm scale bar. [Inset: The gaussian distribution of the particle size obtained from analysing ~200 particles). **(d)** XRD pattern confirming the amorphous nature of the CDs.

6.3.4 Photoluminescence quenching experiments with **H[*o*-COSAN]**

In a typical PL. experiment, a 3 mL aqueous solution of CDs is prepared by adjusting the absorbance at the excitation wavelength to be ~0.1, to avoid back-scattering. Thus, 0.01 mL CD and 0.07 mL CD-APMS in 3 mL aqueous solution yields an absorbance value of ~0.1 at 332 nm. [*o*-COSAN]$^-$ as described in the previous chapter has distinct UV-vis characteristics with an absorption peak at 446 nm. With 1 mM H[*o*-COSAN] acting as the quencher, aliquots of 0.01 mL per addition of H[*o*-COSAN] was added sequentially to the CD solution, to yield a final concentration of 100 μM H[*o*-COSAN], ie. 35 additions. The titration of H[*o*-COSAN] to CD as well as CD-APMS were systematically monitored using steady-state measurements, UV-vis and photoluminescence measurements with λ_{ex} as 333 nm.

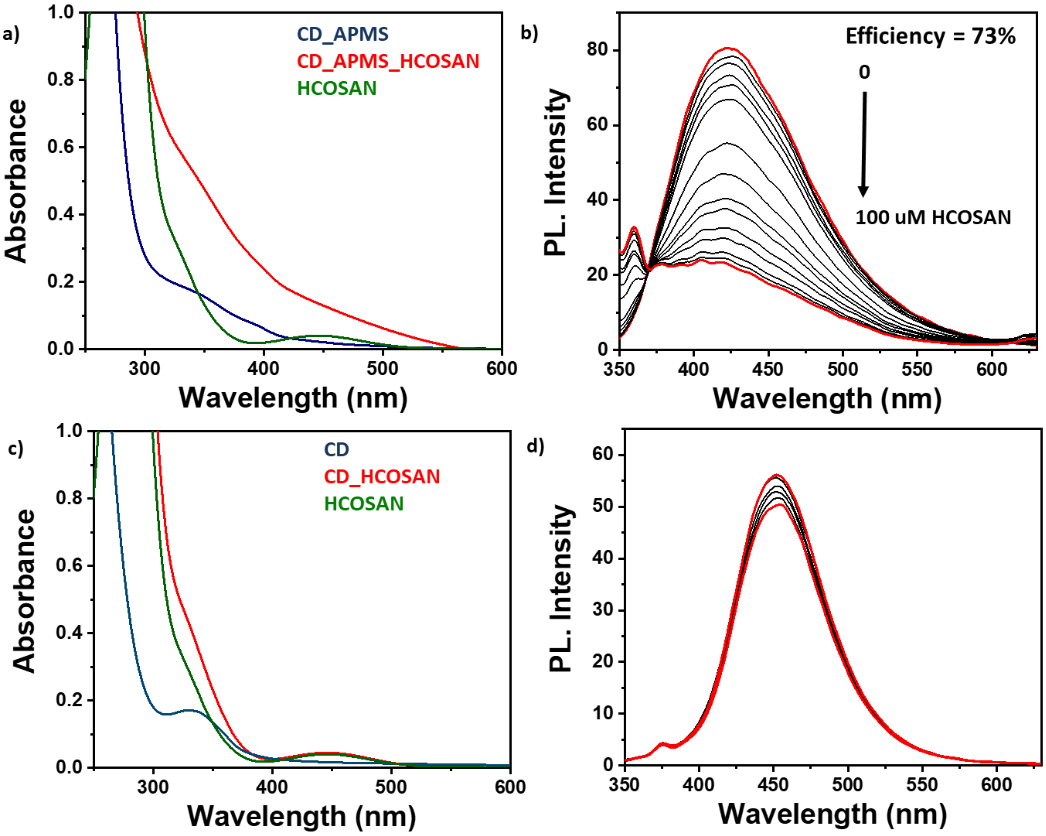

Fig. 6.3 (a) Absorption spectra & **(b)** Photoluminescence spectra of CD-APMS titrated against 1 mM H[*o*-COSAN] showing a quenching efficiency of 73%. **(c)** Absorption spectra & **(d)** Photoluminescence spectra of CD titrated against 1 mM H[*o*-COSAN] showing negligible quenching.

Fig. 6.3 displays the results obtained from the PL. quenching measurements. It can be observed that CD-APMS upon interacting with H[*o*-COSAN] experiences a decrease in the PL. intensity with increasing amount of H[*o*-COSAN]. On the other hand, CD upon interacting with H[*o*-COSAN], displays a negligible decrease in the PL. intensity thereby indicating the lack of interaction between CD and [*o*-COSAN]$^-$. As mentioned earlier, [*o*-COSAN]$^-$ interacts strongly with the amine groups on the surface of CD-APMS through N-H···H-B dihydrogen bonds, which eventually leads to PL. quenching with an efficiency of 73%.

The process of quenching, as mentioned in the introduction, can be either static or dynamic in nature. Static quenching often results in an altercation in the absorption spectra due to the strong ground-state interactions between the fluorophore and the quencher, without translating these effects to the PL. characteristics. Dynamic quenching, on the contrary, does not display any changes in the absorption spectra as it is an excited state phenomenon.[6] Notably, it can be observed that the absorption spectra obtained in the absence and presence of [*o*-COSAN]$^-$ for CD-APMS greatly varies whereas for CD, the H[*o*-COSAN] peak is still observable. Thus, it can be inferred that the mechanism of PL. quenching of CD-APMS with [*o*-COSAN]$^-$ could be static in nature.

The ground-state interaction was reinforced further by Stern-Volmer analysis. The plot of I_0/I *vs.* [Q] was linear with the slope (K_{SV}) calculated as 2.6×10^6 M^{-1} ($R^2 = 0.99$) (Fig.6.4).

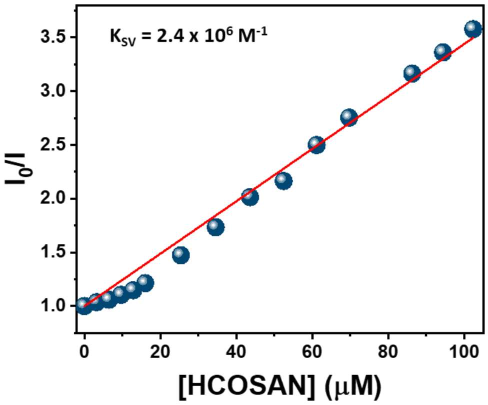

Fig.6.4 Stern-Volmer analysis plot corresponding to PL. quenching of CD-APMS by [*o*-COSAN]$^-$.

It is noteworthy that, both static and dynamic quenching result in a linear Stern-Volmer plot with I_0/I as the y-axis. The difference occurs in lifetime measurements wherein the static quenching does not portray a PL. quenching but dynamic quenching does. This is due to the fact that one is a ground-state phenomenon while the other is an excited state one. Hence, Stern-Volmer plotted with relative lifetime values in the absence and presence of quencher would yield a straight line parallel to the x-axis for static quenching and a linear plot similar to the relative PL. intensities plot for dynamic quenching.

6.3.5 Temperature dependent photoluminescence quenching studies

For the scope of this chapter, even though we have not been able to perform time-resolved measurements due to technical difficulties, another way to distinguish between static and dynamic quenching is temperature dependent PL. quenching measurements. In case of static quenching, with increase in temperature the quenching efficiency decreases as the weak complex formed between the fluorophore and the quencher is dissociated at higher temperatures. Contrarily, for dynamic quenching, as the number of collisions increases with increase in temperature, the quenching efficiency also increases.[6]

Hence, to ascertain the nature of photoluminescence quenching temperature dependent PL. measurements were carried. The experiment was similar to the previously described one for CD-APMS except for the use of the temperature controller to maintain the temperature as well as the addition of the aliquots of 1 mM H[*o*-COSAN] (29 additions of 0.01 mL). The PL. quenching experiments were performed at three different temperatures: 298 K, 308 K and 318 K.

From Fig. 6.5, it can be observed that the PL. quenching efficiency decreases with increase in temperature. Hence, it can be inferred that the quenching mechanism is static in nature. The Stern-Volmer analysis also conferred with the same even though for 308 K, a deviation from the linearity was observed suggestive of a combination of both dynamic and static quenching (Fig. 6.6).

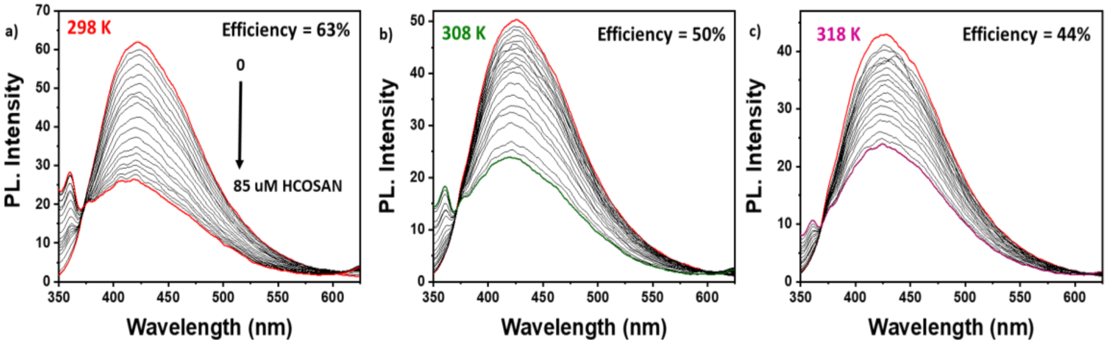

Fig. 6.5 Photoluminescence quenching studies with CD-APMS and 1 mM H[*o*-COSAN] at different temperatures: **(a)** 289 K; **(b)** 308 K & **(c)** 318 K.

Hence, it is rationale to conclude that pre-dominantly the quenching of photoluminescence of the amine functionalized carbon dots by [*o*-COSAN]$^-$ occurs by the formation of a non-emissive ground-state complex. Thus, the nature of quenching is static but the possibility of a dynamic quenching cannot be ruled out as well.

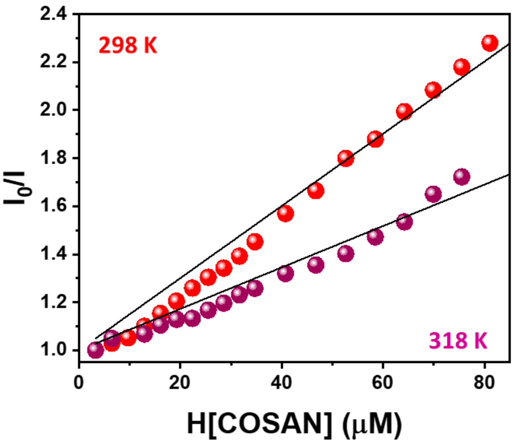

Fig. 6.6 Stern-Volmer plot for the different PL. quenching studies carried out different temperatures.

6.3.6 Estimation of the energy levels of CDs

The optical band gap (E_g) of the CDs were calculated using Tauc plot considering a direct band gap as is commonly reported for CDs in literature.[49–51] Tauc method is based on the formula (Eq.4):

$$(\alpha h\nu)^{1/\gamma} = B(h\nu - E_g) \qquad \textbf{Eq.4}$$

where α is the energy-dependent absorption coefficient (α = 2.303 A), h is the Planck's constant, ν is the frequency of the photon and E_g is the band gap with B being a constant. The γ-factor varies as 2 or ½ for direct or indirect band gap, respectively.[52,53]

Following the equation, $(\alpha h\nu)^{1/2}$ *vs.* hν was plotted to obtain the optical band gap for the CDs (Fig. 6.7) using the wavelength and absorbance values (A) obtained from UV-visible spectra. E_g was calculated by extrapolating the linear region of the curve to obtain the x-intercept. From the graph, the E_g for CDs were estimated to be around 3.34 eV.

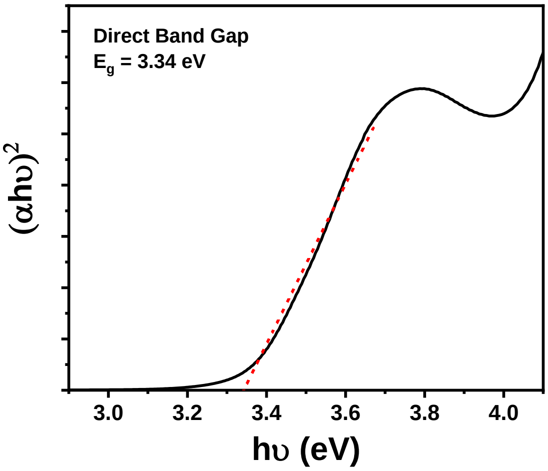

Fig.6.7 Tauc plot to estimate the optical band gap of CDs considering a direct band gap.

Generally, cyclic voltametric measurements are carried out to measure either the HOMO or the LUMO levels of a molecule. Since CDs are redox-inactive, electrochemical impedance (EIS) measurements were carried out to obtain the HOMO level of CD using the Mott-Schottky plots.[50] Mott-Schottky plots describes the relation between inverse square of capacitance (C) *vs.* the potential between an electrolyte and a semiconductor. At $1/C^2 = 0$ and for one electron transfer, the flat-band potential (V_{fb}) (potential at which the depletion layer is absent as the redox fermi level of the electrolyte is equal to the fermi level of the semiconductor) is calculated as (Eq. 5)[54]:

$$\mathbf{V_{fb} = V - 0.025\ (in\ V)} \qquad \textbf{Eq.5}$$

where V is the x-intercept of the Mott-Schottky plot obtained from the EIS measurements.

EIS measurements were carried out using 0.1 mL of CD dissolved in 0.2 M PBS solution (5 mL) using a three-electrode system with glassy carbon as the reference, Pt as the counter and Ag wire as the reference electrode. Fig. 6.8 displays the Nquist plot obtained from the impedance measurement of the CDs confirming the semi-conductor behaviour of the material.

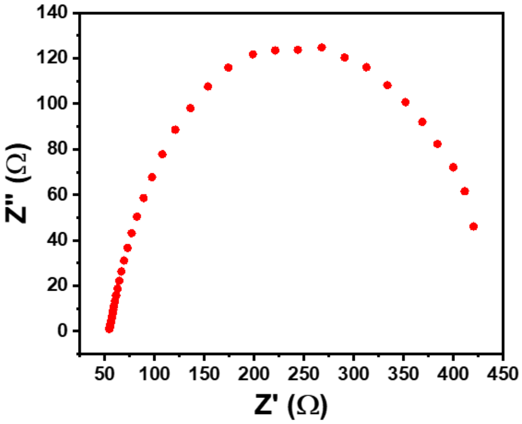

Fig.6.8 Nquist plot obtained for the CDs from the electrochemical impedance measurements.

The Mott-Schottky plots were obtained using the FRA potentiostatic mode in the Autolab PGSTAT302N potentiostat/galvanostat from Metrohm and measured for frequency window of $10^3 – 10^5$ Hz. A representative plot obtained for the frequency 10^3 Hz is shown in Fig. 6.9(a). Fig 6.9(b) displays the plot for three different frequencies in order to obtain an average flat-band potential by extrapolating the linear region to the x-intercept.

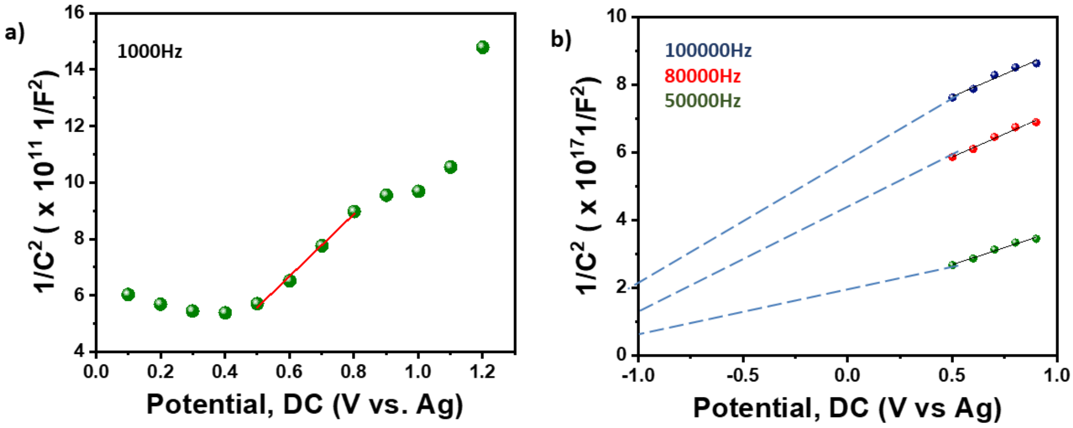

Fig. 6.9 (a) Mott-Schottky plot obtained for CDs from EIS measurements at 10^3 Hz. **(b)** Mott-Schottky plots of different frequencies to measure the V_{fb}.

From the graph, the flat-band potential (V_{fb}) was estimated to be -1.52 ± 0.6 V (*vs.* Ag). Thus, the equivalent energy was calculated in vacuum as -3.2 eV which corresponds to the HOMO level of the CDs.

As we have calculated, the optical band gap (from Tauc plot) and the HOMO level (from Mott-Schottky plot) it was possible to calculate the LUMO level of the CDs as +0.14 eV (*vs.* vacuum).

6.3.7 Photo-oxidation of alcohols using CD-APMS/[o-COSAN]⁻ hybrids

As described in the previous chapters, the heterogenous photo-catalytic activity of the anchored [*o*-COSAN]$^-$ was studied for the oxidation of 1-phenylethanol in water (pH = 7, K_2CO_3) using $Na_2S_2O_8$ as the sacrificial or oxidizing agent. The experiments were performed by exposing the reaction quartz tubes containing 0.02 mM H[*o*-COSAN] (0.0125 mL), the respective amount of CDs/CD-APMS and 20 mM 1-phenylethanol (0.0123 mL) in presence of 40 mM $Na_2S_2O_8$ and 5 mL K_2CO_3 to UV irradiation (~300 nm) placed in a photo-reactor at room temperature and atmospheric pressure. The catalysts were separated using liquid-liquid extraction using dichloromethane (DCM) at the end of the experiments and the reaction products were quantified using ^{1}H NMR analysis.

The photocatalysis was performed using both, CDs as well as CD-APMS, to elucidate the effect of [*o*-COSAN]$^-$ interaction as well as to postulate a speculative mechanism of PL. quenching. As the molar extinction coefficient for CDs have not been reported, the concentrations used in catalysis for the CDs are in terms of their relative absorbances. Upon performing the experiments, it was observed that the catalytic efficiency vastly decreased from ≥ 99% for CDs without amine functionalization to 78% for CD-APMS. Consequently, with increasing concentration of the CD-APMS as 3, 12 and 120 times the photocatalytic efficiency also decreased as 50%, 26% and 16%, respectively (Fig.6.10). On the contrary, the catalytic yield remained unaffected due to the presence of CDs and an efficiency of ~95% was observed in all cases. Table 6.1 summarizes the various yields obtained for the photocatalytic studies.

Table 6.1 Summarizing the photocatalytic yield obtained in various concentrations of CD s and CD-APMS in presence the catalyst, [*o*-COSAN]$^{-}$.

Catalyst	Yield (%)
1x CD-APMS-COSAN	78
3x CD-APMS-COSAN	50
12x CD-APMS-COSAN	26
120x CD-APMS-COSAN	16
1x CDs: 1xH-COSAN	93
3x CDs: 1xH-COSAN	≥99
12x CDs: 1xH-COSAN	95
120x CDs: 1H-COSAN	91

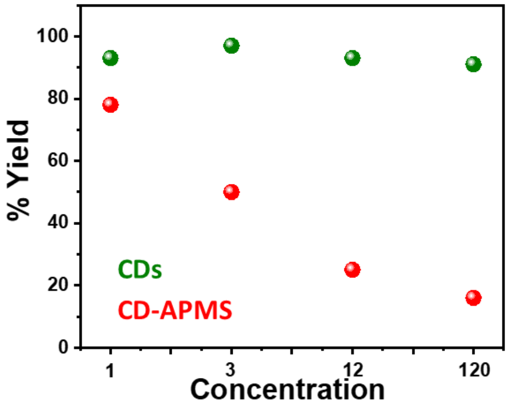

Fig. 6.10 The photocatalytic yields obtained for the various concentrations of CDs and CD-APMS in presence of 0.02 mM [*o*-COSAN]$^{-}$.

From the photocatalytic experiment, it is possible to assume that due to the formation of stable ground-state complex between CD-APMS and [*o*-COSAN]$^{-}$, the photo-excited electron of [*o*-COSAN]$^{-}$ is unable to participate in the photocatalysis. The plausibility of decrease in the yield due to shielding or masking of irradiation source considering the presence of a competing chromophore can be eliminated as in presence of CDs, the yield remains unaffected and has high efficiency. A rather more compelling explanation for the observed decrease in the photocatalytic yield can be obtained by considering the energy levels of CDs and [*o*-COSAN]$^-$ (Fig. 6.11).

From the energy levels obtained previously for the CDs and from literature for [*o*-COSAN]$^-$, there exists a possibility for photoinduced electron transfer with [*o*-COSAN]$^-$ as the donor and CDs as the acceptor. Due to enhanced proximity of [*o*-COSAN]$^-$ and CD-APMS, the electron transfer is more easily facilitated than in CD and [*o*-COSAN]$^-$ combination.

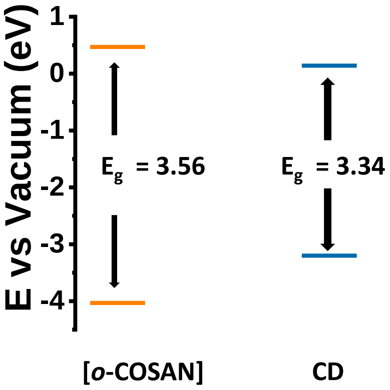

Fig.6.11 Energy levels with respect to vacuum of [*o*-COSAN]$^-$ and CDs indicative of a plausible photo induced electron transfer.

Blank experiments with carbon quantum dots alone were also performed wherein the catalytic yields were 18% and 14% for CD-APMS and CDs, respectively. Hence, decrease in yield even below the blank experiment (16% at 120 times CD-APMS concentration), weighs highly in favor of a photoinduced electron transfer rendering both CD-APMS as well as [*o*-COSAN]$^-$ inefficient as photocatalysts.

6.4 Conclusion

We have successfully synthesized, functionalized as well as characterized blue emitting, aqueous stable CDs. We were able to thoroughly investigate the fundamentals of the photophysical process underlying between CD-APMS and [*o*-COSAN]$^-$. From the various experiments and calculations, it seems that the PL. quenching of CD-APMS by [*o*-COSAN]$^-$ is highly likely static in nature owing to the observations such as perturbation in the absorption spectra, decreasing PL. efficiency with increasing temperature as well as the decrease in the photocatalytic yield. Nevertheless, the photophysical process occurring is complex and can be a combination of various quenching mechanisms. With this study, we were able to show the more likeliness of one particular quenching mechanism.

Understanding these fundamental photophysical processes helps in improving the applicability of these hybrid structures. The CD-APMS:[*o*-COSAN]$^-$ has the potential for several synergistic applications such as thernostic agents where CD-APMS can acts fluorescent labels with an 'on/off' mechanism while [*o*-COSAN]$^-$ can find its application in therapies such as boron neutron capture therapy (BNCT) or as tunable photocatalysts (Scheme 6.5).

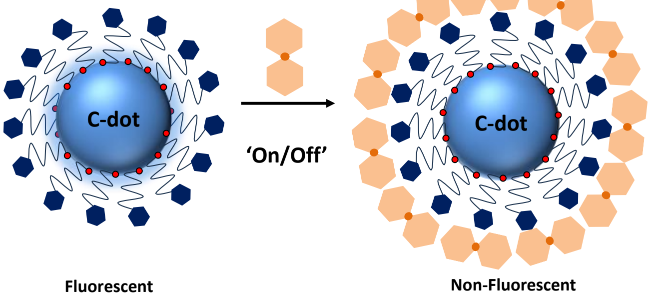

Scheme 6.5 Schematic representation of the possible 'on/off' mechanism owing to the interaction between CD-APMS and [*o*-COSAN]$^-$.

The CD-APMS:[*o*-COSAN]$^-$ hybrid structures has immense potential waiting to be explored.

6.5 References

1 M. Tebyetekerwa, J. Zhang, Z. Xu, T. N. Truong, Z. Yin, Y. Lu, S. Ramakrishna, D. Macdonald and H. T. Nguyen, Mechanisms and Applications of Steady-State Photoluminescence Spectroscopy in Two-Dimensional Transition-Metal Dichalcogenides, *ACS Nano*, 2020, **14**, 14579–14604.

2 M. Anpo and M. Che, eds. W. O. Haag, B. C. Gates and H. B. T.-A. in C. Knözinger, Academic Press, 1999, vol. 44, pp. 119–257.

3 J. Lefebvre, S. Maruyama and P. Finnie, eds. A. Jorio, G. Dresselhaus and M. S. Dresselhaus, Springer Berlin Heidelberg, Berlin, Heidelberg, 2008, pp. 287–319.

4 N. Siraj, B. El-Zahab, S. Hamdan, T. E. Karam, L. H. Haber, M. Li, S. O. Fakayode, S. Das, B. Valle, R. M. Strongin, G. Patonay, H. O. Sintim, G. A. Baker, A. Powe, M. Lowry, J. O. Karolin, C. D. Geddes and I. M. Warner, Fluorescence, Phosphorescence, and Chemiluminescence, *Anal. Chem.*, 2016, **88**, 170–202.

5 D. E. Koppel, D. Axelrod, J. Schlessinger, E. L. Elson and W. W. Webb, Dynamics of fluorescence marker concentration as a probe of mobility, *Biophys. J.*, 1976, **16**, 1315–1329.

6 J. R. Lakowicz, *Principles of Fluorescence Spectroscopy*, Springer US, Baltimore, MD (EE.UU.), 3rd edn., 2006.

7 M. R. Eftink, J. R. Lakowicz, Springer US, Boston, MA, 2002, pp. 53–126.

8 G. K. ROLLEFSON and H. BOAZ, Quenching of fluorescence in solution., *J. Phys. Colloid Chem.*, 1948, **52**, 518–527.

9 J. R. Barrio, G. L. Tolman, N. J. Leonard, R. D. Spencer and G. Weber, Flavin 1, N 6 -ethenoadenine dinucleotide: dynamic and static quenching of fluorescence., *Proc. Natl. Acad. Sci. U. S. A.*, 1973, **70**, 941–943.

10 M. R. Eftink and C. A. Ghiron, Fluorescence quenching studies with proteins, *Anal. Biochem.*, 1981, **114**, 199–227.

11 M. R. Wasielewski, Photoinduced Electron Transfer in Supramolecular Systems for Artificial Photosynthesis, *Chem. Rev.*, 1992, **92**, 435–461.

12 M. Eichelbaum and K. Rademann, Plasmonic enhancement or energy transfer? on the luminescence of gold-, silver-, and lanthanide-doped silicate glasses and its potential for light-emitting devices, *Adv. Funct. Mater.*, 2009, **19**, 2045–2052.

13 L. Stryer, Fluorescence Energy Transfer as a Spectroscopic Ruler, *Annu. Rev.*

Biochem., 1978, **47**, 819–846.

14 R. Plass, S. Pelet, J. Krueger, M. Grätzel and U. Bach, Quantum dot sensitization of organic-inorganic hybrid solar cells, *J. Phys. Chem. B,* 2002, **106**, 7578–7580.

15 K. E. Sapsford, L. Berti and I. L. Medintz, Materials for fluorescence resonance energy transfer analysis: Beyond traditional donor-acceptor combinations, *Angew. Chemie - Int. Ed.*, 2006, **45**, 4562–4588.

16 K. Tvrdy, P. A. Frantsuzov and P. V. Kamat, Photoinduced electron transfer from semiconductor quantum dots to metal oxide nanoparticles, *Proc. Natl. Acad. Sci.*, 2011, **108**, 29–34.

17 V. K. Praveen, C. Ranjith and E. Bandini, Oligo(phenylenevinylene) hybrids and self-assemblies: versatile materials for excitation energy transfer, *Chem. Soc. Rev.* 2014, **43**, 4222–4242.

18 A. Ishizaki, T. R. Calhoun, G. S. Schlau-Cohen and G. R. Fleming, Quantum coherence and its interplay with protein environments in photosynthetic electronic energy transfer, *Phys. Chem. Chem. Phys.*, 2010, **12**, 7319.

19 M. R. Eftink and C. A. Ghiron, Exposure of Tryptophanyl Residues in Proteins. Quantitative Determination by Fluorescence Quenching Studies, *Biochemistry*, 1976, **15**, 672–680.

20 C. A. M. Seidel, A. Schulz and M. H. M. Sauer, Nucleobase-specific quenching of fluorescent dyes. 1. Nucleobase one-electron redox potentials and their Correlation with static and dynamic quenching efficiencies, *J. Phys. Chem.*, 1996, **100**, 5541–5553.

21 C. Fan, S. Wang, J. W. Hong, G. C. Bazan, K. W. Plaxco and A. J. Heeger, Beyond superquenching: Hyper-efficient energy transfer from conjugated polymers to gold nanoparticles, *Proc. Natl. Acad. Sci. U. S. A.*, 2003, **100**, 6297–6301.

22 Q. Zhou and T. M. Swager, Methodology for Enhancing the Sensitivity of

Fluorescent Chemosensors: Energy Migration in Conjugated Polymers, *J. Am. Chem. Soc.*, 1995, **117**, 7017–7018.

23 S. Kundu and A. Patra, Nanoscale Strategies for Light Harvesting, *Chem. Rev.*, 2017, **117**, 712–757.

24 G. J. Hedley, A. Ruseckas and I. D. W. Samuel, Light Harvesting for Organic Photovoltaics, *Chem. Rev.*, 2017, **117**, 796–837.

25 A. Renaud, F. Grasset, B. Dierre, T. Uchikoshi, N. Ohashi, T. Takei, A. Planchat, L. Cario, S. Jobic, F. Odobel and S. Cordier, Inorganic Molybdenum Clusters as Light-Harvester in All Inorganic Solar Cells: A Proof of Concept, *ChemistrySelect*, 2016, **1**, 2284–2289.

26 K. V. Rao, A. Jain and S. J. George, Organic–inorganic light-harvesting scaffolds for luminescent hybrids, *J. Mater. Chem. C*, 2014, **2**, 3055–3064.

27 C.-H. M. Chuang, P. R. Brown, V. Bulović and M. G. Bawendi, Improved performance and stability in quantum dot solar cells through band alignment engineering, *Nat. Mater.*, 2014, **13**, 796–801.

28 M. Bruchez Jr., Semiconductor Nanocrystals as Fluorescent Biological Labels, *Science (80-.).*, 1998, **281**, 2013–2016.

29 M. Lunz, V. A. Gerard, Y. K. Gun'Ko, V. Lesnyak, N. Gaponik, A. S. Susha, A. L. Rogach and A. L. Bradley, Surface plasmon enhanced energy transfer between donor and acceptor CdTe nanocrystal quantum dot monolayers, *Nano Lett.*, 2011, **11**, 3341–3345.

30 A. R. Clapp, I. L. Medintz, J. M. Mauro, B. R. Fisher, M. G. Bawendi and H. Mattoussi, Fluorescence Resonance Energy Transfer between Quantum Dot Donors and Dye-Labeled Protein Acceptors, *J. Am. Chem. Soc.*, 2004, **126**, 301–310.

31 X. Xu, R. Ray, Y. Gu, H. J. Ploehn, L. Gearheart, K. Raker and W. A. Scrivens, Electrophoretic Analysis and Purification of Fluorescent Single-Walled Carbon Nanotube Fragments, *J. Am. Chem. Soc.*, 2004, **126**, 12736–12737.

32 A. B. Bourlinos, A. Stassinopoulos, D. Anglos, R. Zboril, M. Karakassides and E. P. Giannelis, Surface Functionalized Carbogenic Quantum Dots, *Small*, 2008, **4**, 455–458.

33 Z. Zhang, T. Zheng, X. Li, J. Xu and H. Zeng, Progress of Carbon Quantum Dots in Photocatalysis Applications, *Part. Part. Syst. Charact.*, 2016, **33**, 457–472.

34 L. Cao, X. Wang, M. J. Meziani, F. Lu, H. Wang, P. G. Luo, Y. Lin, B. A. Harruff, L. M. Veca, D. Murray, S.-Y. Xie and Y.-P. Sun, Carbon Dots for Multiphoton Bioimaging, *J. Am. Chem. Soc.*, 2007, **129**, 11318–11319.

35 H. Liu, T. Ye and C. Mao, Fluorescent Carbon Nanoparticles Derived from Candle Soot, *Angew. Chemie Int. Ed.*, 2007, **46**, 6473–6475.

36 S. C. Ray, A. Saha, N. R. Jana and R. Sarkar, Fluorescent Carbon Nanoparticles: Synthesis, Characterization, and Bioimaging Application, *J. Phys. Chem. C*, 2009, **113**, 18546–18551.

37 Y.-P. Sun, B. Zhou, Y. Lin, W. Wang, K. A. S. Fernando, P. Pathak, M. J. Meziani, B. A. Harruff, X. Wang, H. Wang, P. G. Luo, H. Yang, M. E. Kose, B. Chen, L. M. Veca and S.-Y. Xie, Quantum-Sized Carbon Dots for Bright and Colorful Photoluminescence, *J. Am. Chem. Soc.*, 2006, **128**, 7756–7757.

38 S.-T. Yang, X. Wang, H. Wang, F. Lu, P. G. Luo, L. Cao, M. J. Meziani, J.-H. Liu, Y. Liu, M. Chen, Y. Huang and Y.-P. Sun, Carbon Dots as Nontoxic and High-Performance Fluorescence Imaging Agents, *J. Phys. Chem. C*, 2009, **113**, 18110–18114.

39 Q. Li, T. Y. Ohulchanskyy, R. Liu, K. Koynov, D. Wu, A. Best, R. Kumar, A. Bonoiu and P. N. Prasad, Photoluminescent Carbon Dots as Biocompatible Nanoprobes for Targeting Cancer Cells in Vitro, *J. Phys. Chem. C*, 2010, **114**, 12062–12068.

40 C. Ji, Y. Zhou, R. M. Leblanc and Z. Peng, Recent Developments of Carbon Dots in Biosensing: A Review, *ACS Sensors*, 2020, **5**, 2724–2741.

41 S.-T. Yang, L. Cao, P. G. Luo, F. Lu, X. Wang, H. Wang, M. J. Meziani, Y. Liu, G. Qi and Y.-P. Sun, Carbon Dots for Optical Imaging in Vivo, *J. Am. Chem. Soc.*, 2009, **131**, 11308–11309.

42 I. Guerrero, A. Saha, J. A. M. Xavier, C. Viñas, I. Romero and F. Teixidor, Noncovalently Linked Metallacarboranes on Functionalized Magnetic Nanoparticles as Highly Efficient, Robust, and Reusable Photocatalysts in Aqueous Medium, *ACS Appl. Mater. Interfaces*, 2020, **12**, 56372–56384.

43 I. Guerrero, Z. Kelemen, C. Viñas, I. Romero and F. Teixidor, Metallacarboranes as Photoredox Catalysts in Water., *Chemistry*, 2020, **26**, 5027–5036.

44 S. R. Erga, B. Hamre and Ø. Frette, Testing Fluorescence Lifetime Standards using Two-Photon Excitation and Time-Domain Instrumentation : Fluorescein , Quinine Sulfate and Green Fluorescent Protein, 2018, 1065–1073.

45 J. Ann Maria Xavier, G. Devatha, S. Roy, A. Rao and P. P. Pillai, Electrostatically regulated photoinduced electron transfer in “cationic” eco-friendly CuInS2/ZnS quantum dots in water, *J. Mater. Chem. A*, 2018, **6**, 22248–22255.

46 G. Devatha, S. Roy, A. Rao, A. Mallick, S. Basu and P. P. Pillai, Electrostatically driven resonance energy transfer in “cationic” biocompatible indium phosphide quantum dots, *Chem. Sci.*, 2017, **8**, 3879–3884.

47 R. Ludmerczki, S. Mura, C. M. Carbonaro, I. M. Mandity, M. Carraro, N. Senes, S. Garroni, G. Granozzi, L. Calvillo, S. Marras, L. Malfatti and P. Innocenzi, Carbon Dots from Citric Acid and its Intermediates Formed by Thermal Decomposition, *Chem. - A Eur. J.*, 2019, **25**, 11963–11974.

48 A. Sharma, T. Gadly, A. Gupta, A. Ballal, S. K. Ghosh and M. Kumbhakar, Origin of Excitation Dependent Fluorescence in Carbon Nanodots, *J. Phys. Chem. Lett.*, 2016, **7**, 3695–3702.

49 M. Masteri-Farahani and F. Askari, Design and photophysical insights on

graphene quantum dots for use as nanosensor in differentiating methamphetamine and morphine in solution, *Spectrochim. Acta Part A Mol. Biomol. Spectrosc.*, 2019, **206**, 448–453.

50 Q. Wang, J. Li, X. Tu, H. Liu, M. Shu, R. Si, C. T. J. Ferguson, K. A. I. Zhang and R. Li, Single Atomically Anchored Cobalt on Carbon Quantum Dots as Efficient Photocatalysts for Visible Light-Promoted Oxidation Reactions, *Chem. Mater.*, 2020, **32**, 734–743.

51 J. Kumar, Ansh and M. Shrivastava, Introduction of Near to Far Infrared Range Direct Band Gaps in Graphene: A First Principle Insight, *ACS Omega*, 2021, **6**, 5619–5626.

52 P. Makuła, M. Pacia and W. Macyk, How To Correctly Determine the Band Gap Energy of Modified Semiconductor Photocatalysts Based on UV–Vis Spectra, *J. Phys. Chem. Lett.*, 2018, **9**, 6814–6817.

53 J. Tauc, Optical properties and electronic structure of amorphous Ge and Si, *Mater. Res. Bull.*, 1968, **3**, 37–46.

54 K. Gelderman, L. Lee and S. W. Donne, Flat-Band Potential of a Semiconductor: Using the Mott–Schottky Equation, *J. Chem. Educ.*, 2007, **84**, 685.

General Conclusions & Future Prospects

In this thesis, we have navigated through the captivating and ever-evolving landscape of θ-metallacarboranes and nanoparticles, illuminating their multifaceted roles and potentials across diverse scientific disciplines. Through a comprehensive exploration encompassing synthesis, characterization, and applications, we have unveiled the intriguing synergy between these two materials.

Each of the chapter described in the thesis can be ascribed to a specific property of θ-metallacarboranes and its associated applications along with the integration of nanoparticles. Thus,

- ✓ In chapter 2, we have successfully demonstrated the potential application of metallacarboranes as 'universal' internal reference systems capable of being employed in both, aqueous and non-aqueous systems without any structural ramifications. We have thoroughly investigated their electrochemical parameters in various conditions such as different metallacarboranes concentrations, electrolytes, scan rates, pH as well as temperature. The work has been published as a peer-reviewed article in *Chem. Commun.* titled "*Potential Application of Metallacarboranes as an Internal Reference: An Electrochemical comparative study to Ferrocene.*"
- ✓ In chapter 3, we have demonstrated the application of metallacarboranes as a 'small molecule' probe for elucidating the 'effective' surface of a protein using electrochemistry. We were able to classify the proteins into two different groups based on their interactions with [*o*-COSAN]$^-$ as well as propose a possible interpretation. The work highlights the potential application of small molecules such as metallacarboranes in analysing a protein in its intrinsic form and environment. The work has been recently published as an advanced article in the journal *J. Mater. Chem. B* as "*Single Stop Analysis of a Protein Surface using Molecular Probe Electrochemistry.*"
- ✓ In chapter 4, we have explored the central theme of integrating metallacarboranes with surface engineered magnetic nanoparticles for various applications such as photocatalysis as well as sensing. The photocatalytic

ability of the heterogenous metallacarborane and magnetic nanoparticle system for the oxidation of alcohols in water have been studied. The catalysis resulted in high yields and selectivity while being recyclable and reusable. We have also described a novel co-precipitation method for the synthesis of size-controlled and scalable magnetic nanoparticles capable of being employed for diverse applications. The chapter comprises of two different articles, of which one has been published in the peer-reviewed journal *ACS Appl. Mater. Interfaces* as "*Noncovalently linked Metallacarboranes on Functionalized Magnetic Nanoparticles as Highly Efficient, Robust and Reusable Photocatalysts in Water*" while the second work has been submitted to *Int. J. Mol. Sci.* titled as "Synthesis of Colloidally Long-Lived Iron oxide Magnetic Nanoparticles: A Simplistic Laboratory Approach."

- ✓ In chapter 5, we have demonstrated the ability of metallacarboranes, [*o*-COSAN]$^{-}$, as 'small molecule' electrode for the complete splitting of water using light without any sacrificial agent or co-catalysts. We have also demonstrated the absence of fluorescence in [*o*-COSAN]$^{-}$, both experimentally and theoretically. We were also able to demonstrate the application of oxidation of alcohols without any sacrificial agent as an indirect measure of oxygen produced. The manuscript for the work is under preparation.
- ✓ In chapter 6, we have studied the photophysical interaction of [*o*-COSAN]$^{-}$ with amine functionalized carbon quantum dots. We have successfully characterized and surface functionalized the carbon dots without altering the photophysical properties. The interaction with [*o*-COSAN]$^{-}$ led to fluorescence quenching of the carbon dots and possible interpretations for the observed phenomenon has been explored in the chapter and the manuscript for the work is also under preparation.

Through rigorous experimentation and inter-disciplinary collaborations, the doctoral thesis contributes to the growing knowledge of metallacarboranes and nanoparticles. It emphasizes their adaptability as advanced materials for contemporary challenges. Ultimately, our research broadens our understanding of these intriguing molecules and paves way for transformative applications with enormous potential.

ANNEX

ChemComm

ROYAL SOCIETY OF CHEMISTRY

COMMUNICATION

View Article Online
View Journal | View Issue

Cite this: *Chem. Commun.*, 2022, 58, 4196

Received 21st January 2022,
Accepted 4th March 2022

DOI: 10.1039/d2cc00424k

rsc.li/chemcomm

Potential application of metallacarboranes as an internal reference: an electrochemical comparative study to ferrocene†

Jewel Ann Maria Xavier,[a] Clara Viñas,[a] Encarnación Lorenzo,[bcd] Tania García-Mendiola *[bc] and Francesc Teixidor *[a]

Ferrocene and its derivatives have been extensively used as an internal reference in electrochemical processes. Yet, they possess limitations such as solvent restrictions that require chemical modifications. In this regard, we have studied the use of metallacarboranes $[3,3'\text{-M}(1,2\text{-C}_2\text{B}_9\text{H}_{11})_2]^-$ (M = Co, Fe) as general internal reference systems and have proven their suitability by thoroughly investigating their electrochemical properties in both aqueous and organic electrolytes without any derivatization.

To evaluate any electrochemical process, it is always necessary that it be compared with another electrochemical process that serves as a reference. Typically, we use reference electrodes such as the standard hydrogen electrode (SHE), normal hydrogen electrode (NHE), reversible hydrogen electrode (RHE), the various forms of Ag/AgCl electrodes, or saturated calomel electrode (SCE), among others. In all of these, water is a key component. What happens when we want to compare that electrochemical process of interest which takes place in water to the same one in an organic solvent or to a very similar one having compounds insoluble in water but soluble in an organic solvent? What if we simply want to compare a series of electrochemical processes in water and in organic solvents?[1] Can we use the electrodes that work in aqueous solutions for non-aqueous systems as well?[2] Yes, but after the initial few experiments the reference potentials are altered and unmeasurable junction potentials develop.[3] Hence, using the same reference electrodes to measure aqueous or non-aqueous redox systems is not the most appropriate in principle as the potentials measured are not directly comparable. One way to avoid this problem is to use as internal reference a highly reversible electrochemical couple that is soluble in organic solvents. This led to the extensive use of ferrocene,[4] or cobaltocene[5] or decamethylferrocene,[6] as the internal reference redox systems (Table S3, ESI†). While ferrocene is insoluble in water, derivatives of ferrocene such as ferrocene carboxylic acid (FCA),[7] ferrocenemethanol (FcMe)[8] and ferrocene acetic acid (FAA)[4a] which go through one-electron oxidation to the ferricinium state, similar to ferrocene, are soluble in water. These are generally referred to as internal standards for a quasi-reference electrode (QRE).[9] Thus, with QRE, it became possible to compare the same electroactive couple in both water and non-aqueous media, but this is not highly accurate because the functional modifications on the parent electroactive species does indeed affect the redox potential of the electrochemical couple.[10] Up until now, we have discussed about the electrochemical couples that were originally opted for organic solvents which had to be chemically modified to be adapted to aqueous solvents. However, there is a highly reversible redox active electrolyte of great significance in aqueous media, namely the ferricyanide to ferrocyanide couple.[11] It is noteworthy that all the internal standards described are complexes in which one of their electroactive pairs fulfills the 18e$^-$ rule and are octahedrally coordinated to avoid, as much as possible, a preceding and following interaction of the metal with the solvent so that it cannot significantly alter the formal potential ($E^{0\prime}$) value. Indeed, all these participate in outer sphere electron transfer mechanisms. As a rule, all the possible internal standards for aqueous media are either anions or alcohols and those for non-aqueous media are neutral. Therefore, there is no internal standard currently available that is suitable, without any modification, for both water and organic solvents.

Metallacarboranes form an interesting class of polyhedral carborane clusters, akin to ferrocene, having an empirical formula of $[\text{M}(\text{C}_2\text{B}_9\text{H}_{11})_2]^-$, (M = Co, Fe), where the metal occupies a shared vertex merging the two icosahedra units

---

[a] *Institut de Ciencia de Materials de Barcelona (ICMAB-CSIC), Campus de la UAB, Bellaterra, Spain. E-mail: teixidor@icmab.es*

[b] *Departamento Quimica Analítica y Analisis Instrumental, Universidad Autónoma de Madrid, Spain*

[c] *Institute for Advanced Research in Chemical Sciences (IAdChem), Universidad Autónoma de Madrid, Ciudad Universitaria de Cantoblanco, 28049, Madrid, Spain*

[d] *IMDEA-Nanociencia, Ciudad Universitaria de Cantoblanco, 28049, Madrid, Spain*

† Electronic supplementary information (ESI) available. See DOI: 10.1039/d2cc00424k

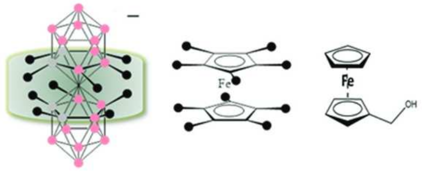

Scheme 1 Schematic representation of the 'canopy effect' for $[3,3'\text{-}M(1,2\text{-}C_2B_9H_{11})_2]^-$ (M = Co, Fe) in comparison to the planar ferrocene (Fc) and ferrocene methanol (FcMe).

producing a θ shape molecular anion.[12] Interestingly, these compounds can be soluble in both aqueous and non-aqueous systems without any structural modifications depending on the cation, unlike ferrocene. Structurally, due to the 3-dimensional nature of the cluster, a 'canopy effect' is produced which better shields the redox active metal center from the external solvent environment in comparison to ferrocene which offers only a 2-dimensional rigidity to the metal center (Scheme 1). Notably, $M'[3,3'\text{-}M(1,2\text{-}C_2B_9H_{11})_2]$ (M = Co, Fe), when M′ = Na, K is water soluble and when M′ = Cs is soluble in electrochemically common non-aqueous solvents.[13] When M′ = H, it is soluble in both the mediums but as it is a strong acid, it can lead to possible interactions with the solvent. Therefore, for this study, we have focused on the salts of alkaline ions. Herein, we discuss the potential application of $[M(C_2B_9H_{11})_2]^-$ as an internal reference by conducting a comparative study with the currently accepted and widely employed internal reference ferrocene and its analogues.

These carborane clusters are gaining popularity among a broad scientific community owing to their attractive properties such as non-localized negative charge and 3D-aromaticity,[14] ability to form hydrogen, $C_c\text{–}H\cdots O$ and dihydrogen, $C_c\text{–}H\cdots B\text{–}H$, bonds,[15] water solubility[13] and easy derivatization similar to organic compounds.[16] In this study, we have focused on the electrochemical properties of $[3,3'\text{-}Co(1,2\text{-}C_2B_9H_{11})_2]^-$ (denoted as [*o*-COSAN]$^-$) and $[3,3'\text{-}Fe(1,2\text{-}C_2B_9H_{11})_2]^-$ (denoted as [*o*-FESAN]$^-$) exploiting the reversible redox active pairs, $Co^{3+/2+}$ and $Fe^{3+/2+}$ and comparing its aqueous and non-aqueous behavior in dry acetonitrile and water as solvents with ferrocene (Fc) and ferrocene methanol (FcMe) in the same solvents. The study was undertaken using cyclic voltammetry (CV) with a three-electrode system of glassy carbon (working), Pt wire (auxiliary) and Ag/AgCl or saturated calomel electrode (SCE) (reference).

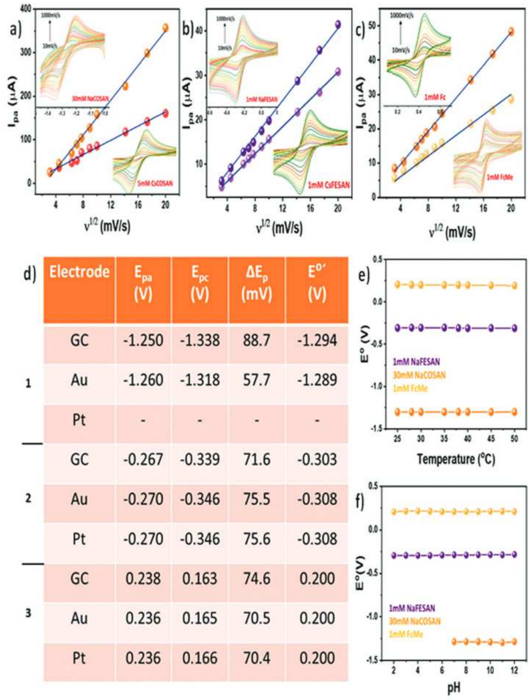

	Electrode	E_{pa} (V)	E_{pc} (V)	ΔE_p (mV)	$E^{0\prime}$ (V)
	GC	-1.250	-1.338	88.7	-1.294
1	Au	-1.260	-1.318	57.7	-1.289
	Pt	-	-	-	-
	GC	-0.267	-0.339	71.6	-0.303
2	Au	-0.270	-0.346	75.5	-0.308
	Pt	-0.270	-0.346	75.6	-0.308
	GC	0.238	0.163	74.6	0.200
3	Au	0.236	0.165	70.5	0.200
	Pt	0.236	0.166	70.4	0.200

Fig. 1 Formal potential ($E^{0\prime}$) and peak potential separation (ΔE_p) obtained in different experimental conditions. (a) Anodic peak current (i_{pa}) *vs.* $\nu^{1/2}$ for Na[*o*-COSAN] (orange) and Cs[*o*-COSAN] (red). (b) Anodic peak current (i_{pa}) *vs.* $\nu^{1/2}$ for Na[*o*-FESAN] (purple) and Cs[*o*-COSAN] (violet). (c) Anodic peak current (i_{pa}) *vs.* $\nu^{1/2}$ for Fc (light orange) and FcMe (yellow). Insets in each figure shows the CV for the respective linear trends. (d) Tabular description of $E^{0\prime}$ and ΔE_p for different working electrodes in 0.3 M KNO_3 *vs.* Ag/AgCl (1 M KCl) at 100 mV s^{-1}. 1 – Na[*o*-COSAN], 2 – Na[*o*-FESAN], 3 – FcMe. (e) Temperature dependence of $E^{0\prime}$ with GC as the working electrode. (f) Variation of $E^{0\prime}$ with PH using 0.1 M Britton–Robinson buffer as the electrolyte.

Electrolytes play a significant role in determining the charge-transfer kinetics in any electrochemical process. Hence, it is important to investigate the effect of different electrolytes on a redox system. Consequently, a series of CV measurements were carried out using different electrolytes such as KNO_3, NaCl, phosphate buffer, among others, with Na[*o*-COSAN] and Na[*o*-FESAN] in comparison to FcMe (Fig. S1, ESI†). The experiments showed that the metallacarboranes behaved reversibly with negligible variations in the formal potential ($E^{0\prime}$) (Table S1, ESI†) in different electrolytes and among them, KNO_3 was chosen as the electrolyte for the subsequent experiments. A high concentration of the electrolyte is required to ensure efficient charge transfer by increasing the conductivity of the solution as well as limiting the migration of the analyte.[17] CV measurements were performed by sequentially increasing the concentration of the electrolyte to understand the impact of varying electrolyte concentrations. Expectedly, at lower concentrations of the electrolyte the charge transfer was limited and hence the peak potential separation (ΔE_p) was large in all the compounds investigated including FcMe (Fig. S2, ESI†). Even in non-aqueous solvent, where tetrabutylammonium perchlorate (TBAP) was used as the electrolyte, a similar tendency was observed (Fig. S3, ESI†). The optimum concentration of the electrolyte for the study was chosen as 0.3 M. Another important parameter which greatly affects the electrochemical behaviour of a redox system is the scan rate (ν). Scan rate dictates the rate of change of potential and a higher scan rate would imply a faster decrease in the diffusion layer, thereby producing higher peak currents.[18] Fig. 1a–c shows the linear dependency of the anodic peak current (i_{pa}) with the square root of the scan rate ($\nu^{1/2}$) in accordance to the Randles–Sevcik equation. Fig. 1a and b show the variation of the anodic peak current for $[o\text{-COSAN}]^-$ and $[o\text{-FESAN}]^-$, respectively (Fig. S4a–c, ESI†). A similar trend was also observed for the experiments performed in organic electrolyte using Cs[*o*-COSAN] and Cs[*o*-FESAN] in comparison to Fc (Fig. S4d–f, ESI†). Therefore, it can be inferred that the redox process of $[o\text{-COSAN}]^-$ and $[o\text{-FESAN}]^-$ is a diffusion-controlled reversible process. The formal potential ($E^{0\prime}$) and the peak potential separation (ΔE_p) were also constant with small variations in different scan rates. These results are encouraging and asserts the capability of $[3,3'\text{-M}(1,2\text{-C}_2\text{B}_9\text{H}_{11})_2]$ (M = Co, Fe) as an internal reference.

A major factor to contemplate while considering any new redox system as a reference for electrochemical studies is to understand its behaviour in a solvent system. Previously, we have shown that due to the ability of the metallacarboranes to form strong hydrogen and di-hydrogen bonds, $[o\text{-COSAN}]^-$ has a remarkable ability to self-assemble in the form of vesicles and micelles in an aqueous environment.[19] Hence, to substantiate that the self-assembling ability of $[o\text{-COSAN}]^-$ and $[o\text{-FESAN}]^-$ has negligible influence on the $E^{0\prime}$ of the redox couple, CV measurements were performed in water solutions with different concentration of the Na salts of the metallacarboranes (Fig. S5, ESI†). The concentration was varied from 5–50 mM for Na[*o*-COSAN] and 1–65 mM for Na[*o*-FESAN]. To notice, while the peak potential separation (ΔE_p) remained in the range for one-electron transfer process for Na[*o*-COSAN] in all concentrations, for Na[*o*-FESAN] at higher concentrations (from 50 mM), the ΔE_p was larger (Table S2, ESI†). This can be ascribed to the high barrier rendered to the electron transfer kinetics due to the formation of vesicles in Na[*o*-FESAN] whereas in the case of Na[*o*-COSAN], the vesicle formation did not show any profound effect on the electrochemical response. Nevertheless, both the metallacarboranes showed highly reversible electrochemical behavior for a wide range of concentration with a constant formal potential of −1.282 V and −0.283 V for Na[*o*-COSAN] and Na[*o*-FESAN], respectively.

The pH of an electrolytic solution greatly influences the Nernstian equilibrium of an electrochemical process. Depending on the pH, the redox activity of the electroactive species may vary and in case of metals an acidic pH can even lead to corrosion.[20] Hence, it becomes important to ascertain the electrochemical response of the internal references in varying pH conditions. Subsequently, pH dependent CV experiments were performed using 0.1 M Britton–Robinson (BR) buffer as the electrolyte (Fig. S6, ESI†). Upon varying the pH from 2–12, the formal potential ($E^{0\prime}$) and the peak potential separation (ΔE_p) were fairly constant for Na[*o*-FESAN] at −0.291 V and 74 mV, respectively, and comparable to the tendency of FcMe (Fig. 1f, ESI†). However, for Na[*o*-COSAN] as the potential window was very close to the water reduction peak, at acidic pH it was difficult to observe an electrochemical response. Conversely, at basic pH, the $E^{0\prime}$ was constant at −1.285 V (Fig. 1f) while some fluctuations were observed in the ΔE_p (Fig. S7, ESI†). In general, most of the electrochemical experiments are carried out at ambient temperature. But while considering the ability of a compound to be used as an internal reference it is relevant to subject it to harsh conditions and understand the behaviour. Therefore, CV measurements in temperature ranges from 25–50 °C were carried out (Fig. S8, ESI†). From the experiments, it was observed that the temperature did not influence the formal potential ($E^{0\prime}$) and the peak potential separation (ΔE_p) in Na[*o*-COSAN] and Na[*o*-FESAN] and that the compounds were thermally stable throughout the measurement (Fig. 1e and Fig. S9, ESI†). Different working electrode materials can influence the electrochemical response due to adsorption, difference in electron transfer kinetics as well as occurrence of electrode specific chemical reactions. Fig. 1d describes the various peak potentials along with formal

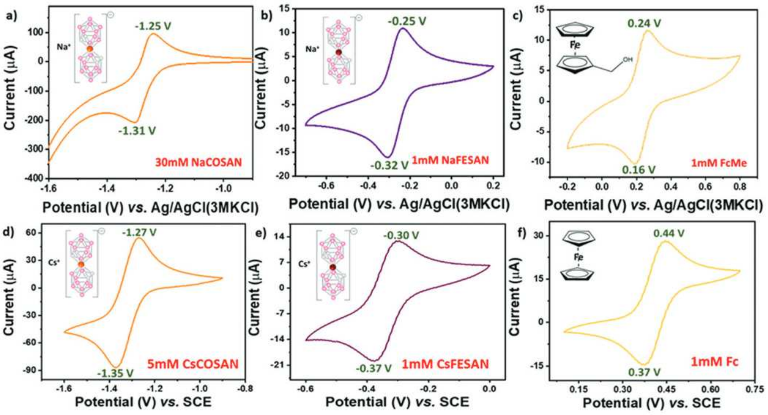

Fig. 2 Cyclic voltammograms for the reversible redox systems investigated with GC as the working electrode and Pt wire as the auxiliary electrode, measured at 100 mV s^{-1}. (a) 30 mM Na[*o*-COSAN] in 0.3 M KNO_3. (b) 1 mM Na[*o*-FESAN] in 0.3 M KNO_3. (c) 1 mM FcMe in 0.3 M KNO_3. (d) 5 mM Cs[*o*-COSAN] in 0.3 M TBAP/dry AcN. (e) 1 mM Cs[*o*-FESAN] in 0.3 M TBAP/dry AcN. (f) 1 mM Fc in 0.3 M TBAP/dry AcN.

and peak separation potentials for different electrodes such as glassy carbon, Au and Pt. Changing the electrode material had negligible influence on the potentials for Na[*o*-COSAN] as well as Na[*o*-FESAN] and hence, suggests that these metallacarboranes interact minutely with the electrode materials (Fig. S10, ESI†). Equivalent studies were also performed in non-aqueous solvents and similar results were obtained (Fig. S11, ESI†). Interestingly, the Cs salts of the metallacarboranes are partially soluble in water, particularly Cs[*o*-FESAN]. The comparison of the CVs of Na[*o*-FESAN] and Cs[*o*-FESAN] in aqueous solvent shows similar peak potentials with slight reduction in peak currents (Fig. S12, ESI†). Hence, Cs[*o*-FESAN] can ideally be used as an internal reference in both solvent systems, but preferably in organic solvents.

In this article, we have demonstrated the redox reversible behavior of $[3,3'\text{-M}(1,2\text{-C}_2\text{B}_9\text{H}_{11})_2]$ (M = Co, Fe) in different electrochemical environments and conditions with regard to Fc and FcMe. Fig. 2 shows the electrochemical response for the compounds investigated with the $E^{0\prime}$ as −1.28 V, −1.27 V, −0.28 V and −0.29 V (*vs.* Ag/AgCl) as well as ΔE_p as 60 mV, 80 mV, 70 mV and 70 mV for Na[*o*-COSAN], Cs[*o*-COSAN], Na[*o*-FESAN] and Cs[*o*-FESAN], respectively. The main characteristics required for an internal reference is to have constant peak potentials and redox behaviour with high thermal and chemical stability. The various CV experiments performed have shown that the metallacarboranes, particularly $[o\text{-FESAN}]^-$, has a steady redox response with remarkable thermal and chemical stability and a $E^{0\prime}$ very near to NHE, closer than Fc. All these results are suggestive of the potential use of $[3,3'\text{-M}(1,2\text{-C}_2\text{B}_9\text{H}_{11})_2]^-$ (M = Co, Fe) as an internal reference in both aqueous and non-aqueous solvents, without any structural or functional modifications. Precisely, the same internal reference for both organic and aqueous electrolytes. As a proof of concept we have tested these electrodes as internal references in a THF:water mixture and have proven a superior performance than the conventional Ag/AgCl electrode that experienced a drift.

This work was funded by the Spanish Ministry of Science, through the "Severo Ochoa" Programme for Centres of Excellence in R&D (CEX2019-000917-S) as well as the Ministerio de Economia y Competitividad (PID2019-106832RB-I00), (PID2020-116728RB-I00, CTQ2015-71955-RED ELECTROBIONET) and Generalitat de Catalunya (2017SGR1720) are appreciated. J. A. M. Xavier acknowledges DOC-FAM programme under the Marie Sklodowska-Curie grant agreement no. 754397 and is enrolled in the PhD programme in UAB. Support from the Community of Madrid (TRANSNANOAVANSENS S2018/NMT-4349), is acknowledged.

Conflicts of interest

There are no conflicts to declare.

Notes and references

1 P. Zanello, *Inorganic Electrochemistry*, The Royal Society of Chemistry, 2003.
2 A. A. J. Torriero, S. W. Feldberg, J. Zhang, A. N. Simonov and A. M. Bond, *J. Solid State Electrochem.*, 2013, **17**, 3021–3026.
3 M. P. S. Mousavi, S. A. Saba, E. L. Anderson, M. A. Hillmyer and P. Bühlmann, *Anal. Chem.*, 2016, **88**, 8706–8713.
4 (*a*) R. R. Gagne, C. A. Koval and G. C. Lisensky, *Inorg. Chem.*, 1980, **19**, 2854–2855; (*b*) G. Gritzner and J. Kuta, *Pure Appl. Chem.*, 1984, **56**, 461–466.
5 M. J. A. Shiddiky, A. A. J. Torriero, C. Zhao, I. Burgar, G. Kennedy and A. M. Bond, *J. Am. Chem. Soc.*, 2009, **131**, 7976–7989.
6 (*a*) M. Matsumoto and T. W. Swaddle, *Inorg. Chem.*, 2004, **43**, 2724–2735; (*b*) I. Noviandri, K. N. Brown, D. S. Fleming, P. Gulyás, P. A. Lay, A. Masters and L. Phillips, *J. Phys. Chem. B*, 1999, **103**, 6713–6722.
7 S. McCormack, N. R. Russell and J. F. Cassidy, *Electrochim. Acta*, 1992, **37**, 1939–1944.
8 H. M. A. Amin, Y. Uchida, E. Kätelhön and R. G. Compton, *J. Electroanal. Chem.*, 2021, **880**, 114891.
9 K. Z. Brainina, A. V. Tarasov and M. B. Vidrevich, *Chemosensors*, 2020, **8**, 15.
10 (*a*) A. A. J. Torriero, *Med. Analyt. Chem. Int. J.*, 2019, **2**, 2–4; (*b*) A. A. J. Torriero, *Electrochim. Acta*, 2014, **137**, 235–244; (*c*) A. Paul, R. Borrelli, H. Bouyanfif, S. Gottis and F. Sauvage, *ACS Omega*, 2019, **4**, 14780–14789.
11 (*a*) S. D. Collyer, F. Davis, A. Lucke, C. J. M. Stirling and S. P. J. Higson, *J. Electroanal. Chem.*, 2003, **549**, 119–127; (*b*) P. Fischer, P. Mazúr and J. Krakowiak, *Molecules*, 2022, **27**, 560.
12 (*a*) R. A. Wiesboeck and M. F. Hawthorne, *J. Am. Chem. Soc.*, 1964, **86**, 1642; (*b*) R. N. Grimes, *Carboranes*, Elsevier Inc., New York, 3rd edn, 2016.
13 M. Tarrés, C. Viñas, P. González-Cardoso, M. M. Hänninen, R. Sillanpää, V. Dordovic, M. Uchman, F. Teixidor and P. Matejcek, *Chem. – Eur. J.*, 2014, **20**, 6786.
14 (*a*) C. Masalles, J. Llop, C. Viñas and F. Teixidor, *Adv. Mater.*, 2002, **14**, 826–829; (*b*) J. Poater, M. Solà, C. Viñas and F. Teixidor, *J. Am. Chem. Soc.*, 2020, **142**, 9396.
15 (*a*) D. Brusselle, P. Bauduin, L. Girard, A. Zaulet, C. Viñas, F. Teixidor, I. Ly and O. Diat, *Angew. Chem., Int. Ed.*, 2013, **52**, 12114–12118; (*b*) C. E. Housecroft, *J. Organomet. Chem.*, 2015, **798**, 218; (*c*) M. J. Hardie and C. L. Raston, *Chem. Commun.*, 2001, 905.
16 D. Olid, R. Núñez, C. Viñas and F. Teixidor, *Chem. Soc. Rev.*, 2013, **42**, 3318–3336.
17 (*a*) H. P. Bennetto, *Annu. Rep. Prog. Chem., Sect. A: Gen., Phys. Inorg. Chem.*, 1973, **70**, 223–248; (*b*) N. Matubayasi, *Surface tension and related thermodynamic quantities of aqueous electrolyte solutions*, Taylor & Francis, Boca Raton, 2014; (*c*) S. Srinivasan, *Electrode/Electrolyte Interfaces Structure and Kinetics of Charge Transfer*, Springer US, Boston, MA, 2006, pp. 27–92.
18 A. J. Bard and L. R. Faulkner, *Electrochemical methods: fundamentals and applications/Allen*, Wiley, New York, 1980.
19 (*a*) P. Bauduin, S. Prevost, P. Farràs, F. Teixidor, O. Diat and T. Zemb, *Angew. Chem., Int. Ed.*, 2011, **50**, 5298–5300; (*b*) M. Uchman, V. Ďorďovič, Z. Tošner and P. Matějíček, *Angew. Chem., Int. Ed.*, 2015, **54**, 14113; (*c*) D. C. Malaspina, C. Viñas, F. Teixidor and J. Faraudo, *Angew. Chem., Int. Ed.*, 2020, **59**, 3088.
20 N. Elgrishi, K. J. Rountree, B. D. McCarthy, E. S. Rountree, T. T. Eisenhart and J. L. Dempsey, *J. Chem. Educ.*, 2018, **95**, 197–206.

Journal of
Materials Chemistry B

ROYAL SOCIETY
OF CHEMISTRY

PAPER

View Article Online
View Journal

Cite this: DOI: 10.1039/d3tb00816a

Single stop analysis of a protein surface using molecular probe electrochemistry†

Jewel Ann Maria Xavier, Isabel Fuentes, Miquel Nuez-Martínez, Clara Viñas and Francesc Teixidor *

Visualization of a protein in its native form and environment without any interference has always been a challenging task. Contrary to the assumption that protein surfaces are smooth, they are in fact highly irregular with undulating surfaces. Hence, in this study, we have tackled this ambiguous nature of the 'surface' of a protein by considering the 'effective' protein surface (EPS) with respect to its interaction with the geometrically well-defined and structurally inert anionic molecule $[3,3'\text{-Co}(1,2\text{-C}_2\text{B}_9\text{H}_{11})_2]^-$, abbreviated as $[o\text{-COSAN}]^-$, whose stability, propensity for amine residues, and self-assembling abilities are well reported. This study demonstrates the intricacies of protein surfaces exploiting simple electrochemical measurements using a 'small molecule' redox-active probe. This technique offers the advantage of not utilizing any harsh experimental conditions that could alter the native structure of the protein and hence the protein integrity is retained. Identification of the amino acid residues which are most involved in the interactions with $[3,3'\text{-Co}(1,2\text{-C}_2\text{B}_9\text{H}_{11})_2]^-$ and how a protein's environment affects these interactions can help in gaining insights into how to modify proteins to optimize their interactions particularly in the fields of drug design and biotechnology. In this research, we have demonstrated that $[3,3'\text{-Co}(1,2\text{-C}_2\text{B}_9\text{H}_{11})_2]^-$ anionic small molecules are excellent candidates for studying and visualizing protein surfaces in their natural environment and allow proteins to be classified according to the surface composition, which imparts their properties. $[3,3'\text{-Co}(1,2\text{-C}_2\text{B}_9\text{H}_{11})_2]^-$ 'viewed' each protein surface differently and hence has the potential to act as a simple and easy to handle cantilever for measuring and picturing protein surfaces.

Received 12th April 2023,
Accepted 28th July 2023

DOI: 10.1039/d3tb00816a

rsc.li/materials-b

Introduction

The shape of a protein is a consequence of the order of its amino acids, its hydrogen bond interactions, and very fundamentally its tertiary structure, which is influenced by the environment in which the protein operates. All of these factors define a protein's function, since the protein's ability to interact with other molecules depends on its structure, and a fundamental aspect of this interaction is the protein's surface.[1,2] The 'surface' of a protein is an ambiguous term as it depends on a number of factors, most notably the specific environment in which the protein is situated. The effect of different ions and solvent molecules surrounding the protein on its structure is significant. Most often, a ball-park surface area is calculated by considering the hydrodynamic or Stokes radius in the case of proteins. In this approximation, a uniform sphere with a smooth surface having the same hydrodynamic properties as the biomolecule is considered.[3,4] A major drawback to this approximation is that it does not account for the protein shape, which can be either globular or non-globular and is highly irregular, nor the environment of the protein.[5–8] The interaction of the amino acid residues with different ions can result in altering the surface of the proteins.[9–11] Contrary to the assumption that protein surfaces are smooth, they are in fact highly irregular with undulating surfaces. The current state-of-the-art techniques for studying a protein are either by X-ray and neutron diffraction studies of crystallized proteins, cryo-electron microscopy (cryo-EM), and nuclear magnetic resonance (NMR) spectroscopy or through computer modelling.[12–20] Recent developments in the field of fluorescence imaging have shown the use of dyes forming covalent bonds with specific amino acid residues such as lysine-161 in human serum albumin (HSA) for *in-vivo* studies which also allows for better understanding of the proteins.[21,22] Studies involving direct electrochemical measurements of proteins to assess the surface are common but more often tend to subject the proteins to unnecessary stresses such as application of high voltage leading to denaturalization.[23–25] Moreover, most of the

---

Institut de Ciencia de Materials de Barcelona (ICMAB-CSIC), Campus de la UAB, Bellaterra, Spain. E-mail: jxavier@icmab.es, isa7391@gmail.com, mnuez@icmab.es, clara@icmab.es, teixidor@icmab.es

† Electronic supplementary information (ESI) available. See DOI: **https://doi.org/10.1039/d3tb00816a**

redox active amino acids such as tyrosine and tryptophan are non-polar and hence prefer to be located in the interior of the proteins with very few residues on the surface.[26] All these strategies fail to visualize the protein in its native form and environment. Therefore, to overcome this problem, we reasoned, why not reap the benefits from an electroactive compound external to the protein that interacts strongly with the polar residues and has self-assembling properties? The approach is challenging as we would need a water-soluble substance which is redox-reversible, has an electrochemical response well within the window of application in water, interacts rapidly and strongly with the basic groups on the residues and has self-assembly properties so as to fill the available surface area of the protein to the maximum extent. What could be the substance that satisfies all these requirements?

In this study, we aim at gaining molecular level understanding of the 'effective protein surface' (EPS) using a geometrically well-defined and structurally inert anionic molecule $[3,3'\text{-Co}(1,2\text{-C}_2\text{B}_9\text{H}_{11})_2]^-$, known as [*o*-COSAN]$^-$, whose stability, tendency for amine residues through the formation of strong N–H···B–H di hydrogen bonds and self-assembling abilities are well documented.[27–32] Another notable type of assembly that has been reported is based on the *nido*-$[\text{C}_2\text{B}_9\text{H}_{11}]^-\cdots\pi$ interactions. These interactions give rise to a range of photophysical properties, including aggregation-induced emission and aggregation-caused quenching, all within a single molecule.[33] The 'effective protein surface' describes the actual protein form with its anomalies and irregularities in its native environment contrary to the smooth sphere visualized using the Stokes radius. $[3,3'\text{-Co}(1,2\text{-C}_2\text{B}_9\text{H}_{11})_2]^-$ is a θ-shaped metallacarborane complex where the metal ion is sandwiched between the two dicarbollide clusters. Depending on the relative positions of the carbon atoms, three distinct rotamers can be observed (Fig. 1a), Previously, we had observed and demonstrated using DFT calculations that the cisoid rotamer exhibits a distinct 'hydrophilic' polar head region and a 'hydrophobic' apolar tail region.[28] This unique configuration enables the cisoid rotamer to display surfactant-like behavior, contrary to the transoid rotamer (Fig. 1b).[34] Moreover, the reversible redox capacity of $[3,3'\text{-Co}(1,2\text{-C}_2\text{B}_9\text{H}_{11})_2]^-$ and $[3,3'\text{-Fe}(1,2\text{-C}_2\text{B}_9\text{H}_{11})_2]^-$ in water has also been well defined and these molecules have been postulated as universal internal ref. 35. Thus, using readily available electrochemical cyclic voltammetry or differential pulse electrochemical techniques and $[3,3'\text{-Co}(1,2\text{-C}_2\text{B}_9\text{H}_{11})_2]^-$, we will learn about the EPS and establish the mechanisms of ion–protein interactions. We propose $[3,3'\text{-Co}(1,2\text{-C}_2\text{B}_9\text{H}_{11})_2]^-$ as a 'small molecule probe' analogous to a cantilever in scanning transmission electron microscopy (STEM) for identifying the nature of a protein's surface in its native or almost native form.[36,37]

We, among others, have recently demonstrated that the $[3,3'\text{-Co}(1,2\text{-C}_2\text{B}_9\text{H}_{11})_2]^-$ anion strongly interacts with bovine serum albumin (BSA) with a molar ratio 100 : 1.[38–40] The interaction as well as the molar ratio were assessed by measuring the changes in physical properties, including fluorescence and size, through techniques such as fluorescence spectroscopy, dynamic light scattering (DLS), zeta potential analysis, or studying the precipitated complex using energy-dispersive X-ray spectroscopy (EDX) or elemental analysis. Among these studies, dynamic light scattering (DLS) and zeta potential measurements played a crucial role. DLS provided valuable information about the hydrodynamic diameter of the complex, allowing us to propose a model in which BSA is encapsulated by $[3,3'\text{-Co}(1,2\text{-C}_2\text{B}_9\text{H}_{11})_2]^-$ in an end-on position. On the other hand, zeta potential measurements reaffirmed the presence of the anion on the BSA surface by confirming the negative charge it imparted. Interestingly, the total number of basic amino acid (lysine, arginine and histidine) residues in a BSA molecule is also 100 which coincides with the number of $[3,3'\text{-Co}(1,2\text{-C}_2\text{B}_9\text{H}_{11})_2]^-$.[41,42] If we were to consider that $[3,3'\text{-Co}(1,2\text{-C}_2\text{B}_9\text{H}_{11})_2]^-$ interacts strongly with the basic amino acid residues, the conclusion seemed very straightforward. There was one $[3,3'\text{-Co}(1,2\text{-C}_2\text{B}_9\text{H}_{11})_2]^-$ for every basic residue. Would it all be that easy? Or is the BSA an ideal model? We will see throughout this article that there are several other factors that must influence the ratio of $[3,3'\text{-Co}(1,2\text{-C}_2\text{B}_9\text{H}_{11})_2]^-$ molecules *vs.* basic residues. We have postulated the potential application of $[3,3'\text{-Co}(1,2\text{-C}_2\text{B}_9\text{H}_{11})_2]^-$ as a 'universal' robust shield on proteins which would protect them from denaturalization at high temperatures and retain their activity, irrespective of the nature of the protein.[38] But it was not to be, as the initial experiments with enzymes suggested that $[3,3'\text{-Co}(1,2\text{-C}_2\text{B}_9\text{H}_{11})_2]^-$

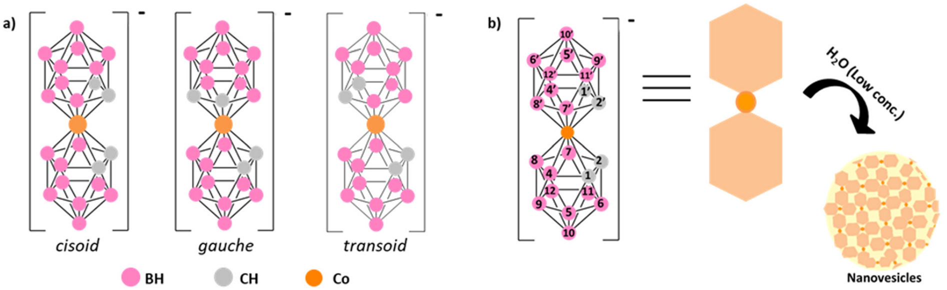

Fig. 1 (a) Schematic representation of the three different rotamers of [*o*-COSAN]$^-$: cisoid, *gauche* and transoid. (b) The formation of nanovesicles at a low concentration of the *cis*-[*o*-COSAN]$^-$ rotamer in an aqueous solvent.

was not capable of shielding them all. This beseeched us to ponder on whether $[3,3'\text{-Co}(1,2\text{-C}_2\text{B}_9\text{H}_{11})_2]^-$ really viewed all protein surfaces in the same way.

Interestingly, the strong interaction between the BSA and the $[3,3'\text{-Co}(1,2\text{-C}_2\text{B}_9\text{H}_{11})_2]^-$ cage raises high expectations such as that suggested by Goszczynski and coworkers to enhance the activity of therapeutic peptides.[43] Our primary investigations were carried out with BSA and $[3,3'\text{-Co}(1,2\text{-C}_2\text{B}_9\text{H}_{11})_2]^-$ in pure water, without any buffer or other additives.[38,44] In the body, however, the proteins are in an environment with a high electrolyte content and physiological pH. Hence, it is rationale to investigate the behavior of θ-metallacarboranes under physiological conditions and to draw conclusions about the capabilities of $[3,3'\text{-Co}(1,2\text{-C}_2\text{B}_9\text{H}_{11})_2]^-$ in understanding the protein surface better. In this article, we address these issues and provide a method for interpreting the protein surface areas in terms of EPS. Hence, the study developed here focuses on the application of simple electrochemical techniques for understanding the EPS and consequently its properties and functions under native or near native conditions using a highly suitable redox reversible probe.[45]

The electrochemical experiments are performed in 0.1 M NaCl which acts as the electrolyte. Both Na^+ and Cl^- are part of the Hofmeister series and are chaotropic in nature.[46,47] As a result, the hydrodynamic radius varies in the presence and absence of NaCl and hence the surface area. We also hypothesize that in the presence of NaCl, the polar amino acid residues become even more exposed in comparison to pure water which could imply an even higher ratio of $[3,3'\text{-Co}(1,2\text{-C}_2\text{B}_9\text{H}_{11})_2]^-$ on the surface, limited by surface availability due to the plausible competition between $[3,3'\text{-Co}(1,2\text{-C}_2\text{B}_9\text{H}_{11})_2]^-$ and the anions in the electrolyte. The cyclic voltammetry method adopted is gentle enough to avoid protein denaturation, especially considering the protective effect of $[3,3'\text{-Co}(1,2\text{-C}_2\text{B}_9\text{H}_{11})_2]^-$. In this work, we successfully demonstrate the feasibility of $[3,3'\text{-Co}(1,2\text{-C}_2\text{B}_9\text{H}_{11})_2]^-$ as a 'small molecule' probe interacting with protein residues within their natural environment. Moreover, our findings reveal that the graphical profile of current intensity *versus* protein concentration differs across the proteins investigated. Although these comparisons have been conducted experimentally, we are certain that with the aid of an appropriate algorithm, we could obtain high-resolution visualizations of the protein surface within its natural environment.

Results and discussion

Experimental evidence for the interaction of [*o*-COSAN]$^-$ with basic amino acids

The preparation of the electroactive component in potentiometric membranes for the detection of amino acids was based on the high insolubility of the [YH] $[3,3'\text{-Co}(1,2\text{-C}_2\text{B}_9\text{H}_{11})_2]$ salt in water, with Y being the amino acid under consideration.[42,48] The same concept was applied to stabilize magnetic nanoparticles decorated with amine groups incorporating $[3,3'\text{-Co}(1,2\text{-C}_2\text{B}_9\text{H}_{11})_2]^-$ anions.[49] However, these studies offered a vague and general overview of the possible interactions. Hence, in order to gain a deeper insight particularly at the molecular level, a study was performed to visualize the $[3,3'\text{-Co}(1,2\text{-C}_2\text{B}_9\text{H}_{11})_2]^-$/amino acid interaction *via* ^{1}H- and ^{11}B-NMR spectroscopies to observe the variations in the resonances assumed to be involved in the $[3,3'\text{-Co}(1,2\text{-C}_2\text{B}_9\text{H}_{11})_2]^-$/amino acid interaction [refer the ESI† for further details].

The experiments were performed at a fixed $\text{Na}[3,3'\text{-Co}(1,2\text{-C}_2\text{B}_9\text{H}_{11})_2]$ concentration of 2 mM in D_2O with increasing concentrations of the amino acids. The influence of the amino acid on the whole spectrum was studied and the resonance due to the B–H of $[3,3'\text{-Co}(1,2\text{-C}_2\text{B}_9\text{H}_{11})_2]^-$ appearing at 2.60 ppm was taken as the reference (Fig. S1, ESI†). The amino acids studied were L-glutamine, L-arginine, L-lysine and L-histidine of which the latter three contain basic functionalities in the side chains, while L-glutamine was chosen as a representative amino acid for other amino acids such as serine, methionine or alanine, among many others.

Fig. 2 encompasses the results of this study and it can be observed that for the basic amino acids, L-arginine, L-lysine and L-histidine, the intensity of the $^1\text{H}\{^{11}\text{B}\}$-NMR $[3,3'\text{-Co}(1,2\text{-C}_2\text{B}_9\text{H}_{11})_2]^-$ B–H (4,4′,7,7′) signal decreases as a consequence of the increase of the amino acid/$[3,3'\text{-Co}(1,2\text{-C}_2\text{B}_9\text{H}_{11})_2]^-$ ratio (Fig. S3, S5 and S7, ESI†). However, this decrement is neither proportional to the amount of the amino acid added which seems to indicate the existence of an equilibrium, nor is it equal for all the three amino acids studied. For instance, in the case of lysine, the B–H signal in the ^1H-$\{^{11}\text{B}\}$ NMR vanishes completely, while the decrease in intensity is

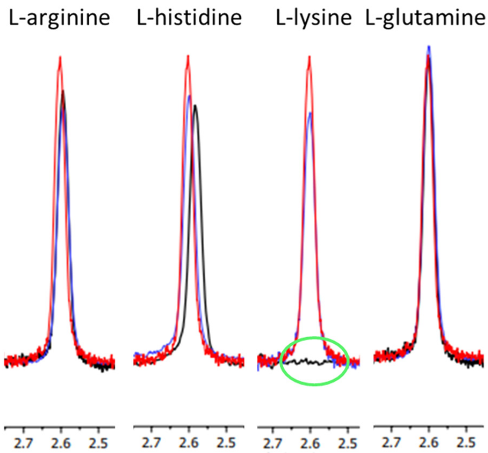

Fig. 2 $^1\text{H}\{^{11}\text{B}\}$-NMR spectra in the range of 2.8 to 2.4 ppm B–H (4,4′,7,7′) obtained for the different mixtures of [*o*-COSAN]$^-$ and the amino acids (L-arginie, L-histidine, L-lysine and L-glutamine). Na[*o*-COSAN] 2 mM appears in red, Na[*o*-COSAN] 2 mM + 2 mM of the corresponding amino acid appears in blue and Na[*o*-COSAN] 2 mM + 60 mM of the corresponding amino acid appears in black; the green circle highlights the flatline due to interaction with L-lysine at 60 mM. The solvent used was D_2O.

limited in the case of arginine and histidine and such a decrease was not observed for glutamine (Fig. 2).

These data already suggest that the interaction of different amino acids with $[3,3'\text{-Co}(1,2\text{-C}_2\text{B}_9\text{H}_{11})_2]^-$ is not the same; strong for the amino acids with basic residues with L-lysine having the strongest interaction and weak or non-existent for the remaining amino acids. And what can be the origin for the disappearance of the B–H resonances? Our interpretation is that nanoscopic aggregates are generated between the basic amino acids and $[3,3'\text{-Co}(1,2\text{-C}_2\text{B}_9\text{H}_{11})_2]^-$, which are much larger than the individual components and are likely to take on a landscape layout. When $[3,3'\text{-Co}(1,2\text{-C}_2\text{B}_9\text{H}_{11})_2]^-$ molecules form aggregates with basic amino acids, the local environment around each molecule changes. This altered environment affects the electronic properties and motion of the molecules, leading to changes in the NMR signal. The formation of aggregates can cause significant line broadening, making the signal appear wider and less distinct in the NMR spectrum.[34] It should be noted that neither colloids nor precipitates were observed during the measurement of these experiments.

Consistent with these results are the $^{11}\text{B}\{^1\text{H}\}$-NMR spectra of the $[3,3'\text{-Co}(1,2\text{-C}_2\text{B}_9\text{H}_{11})_2]^-$/amino acid complexes. The $^{11}\text{B}\{^1\text{H}\}$-NMR spectrum of $\text{Na}[3,3'\text{-Co}(1,2\text{-C}_2\text{B}_9\text{H}_{11})_2]$ displays different characteristics when recorded in water or in acetone (Fig. S2, ESI†). In water, the different signals are much wider than in acetone because in one case, the spectra recorded correspond to free rotating molecules, whereas in water, the spectrum of aggregates is recorded, due to self-assembly, forming larger structures that are more difficult to rotate. Therefore, the $^{11}\text{B}\{^1\text{H}\}$-NMR spectrum will be broader when there is interaction between $[3,3'\text{-Co}(1,2\text{-C}_2\text{B}_9\text{H}_{11})_2]^-$ and the amino acid. And in fact, that is what has been observed (Fig. S4 and S6, ESI†). Although there is a decrease in the intensity of the signal, it does not disappear as in the case of the proton spectrum; instead it widens, but not to the point of fading. As observed in the case of $^1\text{H}\{^{11}\text{B}\}$-NMR, the interaction is more evident with L-lysine than for L-arginine and L-histidine, and no signal affectation is observed with glutamine (Fig. 3).

Intensity of current *vs.* ratio of [protein]/[*o*-COSAN]$^-$

The study involves dissolving a given amount of the electrochemically redox-reversible $\text{Na}[\text{Co}(\text{C}_2\text{B}_9\text{H}_{11})_2]$ to which increasing amounts of a protein are added and the current is measured in response to varying potential levels [refer the ESI† for further details]. To perform the experiment, both $[3,3'\text{-Co}(1,2\text{-C}_2\text{B}_9\text{H}_{11})_2]^-$ and the protein must be soluble in water. Since an amperometric property is to be measured, an electrolyte is required, which allows the protein to be in an environment comparable to the physiological one. A point to be pondered upon is that neither the applied potential nor the current intensity conditions should affect the stability of the protein. Following this experiment, a graph is obtained from the DPV (differential pulse voltammetry) experiment, wherein the concentration of $[3,3'\text{-Co}(1,2\text{-C}_2\text{B}_9\text{H}_{11})_2]^-$ remains constant, while the protein concentration increases sequentially (Fig. S9, ESI†). A similar experiment has also been described using $[3,3'\text{-Fe}(1,2\text{-C}_2\text{B}_9\text{H}_{11})_2]^-$ and its interaction with DNA for developing a DNA bio-sensor.[50] The major contribution to the intensity (current, μA) is from $[3,3'\text{-Co}(1,2\text{-C}_2\text{B}_9\text{H}_{11})_2]^-$ that remains free in the solution. Although $[3,3'\text{-Co}(1,2\text{-C}_2\text{B}_9\text{H}_{11})_2]^-$ bound to the protein can also participate in the electron transfer process involving the electrode, the intensity would be much lower in comparison to free $[3,3'\text{-Co}(1,2\text{-C}_2\text{B}_9\text{H}_{11})_2]^-$ and hence for initial purposes, it can be considered negligible. Thus, the current is the highest in the absence of any interacting protein and decreases with the increasing amount of protein in the solution, but it never intersects the y-axis at 0 because of the bounded $[3,3'\text{-Co}(1,2\text{-C}_2\text{B}_9\text{H}_{11})_2]^-$. As mentioned before, we are not considering the residual intensity due to the bounded $[3,3'\text{-Co}(1,2\text{-C}_2\text{B}_9\text{H}_{11})_2]^-$, but this residual current could provide

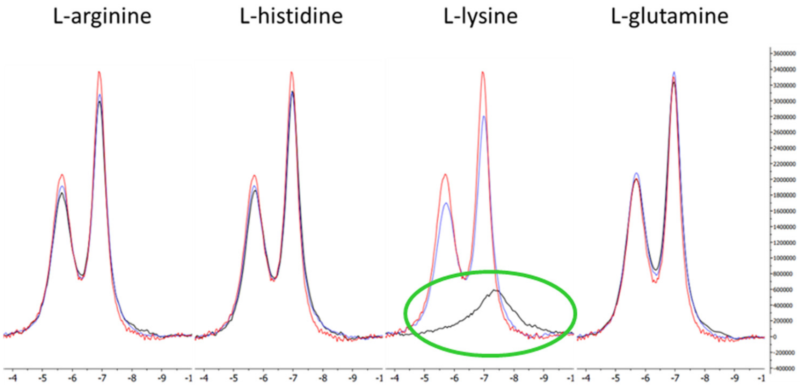

Fig. 3 $^{11}\text{B}\{^1\text{H}\}$-NMR spectra in the range of −4 to −10 ppm (B (4,4′,7,7′,9,9′,12,12′) signal region) obtained for the different mixtures of [*o*-COSAN]$^-$ and the amino acids. Na[*o*-COSAN] 2 mM as a reference appears in red, Na[*o*-COSAN] 2 mM + 2 mM of the corresponding amino acid appears in blue and Na[*o*-COSAN] 2 mM + 60 mM of the corresponding amino acid appears in black; the green circle highlights the broader signal due to interaction with L-lysine at 60 mM. The solvent used was D_2O.

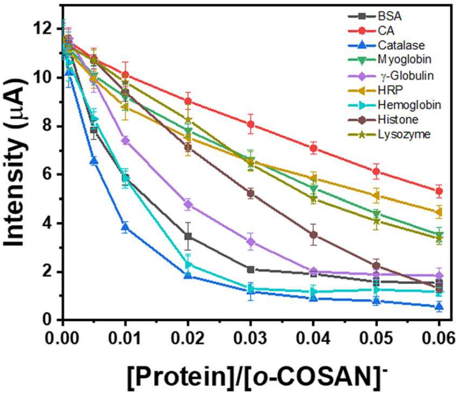

Fig. 4 The current *vs.* the ratio of protein to [*o*-COSAN]$^-$ obtained from the DPV experiment for different proteins measured in 0.1 M NaCl with glassy carbon (GC) as the working electrode and Ag/AgCl(3 M KCl) as the reference electrode.

deeper insights with further advancements in the technique and the development of an appropriate algorithm that would enable high-resolution visualizations of the protein surface within its natural environment. The nature of the curve is different for the different proteins indicative of an underlying factor responsible for the differences in interaction of the protein with $[3,3'\text{-Co}(1,2\text{-}C_2B_9H_{11})_2]^-$. The aim of the study is to understand and elucidate the factors responsible for these differences. For these studies, the key information is gathered from the BSA interacting with $[3,3'\text{-Co}(1,2\text{-}C_2B_9H_{11})_2]^-$, which, as mentioned earlier, can be considered ideal, as the surface obtained by DLS titration with $[3,3'\text{-Co}(1,2\text{-}C_2B_9H_{11})_2]^-$, whose dimensions are well defined, coincides with the number of basic amino residues in the protein.[38] The following plot (Fig. 4) represents the electroactive $[3,3'\text{-Co}(1,2\text{-}C_2B_9H_{11})_2]^-$ current *vs.* the [protein]/$[3,3'\text{-Co}(1,2\text{-}C_2B_9H_{11})_2]^-$ ratio at a fixed $[3,3'\text{-Co}(1,2\text{-}C_2B_9H_{11})_2]^-$ concentration of 10^{-3} M in 10^{-1} M NaCl solution (Table S1, ESI†).

Bound [*o*-COSAN]$^-$ *vs.* ratio of [protein]/[*o*-COSAN]$^-$

Since the study focuses on understanding the interaction of $[3,3'\text{-Co}(1,2\text{-}C_2B_9H_{11})_2]^-$ with the proteins, a more appropriate parameter to consider would be the amount of $[3,3'\text{-Co}(1,2\text{-}C_2B_9H_{11})_2]^-$ bound on the surface of the protein. Tentatively, we can calculate the amount of $[3,3'\text{-Co}(1,2\text{-}C_2B_9H_{11})_2]^-$ bound on the surface of a protein by taking the difference between the initial intensity of $[\text{Co}(C_2B_9H_{11})_2]^-$ in the absence of any protein and the intensity of $[3,3'\text{-Co}(1,2\text{-}C_2B_9H_{11})_2]^-$ in the presence of a protein. This is a rough estimate as some of the $[3,3'\text{-Co}(1,2\text{-}C_2B_9H_{11})_2]^-$ on the surface will be electrochemically active, but for the purpose of this research, it seems to be a fairly good approximation. Thus, if we represent bound $[\text{Co}(C_2B_9H_{11})_2]^-$ current *vs.* the [protein]/$[3,3'\text{-Co}(1,2\text{-}C_2B_9H_{11})_2]^-$ ratio, taking bound $[3,3'\text{-Co}(1,2\text{-}C_2B_9H_{11})_2]^-$ as:

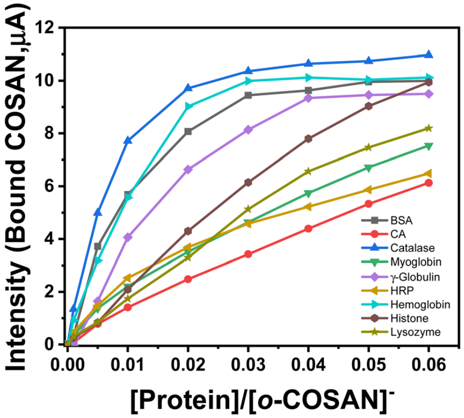

Fig. 5 The calculated intensity for the bound [*o*-COSAN]$^-$ *vs.* the protein to [*o*-COSAN]$^-$ fraction for different proteins.

Bound $[3,3'\text{-Co}(1,2\text{-}C_2B_9H_{11})_2]^-$ = Initial intensity of $[3,3'\text{-Co}(1,2\text{-}C_2B_9H_{11})_2]^-$ − Intensity of $[3,3'\text{-Co}(1,2\text{-}C_2B_9H_{11})_2]^-$ in the presence of protein, the following plot is obtained.

Fig. 5 seems to hint at two types of behaviour which we can assign as two different groups of proteins: one consisting of catalase, hemoglobin, BSA (bovine serum albumin), γ-globulin and the other having histone, HRP (horseradish peroxidase), myoglobin, lysozyme and CA (carbonic anhydrase).

Normalization of the intensity of current with respect to hydrodynamic radius (r_H)

The plots, discussed so far, only take into account the concentration but do not account for the surface area of the protein where the interactions with $[3,3'\text{-Co}(1,2\text{-}C_2B_9H_{11})_2]^-$ actually occurs. As we shall see, the currents can be roughly correlated with the surface of the proteins.

For harmonization, the factor $(r_H)^2$ has been taken into consideration, with r_H being the hydrodynamic radius of the protein. Thus, the next plot considers the normalized *current density* that is obtained by considering the $(r_H)^2$ in the denominator as:

$$\text{Normalized current density} = \text{Bound } [3,3'\text{-Co}(1,2\text{-}C_2B_9H_{11})_2]^-/(r_H)^2\ (r_H - \text{Hydrodynamic radius})$$

The hydrodynamic radius for a protein can be described as the Stokes radius, which refers to the radius of a sphere having the same hydrodynamic properties as the biomolecule.[51,52] The radii reported in these studies are obtained from the literature wherein they have been estimated in the presence of a buffer such as Tris-HCl. We have also verified these values through DLS experiments carried out in 0.1 M NaCl. In the graph, the y-axis represents the normalized *current density*, taking into consideration the surface area as ${r_H}^2$ since the surface area for a sphere is $4\pi r^2$. Table 1, Fig. 6 and Fig. S10 (ESI†) provide an overview of all the proteins studied.

Table 1 The hydrodynamic radius as well as the calculated surface area/4π, with the two different classifications of the curves as type I and type II; the two borderline proteins are highlighted in italics

Protein (Type)	Hydrodynamic radius (nm)	Surface Area/4π (nm^2)
Histone (I)	5.78	33.41
γ-Globulin (I)	5.6	31.36
Catalase (I)	5.22	27.25
BSA (I)	4.1	16.81
Hemoglobin (I)	*3.2*	*10.24*
HRP (II)	*3*	*9*
CA (II)	2.01	4.04
Lysozyme (II)	2	4
Myoglobin (II)	1.9	3.61

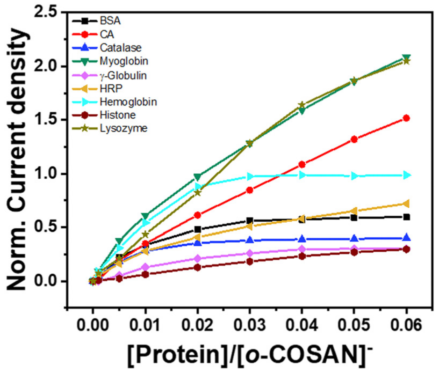

Fig. 6 The normalized current density calculated by considering the surface area of each of the protein *vs.* the protein to [*o*-COSAN]$^-$ fraction for different proteins.

After considering the surface as $(r_H)^2$, the same grouping of proteins as before is retained: γ-Globulin, catalase, BSA and hemoglobin to which the histone with some reservations could be integrated. All these proteins display a characteristic 'plateau'. With the exception of hemoglobin, all these proteins have a low maximum current density value in comparison to the remaining ones. Indeed, these proteins that exhibit a plateau attain a current density limit, while those without a plateau continue to increase, reaching values two or three times higher. Consequently, at the 0.06 [protein]/[3,3′-Co(1,2-$C_2B_9H_{11})_2]^-$ ratio, the normalized current density does not exceed 0.6 for BSA, catalase, γ-globulin, and histone, while others at this ratio show values of 1.6 for CA, 2.0 for myoglobin and lysozyme. There are two exceptions, one for each group, hemoglobin with a current density of 1.0, in the plateau group, and in the non-plateau group, HRP with 0.7.

Deductively, there are two potential types of tendencies; the former that generates a plateau (type I) and the latter having a more continuous slope (type II) as shown in Fig. 7. Consequently, two different protein/[3,3′-Co(1,2-$C_2B_9H_{11})_2]^-$interaction models can be proposed.

The distinctive feature for each of the models proposed is their curvatures occurring at different ratios of protein/[Co($C_2B_9H_{11})_2]^-$. Type I follows a characteristic linearity initially and eventually saturates, whereas Type II has a 'kink' initially and follows a linear path afterwards.

The proteins which follow the patterns are, as follows:

- Type I: Histone, catalase, γ-globulin, hemoglobin and BSA.
- Type II: HRP, myoglobin, lysozyme and CA.

The above behaviour models are proposed solely on the grounds of the experimental data and the following section entails plausible interpretations for the same.

Plausible explanations for the trends observed

In order to interpret the shapes of these curves on the basis of the content of basic residues in the proteins studied, and their density on the surface, we hypothesize that the basic amino acid residues are predominantly present on the protein surface owing to their hydrophilic nature and therefore, can interact strongly with [3,3′-Co(1,2-$C_2B_9H_{11})_2]^-$. Table 2 displays the number of basic amino acid residues and the total number of amino acids in the protein, which would be helpful in interpreting which other factors may be relevant in the analysis of the observed curves. Furthermore, a column has also been added to compare the number of amino acids of each protein with the protein (BSA) that has the highest number which has been assigned as 100.

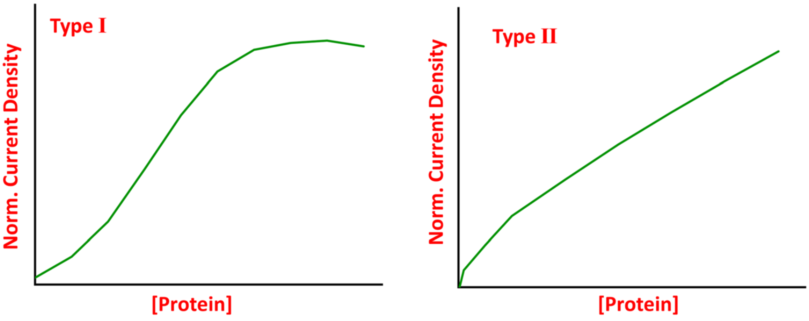

Fig. 7 Two distinctive types (I and II) of tendencies observed after normalizing the current intensity with the surface area obtained using [*o*-COSAN]$^-$ as the 'small molecule' probe.

Table 2 The different basic amino acid residues and the total number of residues present in various proteins

Protein	Lys	His	Arg	Amino acid (AA)	Norm. AA
Histone	13	5	13	133	23
Catalase	23	17	26	488	84
γ-Globulin	15	19	11	390	67
BSA	59	18	23	583	100
Hemoglobin	11	11	3	141	24
HRP	6	4	21	306	52
Myoglobin	19	13	4	151	26
Lysozyme	13	2	13	164	28
CA	24	12	7	257	44

Table 3 Calculations depicting plausible relations to the tendencies observed for the different proteins. In the 5th column, values above 1 correspond to Type I and those below 1 correspond to Type II

Protein (Type)	Basic amino acid (AA)	Basic AA/ Total AA	Basic AA/Area	(Basic AA/Total AA)*Area
Histone (I)	31	0.23	0.92	7.79
Catalase (I)	66	0.14	2.4	3.69
γ-Globulin (I)	45	0.12	1.4	3.62
BSA (I)	100	0.17	5.9	2.88
Hemoglobin (I)	25	0.18	2.4	1.82
HRP (II)	31	0.10	3.4	0.91
Myoglobin (II)	36	0.24	9.97	0.86
Lysozyme (II)	28	0.17	7	0.68
CA (II)	43	0.17	10.6	0.67

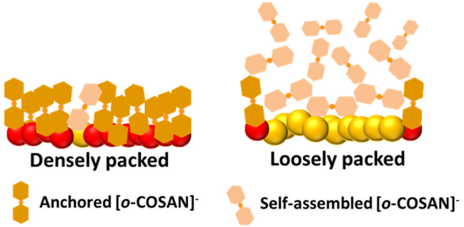

Fig. 8 A visual representation of the two types of protein-[*o*-COSAN]$^-$ interactions observed with regard to the two groups of classification obtained, where the basic amino acid residues are represented in red and the other amino acid residues in yellow.

Table 3 displays the possible interpretations based on the curves observed. Based on our understanding of possible basic amino acid/$[3,3'\text{-Co}(1,2\text{-C}_2\text{B}_9\text{H}_{11})_2]^-$ interactions, we have considered the following: the number of basic amino acids, column 2; the ratio of basic amino acids to the total number of amino acids in the protein, column 3; the density of basic amino acids on the surface, column 4 and the number of basic amino acids on the surface with regard to the total number of amino acids, column 5.

In the plots described above, a saturated curve or plateau is indicative of a strong interaction between the basic residues of the protein and $[3,3'\text{-Co}(1,2\text{-C}_2\text{B}_9\text{H}_{11})_2]^-$. Typically, this is accompanied by a sharp increase in slope, indicating a strong interaction. Initially, when the concentration of $[3,3'\text{-Co}(1,2\text{-C}_2\text{B}_9\text{H}_{11})_2]^-$ exceeds that of the protein, all available binding sites in the protein will be occupied by $[3,3'\text{-Co}(1,2\text{-C}_2\text{B}_9\text{H}_{11})_2]^-$.

Considering columns 2 and 3, we observe that a dispersion of data is generated which does not correlate well with the tendencies observed. For example, if we look at column 3 (Basic AA/Total AA), there is no defined data grouping that correlates with the observed protein characteristics which may or may not lead to the formation of a plateau.

But, when we factor in the surface area, the correlation improves (column 4). Thus, for example, in column 4, three of the four proteins belonging to type II are those which have the highest density of basic amino acids. HRP is the discordant figure among this set of non-plateau-forming proteins, contrasting with BSA in the other group. But this correlation improves dramatically when we consider the number of basic amino acids on the surface with regard to the total number of amino acids. In this case, there is a perfect correlation. The two groups of data generated agree well with the two experimental groups, the former that generates a plateau and the latter which doesn't. Conceptually, the density of amino acids and the total number of amino acids in a protein with certain dimensions are related, but the most relevant difference is that of considering how many basic amino acids exist with respect to the total, which indirectly considers the non-basic characteristics of the other amino acids within the protein.

The reason why one group of proteins has a curve with a marked limit of $[3,3'\text{-Co}(1,2\text{-C}_2\text{B}_9\text{H}_{11})_2]^-$ and the other does not is yet to be determined. The explanation is sustained by the fact that in the former, there is a higher proportion of basic amino acids compared to the total, allowing a greater number of $[3,3'\text{-Co}(1,2\text{-C}_2\text{B}_9\text{H}_{11})_2]^-$ molecules to interact in an end-on disposition, thus forming a robust coating with well-ordered $[3,3'\text{-Co}(1,2\text{-C}_2\text{B}_9\text{H}_{11})_2]^-$, preventing further growth by self-assembling of $[3,3'\text{-Co}(1,2\text{-C}_2\text{B}_9\text{H}_{11})_2]^-$ (Fig. 8). On the other end are proteins having a smaller ratio of basic amino acids which are surrounded by non-basic amino acids that do not interact with the $[3,3'\text{-Co}(\text{C}_2\text{B}_9\text{H}_{11})_2]^-$ molecules. In this scenario, only $[3,3'\text{-Co}(1,2\text{-C}_2\text{B}_9\text{H}_{11})_2]^-$ interacting with the basic residues adopts an end-on orientation. If the basic residues are in close proximity, the end-on alignment is preserved; the latter orientation can expand outward, accounting for the continued growth of $[3,3'\text{-Co}(1,2\text{-C}_2\text{B}_9\text{H}_{11})_2]^-$. By meticulously analysing the current profile relative to protein concentration using an appropriate algorithm, it becomes possible to obtain a high-resolution depiction of the surface in its natural environment. Thus, two sets of $[3,3'\text{-Co}(1,2\text{-C}_2\text{B}_9\text{H}_{11})_2]^-$ can be postulated to be on the surface, those that are ordered due to their interaction with the basic residue and those that are not. These loosely packed $[3,3'\text{-Co}(1,2\text{-C}_2\text{B}_9\text{H}_{11})_2]^-$ facilitates self-assembly which allows unlimited growth in the number of $[3,3'\text{-Co}(1,2\text{-C}_2\text{B}_9\text{H}_{11})_2]^-$ and thereby extending the dimension of the protein/$[3,3'\text{-Co}(1,2\text{-C}_2\text{B}_9\text{H}_{11})_2]^-$ assembly (Fig. 8). Therefore, the proteins could be classified as High Surface Base Density

(HSBD) (Type I) and Low Surface Base Density (LSBD) (Type II), which can be distinguished using [*o*-COSAN]$^-$ as an electrochemical molecular probe.

Indeed, these models are consistent with the higher current intensity for the type II proteins *vs.* type I. Notably, it can be observed that the intensity related to bound [3,3′-Co(1,2-$C_2B_9H_{11})_2]^-$ can reach up to 50% in some type II molecules (Fig. 4), indicating that the bonded [3,3′-Co(1,2-$C_2B_9H_{11})_2]^-$ molecules have more relaxed binding, enabling better interaction with the electrode through exchange phenomena. A further insight into the relevance of the surface represented by $(r_H)^2$ is obtained if the focus is set on the hydrodynamic radius and a graph of the normalised intensity is plotted against the hydrodynamic radius, each at different protein fractions, 0.03, 0.04, 0.05 and 0.06 as shown in Fig. 9 (Fig. S11, ESI†). At the lower protein fractions, a linear relation is obtained. These changes result in a non-linear relation at the two higher protein fractions. However, all of them provide the same information as seen in the following plots. The information is complementary to the former interpretation of the earlier plots and basically *indicates that size and surface behaviour are related*.

In each of the plots (Fig. 9), it can be observed that as the hydrodynamic radius increases, the amount of [3,3′-Co(1,2-$C_2B_9H_{11})_2]^-$ bound on the surface of the protein decreases. A smaller radius implies a higher surface to volume ratio. Hence, it can be assumed that the density of the amino acids, particularly the polar ones, is higher on the surface for smaller proteins as compared to larger ones. As a result, the amino acids which act as an anchoring point for [3,3′-Co(1,2-$C_2B_9H_{11})_2]^-$ would be in close proximity of one another and result in a more densely packed structure. Consequently, the amount of [3,3′-Co(1,2-$C_2B_9H_{11})_2]^-$ bound on the protein surface would be higher. This would imply that smaller the protein, higher would be [3,3′-Co(1,2-$C_2B_9H_{11})_2]^-$ density on the surface.

As can be observed from the graphs, LSBD proteins (CA and HRP) tend to deviate from the trendline but seem to be in order with each other. The deviation can be accounted by considering the fact that the surface area obtained from the hydrodynamic radius may vary from the 'effective' protein surface owing to the different protein structures. The more the difference from the 'effective' surface, more would be the deviation from the trendline. Hence, it is rational to consider that for proteins such as CA and HRP, the deviation from the 'effective' surface is much more prominent than the others. In some ways, this deviation and its magnitude indicate how the defect-free spherical surface is altered by the existence of voids and/or moors, depicting a more realistic view of the interacting surface of a protein.

Influence of the electrolyte

The electrochemical measurements in this study were performed in the presence of an electrolyte, NaCl, in order for the electroactive substance to access the electrode through a

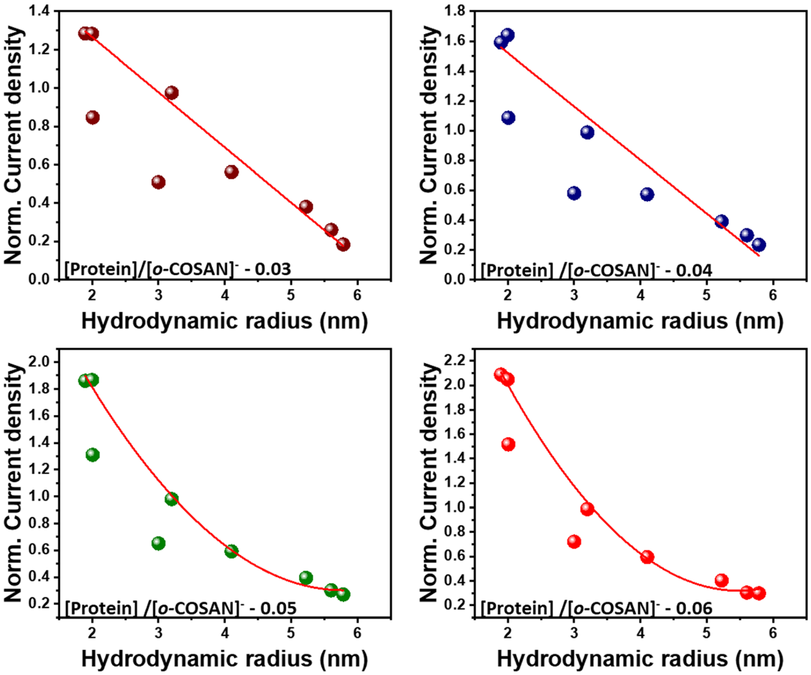

Fig. 9 The normalized current density *vs.* the hydrodynamic radius at different protein/[*o*-COSAN]$^-$ ratios from 0.03 to 0.06. [From smallest to largest hydrodynamic radius: Myoglobin, lysozyme, CA, HRP, hemoglobin, BSA, catalase, γ-globulin and histone].

Table 4 The number of [*o*-COSAN]$^-$ present on the HSBD protein surface

Protein	Hydrodynamic radius (nm)	Intersection (point of maximum coverage)	Number of [*o*-COSAN]$^-$ (experimental)
Histone	5.78	0.041	25
γ-Globulin	5.6	0.027	37
Catalase	5.2	0.013	77
BSA	4.1	0.012	83
Hemoglobin	3.2	0.020	50

diffusion process. In such a scenario where two anions are present, namely Cl^- and $[3,3'\text{-Co}(1,2\text{-}C_2B_9H_{11})_2]^-$ in the ratio 100 : 1, there's a possible competition between the two to occupy the protein surface. In the case of the Cl^- ion, the primary interaction that would come into play would be electrostatics, whereas for $[3,3'\text{-Co}(1,2\text{-}C_2B_9H_{11})_2]^-$, it would involve both electrostatic interaction as well as the N–H···H–B dihydrogen bonds.[41] For these reasons, the interaction of $[3,3'\text{-Co}(1,2\text{-}C_2B_9H_{11})_2]^-$ with the protein is stronger as it is able to displace Cl^- despite the electrolyte being at high concentration in comparison to $[3,3'\text{-Co}(1,2\text{-}C_2B_9H_{11})_2]^-$. Another interesting point to reflect on in such studies is the radius of the proteins. The radii used to account for the surface area of the proteins are the hydrodynamic radii measured under specific conditions. The hydrodynamic radius is mainly representative of the ideal flawless protein surface rather than the reactive functional one with its voids and moors. In this work, DLS measurements were performed in NaCl and the hydrodynamic radii of the different proteins confer with the reported values in buffer solutions (Fig. S12 and Table S2, ESI†). In a previous work, we had studied the interaction of $[3,3'\text{-Co}(1,2\text{-}C_2B_9H_{11})_2]^-$ and BSA in the absence of any electrolyte, only water, and found that the hydrodynamic radius of BSA was 1.6 nm which is smaller in comparison to 4.1 nm reported in this study. This in itself proves the importance and influence of anions and their co-ions in determining the diameter of the protein. If we consider the High Surface Base Density (HSBD) (Type I) proteins such as BSA, catalase, γ-globulin, hemoglobin and histone, an intersecting point corresponding to a particular [protein]/$[3,3'\text{-Co}(1,2\text{-}C_2B_9H_{11})_2]^-$ value can be observed. This point is highly significant as this is the maximum number of tightly bound $[3,3'\text{-Co}(1,2\text{-}C_2B_9H_{11})_2]^-$ molecules that can be present on a single protein molecule. Thus, this is a key number to get an estimate of the number of $[3,3'\text{-Co}(1,2\text{-}C_2B_9H_{11})_2]^-$ molecules on the protein's surface. As can be seen in Table 4, as the protein size increases, the amount of $[3,3'\text{-Co}(1,2\text{-}C_2B_9H_{11})_2]^-$ present on the surface decreases. Hemoglobin is an exception to this general rule, but that can be attributed to the fact that it is on the borderline between HSBD (type I) and Low Surface Base Density (LSBD) (Type II) proteins, as shown in Table 3.

Interestingly, the number of $[3,3'\text{-Co}(1,2\text{-}C_2B_9H_{11})_2]^-$ on the BSA surface is lower in comparison to the study performed in the absence of any electrolyte which was calculated to be 100.[38] What caused this? The answer would simply be the environment in which the protein is surrounded which greatly defines the surface area available. Forthwith, we could state that the water molecules are much more labile and easily replaceable compared to the anions and co-ions of the surroundings that are at a much higher concentration than the $[3,3'\text{-Co}(1,2\text{-}C_2B_9H_{11})_2]^-$ molecules. Secondly, the existing anions and co-ions, as they are not so easily displaced, are retained and form a relatively persistent layer on which the $[3,3'\text{-Co}(1,2\text{-}C_2B_9H_{11})_2]^-$ molecules are deposited which would interfere with the interaction of $[3,3'\text{-Co}(1,2\text{-}C_2B_9H_{11})_2]^-$ with the protein surface. A competition would exist that would depend on the concentration of the competing ions and their relative affinity for the basic residues. Despite all these simplifications used, the results generally seem to be realistic enough to be useful.

Conclusion

This study proves the complexity of what we consider as the 'surface' of a protein. In this study, we have attempted to address the 'surface' of a protein considering the 'effective' protein surface (EPS) with regard to its interaction with the 'small molecule' probe, $[3,3'\text{-Co}(1,2\text{-}C_2B_9H_{11})_2]^-$. We were able to use simple and rational estimations and calculations to explain the tendencies observed in terms of the $[3,3'\text{-Co}(1,2\text{-}C_2B_9H_{11})_2]^-$/protein interactions. We had deliberately used a small molecule that is anionic, redox-active, capable of self-assembly and of producing hydrogen and dihydrogen non-bonding interactions to demonstrate the potential of small molecules with unique characteristics as 'molecular probes' for better visualizations. We were able to demonstrate the correlation of size and polar amino acid residues to the interactions with $[3,3'\text{-Co}(1,2\text{-}C_2B_9H_{11})_2]^-$. We have also shown how the environment of the protein affects the interactions as well as tunes the self-assembly of $[3,3'\text{-Co}(1,2\text{-}C_2B_9H_{11})_2]^-$ and therefore affects the measurements involved. We were indeed, able to demonstrate that $[3,3'\text{-Co}(1,2\text{-}C_2B_9H_{11})_2]^-$ 'viewed' each protein surface differently and hence has the potential to act as a simple and easy to handle cantilever for measuring and picturing the protein surfaces. We have described a novel method for the analysis of a protein in its intrinsic form and environment without any interference. With this work, we aimed to open an avenue for extended research in understanding the surface of a protein particularly using small unique molecular probes such as $[3,3'\text{-Co}(1,2\text{-}C_2B_9H_{11})_2]^-$. Although these comparisons have been carried out experimentally, we are certain that employing a suitable algorithm would allow for high-resolution visualizations of the protein surface in its natural environment.

Author contributions

Conceptualization, F. T. and C. V.; methodology, F. T., J. A. M. X., I. F. and M. N.-M.; formal analysis, F. T., C. V., J. A. and M. X.; writing—original draft preparation, F. T., J. A. M. X. and C. V.; writing—review and editing, all the authors.

Conflicts of interest

The authors declare no conflicts of interest.

Acknowledgements

This work received funding from the Spanish Ministry of Science, through the ''Severo Ochoa'' Programme for Centres of Excellence in R&D (CEX2019-000917-S) as well as the Spanish Ministerio de Ciencia e Innovación (PID2019-106832RB-I00) and Generalitat de Catalunya (2017SGR1720). J. A. M. Xavier acknowledges the DOC-FAM programme under the Marie Sklodowska-Curie grant agreement No. 754397 and is enrolled in the PhD programme in UAB.

References

1 C. I. Branden and J. Tooze, *Introduction to Protein Structure*, Garland Science, 2nd edn, 2012.

2 C. A. Orengo, A. E. Todd and J. M. Thornton, From protein structure to function, *Curr. Opin. Struct. Biol.*, 1999, **9**, 374–382.

3 G. N. Ramachandran, C. Ramakrishnan and V. Sasisekharan, Stereochemistry of polypeptide chain configurations, *J. Mol. Biol.*, 1963, **7**, 95–99.

4 R. M. Jackson and M. J. E. Sternberg, Protein surface area defined, *Nature*, 1993, **366**, 638.

5 V. N. Uversky, Intrinsically disordered proteins from A to Z, *Int. J. Biochem. Cell Biol.*, 2011, **43**, 1090–1103.

6 C. J. Oldfield, Y. Cheng, M. S. Cortese, C. J. Brown, V. N. Uversky and A. K. Dunker, Comparing and Combining Predictors of Mostly Disordered Proteins, *Biochemistry*, 2005, **44**, 1989–2000.

7 K. Mazmanian, K. Sargsyan and C. Lim, How the Local Environment of Functional Sites Regulates Protein Function, *J. Am. Chem. Soc.*, 2020, **142**, 9861–9871.

8 S. L. Speer, W. Zheng, X. Jiang, I.-T. Chu, A. J. Guseman, M. Liu, G. J. Pielak and C. Li, The intracellular environment affects protein–protein interactions, *Proc. Natl. Acad. Sci. U. S. A.*, 2021, **118**(11), e2019918118.

9 B. Yu, C. C. Pletka and J. Iwahara, Quantifying and visualizing weak interactions between anions and proteins, *Proc. Natl. Acad. Sci. U. S. A.*, 2021, **118**(2), e2015879118.

10 Y. Okuno, J. Yoo, C. D. Schwieters, R. B. Best, H. S. Chung and G. M. Clore, Atomic view of cosolute-induced protein denaturation probed by NMR solvent paramagnetic relaxation enhancement, *Proc. Natl. Acad. Sci. U. S. A.*, 2021, **118**(34), e2112021118.

11 Z. Jing, R. Qi, C. Liu and P. Ren, Study of interactions between metal ions and protein model compounds by energy decomposition analyses and the AMOEBA force field, *J. Chem. Phys.*, 2017, **147**, 161733.

12 M. Ozboyaci, D. B. Kokh, S. Corni and R. C. Wade, Modeling and simulation of protein-surface interactions: achievements and challenges, *Q. Rev. Biophys.*, 2016, **49**, e4.

13 T. C. Terwilliger, D. Stuart and S. Yokoyama, Lessons from Structural Genomics, *Annu. Rev. Biophys.*, 2009, **38**, 371–383.

14 C. J. Lanci, C. M. MacDermaid, S. Kang, R. Acharya, B. North, X. Yang, X. J. Qiu, W. F. DeGrado and J. G. Saven, Computational design of a protein crystal, *Proc. Natl. Acad. Sci. U. S. A.*, 2012, **109**, 7304–7309.

15 E. Laine and A. Carbone, Local Geometry and Evolutionary Conservation of Protein Surfaces Reveal the Multiple Recognition Patches in Protein-Protein Interactions, *PLoS Comput. Biol.*, 2015, **11**, 1–32.

16 L. Ronda, S. Bruno, S. Bettati, P. Storici and A. Mozzarelli, From protein structure to function via single crystal optical spectroscopy, *Front. Mol. Biosci.*, 2015, **2**, 2296.

17 U. Heinemann, K. Büssow, U. Mueller and P. Umbach, Facilities and Methods for the High-Throughput Crystal Structural Analysis of Human Proteins, *Acc. Chem. Res.*, 2003, **36**, 157–163.

18 K. Palczewski, T. Kumasaka, T. Hori, C. A. Behnke, H. Motoshima, B. A. Fox, I. Le Trong, D. C. Teller, T. Okada, R. E. Stenkamp, M. Yamamoto and M. Miyano, Crystal Structure of Rhodopsin: A G Protein-Coupled Receptor, *Science*, 2000, **289**, 739–745.

19 Y. Hu, K. Cheng, L. He, X. Zhang, B. Jiang, L. Jiang, C. Li, G. Wang, Y. Yang and M. Liu, NMR-Based Methods for Protein Analysis, *Anal. Chem.*, 2021, **93**, 1866–1879.

20 K. Murata and M. Wolf, Cryo-electron microscopy for structural analysis of dynamic biological macromolecules, *Biochim. Biophys. Acta, Gen. Subj.*, 2018, **1862**, 324–334.

21 Y. Yue, T. Zhao, Y. Wang, K. Ma, X. Wu, F. Huo, F. Cheng and C. Yin, HSA-Lys-161 covalent bound fluorescent dye for in vivo blood drug dynamic imaging and tumor mapping, *Chem. Sci.*, 2022, **13**, 218–224.

22 Y. Yue, T. Zhao, Z. Xu, W. Chi, X. Chai, J. Ai, J. Zhang, F. Huo, R. M. Strongin and C. Yin, Enlarging the Stokes Shift by Weakening the π-Conjugation of Cyanines for High Signal-to-Noise Ratiometric Imaging, *Adv. Sci.*, 2023, **10**, 2205080.

23 F. Zhao, S. M. Matt, J. Bu, O. G. Rehrauer, D. Ben-Amotz and S. A. McLuckey, Joule Heating and Thermal Denaturation of Proteins in Nano-ESI Theta Tips, *J. Am. Soc. Mass Spectrom.*, 2017, **28**, 2001–2010.

24 K. J. Freedman, S. R. Haq, J. B. Edel, P. Jemth and M. J. Kim, Single molecule unfolding and stretching of protein domains inside a solid-state nanopore by electric field, *Sci. Rep.*, 2013, **3**, 1638.

25 W. Chen, Electroconformational denaturation of membrane proteins, *Ann. N. Y. Acad. Sci.*, 2005, **1066**, 92–105.

26 E. V. Suprun, Direct electrochemistry of proteins and nucleic acids: The focus on 3D structure, *Electrochem. Commun.*, 2021, **125**, 106983.

27 M. Uchman, V. Ďorďovič, Z. Tošner and P. Matějíček, Classical Amphiphilic Behavior of Nonclassical Amphiphiles: A Comparison of Metallacarborane Self-Assembly with SDS Micellization, *Angew. Chem.*, 2015, **54**, 14113–14117.

28 D. C. Malaspina, C. Viñas, F. Teixidor and J. Faraudo, Atomistic Simulations of COSAN: Amphiphiles without a Head-and-Tail Design Display ''Head and Tail'' Surfactant Behavior, *Angew. Chem.*, 2020, **59**, 3088–3092.

29 P. Bauduin, S. Prevost, P. Farràs, F. Teixidor, O. Diat and T. Zemb, A Theta-Shaped Amphiphilic Cobaltabisdicarbollide Anion: Transition From Monolayer Vesicles to Micelles, *Angew. Chem.*, 2011, **50**, 5298–5300.

30 P. Farràs, E. J. Juárez-Pérez, M. Lepšík, R. Luque, R. Núñez and F. Teixidor, Metallacarboranes and their interactions: theoretical insights and their applicability, *Chem. Soc. Rev.*, 2012, **41**, 3445–3463.

31 R. N. Grimes, *Carboranes*, Elsevier Inc, New York, 3rd edn, 2016.

32 M. Tarrés, C. Viñas, A. M. Cioran, M. M. Hänninen, R. Sillanpää and F. Teixidor, Towards Multifunctional Materials Incorporating Elastomers and Reversible Redox-Active Fragments, *Chem. – Eur. J.*, 2014, **20**, 15808–15815.

33 D. Tu, H. Yan, J. Poater and M. Solà, The *nido*-Cage$\cdots\pi$ Bond: A Non-covalent Interaction between Boron Clusters and Aromatic Rings and Its Applications, *Angew. Chem.*, 2020, **59**, 9018–9025.

34 C. Viñas, M. Tarrés, P. González-Cardoso, P. Farràs, P. Bauduin and F. Teixidor, Surfactant behaviour of metallacarboranes. A study based on the electrolysis of water, *Dalton Trans.*, 2014, **43**, 5062–5068.

35 J. A. M. Xavier, C. Viñas, E. Lorenzo, T. García-Mendiola and F. Teixidor, Potential application of metallacarboranes as an internal reference: an electrochemical comparative study to ferrocene, *Chem. Commun.*, 2022, **58**, 4196–4199.

36 J.-N. Longchamp, S. Rauschenbach, S. Abb, C. Escher, T. Latychevskaia, K. Kern and H.-W. Fink, Imaging proteins at the single-molecule level, *Proc. Natl. Acad. Sci. U. S. A.*, 2017, **114**, 1474–1479.

37 T. O. Pleshakova, N. S. Bukharina, A. I. Archakov and Y. D. Ivanov, Atomic Force Microscopy for Protein Detection and Their Physicochemical Characterization, *Int. J. Mol. Sci.*, 2018, **19**, 1142.

38 I. Fuentes, J. Pujols, C. Viñas, S. Ventura and F. Teixidor, Dual Binding Mode of Metallacarborane Produces a Robust Shield on Proteins, *Chemistry*, 2019, **25**, 12820–12829.

39 M. Y. Losytskyy, V. B. Kovalska, O. A. Varzatskii, M. V. Kuperman, S. Potocki, E. Gumienna-Kontecka, A. P. Zhdanov, S. M. Yarmoluk, Y. Z. Voloshin, K. Y. Zhizhin, N. T. Kuznetsov and A. V. Elskaya, An interaction of the functionalized closo-borates with albumins: The protein fluorescence quenching and calorimetry study, *J. Lumin.*, 2016, **169**, 51–60.

40 T. M. Goszczyński, K. Fink, K. Kowalski, Z. J. Leśnikowski and J. Boratyński, Interactions of Boron Clusters and their Derivatives with Serum Albumin, *Sci. Rep.*, 2017, **7**, 9800.

41 A.-I. Stoica, C. Kleber, C. Viñas and F. Teixidor, Ion selective electrodes for protonable nitrogen containing analytes: Metallacarboranes as active membrane components, *Electrochim. Acta*, 2013, **113**, 94–98.

42 A.-I. Stoica, C. Viñas and F. Teixidor, Cobaltabisdicarbollide anion receptor for enantiomer-selective membrane electrodes, *Chem. Commun.*, 2009, 4988–4990.

43 K. Fink, J. Boratyński, M. Paprocka and T. M. Goszczyński, Metallacarboranes as a tool for enhancing the activity of therapeutic peptides, *Ann. New York Acad. Sci.*, 2019, **1457**, 128–141.

44 M.-C. Bellissent-Funel, A. Hassanali, M. Havenith, R. Henchman, P. Pohl, F. Sterpone, D. van der Spoel, Y. Xu and A. E. Garcia, Water Determines the Structure and Dynamics of Proteins, *Chem. Rev.*, 2016, **116**, 7673–7697.

45 R. Núñez, M. Tarrés, A. Ferrer-Ugalde, F. F. De Biani and F. Teixidor, Electrochemistry and Photoluminescence of Icosahedral Carboranes, Boranes, Metallacarboranes, and Their Derivatives, *Chem. Rev.*, 2016, **116**, 14307–14378.

46 H. I. Okur, J. Hladílková, K. B. Rembert, Y. Cho, J. Heyda, J. Dzubiella, P. S. Cremer and P. Jungwirth, Beyond the Hofmeister Series: Ion-Specific Effects on Proteins and Their Biological Functions, *J. Phys. Chem. B*, 2017, **121**, 1997–2014.

47 M. G. Cacace, E. M. Landau and J. J. Ramsden, The Hofmeister series: salt and solvent effects on interfacial phenomena, *Q. Rev. Biophys.*, 1997, **30**, 241–277.

48 A.-I. Stoica, C. Viñas and F. Teixidor, History of Cobaltabis(dicarbollide) in Potentiometry, No Need for Ionophores to Get an Excellent Selectivity, *Molecules*, 2022, **27**, 8312.

49 I. Guerrero, A. Saha, J. A. M. Xavier, C. Viñas, I. Romero and F. Teixidor, Noncovalently Linked Metallacarboranes on Functionalized Magnetic Nanoparticles as Highly Efficient, Robust, and Reusable Photocatalysts in Aqueous Medium, *ACS Appl. Mater. Interfaces*, 2020, **12**, 56372–56384.

50 T. García-Mendiola, V. Bayon-Pizarro, A. Zaulet, I. Fuentes, F. Pariente, F. Teixidor, C. Viñas and E. Lorenzo, Metallacarboranes as tunable redox potential electrochemical indicators for screening of gene mutation, *Chem. Sci.*, 2016, **7**, 5786–5797.

51 H. P. Erickson, Size and shape of protein molecules at the nanometer level determined by sedimentation, gel filtration, and electron microscopy, *Biol. Proced. Online*, 2009, **11**, 32–51.

52 V. La Verde, P. Dominici and A. Astegno, Determination of Hydrodynamic Radius of Proteins by Size Exclusion Chromatography, *Bio-protocol*, 2017, **7**, e2230.

ACS APPLIED MATERIALS & INTERFACES

www.acsami.org Research Article

Noncovalently Linked Metallacarboranes on Functionalized Magnetic Nanoparticles as Highly Efficient, Robust, and Reusable Photocatalysts in Aqueous Medium

Isabel Guerrero, Arpita Saha, Jewel Ann Maria Xavier, Clara Viñas, Isabel Romero,* and Francesc Teixidor*

Cite This: *ACS Appl. Mater. Interfaces* 2020, 12, 56372−56384 Read Online

ACCESS | Metrics & More | Article Recommendations | Supporting Information

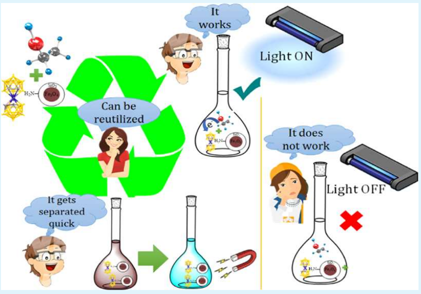

ABSTRACT: A successful homogeneous photoredox catalyst has been fruitfully heterogenized on magnetic nanoparticles (MNPs) coated with a silica layer, keeping intact its homogeneous catalytic properties but gaining others due to the easy magnetic separation and recyclability. The amine-terminated magnetic silica nanoparticles linked noncovalently to H[3,3′-Co(1,2-$C_2B_9H_{11}$)$_2$]$^-$ (H[**1**]), termed MSNPs-NH_2@H[**1**], are highly stable and do not produce any leakage of the photoredox catalyst H[**1**] in water. The magnetite MNPs were coated with SiO_2 to provide colloidal stability and silanol groups to be tethered to amine-containing units. These were the MSNPs-NH_2 on which was anchored, in water, the cobaltabis(dicarbollide) complex H[**1**] to obtain MSNPs-NH_2@H[**1**]. Both MSNPs-NH_2 and MSNPs-NH_2@H[**1**] were evaluated to study the morphology, characterization, and colloidal stability of the MNPs produced. The heterogeneous MSNP-NH_2@H[**1**] system was studied for the photooxidation of alcohols, such as 1-phenylethanol, 1-hexanol, 1,6-hexanediol, or cyclohexanol among others, using catalyst loads of 0.1 and 0.01 mol %. Surfactants were introduced to prevent the aggregation of MNPs, and cetyl trimethyl ammonium chloride was chosen as a surfactant. This provided adequate stability, without hampering quick magnetic separation. The results proved that the catalysis could be speeded up if aggregation was prevented. The recyclability of the catalytic system was demonstrated by performing 12 runs of the MSNPs-NH_2@H[**1**] system, each one without loss of selectivity and yield. The cobaltabis(dicarbollide) catalyst supported on silica-coated magnetite nanoparticles has proven to be a robust, efficient, and easily reusable system for the photooxidation of alcohols in water, resulting in a green and sustainable heterogeneous catalytic system.

KEYWORDS: *nanoparticles, metallacarboranes, surface functionalization, photooxidation, heterogeneous catalysis*

■ INTRODUCTION

One of the challenges of this century is to design catalysts to improve the control of the activity and selectivity of the chemical processes, and, at the same time, they should be compatible and friendly with the environment. Light can be considered an ideal agent for environmentally friendly, green chemical synthesis; unlike many conventional reagents, UVA, visible, and IR lights are nontoxic and generate no waste. There is consensus that solar energy combined with water is the right alternative energy source for the development of non-fossil-based fuels.[1,2] Thus, development of photocatalytic methods and systems for organic transformations is an important challenge in this aspect.[3−5] The photoredox catalysis that uses the absorption of light radiation by a catalyst to generate reactive radicals, that activate stable low-energy organic molecules through single-electron processes (oxidation or reduction), is a successful way of mimicking nature in efficiency and sustainability.

From the perspective of sustainability and industrial applicability, homogeneous catalysts are often expensive and create additional waste and their regeneration is difficult. In this context, grafting of homogeneous catalysts on a solid support with a high surface area, such as magnetic nanoparticles (MNPs), is a good approach.[6−9] Although they have been used in catalysis, their usage has been limited due to their tendency to get oxidized and also to get agglomerated. To overcome this, the MNPs can be coated with a layer of material leading to core−shell magnetic particles for their stabilization and producing a favorable surface on which to link

Received: October 5, 2020
Accepted: November 19, 2020
Published: December 7, 2020

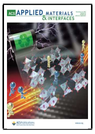

https://dx.doi.org/10.1021/acsami.0c17847
ACS Appl. Mater. Interfaces 2020, 12, 56372−56384

Scheme 1. Synthetic Strategy Used for (a) the Functionalization of MSNPs with Amine Groups, MSNPs-NH_2, and (b) for the Immobilization of H[COSAN], H[1], and MSNPs-NH_2@H[1]

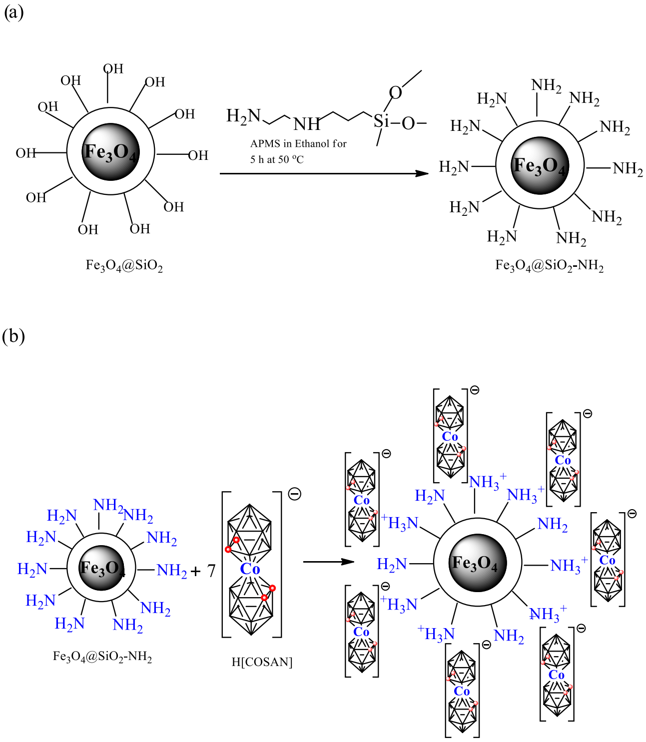

the active sites. Such materials combine the unique magnetic properties of the core with the possibility to further functionalize the surface;[10,1110,11] in addition, the application of an external magnetic field enables the removal of the particles in a simple way.[12−14] Among the coatings of these nanoparticles, silica has been widely used due to its inert properties and because it helps in improving the stability and the physicochemical properties of the MNPs, preventing their aggregation in solution.[15−17] The most important aspect of MNPs coated with silica is that the silanol-terminated surface groups may be modified with various coupling agents to covalently bind to specific ligands.[18,19] This helps to tune the surface of these MNPs coated with silica with different functional groups to obtain differently functionalized MNPs, which can be further used for different purposes. Thus, efficient recyclable photocatalysts based on noble metal nanoparticles have been used, improving the performance of the photocatalytic processes.[20,21] It is to be noted that throughout this introduction we have been talking about covalent bonds either from the ligand to the silica layer or from the ligand to the metal.

Oxidation of organic substrates mediated by transition metals is a relevant process from an industrial point of view.[22−25] Among the oxidation catalytic processes, the photooxidation conversion of alcohols into aldehydes or ketones is of great relevance as shown in the literature.[26−28] This process has practical importance in the hydrogen-based energy technologies because the anodic liberation of protons and electrons can be coupled on a cathode for hydrogen fuel production in an integrated photoelectrochemical cell.[29] Efficient systems supported on silica-coated magnetic nanoparticles for chemical alcohol oxidation have been described in the literature;[30−33] however, no examples of well-defined molecular photoredox catalysts supported on the previously mentioned MNPs have been described.

Cobaltabis(dicarbollide) $[3,3'\text{-Co}(1,2\text{-C}_2\text{B}_9\text{H}_{11})_2]^-$, $[\mathbf{1}]^-$, with two adjacent carbon atoms on the cluster (C_c), is a θ-shape molecule and a representative example of metallabis(dicarbollides) in which one metal ion is shared between two $[\text{C}_2\text{B}_9\text{H}_{11}]^{2-}$ units. The current interesting applications of these compounds lie in their thermal and chemical stability and simple synthesis.[34,35] Other relevant properties of $[3,3'\text{-Co}(1,2\text{-C}_2\text{B}_9\text{H}_{11})_2]^-$ are its nonlocalized negative charge spread all over the molecule;[36] its capacity to produce hydrogen bonds, e.g., C_c−H···O and dihydrogen bonding C_c−H···H−B, that have been proven to participate in their self-assembling;[37−40] water solubility;[41] micelle and vesicle formation;[42−44] and derivatization capacity similar or superior to organic compounds.[36,45] It is reported that $[\mathbf{1}]^-$ presents strong dihydrogen-bonding N−H···H−B interactions with amine groups of amino acids and proteins, making $[\mathbf{1}]^-$ very attractive for ion-selective electrode miniaturization and protecting the reactive surface residues of proteins, respectively.[46,47] Even the interactions via a supramolecular approach seem to be significant in processes of electron transfer and therefore in the effectiveness of photocatalytic systems.[48] The

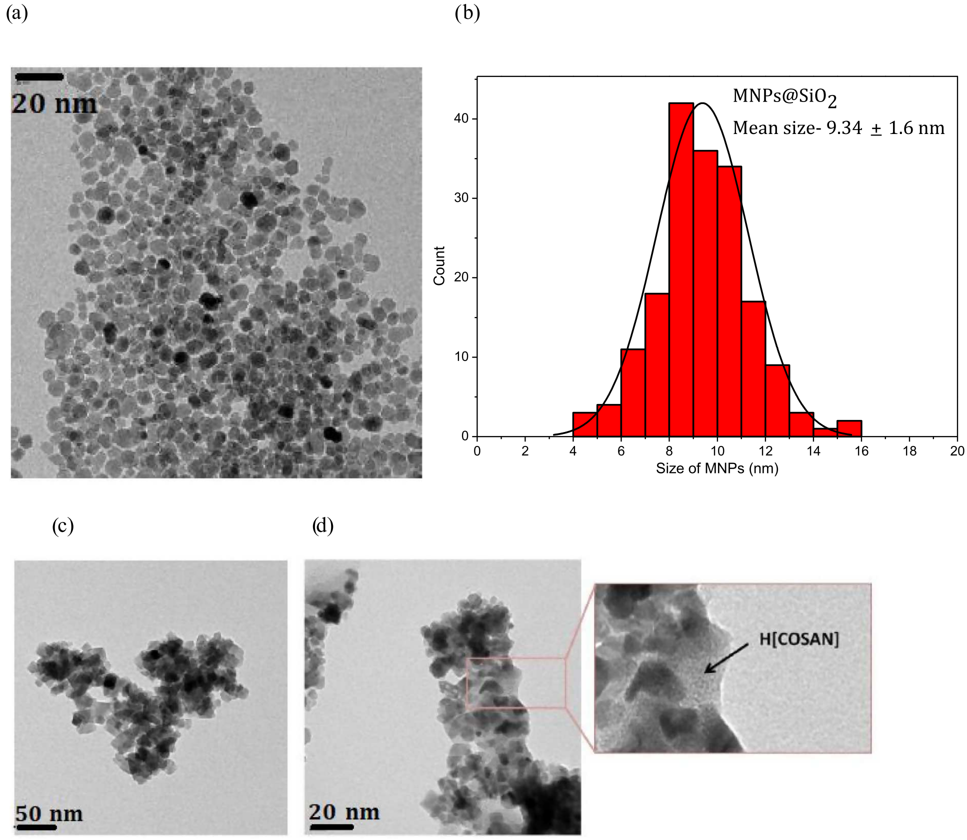

Figure 1. TEM images of (a) MSNPs, (c) MSNPs-NH_2 (11.22 nm), and (d) MSNPs-NH_2@H[**1**] (14.17 nm) and (b) Gaussian size graphs of MSNPs (9.34 nm).

strong dihydrogen-bonding N−H···H−B interaction with amine groups is the key point that has aided in the design of these nonconventional homogenous catalysts reported here.

Metallacarborane compounds have been used as efficient catalysts in different processes.[49−57] Recently, we have also demonstrated that cobaltabis(dicarbollide), [**1**]$^-$, and its chloro derivatives represent efficient tunable homogeneous photoredox catalysts for the oxidation of alcohols in water, through single-electron transfer processes.[58] This behavior has been possible thanks to their lack of photoluminescence, the easy modification of the HOMO−LUMO gap, their high oxidizing power for the couple $Co^{4+/3+}$, and their solubility in water.[59]

In this work, we have aimed at the preparation of heterogeneous catalysts in which the catalyst, which is molecular, is firmly bound to the magnetic support just by nonbonding interactions and with a very efficient and fast process of binding. We shall see that the efficiency of the catalysis extends to many cycles without the loss of conversion.

With all of this in mind, in this paper, we describe the synthesis and characterization of magnetic nanoparticles (MNPs) coated with an inorganic shell of silica (SiO_2) and their functionalization with amine groups (−NH_2), through which the cobaltabis(dicarbollide) complex is attached. The implemented synthetic routes are modified versions of the synthetic procedures described in the literature.[60−62] The anchoring of $H[3,3'\text{-}Co(1,2\text{-}C_2B_9H_{11})_2]$, H[**1**], on magnetic nanoparticles has been studied here for the first time. Also, the colloidal stability of the MNPs in water has been studied using different surfactants, since this is a major issue in catalysis. There exists a conflicting issue of MNPs at present concerning their stability and the magnetic attraction. The more stable the MNP, the longer the time they take to be attracted by the magnet and vice versa. We also report the excellent performance of cobaltabis(dicarbollide) as a heterogeneous catalyst for the photooxidation of aromatic and aliphatic alcohols in water, even using small loading of the catalyst (0.01 mol %) and short catalytic times, along with the re-utilization of the corresponding supported catalyst and its recovery by a magnet.

RESULTS AND DISCUSSION

Catalyst Preparation and Structural and Spectroscopy Characterization. The synthetic strategy followed for the immobilization of $H[3,3'\text{-}Co(1,2\text{-}C_2B_9H_{11})_2]$, H[**1**], on silica-coated Fe_2O_3 magnetic nanoparticles (MSNPs) is shown in

https://dx.doi.org/10.1021/acsami.0c17847

Scheme 1. The anchoring of H[**1**] to MSNP has never been explored before, and it has been done and studied by us for the first time. Cobaltabis(dicarbollide), [**1**]$^-$, is extremely stable in water and can form ion-pair complexes with protonated amino groups ([cation-NH]$^+$[COSAN]$^-$) through an ionic interaction.[46] Thus, the synthetic strategy for the immobilization of H[**1**] is based on the formation of hybrid materials linked by ionic interactions between cobaltabis(dicarbollide) and the functionalized magnetic nanoparticles with amine groups ($-NH_2$), Fe_3O_4@SiO_2-NH_2 (MSNPs-NH_2). Then, these functionalized magnetic nanoparticles were used for attaching the H[**1**] complex to them.

First, the synthesis of Fe_2O_3 magnetic nanoparticles (MNPs) was done using a coprecipitation method,[63,64] and this core of magnetite was then further encapsulated in a silica shell for the formation of silica-coated magnetic nanoparticles, Fe_3O_4@SiO_2 (MSNPs) (Figures S1 and S2). These nanoparticles were functionalized with amine groups (Scheme 1a) by mixing the MSNP with 3-(2-aminoethylamino)propylmethyldimethoxy silane (APMS) in ethanol at 50° for 5 h to achieve the hydrolysis of the methyl groups. The corresponding amine-coated nanoparticles (MSNPs-NH_2) were then mixed with cobaltabis(dicarbollide), [**1**]$^-$, in water and sonicated for 30 min to afford brown silica particles that were washed 10 times with water, separated by a magnet, and dried under vacuum at 80°C, generating the corresponding cobaltabis(dicarbollide) anchored to the silica support Fe_3O_4@SiO_2-NH_2-H[COSAN] (MSNPs-NH_2@H[**1**]) in a noncovalently bonded way (Scheme 1b).

UV−visible spectral and ζ-potential studies were done to quantify the anchoring of H[**1**] on the amine-functionalized silica, Fe_3O_4@SiO_2-NH_2, and also to confirm the presence of metallacarborane on the surface of the nanoparticles, respectively (see Figures S3 and S5).

The UV−vis spectrum corroborates that H[**1**] interacts with the nanoparticles MSNPs-NH_2 since the absorbance of the band at 446 nm decreases with increasing amount of nanoparticles. For every 5 mg of MSNPs-NH_2, 0.14 ± 0.03 mM H[**1**] is consumed to form the anchored complex MSNPs-NH_2@H[**1**]. Saturation takes place when 30 mg of the nanoparticles has been added to the solution, bringing the total amount of metallacarborane anchored to the MSNPs-NH_2 to 0.028 mmol/100 mg of nanoparticles (Figure S3b). In parallel, another UV−vis experiment was performed to check the time required for the extraction of the magnetic nanoparticles with a magnet. It was seen that 10 min was sufficient to attract all of the magnetic nanoparticles and that further time was not required for this procedure (Figure S4).

The positive ζ-potential value of 13.7 mV for MSNPs-NH_2 indicates that ammonium cations are located on the surface of the nanoparticles (Figure S5a).[65] This ζ-potential is between 10 and 30 mV; consequently, this value indicates that the nanoparticles tend to aggregate. When cobaltabis(dicarbollide) [**1**]$^-$ is anchored on the amine/ammonium-functionalized nanoparticles, the ζ-potential becomes negative, −15.2 mV (see Figure S5b), and confirms that [**1**]$^-$ is grafted on the surface of the nanoparticles since [COSAN]$^-$ is an anion and this complex also tends to aggregate.

The nanoparticles synthesized were characterized by different techniques. The XRD pattern (Figure S6) supports the magnetite (Fe_3O_4) structure of the magnetic nanoparticles;[66−68] however, most probably, it is a mix of both magnetite and maghemite (γFe_2O_3) due to the great similarity of the XRDs of both MNPs, as we demonstrated by Fe^{2+} titration earlier.[64] As far as the magnetic separation that we carry out in this work is concerned, both have similar magnetic behavior. Transmission electron microscopy (TEM, Figure 1) was performed to observe the particles' shape and size, and scanning electron microscopy (SEM, Figure S7a) and scanning transmission electron microscopy (STEM, Figure S7b) were carried out to determine their morphology. Figure 1 displays the TEM image obtained for MSNPs (a) and their Gaussian graph (b) and shows the spherical shape characteristic of these nanoparticles with a mean size of 9.34 ± 1.6 nm, which was calculated by measuring the particles manually using ImageJ software and plotting the Gaussian graph. The TEM image of MSNPs-NH_2 (c) shows aggregated particles with a diameter of 11.22 ± 2.13 nm, while TEM of MSNPs-NH_2@H[**1**] (d) displays a mean diameter of 14.17 ± 1.03, 4 nm bigger than the size of amine-coated nanoparticles, confirming the presence of [**1**]$^-$ anchored on these nanoparticles. An enlargement of this last image shows that H[**1**] is preferentially located between MSNPs-NH_2 and tends to aggregate the complex.

SEM image registered for MSNPs (Figure S7) shows the nanoparticles as an aggregated mass of particles but confirms their spherical morphology. Scanning transmission electron microscopy (STEM) was carried out on the samples containing cobaltabis(dicarbollide), [**1**]$^-$, anchored on the nanoparticles functionalized with the amine groups (Figure S7b). This technique combines the advantages of TEM and SEM and helps to obtain both the dark field and bright field images and hence it allows better visualization of the complex [**1**]$^-$ anchored on the MSNP-NH_2. The elemental mapping done on the STEM image (Figure S6c) shows the distribution of boron (blue), iron (red), and silicon (green), enlightening that the majority of H[**1**] is located between the nanoparticles and also that Fe and Si are present in the magnetic nanoparticles, with a lesser quantity of SiO_2.

The chemical composition of the magnetic nanoparticles was studied using IR spectroscopy, energy-dispersive X-ray (EDX) spectrometry, electron diffraction, and electron energy loss spectroscopy (EELS). IR spectra of MSNPs-NH_2 and MSNPs-NH_2@H[**1**] (Figure S8) display bands near 546 cm^{-1} in MSNPs-NH_2 and 542 cm^{-1} in the nanoparticles functionalized with cobaltabis(dicarbollide), MSNPs-NH_2@H[**1**], which can be assigned to $\upsilon_{\mathrm{Fe-O}}$ stretching modes, while the $\upsilon_{\mathrm{Si-O}}$ stretching mode is observed at 1074 and 1071 cm^{-1}, respectively. The bending band corresponding to N−H is observed at 1638 cm^{-1} in MSNPs-NH_2 and at 1632 cm^{-1} in MSNPs-NH_2@H[**1**]. Finally, the IR spectrum of this latter composite displays a band corresponding to the $\upsilon_{\mathrm{B-H}}$ stretching mode at around 2560 cm^{-1}, characteristic of the metallacarborane compound. These absorptions indicate a successful anchoring of complex H[**1**] to the corresponding support.

The presence of Fe and Si in the MSNPs was confirmed by EDX (Figure S9), and the presence of boron in the MSNPs-NH_2@H[**1**] composite, by the EELS spectrum (Figure 2a). The spectrum shows the corresponding boron peak and therefore the anchoring of cobaltabisdicarbollide to the MSNPs.

Magnetic Hysteresis Study. Magnetization curves at 300 K for the nanoparticles before and after the anchoring of cobaltabis(dicarbollide) [**1**]$^-$ are displayed in Figure 2b. The figure shows a saturation magnetization (M_S) value of 29.1 emu/g for the magnetic nanoparticles with negligible changes

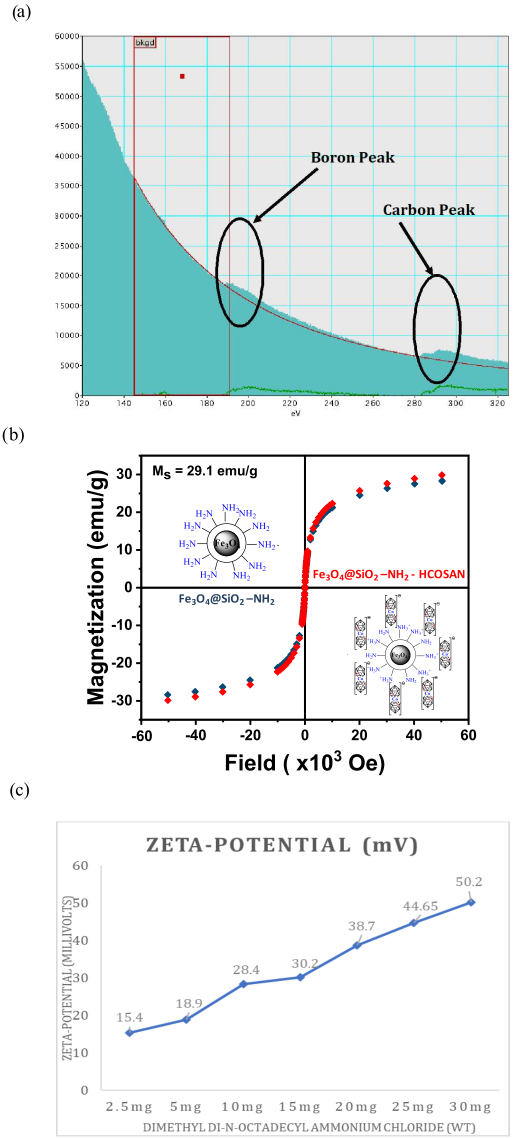

Figure 2. (a) EELS spectrum of MSNPs-NH_2@H[**1**]. (b) Hysteresis cycles recorded at room temperature (300 K) for MSNPs-NH_2 and MSNPs-NH_2@H[**1**]. (c) Stability of $Fe_3O_4@SiO_2$-NH_2 based on the measurement of the ζ-potential upon increasing amounts of dimethyl di-*n*-octadecyl ammonium chloride.

before and after the grafting of $[1]^-$. The study shows that the anchoring of the photocatalyst onto the magnetic nanoparticles does not alter the magnetic behavior of the nanoparticles.

Colloidal Stability. The colloidal stability is an important issue in the study of nanoparticles. The more these magnetic particles are stable in a colloidal state, the more difficult is to separate them by a magnet. Large MNPs show higher magnetization values but less stability in the colloidal state, and they have a greater tendency to aggregate. Thus, a adjustment has to be made, and based on their application, they are synthesized as needed. To improve the stability of the MNPs synthesized in this work, we have used sonication as an effective disaggregating way to keep them dispersed in the colloidal state. We have also coated them with silica to increase the stability. The MSNPs-NH_2@H[**1**] composite last in the suspended state only a few hours; however, it is enough for the applications sought and large enough to facilitate magnetic separation in a few minutes time. Then, to improve stability for catalytic applications that require longer periods, we have coated the surface of the nanoparticles with different surfactants with the goal to increase the viscosity of the medium, which also prevents aggregation.

Thus, to further work on this, we tried five different surfactants that are displayed in Table 1, where the ζ-potential values obtained for each surfactant are given. The stability was checked for amine-functionalized MSNPs-NH_2.

Of these surfactants, dimethyl di-octadecyl ammonium chloride was successful in providing long-term stability. This was so because it increased the viscosity of the medium and hence stopped MSNPs-NH_2 from aggregating. Due to the increase in the viscosity of the medium, the diffusion rate of the particles reduced drastically and hence prevented the particles from aggregating into larger dimensions. However, a major drawback was that these MNPs were harder to extract using an external magnet. Then, different concentrations of dimethyl di-n-octadecyl ammonium chloride were studied (Figure 2c). The trend was the same; the more stable they became, the harder it was to extract them. Up to 15 mg of the surfactant, the dispersion was stable, and with lots of time, a small amount of MNPs could be extracted by the magnet. However, obtaining completely dry MNPs that are free of the surfactant is difficult as it makes the suspension extremely viscous. As mentioned earlier, an adjustment between colloidal stability and ease of MSNPs recovery was made, and for our case, we observed that cetyl trimethyl ammonium chloride (CTAC), the one having the lowest ζ-potential but still higher than 20 mV (negative), was the most suitable.

Photocatalytic Alcohol Oxidation. The heterogeneous photocatalytic activity of the anchored metallacarborane, MSNPs-NH_2@H[**1**], was checked in the oxidation of several alcohols in water (pH = 7, K_2CO_3), using $Na_2S_2O_8$ as the oxidizing agent. All substrates were tested under analogous conditions using a loading of 0.1 or 0.01 mol % of the catalyst based on the amount of complex anchored on the nanoparticles, by exposing the reaction quartz vials to UV irradiation (λ ∼ 300 nm), at room temperature and atmospheric pressure. First of all, the reaction time for the photooxidation process was optimized using 1-phenylethanol as the substrate, and the yield values registered at different times are collected in Figure S10. We have observed a certain degree of aggregation in the nanoparticles after 4 h, which could be responsible for the 76% yield found after 8 h of the catalytic reaction (entry 4). Then, we sonicated the mixture for 3 min after 4 h of the reaction and continued the catalysis until 8 h. In this way, we optimized the reaction times shown in Figure S10, where the total conversion was attained after 8 h of reaction. This time should be chosen as the optimal time to perform the catalytic assays. In all cases, acetophenone was detected as a unique product, the selectivity achieved being >99%.

Table 1. Photocatalytic Oxidation of Alcohols[a]

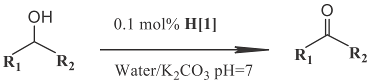

Entry	catalyst	Substrate	Yield(%)(TON)
1	MSNPs-NH_2	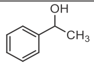	6
2	Na[**1**]	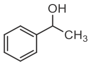	>99 (1000)
3	MSNPs-NH_2@H[**1**]	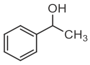	4 [a]
4	MSNPs-NH_2@H[**1**]	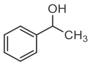	76 (760)[b]
5	MSNPs-NH_2@H[**1**]	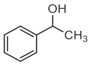	>99 (1000)
6	MSNPs-NH_2@H[**1**]	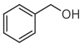	90 (900)
7	MSNPs-NH_2@H[**1**]	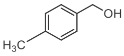	97 (970)
8	MSNPs-NH_2@H[**1**]	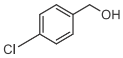	86 (860)
9	MSNPs-NH_2@H[**1**]	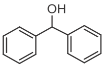	95 (950)
10	MSNPs-NH_2@H[**1**]	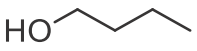	97 (970)
11	MSNPs-NH_2@H[**1**]	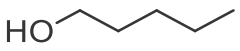	98 (980)
12	MSNPs-NH_2@H[**1**]	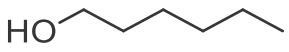	92 (920)
13	MSNPs-NH_2@H[**1**]	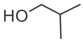	87 (870)
14	MSNPs-NH_2@H[**1**]	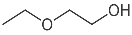	96 (960)
15	MSNPs-NH_2@H[**1**]	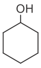	98 (980)

[a] Conditions: MNSPs-NH_2@H[1] or Na[1] (0.1 μmol), substrate (0.1 mmol), $Na_2S_2O_8$ (0.2 mmol), potassium carbonate solution (5 mL) at pH = 7; light irradiation (8 h) using a lamp with λ = 300 nm; sonication after 4 h. [b] Absence of light. [c] Without sonication. Yield values obtained are shown together with turnover number (TON) that is shown in parenthesis. Yields of products were determined by NMR spectroscopy and gas chromatography (GC). [d] MNSPs-NH_2@H[1] or Na[1] (0.1 μmol), substrate (0.1 mmol), $Na_2S_2O_8$ (0.4 mmol), potassium carbonate solution (5 mL) at pH = 7; light irradiation (8 h) using a lamp with λ = 300 nm; sonication after 4 h. **Analysis was done on the neat reaction. No attempt to separate was done.

The results displayed in Table 1 show that the heterogeneous catalyst is highly effective in the photooxidation of aromatic and aliphatic alcohols. Blank experiments using naked MSNPs-NH_2 (entry 1) or carried out in the absence of light (entry 3) yielded <6% of acetophenone, revealing that the metallacarborane-free material is ineffective in the photooxidation process and that light is also needed.

The yields observed in the photooxidation of 1-phenylethanol by the homogeneous complex Na[**1**][58] (entry 2) and by the supported MSNPs-NH_2@H[**1**] (entry 5) are remarkable, >99% in both cases, which seems to indicate that the support does not modify the catalytic properties of the metallacarborane under the same reaction conditions. In general, primary and secondary aromatic alcohols were found to be effective in the photooxidation process, the secondary aromatic alcohols being slightly more reactive than the primary ones. The quantitative conversion was obtained with 1-phenylethanol (entry 5). For the primary aromatic benzyl alcohol, the photooxidation to benzaldehyde presents high yield, 90% (entry 6). The yield values enhanced by the presence of electron-donating substituents on the aromatic ring of the benzyl alcohol (entry 7) but decreased by the presence of electron-withdrawing substituents, such as chloro (entry 8). In the case of the aliphatic alcohols 1-butanol, 1-pentanol, 1-hexanol, and 2-ethoxyethanol, all were oxidized to the corresponding acids with high yields of 97% (entry 10), 98% (entry 11), 92% (entry 12), and 96% (entry 14), respectively. In the case of the oxidation of isobutanol (entry 13), lower yield was obtained, 87%. For the secondary cyclohexanol (entry 15), close to a total conversion to cyclohexanone took place, 98%. We have also extended our study to the oxidation of interesting diols at an industrial level, diethylene glycol and 1,6-hexanediol. In both cases, the corresponding diacid has been obtained with good yields of 75% (entry 16) and 92% (entry 17). Using the same conditions displayed in Table 1, but increasing the amount of oxidizing agent due to the presence of two alcohol groups (ratio applied is 1:1000:4000), the degree of conversion increased to 99 and 95%, respectively. Important to remark is that blank controls have shown that after 8 h of reaction, under these last conditions and in the absence of MSNPs-NH_2@H[**1**] in the reaction pot, no significant oxidation of alcohol occurred (below 10%).

In all of the cases, it was observed that the initial neutral pH of the system decreased from 7 to the range between 5 and 6, and then the pH was readjusted after 4 h of reaction. The selectivity values observed in all of the catalysis experiments were >99%.

We have also verified that the activity arises from the heterogeneous catalyst and not from the release of the active catalytic species from the support during the catalysis, which indicates the presence of a homogeneous (leached) catalyst. Thus, two experiments have been done. The first one consisted of stopping the photooxidation reaction of 1-phenylethanol at 4 h, removing the nanoparticles by a magnet, and continuing the reaction with the rest of the solution until 8 h. We have not observed further reaction in the absence of the MNPs; then, we can assert a lack of metal leaching in our photocatalytic experiment (Figure S10). The second experiment was the evaluation, through UV−visible spectroscopy, of the amount of metallacarborane complex in the reaction solvent after the oxidation of 1-phenylethanol. Figure S11 displays the obtained results, where the absorption band corresponding to the complex is not observed, which again demonstrates that leaching of metallacarborane is negligible for the heterogeneous systems described.

As we have commented before, after 4 h of reaction, we have observed a certain degree of aggregation that has led to a decrease in the activity of the heterogeneous catalyst. In this context, we have studied the effect of the presence of the surfactant, cetyl trimethyl ammonium chloride (CTAC) (0.4 mM), on the oxidation of 1-phenylethanol by the heterogeneous MSNPs-NH_2@H[**1**] system. A concentration of 0.4 mM of the surfactant was found to be the best adjustment between the stability of the nanoparticles in solution and their recovery employing a magnet.

Figure 3 shows the yields obtained at 1, 2, and 4 h of the catalytic process. We can observe that total conversion of 1-phenylethanol was achieved in 4 h of reaction, and even after 2 h, a high yield of 95% was obtained; the selectivity values were >99% in all cases. These results confirm the positive effect of the surfactant on the catalytic performance of the nanoparticles since, on one hand, (i) the presence of surfactant does not detract the activity of the catalyst, which indicates that the surfactant does not block the active sites of the supported catalyst, while, on the other, (ii) the surfactant decreases the aggregation of these nanoparticles during the catalysis. For at least 4 h, the nanoparticles remain highly dispersed. This behavior improves the performance of the heterogeneous catalyst, probably due to a greater number of active centers exposed to the substrate, which could facilitate their interaction.

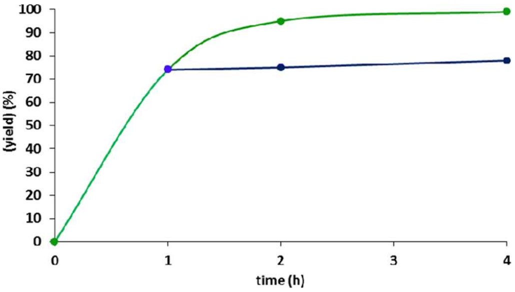

Figure 3. Plot of yield as a function of time for the photoredox catalysis of 1-phenylethanol using MNSPs-NH_2@H[**1**] as the catalyst in the presence of 0.4 mM cetyl trimethyl ammonium chloride (CTAC) as a surfactant. The blue curve shows the dependence of substrate yield on the reaction time after the catalyst was removed at 4 h. Conditions: MNSPs-NH_2@H[**1**] (0.1 μmol), substrate (0.1 mmol), $Na_2S_2O_8$ (0.2 mmol), CTAC (2 μmol), potassium carbonate solution (5 mL) at pH = 7; light irradiation using a lamp with λ = 300 nm.

Based on the above results, we have studied the photooxidation of alcohols in the presence of surfactant, using the same conditions displayed in Figure 3 and considering 2 and 4 h as the optimal times to perform the catalytic assays. The yield values obtained are gathered in Table 2. In all cases, selectivity values >99% were achieved. The results show that MSNPs-NH_2@H[**1**] is also an efficient catalyst for the photooxidation of alcohols in times as short as 2 h and 4 h, which corroborate the positive effect of the surfactant on the catalytic behavior. We have reduced the catalyst load to 0.01 mol % vs the used 0.1 mol %, corresponding to ratios of 1:10 000:20 000 of the catalyst/substrate/oxidizing agent, in the oxidation of 1-phenylethanol (1b), and we have obtained a yield >99% corresponding to TON = 10 000. This value is similar to the previously obtained value in homogeneous conditions after 8 h, but in this case, we have used short reaction times, 4 h.

We have also verified the performance of the heterogeneous catalyst by removing the nanoparticles after 1 h of operation by magnetic separation, followed by reaction with the rest of the solution until 4 h (Figure 3, blue curve). No enhancement of the product yield was observed after removal of the catalyst,

Table 2. Substrate Scope of Photooxidation of Alcohols by MSNPs-NH_2@H[1][a]

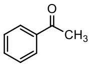 **1** 95%, TON=950 (2h) >99% , TON=1000 (4h) >99% , TON=10000 (4h)[b]	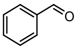 **2** 80%, TON=900 (2h) 95% , TON=950 (4h)	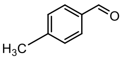 **3** 94%, TON=940 (2h) 96% , TON=960 (4h)
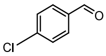 **4** 72%, TON=720 (2h) 83% , TON=830 (4h)	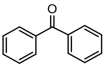 **5** 83%, TON=830 (2h) 90% , TON=900(4h)	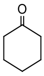 **6** 85%, TON=850 (2h) 98% , TON=980 (4h)
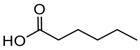 **7** 90%, TON=900 (2h) >99% , TON=1000 (4h)	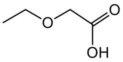 **8** 92%, TON=920 (2h) 95% , TON=950 (4h)	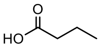 **9** 96%, TON=960 (2h) 98% , TON=980 (4h)
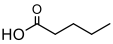 **10** 91%, TON=910 (2h) 94% , TON=940 (4h)	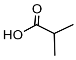 **11** 79%, TON=790 (2h) 84% , TON=840 (4h)	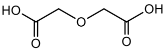 **12** 55%,** TON=550 (2h)[c] 81%,** TON=810(4h)[c]
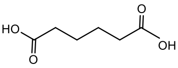 **13** 62%,** TON=620 (2h)[c] 90%,** TON=900 (4h)[c]		

[a] Conditions: MNSPs-NH_2@H[1] (0.1 μmol), substrate (0.1 mmol), $Na_2S_2O_8$ (0.2 mmol), CTAC (2 μmol), potassium carbonate solution (5 mL) at pH = 7; light irradiation using a lamp with λ = 300 nm. Yields and TON values obtained are shown together with the time of the catalyst that is shown in parenthesis. [b] MNSPs-NH_2@H[1] (0.05 μmol), substrate (0.5 mmol), $Na_2S_2O_8$ (1 mmol), CTAC (2 μmol), potassium carbonate solution (5 mL) at pH = 7. [c] MNSPs-NH_2@H[1] (0.1 μmol), substrate (0.1 mmol), $Na_2S_2O_8$ (0.4 mmol), CTAC (2 μmol), potassium carbonate solution (5 mL) at pH = 7. Yields of products were determined by NMR spectroscopy and GC. **Analysis was done on the neat reaction. No attempt to separate was done.

proving that either no leaching or very negligible leaching occurred.

The lifetime of the catalyst and its level of reusability are very important factors for practical applications. In this sense and based on the results shown above, we have investigated the recyclability of the heterogeneous MSNPs-NH_2@H[1] catalytic system in water on two aromatic substrates, 1-phenylethanol and diphenylmethanol (Figure 4a), and on the aliphatic cyclohexanol (Figure 4b). In all cases, after 4 h of catalysis, the heterogeneous catalyst was recovered from the mixture of reaction by magnet separation. Afterward, the particles were washed with water, dried, and exposed to a new load of substrate under the same experimental conditions.

These results are an evidence that the heterogeneous catalyst maintains a good performance throughout the twelve runs, with good yield values for 1-phenylethanol, diphenylmethanol, and cyclohexanol substrates, maintaining the selectivity values >99%. The overall turnover numbers (TONs) are 11960 for 1-phenylethanol, 9490 for diphenylmethanol, and 11 180 for cyclohexanol. To the best of our knowledge, these values are among the highest turnover numbers achieved in alcohol photoredox oxidation in heterogeneous conditions. We have also observed that the activity of the catalysts does not decrease through the repeated uses. The high stability shown by the catalyst seems to be due to the favorable nonbonding interactions mostly B−H···H−N between cobaltabis(dicarbollide), $[1]^-$, and NH_3^+ groups of the nanoparticles that lead to the formation of a hybrid material with enhanced stability. A UV−visible analysis of the solutions after the consecutive recycling experiments indicated that no noticeable loss of catalyst takes place (Figure S10). The morphology of the recovered catalyst was analyzed, after 12 runs, in the

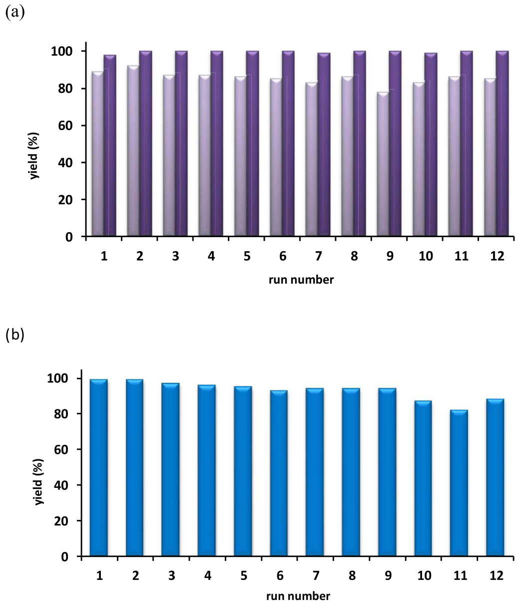

Figure 4. Yield values obtained throughout a number of successive reuses of the catalyst MSNPs-NH_2@H[**1**] in the photooxidation of (a) diphenylmethanol (light purple) and 1-phenylethanol (dark purple) and (b) cyclohexanol. Conditions: MNSPs-NH_2@H[**1**] (0.1 μmol), substrate (0.1 mmol), $Na_2S_2O_8$ (0.2 mmol), CTAC (2 μmol), potassium carbonate solution (5 mL) at pH = 7; light irradiation using a lamp with λ = 300 nm, 4 h per run.

photooxidation of 1-phenylethanol. The SEM image obtained was compared with that of the catalyst before the catalysis (Figure S12). The results show that the morphology is maintained.

CONCLUSIONS

In this work, we demonstrated the feasibility to heterogenize a successful homogeneous photoredox catalyst on a system that can be easily separated from the solution media. We aimed to develop a system where no chemical bonding was necessary to link the homogeneous catalyst to the support particle so that the adhesion of both components, the support and the catalyst, was easily made; we also observed that the activity and selectivity of the original homogeneous catalyst was fully preserved, reaching yield values close to 100%, and that no leakage of the catalyst took place so that multiple runs could be made with no loss of activity. We also observed that high activity did not involve hard working up. We designed the experiments on the basis of magnetic nanoparticles (MNPs) on which the photoredox catalyst was firmly bound. This would facilitate magnetic separations of the catalyst from the liquid containing the modified substrate. The nonbonding linkage between the "homogeneous catalyst" and the MNPs was based on the well-established interaction between the θ-shape metallabis(dicarbollide) $[\mathbf{1}]^-$ and ammine or ammonium functionalities. Thus, the magnetite MNPs were first coated with SiO_2 to provide a certain degree of stability to the MNPs and importantly enough silanol groups to be tethered to ammine-carrying units. These were the MSNPs-NH_2 on which was easily anchored, in water, the photoredox catalyst H[3,3′-Co(1,2-$C_2B_9H_{11}$)$_2$], H[**1**], to generate MSNPs-NH_2@H[**1**]. Dedicated techniques have been utilized to study the morphology, characterization, and colloidal stability of the MNPs produced. To optimize the MNPs, the model was the homogeneous catalysis performance of H[**1**] in the oxidation of alcohols that did require about 8 h of reaction to achieve near 100% conversion. Thus, the stability study of the MNPs was performed for this period of time. As the reaction does produce H^+ and pH tuning was advisable to reach high conversion, the reaction was stopped at 4 h for pH adjustment, so we aimed at maintaining the MNPs in a stable colloidal form for a minimum of 4 h. Then, by sonication, they were set back into a colloidal stable phase for an additional reaction period of 4 h. This was successful, and catalyst loads of 0.1 and 0.01 mol % were studied. The substrates studied did contain either aromatic or aliphatic groups. Representative examples are 1-phenylethanol, 1-hexanol, 1,6-hexanediol, or cyclohexanol. To the best of our knowledge, the catalyst/substrate ratios indicated are among the highest ever reported. We had the feeling, however, that the reaction could even take less time and that there still was the opportunity to lessen it if we could prevent aggregation somehow. For this purpose, several surfactant agents were studied in combination with the MNPs and their ζ-potentials were studied. Even though some did provide excellent colloidal stability, they were in turn difficult to separate magnetically. We decided to use cetyl trimethyl ammonium chloride (CTAC) that provided an adequate ζ-potential, and thus adequate stability, without hampering quick magnetic separation. The results with a 1:20 ratio of the catalyst to surfactant proved our hypothesis and demonstrated that the reaction could be speeded up if aggregation was prevented. Again, however, one must balance if shortening of time for the reaction could compensate a more difficult working up.

As a last set of experiments, we demonstrates the recyclability of the system, and to do this categorically, we applied 12 runs to the MSNPs-NH_2@H[**1**] catalyst and studied the variation in selectivity and yield. The catalytic studies were done on the photooxidation of 1-phenylethanol, diphenylmethanol, and cyclohexanol substrates and demonstrated the effective recyclability of the catalytic systems throughout the successive 12 runs in all three cases, keeping high conversion and selectivity values. Overall, the cobaltabis(dicarbollide) catalyst supported on silica-coated magnetite nanoparticles has proven to be a robust, efficient, and easily reusable system for the photooxidation of alcohols in water, resulting in a green and sustainable heterogeneous catalytic system.

EXPERIMENTAL SECTION

Materials. All reagents used in the present work were obtained from Aldrich Chemical and were used without further purification. $[NH_4]OH$ (30% as NH_3) was purchased from Panreac AppliChem and used as received.

Reagent-grade organic solvents were obtained from SDS, and high-purity deionized water was obtained by passing distilled water through a nanopure Milli-Q water purification system.

H[3,3′-Co(1,2-$C_2B_9H_{11}$)$_2$], H[**1**], was synthesized from commercial Cs[3,3′-Co(1,2-$C_2B_9H_{11}$)$_2$] (Katchem spol. s r.o.) following a method described in the literature.[37,41,69]

Instrumentation and Measurements. IR spectra were recorded on an JASCO FTIR-4600 spectrometer. UV−vis spectroscopy was performed on a Cary-5000 Scan (Varian) UV−Vis−NIR spectrophotometer with 1 cm quartz cells. Transmission electron microscopy (TEM) studies were carried out using JEOL JEM 1210 at 120 kV. Scanning electron microscopy (SEM) and energy-dispersive X-ray spectroscopy (EDX) analyses were done using a QUANTA FEI 200 FEG-ESEM device. The solid sample was analyzed for this. HRTEM was done using JEM-2011 at 200 kV with 0.18 nm resolution. High-resolution SEM (HRSEM) was done using a Zeiss Merlin instrument. ImageJ software was used for measuring the particles. ζ-Potential studies were carried out using a Zetasizer Nano ZS (for DLS light source, a He-Ne laser was used, 633 nm, max 4 mW, backscattering angle used was 173°, and for ζ-potential, electrophoretic light scattering principle was used for the measurements). The magnetization hysteresis cycle was measured using a Quantum Design MPMS-XL system at 300 K with a maximum of 60 kOe. Scanning transmission microscopy (STEM) and EELS measurements were done using an FEI Tecnai F20 S/TEM HRTEM device at 200 kV. GC measurements were taken with a Shimadzu GC-2010 gas chromatography apparatus equipped with an Astec CHIRALDEX G-TA column and an flame ionization detector (FID) detector.

Preparations. Magnetic nanoparticles (MNPs) were prepared according to literature procedures,[60] using the aqueous coprecipitation method. This core was then further encapsulated in a silica shell using the Stober process.[70] After having the MNPs coated with SiO_2, (MSNPs) they were further functionalized by amino groups.

Synthesis of Fe_3O_4 Core. First, sodium hydroxide (NaOH, 15 g) was dissolved in 25 mL of double-distilled water. Then, a mixture of $FeCl_2·4H_2O$ (2 g), $FeCl_3·6H_2O$ (5.2 g), double-distilled water (25 mL), and HCl (0.85 mL, 12 M) was added dropwise with vigorous stirring to make a black solid product. The resultant mixture was heated using an oil bath for 4 h at 80 °C. The black magnetite solid MNPs were isolated using an external magnet, washed three times with deionized water and finally once with ethanol, and then dried at 80 °C for 10 h.

Synthesis of $Fe_3O_4@SiO_2$ Core−Shells (MSNPs). Fe_3O_4 (0.5 g, 2.1 mmol) was dispersed in a mixture of ethanol (100 mL) and deionized water (25 mL) for 30−40 min using an ultrasound bath. Then, 2.5 mL of NH_3 (30% for analysis) was added followed by the dropwise addition of tetraethoxysilane (TEOS) (1.5 mL). This solution was stirred mechanically for 6 h at room temperature. Then, the product $Fe_3O_4@SiO_2$ was separated using an external magnet, washed three times with deionized water and finally with ethanol, and then dried at 80 °C for 10 h. For this reaction, we designed a new Teflon covered system with a crystal mechanical stirring rod (see Supporting Information, SI).

Small and Large Particles. The smaller silica-coated particles are synthesized using the standard silica coating procedure reported above. In the case of larger particles, the magnetite core reaction mixture is stirred for 6 h and the silica reaction is stirred for 12 or 18 h depending on the size needed to be produced. The quantity of TEOS to be added can also be controlled depending on the necessity of thickness of the shell. The biggest advantage of this method lies in the fact that it helps to change the size of the particles by modifying the time and temperature of the reaction. The silica coating using the Stober process can also be done at a mild temperature of 40 °C in need of thicker coatings over the magnetite core. This flexibility in the process makes it attractive, but the disadvantage of this procedure lies in less control of the monodispersity of the particles.

Synthesis of Amine-Functionalized Silica, $Fe_3O_4@SiO_2$-NH_2 (MSNPs-NH_2). A mixture of $Fe_3O_4@SiO_2$ (200 mg) was dispersed in ethanol (45 mL). Then, 5 mL of 3-(2-aminoethylamino)-propylmethyldimethoxy silane (APMS) was dissolved in 20 mL of ethanol and added to the suspension of $Fe_3O_4@SiO_2$ in ethanol. The pH value of the reaction mixture was set to 11 using tetramethylammonium hydroxide (TMAH). The reaction mixture was then heated to 50 °C and stirred for 5 h. After aging for a night, the suspension of functionalized nanoparticles was completely stable. It was then precipitated using NaCl solution. Then, the nanoparticles were thoroughly washed with distilled water using magnetic separation and finally dried at 80 °C in vacuo.

For this amine functionalization, instead of APMS, other reagents like (3-aminopropyl)triethoxy silane (APTES) or (3-aminopropyl)-trimethoxy silane (APTMS) can also be used, which give the same result.

*Synthesis of Cosane-Functionalized Silica, $Fe_3O_4@SiO_2$-NH_2-H[COSAN], (MSNPs-NH_2@H[**1**]).* $Fe_3O_4@SiO_2$-NH_2 (50 mg) was suspended in 10 mL of water containing 5 mM H[3,3′-Co(1,2-$C_2B_9H_{11})_2$], H[**1**]. The mixture was sonicated in an ultrasound bath for 30 min and then washed 10 times with water using magnetic separation. Finally, the sample was dried under vacuum at 80 °C.

UV−Visible Studies. The sample for this experiment was prepared by mixing 5 mg of $Fe_3O_4@SiO_2$-NH_2 in a solution of 1 mM H[**1**] (16.3 mg) in 50 mL of water, sonicating for 15 min, and then collecting the MNPs with the help of a magnet for about 10 min. The MNPs are concentrated at the bottom of the flask, and the clear liquid at the top is studied using UV−visiblespectrometry (see Figure 1a). This procedure is done for 5, 10, 15, 20, 25, and 30 mg of $Fe_3O_4@SiO_2$-NH_2 keeping constant the amount of H[**1**]. The UV−visible absorbance decreases with the addition of magnetic nanoparticles, and the difference between the two absorbance peaks permits quantification of H[**1**] anchored to the surface of the nanoparticles.

Colloidal Stability. $Fe_3O_4@SiO_2$-NH_2 (5 mg) was suspended using ultrasound sonication in 10 mL of distilled water in five different vials. After 5 min of sonication, the MNPs were well dispersed in water. Then, 2.5 mg of five different surfactants was added in each vial and sonicated further for another 5 min. These samples were then taken to be tested using ζ-potential to check the stability. After that, another 2.5 mg of the surfactants was added in their respective vials totaling the amount of surfactant to be 5 mg in each vial, sonicated for another 5 min, and tested for ζ-potential values. This was continued further by the addition of up to 30 mg of surfactant in each of their respective vials, followed by sonication and then testing their stability using ζ-potential.

Catalytic Studies. *Alcohol Oxidation.* Alcohol (0.1 mmol) and $Na_2S_2O_8$ (0.2 mmol) were dissolved in 5 mL of water (K_2CO_3, pH = 7) together with 5 mg of MSNP-NH_2@H[**1**] (0.1 μmol catalyst). The amount of heterogenized catalyst was calculated taking into account the functionalization of magnetic nanoparticles. In the case of addition of the surfactant cetyl trimethyl ammonium chloride, the concentration used was 0.4 mM. The general photocatalytic oxidation experiments were all performed by exposing the reaction quartz vials to UV irradiation ($\lambda \sim 300$ nm), at room temperature and atmospheric pressure, for different times. The complex/substrate/sacrificial oxidant ratios used (1:1000:2000 and 1:10 000:20 000 that correspond to concentrations of 0.02:20:40 mM and 0.01:100:200 mM) were varied according to the study. For every experiment, light illumination was supplied by a light reactor with twelve lamps that produce UVA light at room temperature. A magnet was used for the separation of the catalytic material from the reaction medium. The reaction products were extracted with dichloromethane (3 × 10 mL). The combined organic phases were dried over sodium sulfate, and the solvent was evaporated under reduced pressure. To check the reproducibility of the reactions, all of the experiments were carried out three times. The reaction products were quantified using ^1H NMR spectroscopy and confirmed by gas chromatography−mass spectrometry (GC−MS) analysis.

Recycling Experiments. The reaction conditions indicated above were used in these experiments. After finishing each run, the heterogeneous catalyst was separated by a magnet, washed four times with water, and reused in a subsequent run.

ASSOCIATED CONTENT

Supporting Information

The Supporting Information is available free of charge at https://pubs.acs.org/doi/10.1021/acsami.0c17847.

Synthesis of the Fe_3O_4 core (MNP) and $Fe_3O_4@SiO_2$ core (MSNP) and their full characterization; UV−vis spectra at different times of extraction of the MNPs, EDX spectrum of Fe_3O_4@SiO_2 (MSNP), electron diffraction pattern of Fe_3O_4@SiO_2-NH_2 (MSNPs-NH_2), plot of yield as a function of time for the photoredox catalysis of 1-phenylethanol using MNSPs-NH_2@H[**1**] as the catalyst, UV−vis spectra corresponding to a solution of 0.02 mM H[**1**] in 5 mL of water, UV−visible spectra of the solutions after the oxidation of 1-phenylethanol by the MNSPs-NH_2@H[**1**] catalyst throughout the different reuses, and SEM images of MSNPs-NH_2@H[**1**] before the photooxidation of 1-phenylethanol and after 12 reuses (PDF)

AUTHOR INFORMATION

Corresponding Authors

Isabel Romero − *Departament de Química and Serveis Tècnics de Recerca, Universitat de Girona, E-17003 Girona, Spain;* orcid.org/0000-0003-4805-8394; Email: marisa.romero@udg.edu

Francesc Teixidor − *Institut de Ciencia de Materials de Barcelona, ICMAB-CSIC, E-08193 Bellaterra, Spain;* orcid.org/0000-0002-3010-2417; Email: teixidor@icmab.es

Authors

Isabel Guerrero − *Institut de Ciencia de Materials de Barcelona, ICMAB-CSIC, E-08193 Bellaterra, Spain; Departament de Química and Serveis Tècnics de Recerca, Universitat de Girona, E-17003 Girona, Spain*

Arpita Saha − *Institut de Ciencia de Materials de Barcelona, ICMAB-CSIC, E-08193 Bellaterra, Spain*

Jewel Ann Maria Xavier − *Institut de Ciencia de Materials de Barcelona, ICMAB-CSIC, E-08193 Bellaterra, Spain*

Clara Viñas − *Institut de Ciencia de Materials de Barcelona, ICMAB-CSIC, E-08193 Bellaterra, Spain;* orcid.org/0000-0001-5000-0277

Complete contact information is available at: https://pubs.acs.org/10.1021/acsami.0c17847

Notes

The authors declare no competing financial interest.

ACKNOWLEDGMENTS

This research has been financed by MINECO (CTQ2016-75150-R and CTQ2015-66143-P) and Generalitat de Catalunya (2017 SGR 1720). The "Severo Ochoa" Program for Centers of Excellence in R&D 234 (SEV-2015-0496) is appreciated. J.A.M.X. thanks the DOC-FAM programme funded by the European Union's Horizon 2020 research and innovation programme under the Marie Sklodowska-Curie grant agreement No. 754397.

REFERENCES

(1) Crabtree, R. H. Energy Production and Storage−Inorganic Chemical Strategies for a Warming World. In *Encyclopedia of Inorganic Chemistry*, 2nd ed.; John Wiley & Sons, Inc., 2010; pp 73−87.

(2) Renger, G. Energy Transfer and Trapping in Photosystem II. In *The Photosystems: Structure, Function, and Molecular Biology*, 1st ed.; Barber, J., Ed.; Elsevier Science Publishers: Amsterdam, The Netherlands, 1992; pp 45−99.

(3) Xia, Y.; Xiao, K.; Cheng, B.; Yu, J.; Jiang, L.; Antonietti, M.; Cao, S. Improving Artificial Photosynthesis over Carbon Nitride by Gas-Liquid-Solid Interface Management for Full Light-Induced CO_2 Reduction to C-1 and C-2 Fuels and O-2. *ChemSusChem* **2020**, *13*, 1730−1734.

(4) Savateev, A.; Antonietti, M. Ionic Carbon Nitrides in Solar Hydrogen Production and Organic Synthesis: Exciting Chemistry and Economic Advantages. *ChemCatChem* **2019**, *11*, 6166−6176.

(5) Savateev, A.; Ghosh, I.; König, B.; Antonietti, M. Photoredox Catalytic Organic Transformations using Heterogeneous Carbon Nitrides. *Angew. Chem., Int. Ed.* **2018**, *57*, 15936−15947.

(6) Sharma, R. K.; Dutta, S.; Sharma, S.; Zboril, R.; Varma, R. S.; Gawande, M. B. Fe_3O_4 (Iron Oxide)-Supported Nanocatalysts: Synthesis, Characterization and Applications in Coupling Reactions. *Green Chem.* **2016**, *18*, 3184−3209.

(7) Wang, D.; Astruc, D. Fast-Growing Field of Magnetically Recyclable Nanocatalysts. *Chem. Rev.* **2014**, *114*, 6949−6985.

(8) Zhang, Q.; Yang, X.; Guan, J. Applications of Magnetic Nanomaterials in Heterogenous Catalysis. *ACS Appl. Nano Mater.* **2019**, *2*, 4681−4697.

(9) Gawande, M. B.; Branco, P. S.; Varma, R. S. Nano-Magnetite (Fe_3O_4) as a Support for Recyclable Catalysts in the Development of Sustainable Methodologies. *Chem. Soc. Rev.* **2013**, *42*, 3371−3393.

(10) Santra, S.; Tapec, R.; Theodoropoulou, N.; Dobson, J.; Hebard, A.; Tan, W. Synthesis and Characterization of Silica-Coated Iron Oxide Nanoparticles in Microemulsion: The Effect of Nonionic Surfactants. *Langmuir* **2001**, *17*, 2900−2906.

(11) Yang, H.; Zhang, S. Q.; Chen, X. L.; Zhuang, Z. H.; Xu, J. G.; Wang, X. R. Magnetite-Containing Spherical Silica Nanoparticles for Biocatalysis and Bioseparations. *Anal. Chem.* **2004**, *76*, 1316−1321.

(12) Ertem, E.; Murillo-Cremaes, N.; Carney, R. P.; Laromaine, A.; Janeček, E.-R.; Roig, A.; Stellacci, F. A Silica-based Magnetic Platform Decorated with Mixed Ligand Gold Nanoparticles: A Recyclable Catalyst for Esterification Reactions. *Chem. Commun.* **2016**, *52*, 5573−5576.

(13) Shylesh, S.; Schünemann, V.; Thiel, W. Magnetically Separable Nanocatalysts: Bridges between Homogeneous and Heterogeneous Catalysis. *Angew. Chem., Int. Ed.* **2010**, *49*, 3428−3459.

(14) Salih, K. S. M.; Mamone, P.; Dörr, G.; Bauer, T. O.; Brodyanski, A.; Wagner, C.; Kopnarski, M.; Klupp-Taylor, R. N.; Demeshko, S.; Meyer, F.; Schünemann, V.; Ernst, S.; Gooßen, L. J.; Thiel, W. R. Facile Synthesis of Monodisperse Maghemite and Ferrite Nanocrystals from Metal Powder and Octanoic Acid. *Chem. Mater.* **2013**, *25*, 1430−1435.

(15) Gawande, M. B.; Monga, Y.; Zboril, R.; Sharma, R. K. Silica-Decorated Magnetic Nanocomposites for Catalytic Applications. *Coord. Chem. Rev.* **2015**, *288*, 118−143.

(16) Agotegaray, M. A.; Lassalle, V. L. *Silica-Coated Magnetic Nanoparticles*, 1st ed.; Springer Publications: Cham, Switzerland, 2017.

(17) Manrique, E.; Ferrer, I.; Lu, C.; Fontrodona, X.; Rodríguez, M.; Romero, I. A Heterogeneous Ruthenium dmso Complex Supported onto Silica Particles as a Recyclable Catalyst for the Efficient Hydration of Nitriles in Aqueous Medium. *Inorg. Chem.* **2019**, *58*, 8460−8470.

(18) Varna, M.; Ratajczak, P.; Ferreira, I.; Leboeuf, C.; Bousquet, G.; Janin, A. In vivo Distribution of Inorganic Nanoparticles in Preclinical Models. *J. Biomater. Nanobiotechnol.* **2012**, *3*, 269−279.

(19) Ferrer, I.; Fontrodona, X.; Roig, A.; Rodriguez, M.; Romero, I. A Recoverable Ruthenium Aqua Complex Supported on Silica Particles: An Efficient Epoxidation Catalyst. *Chem. - Eur. J.* **2017**, *23*, 4096−4107.

(20) Huang, S.; Xu, Y.; Xie, M.; Ma, Y.; Yan, J.; Li, Y.; Zhao, Y.; Xu, H.; Li, H. Multifunctional C-Doped $CoFe_2O_4$ Material as Cocatalyst to Promote Reactive Oxygen Species Generation over Magnetic Recyclable C−CoFe/Ag−AgX Photocatalysts. *ACS Sustainable Chem. Eng.* **2018**, *6*, 11968−11978.

(21) Fu, W.; Xu, X.; Wang, W.; Shen, J.; Ye, M. In-Situ Growth of $NiFe_2O_4$/2D MoS_2 p-n Heterojunction Immobilizing Palladium Nanoparticles for Enhanced Visible-Light Photocatalytic Activities. *ACS Sustainable Chem. Eng.* **2018**, *6*, 8935−8944.

(22) De Faveri, G.; Ilyashenko, G.; Watkinson, M. Recent Advances in Catalytic Asymmetric Epoxidation Using the Environmentally Benign Oxidant Hydrogen Peroxide and Its Derivatives. *Chem. Soc. Rev.* **2011**, *40*, 1722−1760.

(23) Manrique, E.; Fontrodona, X.; Poater, A.; Sola, M.; Rodríguez, M.; Romero, I. Reusable Manganese Compounds Containing Pyrazole-Based Ligands for Olefin Epoxidation Reactions. *Dalton Trans.* **2015**, *44*, 17529−17543.

(24) Manrique, E.; Fontrodona, X.; Rodríguez, M.; Romero, I. A Ruthenium(II) Aqua Complex as Efficient Chemical and Photochemical Catalyst for Alkene and Alcohol Oxidation. *Eur. J. Inorg. Chem.* **2019**, *15*, 2124−2133.

(25) Fontanet, M.; Rodríguez, M.; Viñas, C.; Teixidor, F.; Romero, I. Carboranycarboxylate Complexes as Efficient Catalysts in Epoxidation Reactions. *Eur. J. Inorg. Chem.* **2017**, 4425−4429.

(26) Hoover, J. M.; Stahl, S. S. Highly Practical Copper(I)/TEMPO Catalyst System for Chemoselective Aerobic Oxidation of Primary Alcohols. *J. Am. Chem. Soc.* **2011**, *133*, 16901−16910.

(27) Jensen, D. R.; Schultz, M. J.; Mueller, J. A.; Sigman, M. S. A Well-Defined Complex for Palladium-Catalyzed Aerobic Oxidation of Alcohols: Design, Synthesis, and Mechanistic Considerations. *Angew. Chem., Int. Ed.* **2003**, *42*, 3810−3813.

(28) Jiang, X.; Zhang, J.; Ma, S. Iron Catalysis for Room-Temperature Aerobic Oxidation of Alcohols to Carboxylic Acids. *J. Am. Chem. Soc.* **2016**, *138*, 8344−8347.

(29) Esswein, A. J.; Nocera, D. G. Hydrogen Production by Molecular Catalysis. *Chem. Rev.* **2007**, *107*, 4022−4047.

(30) Oliveira, R. L.; Kiyohara, P. K.; Rossi, L. M. High Performance Magnetic Separation of Gold Nanoparticles for Catalytic oxidation of Alcohols. *Green Chem.* **2010**, *12*, 144−149.

(31) Sharma, R. K.; Yadav, M.; Monga, Y.; Gaur, R.; Adholeya, A.; Zboril, R.; Varma, R. S.; Gawande, M. B. Silica-Based Magnetic Manganese Nanocatalyst—Applications in the Oxidation of Organic Halides and Alcohols. *ACS Sustainable Chem. Eng.* **2016**, *4*, 1123−1130.

(32) Karimpour, T.; Safaei, E.; Karimi, B.; Lee, Y.-I. Iron(III) Amine Bis(phenolate) Complex Immobilized on Silica-Coated Magnetic Nanoparticles: A Highly Efficient Catalyst for the Oxidation of Alcohols and Sulfides. *ChemCatChem* **2018**, *10*, 1889−1899.

(33) Hosseinzadeh-Khanmiri, R.; Kamel, Y.; Keshvari, Z.; Mobaraki, A.; Shahverdizadeh, G. H.; Vessally, E.; Babazadeh, M. Synthesis and Characterization of a Ni Nanoparticle Stabilized on Ionic Liquid-functionalized Magnetic Silica Nanoparticles for Tandem Oxidative Reaction of Primary Alcohols. *Appl. Organomet. Chem.* **2018**, *32*, No. e4452.

(34) Grimes, R. N. *Carboranes*, 3rd ed.; Elsevier Inc., 2016.

(35) Bennour, I.; Cioran, A. M.; Teixidor, F.; Viñas, C. 3,2,1 and Stop! An Innovative, Straightforward and Clean Route for the Flash Synthesis of Metallacarboranes. *Green Chem.* **2019**, *21*, 1925−1928.

(36) Masalles, C.; Llop, J.; Viñas, C.; Teixidor, F. Extraordinary Overoxidation Resistance Increase in Self-Doped Polypyrroles by Using Non-conventional Low Charge Density Anions. *Adv. Mater.* **2002**, *14*, 826−829.

(37) Hardie, M. J.; Raston, C. L. Solid State Supramolecular Assemblies of Charged Supermolecules (Na[2.2.2]cryptate)$^+$ and Anionic Carboranes with Host Cyclotriveratrylene. *Chem. Commun.* **2001**, *26*, 905−906.

(38) Fox, M. A.; Huges, A. K. Cage C−H···X Interactions in Solid-state Structures of Icosahedral Carboranes. *Coord. Chem. Rev.* **2004**, *248*, 457−476.

(39) Brusselle, D.; Bauduin, P.; Girard, L.; Zaulet, A.; Viñas, C.; Teixidor, F.; Ly, I.; Diat, O. Lyotropic Lamellar Phase Formed from Monolayered θ-Shaped Carborane-Cage Amphiphiles. *Angew. Chem., Int. Ed.* **2013**, *52*, 12114−12118.

(40) Zaulet, A.; Teixidor, F.; Bauduin, P.; Diat, O.; Hirva, P.; Ofori, A.; Viñas, C. Deciphering the Role of the Cation in Anionic Cobaltabisdicarbollide Clusters. *J. Organomet. Chem.* **2018**, *865*, 214−225.

(41) Tarrés, M.; Viñas, C.; Gonzalez-Cardoso, P.; Hänninen, M. M.; Sillanpää, R.; Dordovic, V.; Uchman, M.; Teixidor, F.; Matějíček, P. Aqueous Self-Assembly and Cation Selectivity of Cobaltabisdicarbollide Dianionic Dumbbells. *Chem. - Eur. J.* **2014**, *20*, 6786−6794.

(42) Bauduin, P.; Prevost, S.; Farras, P.; Teixidor, F.; Diat, O.; Zemb, T. A Theta-shaped Amphiphilic Cobaltabisdicarbollide Anion: Transition from Monolayer Vesicles to Micelles. *Angew. Chem., Int. Ed.* **2011**, *50*, 5298−5300.

(43) Ďord‡ovič, V.; Tosner, Z.; Uchman, M.; Zhigunov, A.; Reza, M.; Ruokolainen, J.; Pramanik, G.; Cígler, P.; Kalíková, K.; Gradzielski, M.; Matějíček, P. Stealth Amphiphiles: Self-Assembly of Polyhedral Boron Clusters. *Langmuir* **2016**, *32*, 6713−6722.

(44) Uchman, M.; Dordovic, V.; Tosner, Z.; Matějíček, P. Classical Amphiphilic Behavior of Nonclassical Amphiphiles: A Comparison of Metallacarborane Self-Assembly with SDS Micellization. *Angew. Chem., Int. Ed.* **2015**, *54*, 14113−14117.

(45) Olid, D.; Nuñez, R.; Viñas, C.; Teixidor, F. Methods to Produce B−C, B−P, B−N and B−S Bonds in Boron Clusters. *Chem. Soc. Rev.* **2013**, *42*, 3318−3336.

(46) Stoica, A.; Viñas, C.; Teixidor, F. Cobaltabisdicarbollide Anion Receptor for Enantiomer-Selective Membrane Electrodes. *Chem. Commun.* **2009**, *33*, 4988−4990.

(47) Fuentes, I.; Pujols, J.; Viñas, C.; Ventura, S.; Teixidor, F. Dual Binding Mode of Metallacarborane Produces a Robust Shield on Proteins. *Chem. - Eur. J.* **2019**, *25*, 12820−12829.

(48) Li, H.; Li, F.; Zhang, B.; Zhou, X.; Yu, F.; Sun, L. Visible Light-Driven Water Oxidation Promoted by Host−Guest Interaction between Photosensitizer and Catalyst with a High Quantum Efficiency. *J. Am. Chem. Soc.* **2015**, *137*, 4332−4335.

(49) Behnken, P. E.; Busby, D. C.; Delaney, M. S.; King, R. E.; Kreimendahl, C. W.; Marder, T. B.; Wilczynski, J. J.; Hawthorne, M. F. Metallacarboranes in Catalysis. Kinetics and Mechanism of Acrylate Ester Hydrogenation Catalyzed by *closo*-Rhodacarboranes. *J. Am. Chem. Soc.* **1984**, *106*, 7444−7450. and references therein.

(50) Shen, H.; Xie, Z. *Boron Science, New Technologies and Applications*; Hosmane, N. S., Ed.; CRC Press: Boca Raton, FL, 2012; Chapter 21, pp 517−528.

(51) Bauer, S.; Hey-Hawkins, E. *Boron Science, New Technologies and Applications*; Hosmane, N. S., Ed.; CRC Press: Boca Raton, FL, 2012; Chapter 22, pp 529−579.

(52) *Handbook of Boron Chemistry in Organometallics, Catalysis, Materials and Medicine*; Hosmane, N. S.; Eagling, R., Eds.; Boron in Catalysts; World Science Publishers: New Jersey, 2018; Vol. 2.

(53) Xie, Z. W. Group 4 Metallocenes Incorporating Constrained-Geometry Carboranyl Ligands. *Coord. Chem. Rev.* **2006**, *250*, 259−272.

(54) Han, Y.-F.; Guo-Xin, J. Half-Sandwich Iridium- and Rhodium-Based Organometallic Architectures: Rational Design, Synthesis, Characterization, and Applications. *Acc. Chem. Res.* **2014**, *47*, 3571−3579.

(55) Fisher, S. P.; Tomich, A. W.; Lovera, S. O.; Kleinsasser, J. F.; Guo, J.; Asay, M. J.; Nelson, H. M.; Lavallo, V. Nonclassical Applications of *closo*-Carborane Anions: From Main Group Chemistry and Catalysis to Energy Storage. *Chem. Rev.* **2019**, *119*, 8262−8290.

(56) Teixidor, F.; Flores, M. A.; Viñas, C.; Kivekäs, R.; Sillanpää, R. *exo-nido*-Cyclooctadienerhodacarboranes: Synthesis, Reactivity, and Catalytic Properties in Alkene Hydrogenation. *J. Am. Chem. Soc.* **2000**, *122*, 1963−1973.

(57) Popescu, A. R.; Teixidor, F.; Viñas, C. Metal Promoted Charge and Hapticities of Phosphines: The Uniqueness of Carboranylphosphines. *Coord. Chem. Rev.* **2014**, *269*, 54−84.

(58) Guerrero, I.; Kelemen, Z.; Viñas, C.; Romero, I.; Teixidor, F. Metallacarboranes as Photoredox Catalysts in Water. *Chem. - Eur. J.* **2020**, *26*, 5027−5036.

(59) Nuñez, R.; Tarrés, M.; Ferrer-Ugalde, A.; Fabrizi de Biani, F.; Teixidor, F. Electrochemistry and Photoluminescence of Icosahedral Carboranes, Boranes, Metallacarboranes, and Their Derivatives. *Chem. Rev.* **2016**, *116*, 14307−14378.

(60) Hassani, H.; Zakerinasab, B.; Nasseri, M. A.; Shavakandi, M. The Preparation, Characterization and Application of COOH Grafting on Ferrite−Silica Nanoparticles. *RSC Adv.* **2016**, *6*, 17560−17566.

(61) Arvand, M.; Hassannezhad, M. Magnetic Core−shell Fe_3O_4@SiO_2/MWCNT Nanocomposite Modified Carbon Paste Electrode for Amplified Electrochemical Sensing of Uric Acid. *Mater. Sci. Eng., C* **2014**, *36*, 160−167.

(62) Lu, Z.; Dai, J.; Song, X.; Wang, G.; Yang, W. Facile Synthesis of Fe_3O_4/SiO_2 Composite Nanoparticles from Primary Silica Particles. *Colloids Surf., A* **2008**, *317*, 450−456.

(63) Massart, R. Preparation of Aqueous Magnetic Liquids in Alkaline and Acidic Media. *IEEE Trans. Magn.* **1981**, *17*, 1247−1248.

(64) Oleshkevich, E.; Teixidor, F.; Rosell, A.; Viñas, C. Merging Icosahedral Boron Clusters and Magnetic Nanoparticles: Aiming toward Multifunctional Nanohybrid Materials. *Inorg. Chem.* **2018**, *57*, 462−470.

(65) Clogston, J. D.; Patri, A. K. Zeta Potential Measurement. In *Characterization of Nanoparticles Intended for Drug Delivery. Methods in Molecular Biology (Methods and Protocols)*; McNeil, S., Ed.; Humana Press, 2011; Vol. *697*.

(66) Can, M. M.; Coşkun, M.; Firat, T. A Comparative Study of Nanosized Iron Oxide Particles; Magnetite (Fe_3O_4), Maghemite (γ-Fe_2O_3) and Hematite (α-Fe_2O_3), Using Ferromagnetic Resonance. *J. Alloys Compd.* **2012**, *542*, 241−247.

(67) Gawande, M. B.; Rathi, A. K.; Tucek, J.; Safarova, K.; Bundaleski, N.; Teodoro, O. M. N. D.; Kvitek, L.; Varma, R. S.; Zboril, R. Magnetic Gold Nanocatalyst (Nanocat-Fe-Au): Catalytic Applications for the Oxidative Esterification and Hydrogen Transfer Reactions. *Green Chem.* **2014**, *16*, 4137−4143.

(68) Rathi, A. K.; Gawande, M. B.; Pechousek, J.; Tucek, J.; Aparicio, C.; Petr, M.; Tomanec, O.; Krikavova, R.; Travnicek, Z.; Varma, R. S.; Zboril, R. Maghemite Decorated with Ultra-Small Palladium Nanoparticles (γ-Fe_2O_3−Pd): Applications in the Heck−Mizoroki Olefination, Suzuki Reaction and Allylic Oxidation of Alkenes. *Green Chem.* **2016**, *18*, 2363−2373.

(69) Plešek, J.; Base, K.; Mares, F.; Hanousek, F.; Stibr, B.; Hermanek, S. Potential Uses of Metallocarborane Sandwich Anions for Analysis, Characterization and Isolation of Various Cations and Organic Bases. *Collect. Czech. Chem. Commun.* **1984**, *49*, 2776−2789.

(70) Wang, X.-D.; Shen, Z.-X.; Sang, T.; Cheng, X.-B.; Li, M. F.; Chen, L. Y.; Wang, Z.-S. Preparation of Spherical Silica Particles by Stöber Process with High Concentration of Tetra-Ethyl-Orthosilicate. *J. Colloid Interface Sci.* **2010**, *341*, 23−29.